Grenoble Geomechanics Group

Laboratoire 3SR

Annual Report #1

March 2015

Université Joseph Fourier GRENOBLE

Grenoble INP

cnrs

Grenoble Geomechanics Group

Laboratoire 3SR
Université de Grenoble Alpes
Domaine Universitaire
BP 53
38041 Grenoble cedex 9 France
Phone: (33) 4 76 82 50 27
Website: https://www.3sr-grenoble.fr/

Grenoble Geomechanics Group, https://www.3sr-grenoble.fr/spip.php?rubrique29
Annual Report # 1
PDF version of this report available at: http://projects.3sr-grenoble.fr/geomecanique
Geonum Edition: ISRN GEONUM-NST--2015-01--ENG, 2015.
March 2015

Preface

This is the first year of existence of the Grenoble Geomechanics Group. This group was initiated to put together a team effort in developing advanced experimental and modeling tools to study geomaterials in order to bring a detailed and in-depth understanding of their behaviors.

The studies carried out by the members of the group do not only covers the microscopic scale (grain scale, including clay) or the laboratory sample scale, but also the civil, mining and petroleum engineering field. The present activities greatly benefit from previous internationally recognized developments made in Grenoble in Geomechanics by former members of the laboratoire 3SR.

We are now pursuing these thrilling research activities with the same energy and enthusiasm. Still investing in our own experimental, theoretical and numerical tools, several of them are particularly innovative. For example, with an X-ray tomography equipment associated to the Digital Image Correlation technique, it is now possible to track at the grain scale, the response of highly heterogeneous medium.

We are also enough active to develop different complementary numerical tools based on, for examples, the Lattice Boltzmann Method, Finite Element Method, Finite Difference Method, Material Point Method, Arbitrary Lagrangian–Eulerian approach, Finite Volume Method as well as Discrete Element Method.

In this annual report of the Grenoble Geomechanics Group of the laboratoire 3SR, you will find the contribution of the Ph.D. students and some Post-Docs, which gives an overview of the dynamism of these young researchers.

We take this opportunity to thank all of our sponsors, both public and private which have made these research activities possible.

Frédéric-Victor Donzé for the **Grenoble Geomechanics Group**

Contents

Contenu

Members of the Grenoble Geomechanics Group

 **Abdou Hashem** PhD

 **Aboul Hosn Rodaina** PhD

 **Albaba Adel** PhD

 **Andò Edward Carlo Giorgio** Researcher CNRS

 **Argilaga Claramunt Albert** PhD

 **Bésuelle Pierre** Researcher CNRS

 **Bonilla-Sierra Viviana** PhD

 **Boulon Marc** Emeritus Professor

 **Caillerie Denis** Emeritus Professor

 **Chalak Caroline** PhD

 **Chambon René** Emeritus Professor

 **Chareyre Bruno** Ass. Professor at Grenoble INP

 **Combe Gaël** Professor at Grenoble INP

 **Cuervo Stiven** PhD

 **Dadda Abdelali** PhD

 **Dal Pont Stefano** Professor at UJF

 **Darve Félix** Emeritus Professor

 **Daudon Dominique** Ass. Professor at UJF

 **Deiros Quintanilla Ivan** PhD

 **Desrues Jacques** Research Leader CNRS

 **Donzé Frédéric Victor** Professor at UJF

 **Emeriault Fabrice** Professor at Grenoble INP

 **Gracia Fabio** PhD

 **Houda Moustafa** PhD

 **Jenck Orianne** Ass. Professor at UJF

 **Karatza Zeynep** PhD

 **Khaddour Ghonwa** PhD

 **Lanatà Patrizia** PhD

 **Li ZhaoHua** PhD

 **Loret Benjamin** Professor at Grenoble INP

 **Mahmutovic Dino** PhD

 **Marzougui Donia** PhD

 **Nghiem Huu Luyen** PhD

 **Papachristos Efthymios** PhD

 **Pelizzari Benjamin** PhD

 **Plua Carlos** PhD

 **Richefeu Vincent** Ass. Professor at UJF

 **Roger Eve** PhD

 **Salager Simon** Ass. Professor at UJF

 **Sibille Luc** Ass. Professor at UJF

 **Silva Matias** Post-Doc

 **Tejada Ignacio** Post-Doc

 **Tengattini Alessandro** PhD

 **Tsopela Alexandra** PhD

 **Van den Eijnden Bram** PhD

 **Viggiani Gioacchino (Cino)** Professor at UJF

 **Villard Pascal** Professor at UJF

 **Wiebicke Max** PhD

 **Yuan Chao** PhD

Part One: Characterization of the internal microstructures of geomaterials

Towards the measurement of fabric in granular materials with x-ray tomography

M. Wiebicke[a,b,c], E. Andò[a,c], G. Viggiani[a,c] & I. Herle[b]

[a] *Univ. Grenoble Alpes, 3SR, F-38000, Grenoble, France*

[b] *Technische Universität Dresden, Institute of Geotechnical Engineering, Germany*

[c] *CNRS, 3SR, F-38000, Grenoble, France*

ABSTRACT

Recent developments in experimental geomechanics have enabled the characterization of grain-scale measurements with x-ray computed tomography (CT) and thus paved the way for the micromechanical characterization of granular materials. However, the images coming from x-ray CT are limited with respect to their resolution if a representative specimen is to be investigated [Andò et al, 2013]. When trying to extract the fabric of such images the accuracy of the methods is crucial. This study investigates the accuracy of some standard and advanced approaches to determine different fabric entities with synthetic as well as real images.

INTRODUCTION

In engineering, soil behavior is treated by continuum constitutive models. These are usually based on phenomenological approaches and therefore suffer different drawbacks. In order to overcome these phenomenological approaches and to increase our understanding of soil behavior, it is crucial to start from a micromechanical scale and relate the interactions of the discrete particles that define a granular medium with the macroscopic observations and phenomena that can be and already have been made from standard soil testing. The continuum based constitutive models can then be enhanced using these relations.

Extracting the fabric as one of the characteristics of granular materials has been the topic of numerous studies since a long time. In [Brewer, 1964] the fabric is defined by the spatial arrangement of the solid particles and the associated voids. It can be composed of scalar quantities, such as the local void ratio or the coordination number, and orientational data [Oda et al, 1980]. Possible orientational fabric entities can be the principal particle orientation, the contact normal orientation [Oda, 1972] or a measurement of void fabric [Oda et al, 1985; Li & Li, 2009].

Historically, one way of extracting the fabric has been to inject a polyester resin into a soil specimen and to cut it into thin sections allowing for example the determination of the particle and the contact normal orientation [Oda, 1972]. As this approach is a post-mortem analysis different but similar specimen are loaded to different states and the fabric is then extracted. A

non-destructive way to investigate the relation between fabric and macroscopic behavior is to use two-dimensional rods in special apparatus. Here, photos are taken in defined intervals allowing the micromechanical behavior to be compared to the macroscopic one [Calvetti et al, 1997]. Furthermore, discrete methods are able to simulate the interactions between sets of particles caused by a macroscopic loading [Fu & Dafalias, 2010]. The determination of fabric is fairly easy in the simulations as the positions and geometric relations between the particles are perfectly known. However, all of these approaches are limited either to the nature of post-mortem analyses or the two-dimensional and regular shape of the materials investigated.
This could be overcome with the application of x-ray tomography on granular materials, which was mainly developed in the last two decades [Hall et al, 2010; Viggiani et al, 2013]. However, when trying to image specimen of a representative amount of grains, the resolution of individual grains and grain-to-grain contacts is limited and thus poses problems when trying to extract different fabric entities [Andò et al, 2013]. Applying standard approaches to determine for example the contact normal orientation leads to strongly biased results [Viggiani et al, 2013; Jaquet et al, 2013]. Therefore, quantifying the accuracy of different standard and advanced approaches is crucial in order to deal with the complexity of granular materials. This paper presents a study on the accuracy of the determination of the principal particle orientations, the detection of contacts and the orientation of contact normals using either high resolution x-ray images or synthetic ones.

PARTICLE ORIENTATIONS

One of the above mentioned fabric entities is the principal particle orientation. It can be defined as the eigenvectors of the moment of inertia tensor. The tensor is calculated on a segmented binary image of an individual particle. These orientation vectors can be subject to non-physical changes of orientations [Andò et al, 2012]. It was guessed that the reason for such snapping is either due to the shape of the particles or to the resolution, meaning that for a grain with a low number of voxels defining it, a rotation might cause a loss of a few voxels at a certain side and thus change the principal axis [Andò et al, 2011].

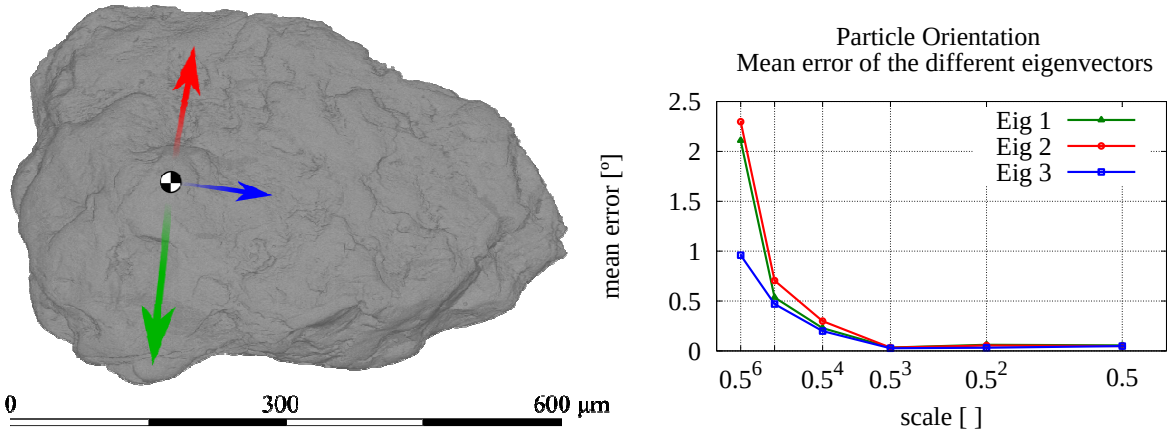

Figure 1**: Particle Orientation. Left: 3D rendering of the high resolution scan of the single Hostun sand grain. The colored arrows represent the eigenvectors of the moment of inertia tensor. Right: Relation between the accuracy of the eigenvectors of the moment of inertia tensor and the scale of the image. The colors in the plot represent the eigenvectors in the 3D rendering.**

To answer the question of whether the snapping of principal particle orientations is caused by the resolution of the image or the shape of the grain, a single Hostun sand grain was scanned using a nano x-ray CT, see figure 1 (left). To assess the accuracy of the determination of the principal particle orientation, a high resolution greyscale image of the Hostun sand grain was rotated via 4 different angles around a defined axis and these different configurations were scaled down to a minimum with a grain resolution corresponding to a typical size measured in an experiment in the x-ray CT. The orientations determined on the original high resolution image were defined as the reference and rotated in the same way as the images. The error was then defined as the angle between the orientations of the high resolution image and the scaled down images.
The results of this study can be seen in figure 1 (right). The mean error was calculated for each scaling using the three eigenvectors and all investigated rotations. As it was expected, the mean error increases with a decreasing resolution of the image. The eigenvector corresponding to the smallest eigenvalue (Eig3, blue vector) of the moment of inertia tensor was found to be the most accurate one for this grain. This is caused by the shape of the grain, as it has a clearly defined long axis which corresponds to this vector. The mean error at a reasonable scale, which is the lowest one investigated here, amounts 1.8° for a highly angular grain and the investigated rotations. It can be expected that the accuracy of this approach for rounded grains is lower as the principal axes are not as clearly defined. Surprisingly, no particle snapping was encountered.
In a further study more rotations around different axes will be considered to get a statistically value idea of the accuracy of this method.

CONTACT DETECTION

Another and probably the more common fabric entity is the orientation of the contact normal between two grains. Apart from the accuracy of the contact orientation, the detection of the contacts is a crucial point itself.
Artificial spheres were chosen in order to investigate the basic behavior of the current techniques. The artificial spheres were created using Kalisphera [Tengattini & Andò, submitted] which takes into account the partial volume effect and is able to blur the apart from that perfect spheres. In figure 2 a slice through the center of two exemplary spheres and a 3D rendering of the two spheres are presented. The spheres are put just in contact without any overlap, but due to the partial volume effect of both spheres in the contact region the contact area is increased, which can clearly be seen in the 3D rendering.

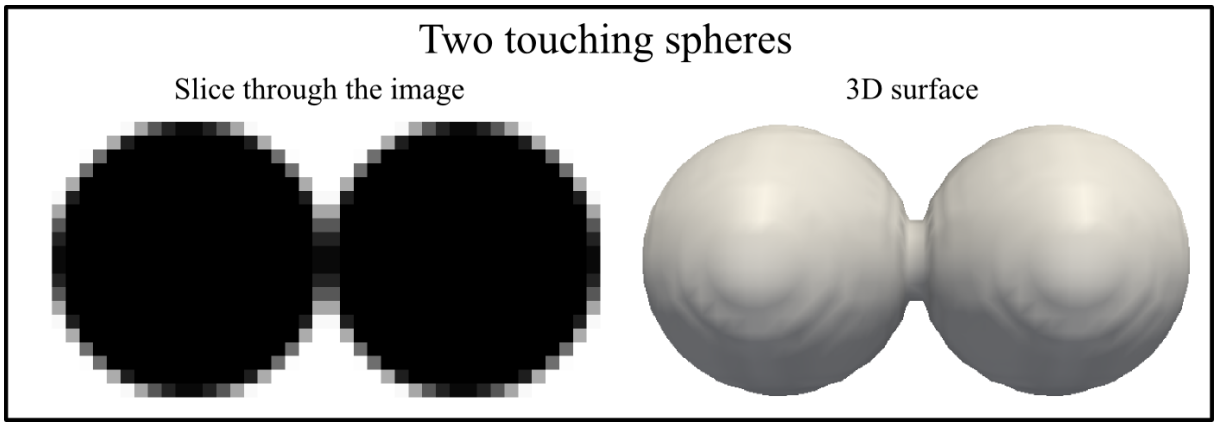

Figure 2: **Image of two touching partial volume spheres created using Kalisphera.**

Limitations of the common (state-of-the-art) approach

To investigate the contact detection two partial volume spheres will be created in a specific distance with a random branch vector in between them. The image is binarized using a global threshold (volumetrically correct threshold is 0.5) and it is checked whether the spheres are in contact or not. If the distance is for example 1 voxel and no contact is found, the image will be blurred until a contact can be found. This analysis was conducted for 4000 pairs of spheres connected with randomly orientated branch vectors.

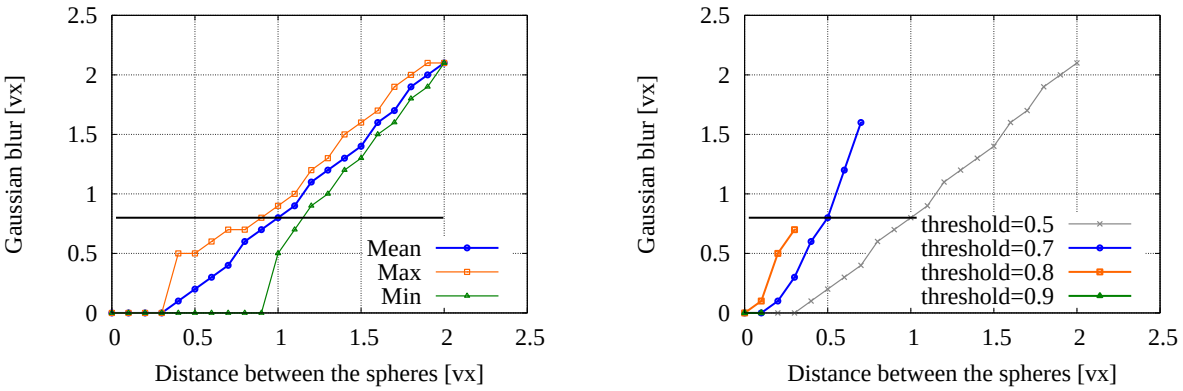

Figure 3: **Investigation on the accuracy of contact detection. A point indicates when a contact is found. The black line marks a system-inherent level of blur [Tengattini & Andò, submitted]. Left: Evaluation of the analysis with 4000 randomly distributed spheres. Global threshold = 0.5. Right: Application of a local threshold on the contact area**.

The result of this approach varying the distance and the blur as described above for different orientations is plotted in figure 3 (left). The points in this graph indicate when a contact is found. Let's take for example the blue continuous line (Mean): for a distance of 1 voxel no contact can be found for the clean image. The blur has to be introduced and increased to a value of 0.8 until a contact is found again. Having a closer look at the 3D rendering in figure 2, the reason of this over-detection becomes obvious. The values of the voxels in the contact region are influenced by the partial volume effect of both spheres. Even if the spheres are not touching, a voxel close to both spheres might get a value higher than the global threshold as both spheres take part of the volume of the considered voxel.
Tengattini & Andò (submitted) found that a reasonable blur in images taken with x-ray CT is about 0.8 voxels. Thus, the mean error of the contact detection at this system-inherent blur lies in between 0.9 and 1.2 voxels, meaning at a distance of up to 1 voxel the state-of-the-art approach will still detect contacts although there are none. In this way, contacts are systematically over-detected, implying a higher number of contacts and making an impact on the statistics of the orientation measurements.

Overcoming the limitations

As contacts should only be selected where they exist, a refinement of the current approach has to be done. After applying the procedure described above, solid voxels in between grains are identified as contacts. These voxels will be taken into account again and a local threshold, which has to be higher than the global one, will be applied on them. Assuming such a local threshold is known, the contacts, that were identified beforehand as contacts but which are none, can be erased from the list of contacts. The image which will be worked on in the following steps, to determine the contact orientation for example, will still be the one

binarized using the global threshold. The local re-thresholding is used only to clean the list of detected contacts as globally too much information would be lost using such a high threshold.
The results of this refined approach are plotted in figure 3 (right) in the same way as before, but only mean values are included. It can clearly be pointed out that the error of contact detection decreases significantly introducing a local threshold. Nevertheless, the local threshold has to be chosen with care in order not to loose contacts. As the images used in this study were purely artificial ones, no recommendation for experiments on real granular materials in x-ray CT can be given so far. Applying the refined approach on images of real granular materials will be subject of a further study.

CONTACT ORIENTATION

To determine contact normal orientations usually a standard watershed approach is used [Gonzalez & Woods, 2007]. Recently, the use of power watersheds to extract contact orientations from images of granular materials was investigated and compared to standard watersheds [Jaquet et al, 2013]. Standard watersheds introduce a strong bias on the resulting orientations and it was found in this study that the random walker method does not introduce such a bias. Furthermore, the application of level set methods on individual grains coming from x-ray CT images was analysed with surprisingly good results [Vlahinic et al, 2013]. In this study, the use and the accuracy of different watershed methods was investigated statistically and the application of level sets was studied.

Watershed methods

In order to assess the performance of the different approaches, they were applied on realistic partial volume spheres, created using Kalisphera [Tengattini & Andò, submitted], as the contact orientation for a pair of spheres is identical to the branch vector, which is imposed. In order to obtain statistically exploitable results, a number of 4000 pairs of spheres with a randomly orientated branch vector were created.
A standard watershed method assigns a label directly to each voxel, whereas the random walker calculates a probability for each voxel of belonging to the either one of two given seeds. The image is then labeled depending on that probability map. Using the probability of the voxels in the contact region, the contact positions can be directly calculated as the 0.5 probability between two neighboring voxels [Jaquet et al, 2013]. The contact orientation can then be determined by fitting a plane onto these intervoxel positions using principal component analysis (PCA) and identifying its normal.
In figure 4 (left) the results of such an investigation for spheres of different diameters are plotted. The error is defined as the angle between the randomly imposed branch vector and the contact normal determined by the evaluation of the watershed results. The random walker approach yields far better results in terms of accuracy. The application of the segmentation approaches on the blurred image gave a lower mean error, indicating that the size of the contact region influences the accuracy as it grows with an increase of blur.

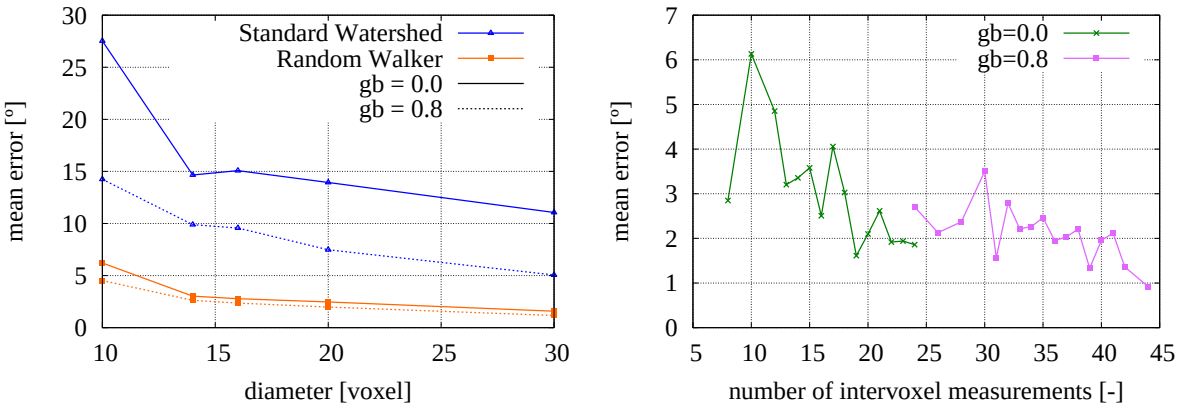

Figure 4: **Accuracy of watershed methods to determine the contact orientation. Left: Relation of mean error and the size of the spheres. Right: Relation of mean error to the number of intervoxel positions used for PCA for spheres of a diameter of 16 voxels and the random walker approach. gb …Gaussian blur.**

Furthermore, the geometrical properties seem to have an impact on the accuracy of the contact orientation as the mean error decreases with an increasing size of the spheres. The number of intervoxel positions used in the PCA was chosen as the property to investigate as the number of data in PCA should have a strong impact on the results. The comparison of the number of intervoxel position and the error for spheres of a diameter = 16 voxels is plotted in figure 4 (right). As assumed, the number of intervoxel positions influences the accuracy of the measurement. The higher the number the lower is the actual error. In this case, 14 intervoxel positions seem to mark a border after which the error oscillates around and below 3°. However, this analysis was done using synthetic spheres and will have to be applied on real images coming from x-ray CT.

Level set method

The level set method describes an individual particle as a continuous distance function called the level set. As it is a continuous function it can be arbitrarily located on a computational grid and thus does not suffer resolution effects. The use of this method to characterize individual particles was shown in [Vlahinic et al, 2013].

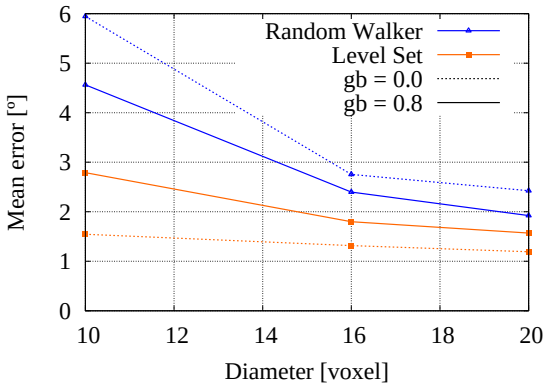

Figure 5: **Contact orientation. Relation of the mean error of 4000 pairs of spheres with their diameter. Comparison of the performance of the level set method and the random walker approach.**

To study the accuracy of the level set method for determining the contact orientation, the same analysis as before was carried out. The constant parameters that control the level set evolution were set to: μ=0.05, λ=3, α=-1.8, β=3 (as defined in equation 4.2 given in [Vlahinic et al, 2012]); the time step and the number of iterations were set to 0.5 and 250, respectively. Furthermore, the labeled image coming from the random walker segmentation served as input for the level set method.
In figure 5 the results of the study relating the mean error of contact orientation with the diameter are shown. The random walker yields a higher mean error for either perfect or blurred images. The level set method results in higher mean errors for blurred compared to perfect images, but still yields a mean error that is lower than 2° in the region of interest.
In a further study of the sensitivity of the level set method towards its input parameters it was found that these values have a high impact. The accuracy of the contact orientation of a single pair of spheres was improved remarkably by primarily adapting the number of iterations and varying the parameters λ and μ. Although figure 5 suggests that a blurred image yields lower accuracy using the level set method, this could not be found true in the sensitivity analysis, as the accuracy depends highly on the calibration of its parameters and the chosen number of iterations.
However, as in this study the number of iterations was prescribed without any measure of convergence, further studies have to be conducted in order to define a measure of convergence and optimize the method.

CONCLUSION

In this study different approaches to extract the fabric of a granular material were investigated with respect to their accuracy. The principal particle orientation was determined using the moment of inertia tensor and it was found to yield relatively low errors for the investigated scales and orientations. Surprising results were obtained in the investigation of the contact detection: using the regular approaches contacts are systematically over-detected due to a combined partial volume effect, which would necessarily lead to noise in the statistical measurements when analyzing real specimens with thousands of grains and contacts between them. Applying a local threshold on contact areas that were identified with the usual approach improves the accuracy substantially. A statistical analysis was conducted on different methods to determine the contact orientation of two touching spheres. The size of the contact area, namely the number of intervoxel positions, appears to be a possible indicator of the accuracy of a measurement. Level sets smooth the way to increase the accuracy of such measurements, but must be further improved.
We have chosen to start from synthetic spheres, where the geometry and thus the contact orientations are well known. This enabled us to precisely quantify the error of the different approaches that were used to determine the contact orientation. The next step will be to carry out a similar analysis on realistic images of materials such as glass ballotini, for which the ground truth of contact orientation is approximately known. The investigation of particle orientation will be applied on a large number of random orientations at the different scales in order to obtain statistically exploitable results.
These advanced techniques and the knowledge of their accuracy and their weaknesses allows a reliable extraction of the fabric of real soils consisting of thousands of grains. The fabric can then be statistically described in different kinds of fabric tensors [Kanatani, 1984]. Using the tensorial description of fabric, the statistical micromechanics can be related to the macroscopic behavior, which finally leads to the possibility of improving existing phenomenological continuum models.

ACKNOWLEDGEMENTS

The work reported in this paper is part of a project funded by the DFG (HE 2933/8-1). The financial support is gratefully acknowledged.

REFERENCES

Andò, E.; Hall, S. A.; Viggiani, G.; Desrues, J. & Besuelle, P. 2012. Experimental micromechanics: grain-scale observation of sand deformation, *Géotechnique Letters* 2, 107-112

Andò, E.; Hall, S. A.; Viggiani, G.; Desrues, J. & Besuelle, P. 2011. Grain-scale experimental investigation of localised deformation in sand: a discrete particle tracking approach, *Acta Geotechnica*.

Andò, E.; Viggiani, G.; Hall, S. A. & Desrues, J. 2013. Experimental micro-mechanics of granular media studied by x-ray tomography: recent results and challenges, *Géotechnique Letters* 3, 142-146

Brewer, R. 1964. *Fabric and mineral analysis of soils*, J. Wiley, New York.

Calvetti, F.; Combe, G. & Lanier, J. 1997. Experimental micromechanical analysis of a 2D granular material: relation between structure evolution and loading path, *Mechanics of Cohesive-frictional Materials* 2, 121-163.

Fu, P. & Dafalias, Y. 2010. Fabric evolution within shear bands of granular materials and its relation to critical state theory, *International Journal for Numerical and Analytical Methods in Geomechanics.*

Gonzalez, R. C.; Woods, R. E. 2007. *Digital Image Processing*, Prentice-Hall, 3rd edition.

Hall, S.A.; Bornert, M.; Desrues, J.; Pannier, Y.; Lenoir, N.; Viggiani, G. & Besuelle, P. 2010. Discrete and continuum analysis of localised deformation in sand using X-ray μCT and volumetric digital image correlation, *Géotechnique* 60, 315-322.

Jaquet, C.; Andò, E.; Viggiani, G. & Talbot, H. 2013. Estimation of Separating Planes between Touching 3D Objects Using Power Watershed, International Symposium on Mathematical Morphology 11.

Kanatani, K.. 1984. Distribution of directional data and fabric tensors, *International Journal of Engineering Science* 22, 149-164.

Li, X. & Li, X. 2009. Micro-macro quantification of the internal structure of granular materials, *Journal of engineering mechanics* 135, 641-656.

Oda, M.; Konishi, J. & Nemat-Nasser, S. 1980. Some experimentally based fundamental results on the mechanical behavior of granular materials, *Géotechnique* 30, 479–495.

Oda, M. 1972. Initial fabrics and their relations to mechanical properties of granular material, *Soils and Foundations* 12, 17-36.

Oda, M.; Nemat-Nasser, S. & Konishi, J. 1985. Stress-induced anisotropy in granular masses, *Soils and Foundations* 25, 85-97.

Tengattini, A. & Andò, E. Kalisphera: an analytical tool to reproduce the partial volume effect of spheres imaged in 3D (Submitted to *Measurement Science and Technology*).

Viggiani, G.; Andò, E.; Jaquet, C. & Talbot, H. 2013. Identifying and following particle-to-particle contacts in real granular media: An experimental challenge, *Powders and Grains, AIP Conf. Proc*. 1542, 60-65.

Vlahinic, I.; Andò, E.; Viggiani, G. & Andrade, J. E. 2013. Towards a more accurate characterization of granular media: extracting quantitative descriptors from tomographic images, *Granular Matter* 16 (2013), 9-21.

Sand displacement field analysis during pile installation using x-ray tomography and digital image correlation

M. Silva & G. Combe
Laboratoire Sols, Solides, Structures, Grenoble, France
matias.silva@3sr-grenobe.fr gael.combe@3sr-grenoble.fr

ABSTRACT

This article presents the results of a 5.5 mm model pile installation on a silica sand sample under isotropic confinement by using X-ray microtomography and three dimensional Digital Image Correlation on a model calibration chamber. The incremental sand displacement field was calculated during the pile installation both locally around the pile tip and for the entire volume. Displacement vectors and normalized strain contours are obtained for each incremental loading step. Evidence of sand flows near the pile tip gives new ideas about the possible mechanisms controlling the lateral friction of piles.

INTRODUCTION

The kinematics behind the installation of driven piles in silica sand remains an area of great uncertainties. Most of the shear capacity of a driven pile takes place on a thin layer of sand in contact with the pile's surface. Several authors have suggested that the time dependent behaviour of this sand layer and possible sand arching effects generated during pile installation would control the long term capacity of driven piles in sand and probably explain the phenomenon of lateral friction set-up, Åstedt et al. (1992), Chow et al. (1998), Axelsson (2000). It is then essential to understand the interaction between the pile and the surrounding soil.

Robinsky & Morrison (1964) using x-ray radiographies during the installation of a model pile concluded that a zone of loose sand will form around the pile during its installation. The sand near the pile's surface is dragged down with the pile movement under the constant confinement of the surrounding soil resulting in the formation of an arc of sand around the pile. Chong (1998) from density measures on large calibration chamber tests, Allersma (1988) and Allersma et al. (2002) from photoelastic observations on a plain strain model, and Van Nes (2004), Ngan-Tillard et al. (2005) and Morita et al. (2007) using x-ray tomography on small laboratory samples have confirmed the presence of a layer of loose sand around the shaft.

White and Bolton (2002) and White and Bolton (2004) using Particle Image Velocimetry (PIV) on a plain strain model suggested that a zone of high density will develop around the pile as the latter embeds deeper into the sand mass. Their results show irrecoverable volume reduction beneath the pile tip resulting from particle breakage and soil compaction. As the pile embeds into this highly overconsolidated sand, a zone of high density will be created around the shaft. White and Bolton suggested that with continuing pile installation the cylindrical cavity of the stiff overconsolidated sand will collapse leading to a reduction in radial stress and to a similar arching phenomenon as the one presented by Robinsky & Morrison (1964). The number of shearing cycles during installation plays a crucial role when comparing results from monotonic and pseudo-dynamic installation, White and Lehane (2004). Yang et al. (2010) reported the presence of a thin layer of compacted broken grains with high particle interlocking around a cyclically jacked model pile

Allersma (1988) observed high stress concentration beneath the pile when embedding in the soil with rotation of principal stresses with the principal stress perpendicular to the tip edge. Recently Jardine et al. (2013) interpreted the sand stress field during the installation of model pile into a pressurized calibration chamber. Their results show similar stress distributions as those suggested by White and Bolton (2004).

This paper presents the first results of an experimental programme devoted to the analysis of the displacement field developed after the installation of a model pile into a silica sand sample in a model calibration chamber using micro tomography (x-ray micro CT) and three dimensional (3D) digital image correlation (DIC).

EXPERIMENTAL ARRANGEMENTS

The tests were conducted in the micro CT tomograph of the laboratory 3SR in Grenoble, France. An un-instrumented 5 mm diameter (B) cone ended aluminum model pile was installed by monotonic loading on a dry silica sand sample under an isotropic confinement pressure.

The sample consists of a 70 mm diameter (D), 100 mm height of Fontainebleau NE34 silica sand. Bolton et al. (1999) concluded from centrifuge tests on model piles with this sand, that the minimum distance between the pile and any hard boundary (D/B) should be at least 10, and that the ratio between pile diameter and the mean particle size (B/d_{50}) should be at least 20. In our case the ratio D/B and B/d_{50} are 14 and 23 respectively. Sample size and mean grain size are restricted by the scanning conditions during x-ray micro CT. Possible scale effects are expected in the results.

Table 1: Index properties of Fontainebleau NE34 sand

e_{min}	e_{max}	d_{10} (mm)	d_{50} (mm)	d_{60} (mm)
0.51	0.90	0.15	0.21	0.23

Samples were prepared by four consecutive layers of 25 mm height and a density of 1.60 gr/cm^3, corresponding to a relative density of approx. 70%. A constant isotropic confinement pressure of 100 kPa was applied during pile installation and scanning.

For practical reasons, the pile was installed from the bottom of the cell monotonically 50 mm into the sand mass at a rate of 0.1 mm/s where a first tomogram was obtained. The pile head load was kept constant during the different tests.

Several tomograms were then obtained after incremental pile displacements ranging from 0.5 to 2.0 mm, in order to perform further digital image correlation analyses to evaluate the incremental displacement field between consecutive loading steps.
The general arrangements for the tests are presented in figure 1.

X-RAY MICRO CT AND 3D-DIC

The pile penetration was done progressively, stopping penetration at defined intervals for 3D scanning. Scans were settled to a tension of 200kV and a current of 150 µA. 1024 radiographies were made of the sand samples for the reconstruction of the entire volume. Using micro CT, a 3D digital image of the x-ray attenuation in the soil sample and the pile was obtained. Two different distances from the x-ray source were considered in order to perform a global and local tomography, which allow focusing on precise zones inside the sample. A resolution of approx. 23 and 43 µm/pixel were obtained for global and local tomography respectively.

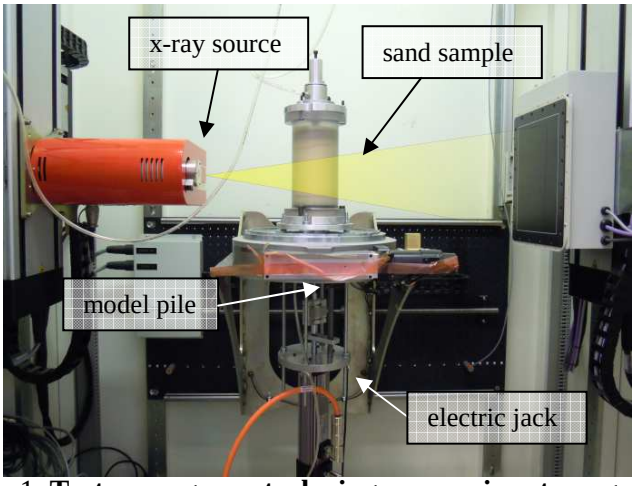

Figure 1: **Test arrangements during x-ray micro tomography**.

An example of the reconstructed volume during a local tomography is presented in figure 2.

The spatial deformation between two consecutive x-ray tomograms was mapped and analyzed by applying 3D-DIC, which compares the texture of character between a predefined volume sample. For the results here presented a 14 pixels side cube was considered.

The full strain tensor field in the form of volumetric strain and maximum shear (distortional) strains was derived using the 3D-DIC code TomoWarp (Hall, 2006; Hall et al., 2010). This code calculates the strains from the derived displacements under continuum assumptions.

Similar techniques were recently used by Paniagua et al. (2013) for the analyses of a penetrating CPT in silts.

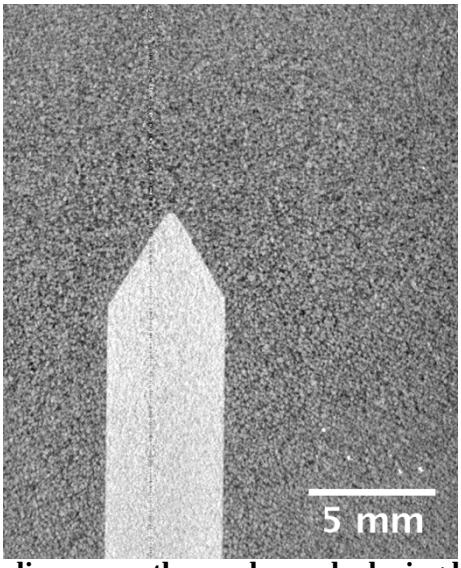

Figure 2: **Vertical slice across the sand sample during local tomography.**

RESULTS

Typical results from an incremental pile displacement are presented in figures 3 and 4. Displacement contours are plotted in the vertical and horizontal axis at normalized distances from the pile axis, *h/r*, where *h* is the distance from the pile axis, and *r* the pile radius.

The results show two distinct areas of particle movements. The first zone, which concentrates most of the movements, is observed beneath the pile tip. The sand particles follow the pile movement in the vertical direction and spread horizontally perpendicularly to the cone ended tip angle, at approx. 60°. Most of the particle displacements are concentrated in a region up to a distance of approx. 1 pile diameter beneath the tip.

A second characteristic area with lower displacement locates behind the tip pile. In this region a thin layer of sand follows the movement of the pile in the vertical direction, whereas the surrounding soil is shows evidence of particle recirculation. Figure 6 shows two dimensional representations of displacement vectors in this area. The displacement field was calculated every 4 pixels. These observations are similar to those obtained by Pater & Nieuwenhuis (1986) using photographic techniques. As the pile movement progresses, sand particles are moved upward in the opposite direction of the pile movement, and against the pile by the surrounding soil. This particle recirculation seems consistent with the radial stress reduction in the soils stresses measured by Jardine et al. (2013).

As presented in Figure 6, the magnitude of the displacement in the area where recirculation takes place is significantly lower than beneath the pile tip. Analyses continue to evaluate the effects of confining pressure, imposed pile displacement and mean particle size.

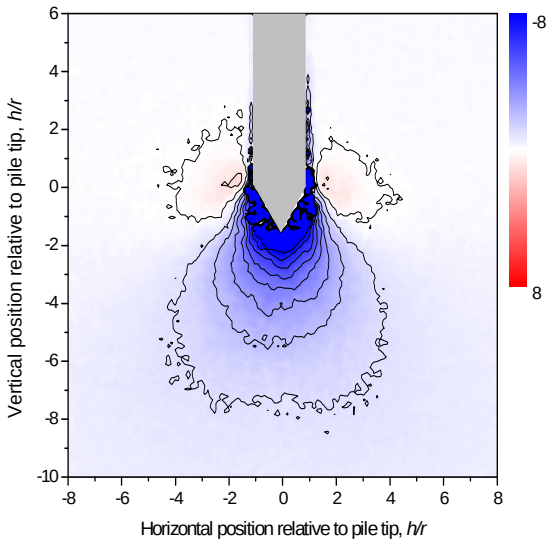

Figure 3: **Incremental displacement along Y-axis after a 2 mm pile head displacement (values in pixel, 1 pixel = 43 µm).**

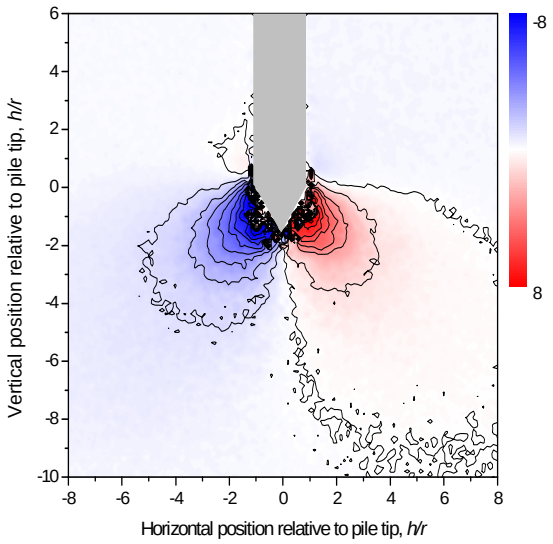

Figure 4: **Incremental displacement along vertical axis after a 2 mm pile head displacement (values in pixel, 1 pixel = 43 µm)**

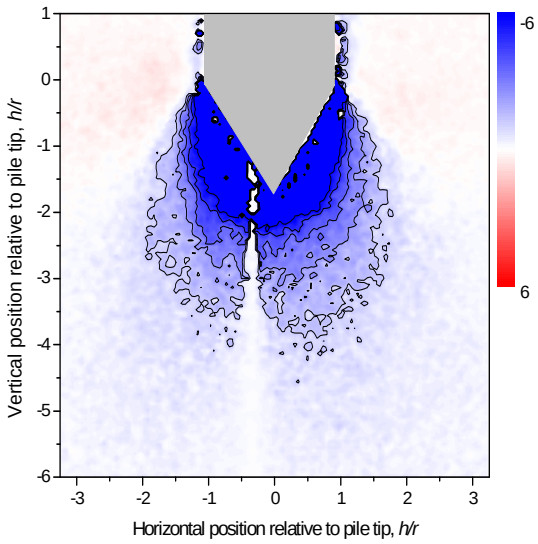

Figure 5: **Incremental displacement along vertical axis after a 2 mm pile head displacement (values in pixel, 1 pixel = 23 µm)**

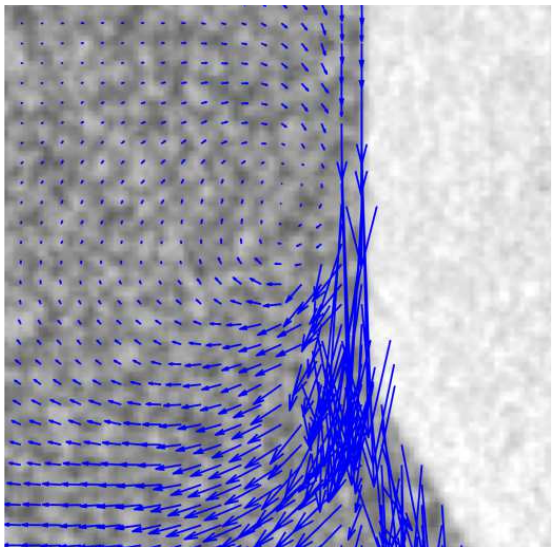

Figure 6: **Two dimensional displacement vectors around the pile tip after a 2 mm pile head displacement. Vectors are amplified by a factor 10.**

The analysis of strain patterns during a loading step can be characterized by figures 7 and 8. The main strains develop mostly around and beneath the pile tip. A zone of high vertical contraction and horizontal extension develops beneath the pile tip as the pile is continuously pushed into the sand. Behind this zone and almost perpendicular to the cone tip edge, a zone of vertical extension and horizontal compression will develop. These results confirm White and Bolton (2004) findings from PIV tests on plain strain models.

The interaction between these two zones would explain the recirculation of sand particles presented in figure 6. As the pile is installed into the sand mass, highly compacted sand particles from beneath the pile tip are pushed radially upwards with the tip movement, and compressed against the pile surface by the surrounding soil.

Figures 9 and 10 show a comparison between the shear strain developed between two different steps of 0.5 and 2 mm. Shear strain concentrate locally around the tip and as the displacement steps increase, the area of influence becomes more important and expands to the pile's shaft.

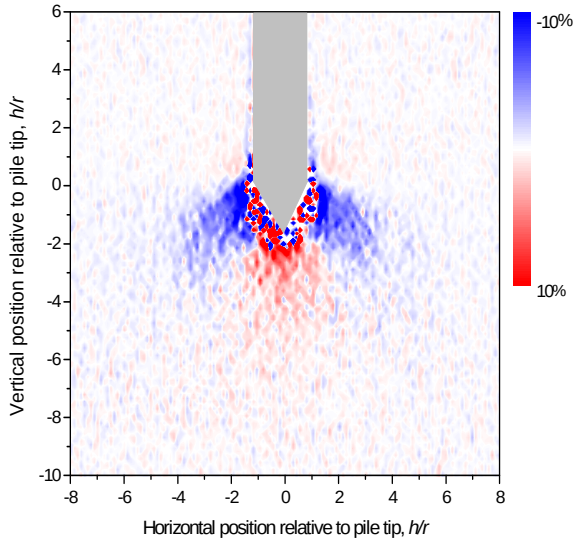

Figure 7: **Incremental horizontal strain after a 2 mm pile head displacement**

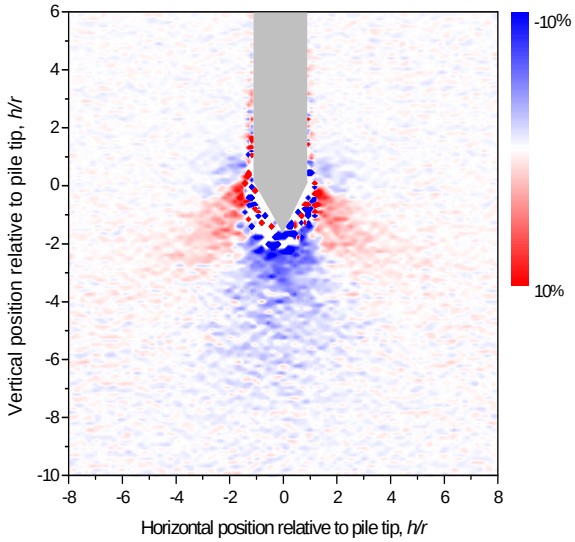

Figure 8: **Incremental vertical strain after a 2 mm pile head displacement**

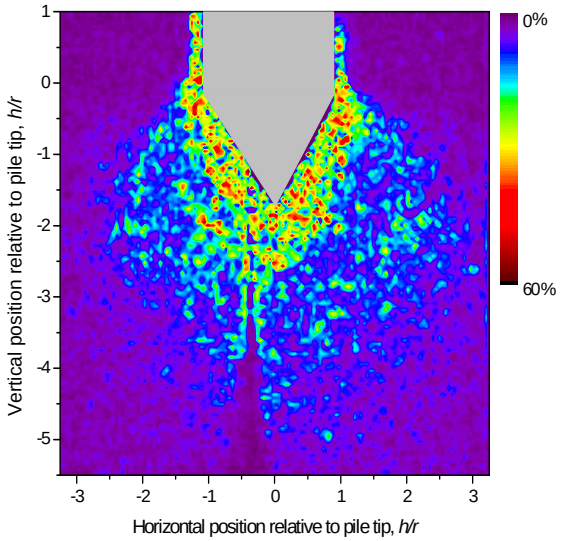

Figure 9: **Incremental shear strain after a 0,5 mm pile head displacement. Local tomography**

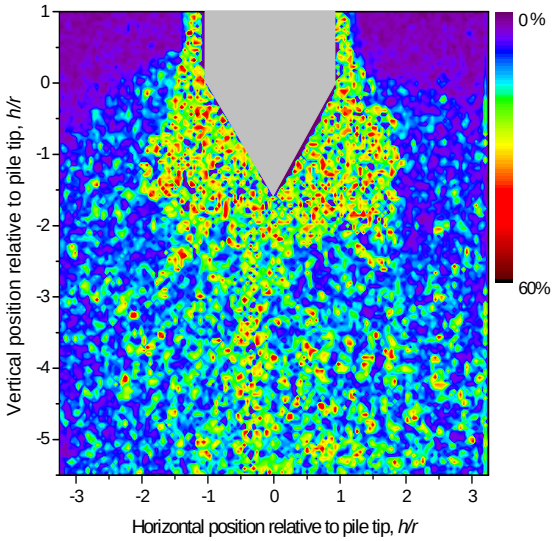

Figure 10: **Incremental shear strain after a 2 mm pile head displacement. Local tomography**

CONCLUSIONS

The combined use of x-ray micro CT with 3D-DIC allows understanding the kinematics behind the installation of a geotechnical probe on a silica sand sample. Different zones of influence for the vertical and horizontal strains were identified. The results suggest the presence of a zone behind the pile tip where recirculation of sand particles takes place.

REFERENCES

Åstedt, B., Weiner, L., & Holm, G. (1992). Increase in bearing capacity with time for friction piles in silt and sand. *Proceedings of Nordic Geotechnical Meeting*, 411-416.

Allersma, H. G. B. (1988). Optical analysis of stress and strain around the tip of a penetrating probe. *Penetration Testing 1988*, Vol. 2, 615–620, Balkema, Rotterdam.

Allersma, H., & Broere, W. (2002). Optical analysis of stress around a penetrating probe in granular material. *Physical modelling in geotechnics: proceedings of the international conference on physical modelling in geotechnics*, 149–154.

Axelsson, G. (2000). Long-Term Set-Up of Driven Piles in Sand. Phd Thesis, Royal Institute of Technology, Sweden.

Bolton, M. D., Gui, M. W., Garnier, J., Corte, J. F., Bagge, G., Laue, J., & Renzi, R. (1999). Centrifuge cone penetration tests in sand. *Géotechnique*, 49(4), 543–552.

Chong, M. K. (1988). Density changes of sand on cone penetration resistance. *Penetration Testing 1988*, Vol. 2, 707–714, Balkema, Rotterdam.

Chow, F. C., Jardine, R. J., Brucy, F., & Nauroy, J. F. (1998). Effects of Time on Capacity of Pipe Piles in Dense Marine Sand. *Journal of Geotechnical and Geoenvironmental Engineering*, 124(3), 254-264.

Hall, S. A. (2006). A methodology for 7D warping and deformation monitoring using time-lapse seismic data. *Geophysics*, 71(4), O21-O31.

Hall, S. A., Bornert, M., Desrues, J., Pannier, Y., Lenoir, N., Viggiani, G., & Besuelle, P. (2010). Discrete and continuum analysis of localised deformation in sand using X-ray uCT and volumetric digital image correlation. *Geotechnique*, 60(5), 315–322.

Jardine, R., Zhu, B., Foray, P., & Yang, Z. (2013). Interpretation of stress measurements made around closed-ended displacement piles in sand. *Geotechnique*, 63(8), 613–627.

Morita, K., Otani, J., Mukunoki, T., Hironaka, J., & Pham, K. D. (2007). Evaluation of vertical and lateral bearing capacity mechanisms of pile foundations using X-ray CT. *Advances in Deep Foundations: International Workshop on Recent Advances of Deep Foundations*, 217–223, Taylor & Francis.

Ngan-Tillard, D., Cheng, X. H., Van Ness, J., & Zitha, P. L. J. (2005). Application of x-ray computed tomography to cone penetration tests in sands. *Proceedings of the Geo-Frontiers, Site Characterization and Modeling*, 1–12.

Paniagua, P., Andò, E., Silva, M., Emdal, A., Nordal, S., & Viggiani, G. (2013). Soil deformation around a penetrating cone in silt. *Géotechnique Letters*, 3, 185–191.

Pater, C. De, & Nieuwenhuis, J. (1986). Method for measuring the deformations of a sand surface. *Geotechnique*, 36(4), 581-585

Robinsky, E. I., & Morrison, C. (1964). Sand displacement and compaction around model friction piles. *Canadian Geotechnical Journal*, 1(2), 81–93.

Van Nes, J. H. . (2004). Application of computerized tomography to investigate strain fields caused by cone penetration in sand. (Master's thesis). Delft University of Technology.

White, D., & Bolton, M. (2002). Observing friction fatigue on a jacked pile. *Centrifuge and Constitutive Modelling: Two extremes*, 347-354.

White, D. J., & Bolton, M. D. (2004). Displacement and strain paths during plane-strain model pile installation in sand. *Géotechnique*, 54(6), 375–397.

White, D. J. D., & Lehane, B. M. B. (2004). Friction fatigue on displacement piles in sand. *Géotechnique*, 54(10), 645–658.

Yang, Z. X., Jardine, R. J., Zhu, B. T., Foray, P., & Tsuha, C. H. C. (2010). Sand grain crushing and interface shearing during displacement pile installation in sand. *Géotechnique*, 60(6), 469–482.

Observing breakage in granular materials with X-ray Computed Tomography

Z. Karatza[1,a,b], E. Andò[b,c], G. Viggiani[b,c], S.-A. Papanicolopulos[a], J. Ooi[a]

[a] *School of Engineering, The University of Edinburgh, Edinburgh EH9 3JL, U.K.*

[b] *Université Grenoble Alpes, 3SR, F-38000, Grenoble, France*

[c] *CNRS, 3SR, F-38000, Grenoble, France*

[1] *Corresponding author:* zeynep.karatza@3sr-grenoble.fr

ABSTRACT

The mechanisms involved in grain crushing/particle breakage is a common research topic in several fields including geomechanics, geoscience and particle technology. This topic is of interest to disciplines including material processing, minerals and mining engineering, geology, geophysics and geomechanics, since changes in the microstructure can lead to significant changes in the macroscopic bulk behaviour of a material. The main goal of this research is to develop a new understanding of the particle breakage mechanisms in a particulate system under specific loading regimes. This is achieved by studying the microscopic changes that an assembly of grains undergoes, while being loaded/deformed. The possibility to study and visualise the 3D volume of a specimen during loading is given by X-ray computed tomography (hereinafter XCT). Two types of granular materials have been studied; a very rounded natural calcitic sand (Caicos ooids) and industrially manufactured almost spherical zeolite. The materials have been subjected to triaxial (only Caicos ooids) and Ko loading (both materials); in both cases the apparatus are specifically designed to enable the imaging through XCT. The specimens have been loaded in increments with a constant strain rate, between which, the tests were paused without unloading, in order to acquire a set of radiographs of the whole specimen. These are later on reconstructed into 3D grey scale images in order to study the evolution of the microstructure and especially grain breakage at different loading stages.

The XCT images enabled the authors to clearly observe broken grains (fragments) unless their size was smaller than the resolution. The comparison between the oedometric loading and the triaxial shows a clear difference at the distribution of the damage. In the first case a diffused pattern of breakage can be observed, indicating that the breakage is attributed to boundary conditions (rigid cell of the oedometer) and transmission of forces between particles, whereas in the second case a very clear strain localisation has been observed and breakage has been induced due to the deviatoric loading and observed mostly in the shear band. Both materials have been loaded to the same

maximum axial stress at the oedometer, however zeolite results to significantly more breakage than Caicos ooids.

INTRODUCTION

The mechanisms involved in grain crushing/particle breakage is of interest to many disciplines including material processing, minerals and mining engineering, geology, geophysics, geomechanics, geoscience and particle technology [e.g., 1-3] and therefore has been a common research topic among them. Particle breakage in geomechanics is important because it can produce changes in the microstructure of a material, that will greatly affect the macroscopic behaviour of the bulk system (e.g., strength, permeability); either that is a specimen in a laboratory or a whole soil formation in nature or in industry. It is understood that breakage can occur under high stresses, however breakage has been observed even at relatively low stresses [4] and in both cases this can lead to important variations in the particle size distribution and/or it can cause discontinuities; an undeniable reason as to why it has been extensively studied experimentally, theoretically and numerically [5].

The possibility to study and visualise a 3D volume of a specimen during loading is given by techniques such as X-ray computed tomography (hereinafter XCT) [e.g., 6-10]. The analysis of the images will be based on full-field measurements [11] that will enable the study and give a deeper insight to phenomena such as grain crushing, grindability, milling and attrition of granular materials.

For the present study two types of granular materials have been studied; a very rounded natural calcitic sand (Caicos ooids) and industrially manufactured almost spherical zeolite. An oedometric (for both materials) and a triaxial (for Caicos ooids) test were carried out, during which XCT was performed in order to gain the most information about breakage in 3D.

EXPERIMENTAL CAMPAIGN

Material Description

The first sand used for this study is Caicos ooids with a D50 of 350μm; a material with very rounded particles that grow from fragments of corals. Ooids are spherical or ellipsoid concretions of calcium carbonate and aragonite crystals (here more than 95% aragonite) arranged around a nucleus. The ooids are forming in marine environments (rich in carbonate calcium), by gaining successive layers (smooth, uniform carbonate coatings) around a nucleus; a process followed by a resting period before the addition of each new layer [12]. Depending on the successive growth and resting periods, variation in the thickness of the coatings and the appearance of the nuclei can be expected, altering the internal porosity of each grain and potentially its strength and stiffness. A sample was collected from Ambergris Shoal in the Caicos platform (Turks and Caicos Islands), in the British West Indies and it has been kindly provided to Laboratoire 3SR in Grenoble, France, by Hubert King of Exxon Mobil.

Zeolites are naturally occurring or synthetic alumosilicates, which exhibiting a well defined, intricate and uniform pore network [13]. They are widely used in industrial applications as adsorbents and catalysts, but also as ion-exchange beds in domestic and commercial water purification; and other applications. The ones used in this study have been manufactured into approximately spherical particles of 1 to 2mm in diameter and the sample was kindly provided to the University of Edinburgh by CWK, Germany.

X-ray Computed Tomography

As far as XCT is concerned, each tomographic scan is a series of acquisitions of radiographs, which are 2D images (projections) of X-ray attenuation of an object. These are made with an X-ray source and are recorded by a detector or an imager, while an object stands between them and rotates in order to acquire radiographs at different orientations. The times the specimen is rotated will define the number of acquisitions, that will be later on reconstructed into a 32-bit grey scale stack of images (3D volume). On the following figure (Figure 1) a radiograph, a reconstructed vertical slice and a 3D reconstructed volume, are illustrated.

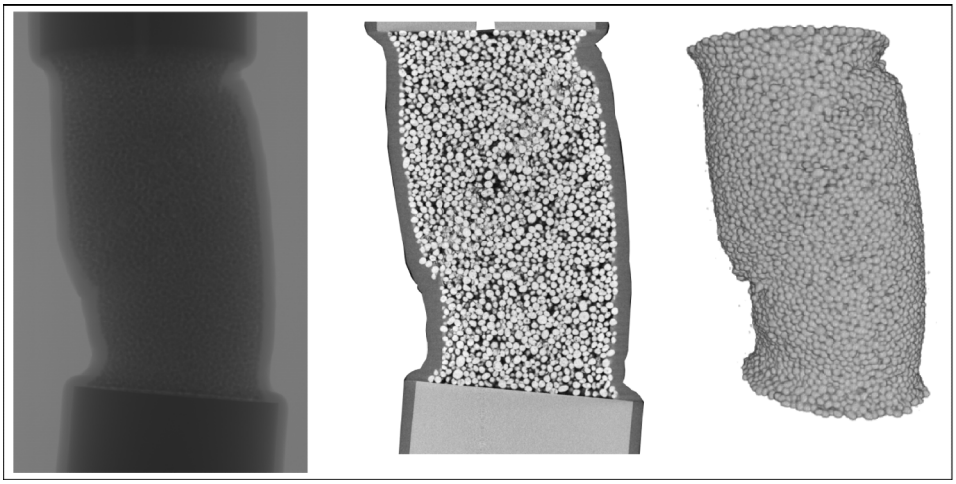

Figure 1: Left: Radiograph, Middle: Vertical slice, Right: 3D volume

Triaxial & Oedometric tests

Two types of tests were performed; a triaxial compression and an oedometric compression test. In order to acquire the radiographs, the specimen needs not to be straining and therefore the loading was paused for the duration of the image acquisition (stress relaxation that can be observed in Figure 2). These increments will be referred to as loading stages. The loading at all tests was ascending with a strain rate of 21μm/min and 50μm/min at the triaxial and oedometrer respectively. Another condition is that the loading apparatus have to be transparent to X-rays and the specimen has to have certain dimensions in order for the beam to penetrate. Based on the aforementioned it is obvious that standard apparatus could not be used and so apparatus specially designed for XCT were used. Tables 1 and 2 provide some basic details of the performed experiments. In the following the tests followed by a number after "ZK" are triaxial tests, where as if "OD" follows, it denotes an oedometer test. Due to the grain size of the zeolite being rather large compared to the size of the triaxial specimen, no triaxial compression was performed on this material.

Table 1: Information about tests on Caicos ooids with XCT

Test Reference	Resolution [μm]	Height [mm]	Diameter [mm]	Number of scans
COZK03	15.5662	23.48	9.36	7
COZK04	15.5662	24.46	10.28	7
COZK05	8.8245	22	10	2
COZKOD03	12.2486	16.72	15	7

Table 2: Information about tests on Zeolite with XCT

Test	Resolution	Height [mm]	Diameter	Number of

Reference	[μm]		[mm]	scans
ZSZKOD03	24.8869	15	45	5
ZSZKOD04	24.8869	15	45	3
ZSZKOD05	24.8869	15	45	7
ZSZKOD06	10.0036	15	15	11
ZSZKOD07	10.0036	15	15	6

RESULTS AND ANALYSIS

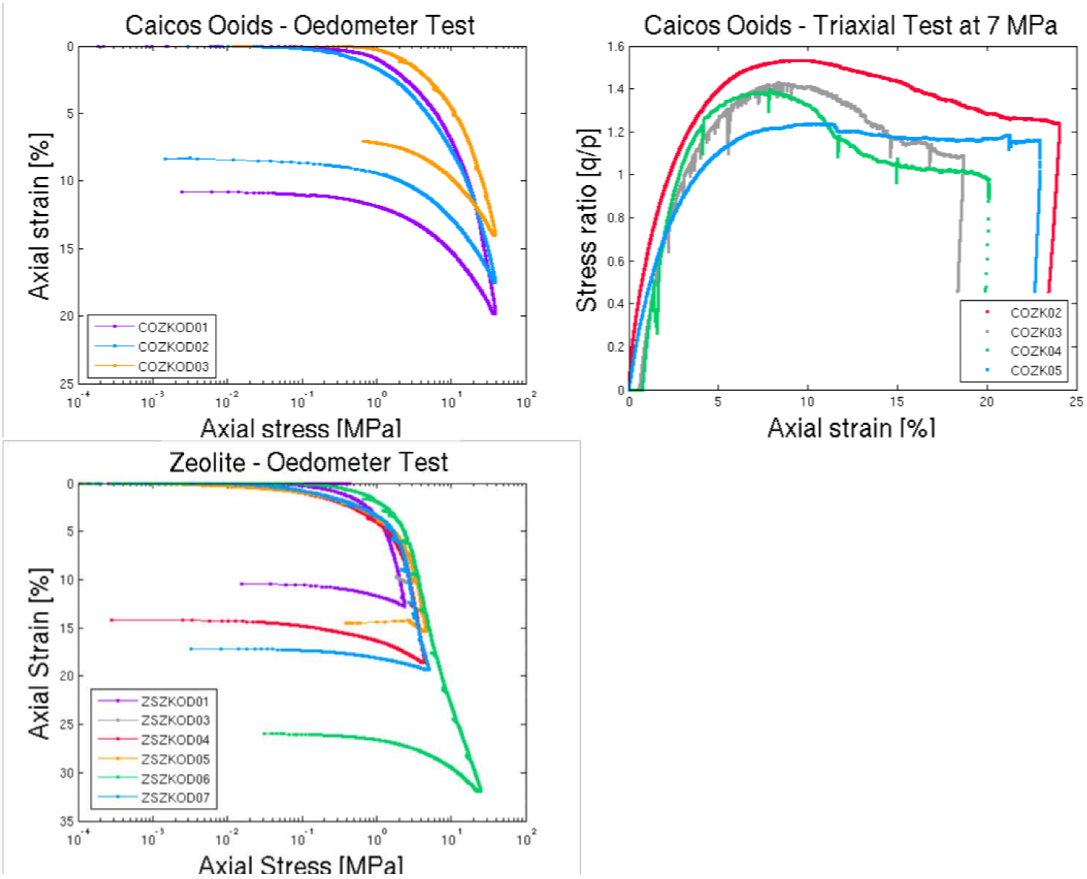

Figure 2: Macroscopic response of all tests and all materials

From the macroscopic response (Figure 2) of the specimens it is clear that both experimental procedures for both materials are fairly reproducible. However the response of the triaxial tests largely depends on the grain size and the initial density of the specimens. The peak stress indicates that COZK02 is the denser specimen, COZK03 and COZK04 have similar densities and COZK05 is the most loose specimen. COZK02 was rather polydisperse compared to the other uniform specimens; therefore the finer particles would fill up the pore space, resulting to a much denser specimen. COZK04 has the smallest grain size and the lowest resolution, whereas COZK03 and COZK05 have the same grain size distribution. Their difference in density is attributed to the preparation method; although the same method was used to prepare the specimens, a slight difference in density would be expected due to human involvement in the process.

Comparing the response of Caicos ooids in triaxial and oedometric loading, it can be observed by the reconstructed images that less breakage occurred, however, as it can be seen from the first plot in Figure 2, was not strained enough (ε_{a_max} = 14.02%) due to limitations of the

loading system to the applied force. In the triaxial, this strain corresponds to post peak yield phase, which is however close to peak and again not much breakage has been observed. However due to the shearing it is expected to have more breakage anyways in a more localised manner. On the other hand comparing the two oedometric tests, zeolite being less strong and much more brittle than Caicos, the authors managed to strain it more (ZSZKOD06 - ε_{a_max} = 21.42%) and produce massive breakage. In Figures 3 and 4 incremental vertical slices of 2 representative experiments are presented.

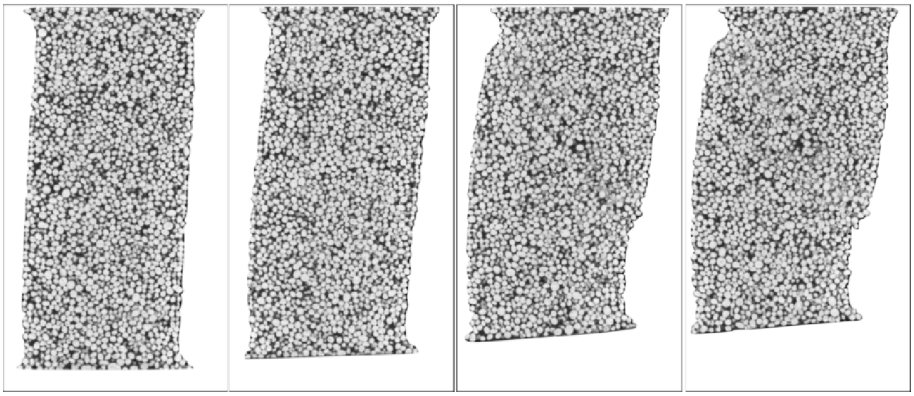

Figure 3: Vertical slices of COZK03 for loading stages 10 to 13

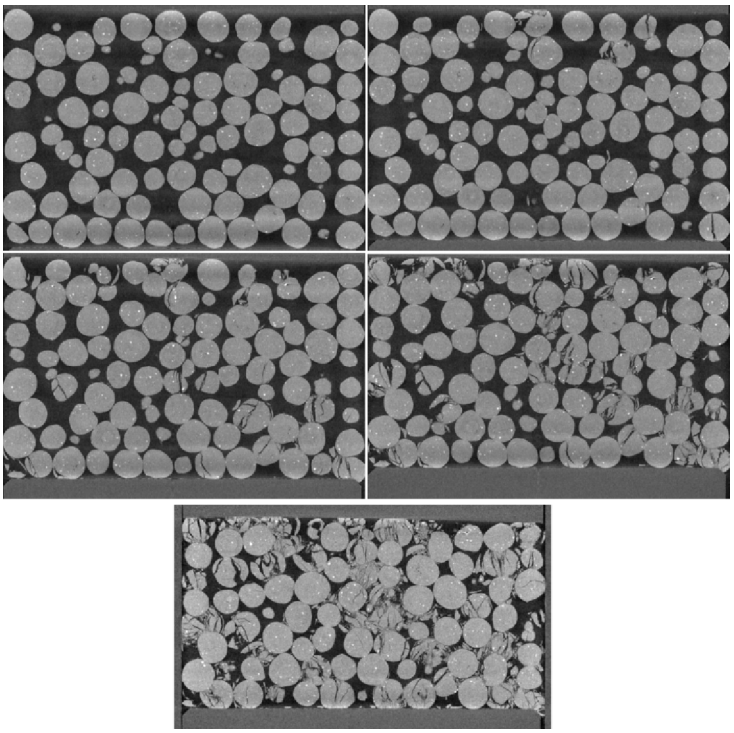

Figure 4: Vertical slices of ZSKOD07 for loading stages 01 to 05

DISCUSSION

In Figure 5 a representative example of the distribution of damage in the specimens as seen in a vertical section (left) and a horizontal section (right) during triaxial loading is presented. The black dashed lines show the position of the cross-section. It is rather clear that during the triaxial more localised damage occurred, which forms a shear band and also while we move away from the shear band the damage becomes less and less, creating different damage zones

of breakage and/or reorientation and/or simple compaction [14]. On the contrary such distinctively well defined patters can not be found in the oedometer, where the damage is randomly distributed in the specimen. In both cases however, there seems to be more breakage on the lower part of the specimens, where the loading is applied than in the upper part. This gives a clear impression of the effect of the moving boundary. Nevertheless, the rest of the boundaries seem not to have an important effect on the breakage, since hardly any broken grains have been identified close to them (rigid oedometric cell and neoprene membrane in triaxial test). However, this does not seem to be the case for the small oedometeric test in zeolite, probably due to the small number of particles in the specimen; it seems that the fewer the particles are, the more damage is observed in the boundaries.

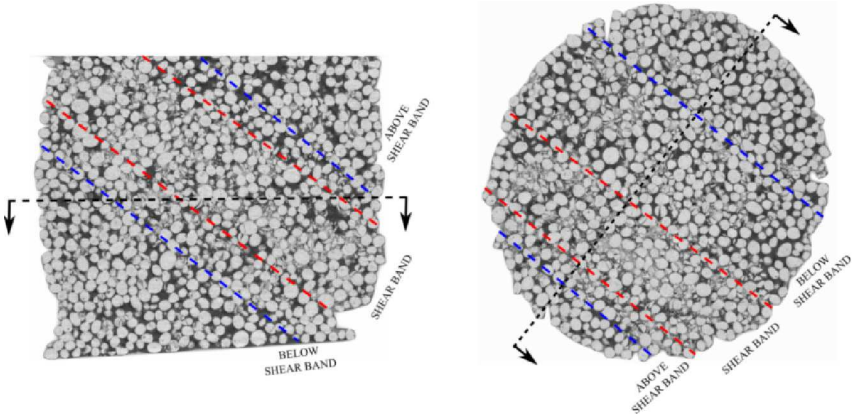

Figure 5: Breakage distribution

To conclude, by simply observing the images and without performing any measurements it can be concluded that COZK04 produced less comminuted volume than COZK03 and COZK05. However, it should be taken into account that while the specimens are strained and more grain breakage occurs, there is a threshold to the size of the fines that can be visualised, based on the resolution. The lower the resolution the more fines can not be identified in the images resulting in a loss of solid volume. Needles to say though, as the initial grain size of COZK04 is smaller than at the other specimens, the potential of breakage of its particles is also reduced comparatively due to the decreased normal contact forces and the lower probability of the grains having defects [15].

The biggest advantage of XCT is that researchers do not have to rely on the observation of damage on the boundary of the specimen and on signal processing for the measurement of bulk properties and of the response of the material. Image processing has allowed both continuous and discrete analysis to be performed for the investigation of various phenomena. Similar studies based on full field measurements can be found in literature [7-10, 16-20] in order to measure the rotations of the grains, to find the coordination number, to analyse shape characteristics of the grains, to describe strain localisation and of course to estimate grain breakage. This information not only helps understand in depth the mechanisms that govern grain crushing, but also constitute more detailed and more improved version of benchmark tests used for calibration and comparison of DEM simulations.

ACKNOWLEDGEMENTS

The authors would like to thank Pascal Charrier for his valuable help during the XCT and Laurent Debove for helping create the oedometric apparatus.

REFERENCES

1. Rudnicki, J.W. 2000. Geomechanics. International Journal of Solids and Structures 37:349-358.
2. Davis, R.O., Selvadurai, A.P.S. 2002. Plasticity and geomechanics. Cambridge University Press.
3. Einav, I. 2007.Breakage mechanicspart I: theory. J Mech Phys Solids 55(6):1274-1297.
4. Luzzani, L., Coop, M.R. 2002. On the relationship between particle breakage and the critical state line of sands. Soils and Foundations 42(2):71-82.
5. Muir Wood, D., Maeda, K. 2007. Changing grading of soil: effect on critical states. Acta Geotechnica 3:3-14.
6. Desrues, J., Chambon, R., Mokni, M., Mazerolle, F. 1996. Void ratio evolution inside shear bands in triaxial sand specimens studied by computed tomography. Géotechnique 46(3): 529-546.
7. Hasan, A., Alshibli, K.A. 2008. Spatial variation of void ratio and shear band thickness in sand using X-ray computed tomography. Géotechnique 58(4):249-257.
8. Hasan, A., Alshibli, K.A. 2010. Experimental assessment of 3D particle-to-particle interaction within sheared sand using synchrotron microtomography. Géotechnique 60(5):369-379.
9. Andò, E., Hall, S.A., Viggiani, G., Desrues, J., Bésuelle, P. 2012. Experimental micromechanics: grain-scale observation of sand deformation. Géotechnique 2:107-112.
10. Andò, E., Viggiani, G., Hall, S.A., Desrues, J. 2013. Experimental micro-mechanics of granular media studied by x-ray tomography: recent results and challenges. Géotechnique 3(3):142-146.
11. Viggiani, G., Hall, S.A. 2012. Full-field measurements, a new tool for laboratory experimental geomechanics. ALERT Doctoral school.
12. Lloyd, R.M., Perkins, R.D., Kerr, S.D. 1987. Beach and shoreface ooid deposition on shallow interior banks, Turks and Caicos islands, British West Indies. Journal of Sedimentary Petrology 57(6):976-982.
13. Müller, P., Tomas, J. 2012. Compression Behavior of Moist Spherical Zeolite 4A Granules. Chemical Engineering & Technology 35(9):1677-1684.
14. Gabrielsen, R.H., Aarland, R.-K., Alsaker, E. 1998. Identification and spatial distribution of fracture in porous, siliciclastic sediments. Structural Geology in Reservoir Characterization. Geological Society, London, Special Publications 127: 49-64.
15. Hardin, B. O. 1985. Crushing of soil particles. J. Geotech. Engineering 111(10): 1177â€“1192.
16. Andrew, M., Druckrey, S.M., Khalid, A., Alshibli, M. 2014. 3D behavior of sand particles using X-ray synchrotron micro-tomography. Proceedings of Geo-Congress.
17. Andò, E., Hall, S.A., Viggiani, G., Desrues, J., Bésuelle, P. 2011. Grain-scale experimental investigation of localised deformation in sand: a discrete particle tracking approach. Acta Geotechnica 7(1):1-13.
18. Garboczi, E.J. 2002. Three-dimensional mathematical analysis of particle shape using X-ray tomography and spherical harmonics: application to aggregates used in concrete. Cement and concrete research 32:1621-1638.
19. Masad, E., Saadeh, S., Al-Rousan, T., Garboczi, E., Little, D. 2005. Computations of particle surface characteristics using optical and X-ray CT images. Computational materials science 34:406-426.
20. Fonseca, J., Sim, W.W., Shire, T., O'Sullivan, C. 2014. Microstructural analysis of sands with varying degrees of internal stability. Géotechnique 64(5):405-411.

Displacement fluctuations in granular materials: a direct manifestation of grain rearrangement

G. Combe, V. Richefeu & G. Viggiani
Laboratoire Sols, Solides, Structures, Grenoble, France
Gael.combe@3sr-grenoble.fr, Vincent.richefeu@3sr-grenoble.fr, Cino.viggiani@3sr-grenoble.fr

ABSTRACT

Grain rearrangement, which is the basic mechanism of irreversible strain in granular materials, results in displacement fluctuations, i.e., the displacements of grains deviate from the value dictated by a continuum field. These fluctuations play a similar role as dislocations in crystals, in the sense that they are at the very origin of irreversible strain in granular materials. The analysis of fluctuations is a hot topic in granular physics and mechanics. However, to the best of the authors' knowledge, it has been investigated so far only by means of numerical (DEM) simulations. We present herein an experimental study of displacement fluctuations in quasi-static deformation of a 2D granular material deformed in a shear apparatus named *1γ2ε*. This apparatus allows a specimen composed of an assembly of rods to be subjected to general 2D-loading conditions, by independently applying normal strain along the vertical and horizontal axes, as well as shear strain. The kinematics of the centers of each rod in the specimen are followed by means of a 2D Particle Image Tracking (PIT) technique, which is applied to a sequence of digital photographs acquired throughout the duration of a test.This experimental work presents clear evidence of spatial organization of fluctuations in vortex-like structures (fluctuation loops) that are observed for different sizes of the strain increment considered (referred to as strain window). For small strain windows, these vortex patterns are quite intermittent, whereas they become more persistent when the size of the strain window is increased. The analysis of the experimental data indicates the existence of a minimum length scale of the fluctuation loops.

INTRODUCTION

In a granular material, a macroscopically homogeneous deformation does not correspond to a homogeneous field of displacement gradient when looking at the individual grains. Due to geometrical constraints at the grain scale (mutual exclusion of grain volumes), grains are not able to displace as continuum mechanics dictates they should. This can be pictured by imagining an individual in a crowd of people who all wish to go to the same place: although the long-term displacement of each individual is equal to the displacement of the crowd, the steps of each individual are erratic. Classical continuum approaches disregard this feature, which is apparent only at *small* strains (*i.e.*, for displacements that are small with respect to the size of rigid grains, or the size of contact indentation for deformable grains). However, the deviation of a grain's displacement from the value dictated by the continuum field (referred to as *fluctuation*) is likely to hold valuable information about the characteristic length(s) involved in grains' rearrangement, which is the principal mechanism of irreversible deformation in granular materials.

Displacement fluctuations, often spatially organized in the form of vortices, have been observed in quasistatic experiments only by Misra et Jiang (1997). Several numerical studies using Discrete Elements (DEM) report similar observations, *e.g.*, Williams and Rege (1997), Kuhn (1999), Combe and Roux (2003), Tordesillas *et al.* (2008), Rechenmacher *et al.* (2011). Radjaï and Roux (2002) investigated such fluctuations by making use of statistical analysis that is typically used in fluid dynamics. The main finding of Radjaï and Roux (2002) was that displacement fluctuations in granular materials show scaling features with striking analogies to fluid turbulence. Inspired by the approach of Radjaï and Roux (2002), the present study analyzes fluctuations measured from experiments on a 2D analogue granular material subjected to (quasi-static) shear.

SHEAR TEST

Shear tests have been performed in the $1\gamma 2\varepsilon$ apparatus, which is essentially a plane stress version of the directional shear cell developed for testing soils (Calvetti *et al*. 1997, Joer *et al.* 1992, Charalampidou *et al.* 2009 for details). Results from only one such test are discussed herein, although the results are consistent throughout the entire programme. In this experiment, an assembly of 2000 2D *grains* (wooden cylinders *6 cm* long) having four different diameters (*8*, *12*, *16* and *20 mm*), was slowly deformed in simple shear at constant vertical stress $\sigma_n = 50\ kPa$, Fig. 1. Note that the contact properties among the (wooden) grains compare with the properties imposed in DEM simulations by Radjaï and Roux (2002). The vertical sides of the enclosing frame are tilted up to $\gamma = 0.26$ ($15°$) while the length of the horizontal sides is kept constant. The shear strain rate is $8.2 \times 10^{-5}\ s^{-1}$, which is small enough to ensure a quasi-static regime according to the inertial number criterion suggested by Combe and Roux (2003). A video of the test can be found at http://youtu.be/B4Dfesn5vhs.

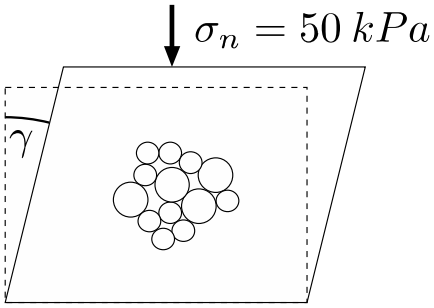

Figure 1. **Sketch of a shear test in the $1\gamma2\varepsilon$ apparatus.**

During the test, the normal (σ_n) and tangential (σ_t) stresses are measured at the boundary of the sample (Richefeu *et al.* 2012). The global stress-strain response is typical of a dense 2D granular material, with a peak friction angle of about $26°$ at $\gamma \approx 0.06$ and a dilatant behaviour throughout. A digital camera was used to acquire 24.5 Mpixels images every 5 seconds (*i.e.*, a shear strain increase of $\Delta\gamma \approx 4 \times 10^{-4}$, called strain window in the following) thoughout the test.

The displacements of all the grains are measured by means of a software named TRACKER specially developed to process the digital images and measure (with sub-pixel resolution) the in-plane displacement and rotation of each individual grain from one image to another. This software uses a discrete grain-scale version of digital image correlation technique hereafter named PIT (Particle Image Tracking) that is well suited for tracking rigid particles. The principle of the PIT technique is detailed in Richefeu *et al.* (2012) and Combe and Richefeu (2013). From the 24.5 Mpixels images taken during the shear test, particles' displacements are assessed with a error that is less than *0.1* pixel (Combe and Richefeu 2013). As an example, Fig. 2 shows the displacements of all grains measured by PIT from *0* to *0.12* shear strain γ.

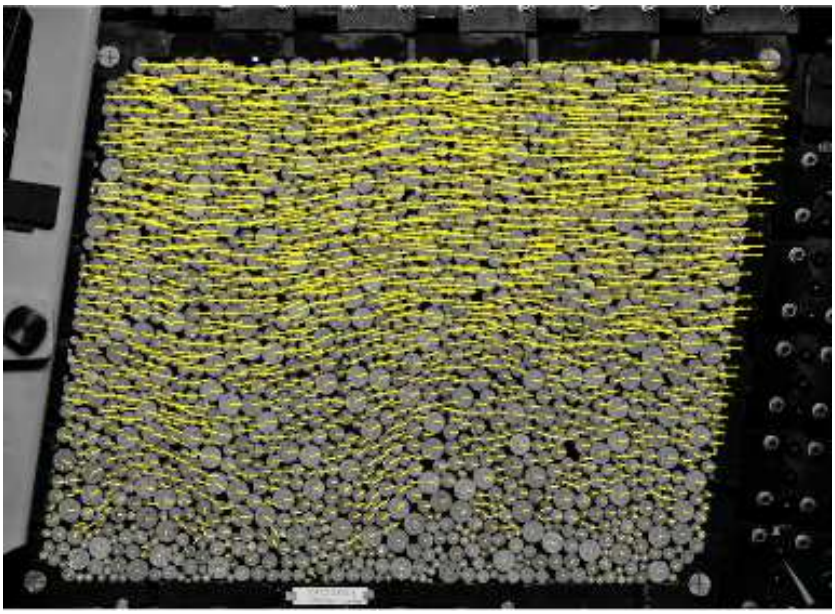

Figure 2. **Particles displacement (maximum displacement = 46mm) in a sheared 2D granular assembly made of 2000 wooden rods. The granular packing is enclosed by a rigid frame initially rectangular (0.56 m × 0.47m). A speckle of black and white points is painted on each cylinder to allow the measurement of particle kinematics by means of the PIT technique.**

FLUCTUATIONS OF DISPLACEMENT

To assess the fluctuations of displacement (angular rotations of grains are also assessed, but not discussed in this paper) in the course of deformation, we consider two possible displacements of each grain during a strain window $\Delta\gamma$ (always positive). The first is the actual displacement vector $\delta\mathbf{r}\left(\gamma,\Delta\gamma\right)$, which depends both on the size of the strain window $\Delta\gamma$ and the level of shear strain γat the beginning of the strain window. The second displacement vector $\delta\mathbf{r}^{*}\left(\gamma,\Delta\gamma\right)$ is the displacement dictated by a homogeneous (*affine*) continuum strain field, *i.e.*, the displacement that the grain's center would have if it moved as a material point in a continuum. The fluctuation of the displacement is defined as the difference between these two displacement vector:

$$\mathbf{u}\left(\gamma,\Delta\gamma\right)=\delta\mathbf{r}\left(\gamma,\Delta\gamma\right)-\delta\mathbf{r}^{*}\left(\gamma,\Delta\gamma\right) \tag{1}$$

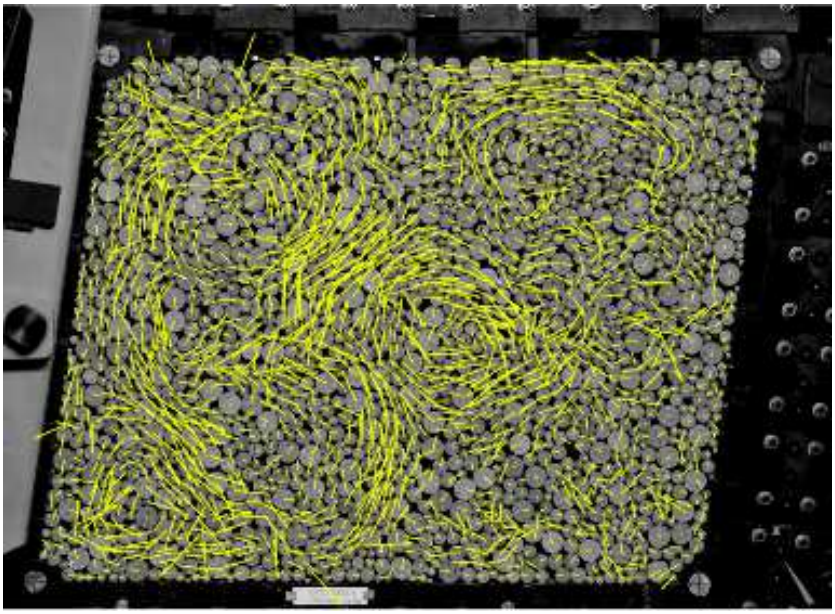

Figure 3. **Displacement fluctuations $u(\Delta\gamma = 0.1,\ \gamma = 0)$ of grains in a sheared 2D granular assembly. The corresponding grains' displacement are shown in Fig. 2. The maximum value of *u* is *18mm*.**

Figure 3 shows a map of the fluctuations **u** associated with the displacement field of Fig. 2. Displacement fluctuations can be conveniently normalized by dividing the vector $\mathbf{u}\left(\gamma,\Delta\gamma\right)$ by the product $\Delta\gamma\ \langle d\rangle$ (where $\langle d\rangle$ is the mean diameter of the grains), which can be interpreted as the average displacement of the grains in the strain window $\Delta\gamma$. This normalized fluctuation,

$$\mathbf{V}\left(\gamma,\Delta\gamma\right)=\frac{\mathbf{u}\left(\gamma,\Delta\gamma\right)}{\Delta\gamma\langle d\rangle}, \tag{1}$$

can also be interpreted as a local (microscopic) strain fluctuation, which is in turn divided by the size of the global (macroscopic) strain window $\Delta\gamma$.

The mean displacement fluctuation $\langle u\rangle$ increases monotonically throughout the test, from *0.066 mm* (for $\Delta\gamma = 10^{-3}$) to *6 mm* (for $\Delta\gamma = 0.25$), this final value correspond to about *10%* of

the average displacement of the grains between the beginning and the end of the shear test. Note that the smallest displacement fluctuation is well above the accuracy of TRACKER. As far as the mean magnitude of normalized fluctuations $\langle V \rangle$ is concerned, a decrease of $\langle V \rangle$ from 3 to 2 is observed; this implies that the average fluctuation of local shear strain $\langle u \rangle / \langle d \rangle$ is two to three times larger than the global strain window $\Delta\gamma$.

PDF OF THE FLUCTUATIONS

Figure 4 shows the probability density function (pdf) of normalized fluctuations $\boldsymbol{V}$ along the x direction for two different strain windows $\Delta\gamma$. Whatever the strain window, a good candidate for the *pdf* is

$$F(V_x, q) = a\left[1 + b(1-q)V_x^2\right]^{\frac{1}{1-q}} \tag{3}$$

This function, named *q-gaussian*, comes from the generalized thermodynamics theory, which is derived from the principle of non-extensive entropy introduced by Tsallis (1988). The parameter q in Eq. (3) quantifies the degree of non-extensivity of the entropy of the system. In the limit of $q \to 1$, the function tends to a *Gaussian* probability density function.

Statistical analysis of the fluctuations shows that whatever the value of $\Delta\gamma$, their spatial average is zero, which is expected for a global homogeneous deformation. A key observation is that the pdf exhibits a wider range of fluctuations with decreasing $\Delta\gamma$, which corresponds to a variation of q from *1.14* to *1.59*. In Richefeu *et al.* (2012), a *Kurtosis* analysis of V_x values was seen to tend to zero asymptotically with increasing size of $\Delta\gamma$. A zero value of kurtosis might indicate that the pdf tends to become Gaussian for $\Delta\gamma \to \infty$, which is confirmed by the decrease of q when $\Delta\gamma$ increases. Very similar *Kurtosis* features and trends have been observed (on DEM simulations) by Radjaï and Roux (2002), who noted that they have striking similarities with turbulent flow of fluids (although no dynamics are associated with these fluctuations).

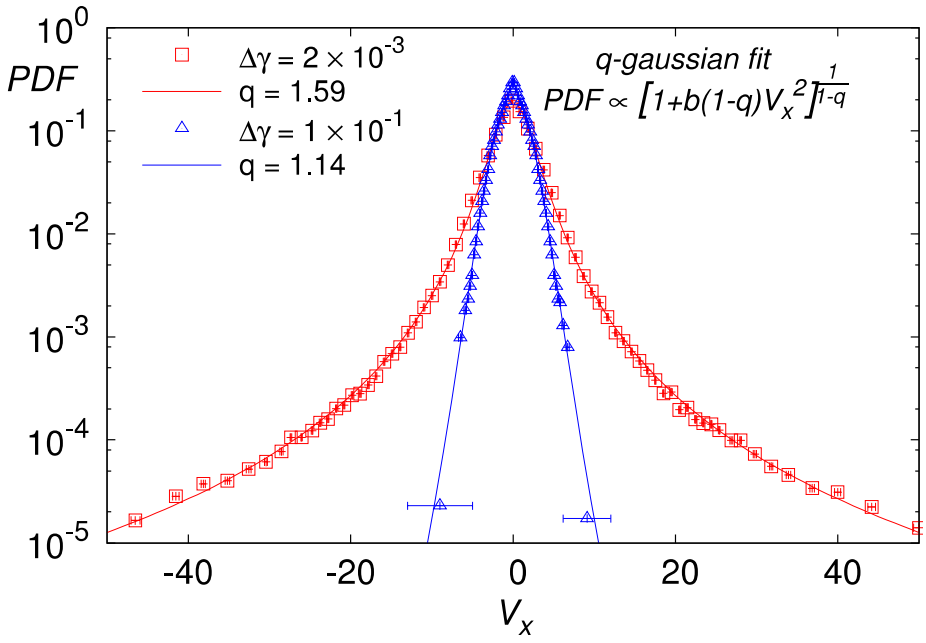

Figure 4. **Probability density function (pdf) of normalized fluctuations V_x projected on the horizontal direction for two different strain windows, $\Delta\gamma = 2 \times 10^{-3}$ and $\Delta\gamma = 10^{-1}$.**

SPATIAL CORRELATIONS OF THE FLUCTUATIONS

To understand the fluctuations, the analysis of their statistics must be supplemented by the study of their spatial distribution.

Spatial correlation of $\boldsymbol{V}$ can be seen, *e.g.*, the *loop patterns* in Fig. 3. Figure 5 shows three normalized fluctuation maps measured for three different values of γ, for two different sizes of the strain window $\Delta\gamma$. On the left, the two fluctuation maps computed for $\Delta\gamma = 2 \times 10^{-3}$ at two different values of γ show that both long-range correlation (blue curve, *40* grain diameter of correlation length) and short--range correlation (red curve, *10* diameter of correlation length) are both observed. This is consistent with *Tsallis* theory, which states that when *q-Gaussian* distributions are observed with $q > 1$ (here $q = 1.59$), then long-range spatial correlations emerge. On the right of Fig. 5, the strain windows used to compute the normalized fluctuation is bigger ($\Delta\gamma = 1.7 \times 10^{-1}$); the statistical distribution of V_x is similar to the one shown in Fig. 4 for $\Delta\gamma = 10^{-1}$. The q value of the *q-Gaussian* fit is smaller than for $\Delta\gamma = 2 \times 10^{-3}$ ($q=1.14$), but still greater than *1* (perfect *Gaussian* distribution). A strong spatial correlation of V_x is found for distances less than $\Delta = 10$ particle diameters. This length roughly corresponds to the minimum radius of the fluctuation loops. A pseudo-period of about $\Delta = 20$ diameters is observed, which is another signature of the loops. This pseudo-periodicity might indicate the existence of a cascade of loop-sizes rather than a unique size − the smallest size being about *10* diameters, and the largest in the order of the sample size. This interpretation was confirmed by Richefeu *et al.* (2012) with a Fourier transform of the fluctuation signal as a function of space, as originally suggested by Radjaï and Roux (2002).

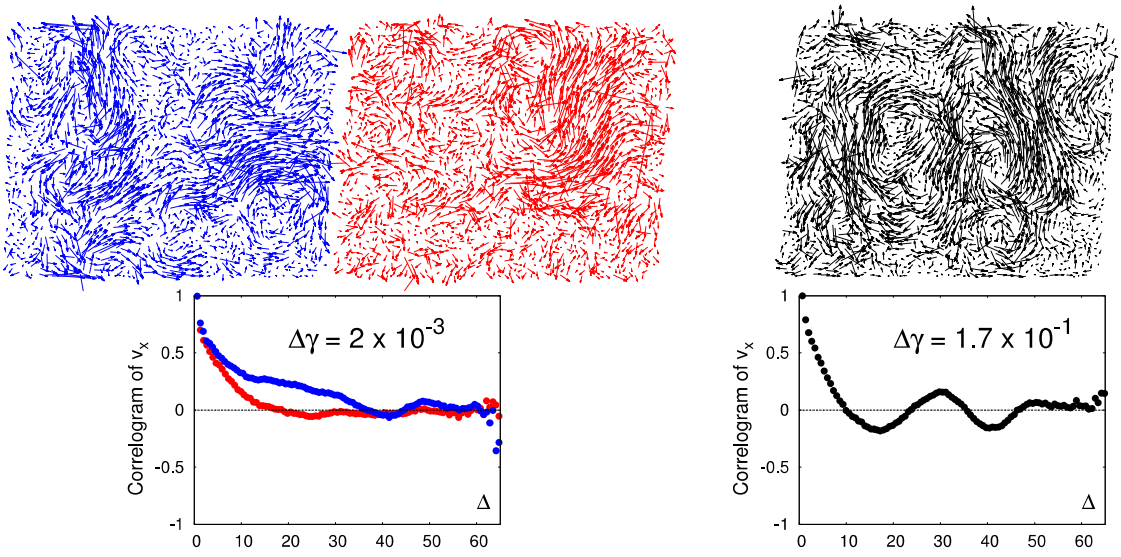

Figure 5. **Maps of the normalised fluctuations for two differents values of $\Delta\gamma$. The curves show the spatial auto-correlogram for the x component of V. Δ is the correlation length expressed in terms of grain diameters.**

CONCLUSIONS

A detailed study of fluctuations of displacements in a granular material subjected to quasistatic shear has revealed that the fluctuations are organized in space and show clear vortex-like patterns, reminiscent of turbulence in fluid dynamics. While these fluctuation loops have been often observed in DEM numerical simulations, on the experimental front they have only been reported (to the authors' best knowledge) in the study by Misra and Jiang (1997). The present study (results of which have already been presented in Richefeu *et al.* 2012) confirms these early findings and brings into the picture the important idea that fluctuation loops have a characteristic minimum radius − equal to 10 mean particle diameters for the material tested.

Displacement fluctuations in granular materials are a direct manifestation of grain rearrangement, therefore they can be thought of as the basic mechanism of irreversible deformation. The statistical analysis of these fluctuation was described by *q-Gaussian* probability distribution, which is a signature of long-range correlation for $q > 1$.

The link between these fluctuations (and their spatial organization) and the deformation of granular materials at the macro scale will be investigated in futur work.

REFERENCES

Calvetti, F., Combe, G., Lanier, J. 1997. Experimental micromechanical analysis of a 2D granular material : relation between structure evolution and loading path. *Mechanics of Cohesive Frictional Materials* 2: 121-163.

Charalampidou, E.-M., Combe, G., Viggiani, G., Lanier, J. 2009. Mechanical behavior of mixtures of circular and rectangular 2D particles, *in Powders and Grains 2009*, edited by M. Nakagawa, and S. Luding, AIP, Golden, USA, 2009, 821-824.

Combe, G., Richefeu, R.. 2013. Tracker: a Particle Image Tracking (PIT) technique dedicated to nonsmooth motions involved in granular packings, *in Powders and Grains 2013*, AIP, Sydney, Australia.

Combe, G., Roux, J.-N. 2003. Discrete numerical simulation, quasistatic deformation and the origins of strain in granular materials, in *3rd International Symposium on Deformation Characteristics of Geomaterials*, edited by di Benedetto *et al.*, Lyon, 2003, 1071-1078.

Joer, H., Lanier, J., Desrues, J., Flavigny, E. 1992. 1γ2ε: A new shear apparatus to study the behaviour of granular materials. *Geotechnical Testing Journal*. 15(2):129-137.

Kuhn, M. R. 1999. Structured deformation in granular materials. *Mechanics of Materials*. 31:407-429.

Misra, A., Jiang, H. 1997. Measured kinematic fields in the biaxial shear of granular materials. Computers and Geotechnics. 20:267-285.

Radjai, F., Roux, S. 2002. Turbulent-like fluctuations in quasi-static flow of granular media. *Phys. Rev. Lett.* 89:064302.

Rechenmacher, A. L., Abedi, S., Chupin, O., Orlando, A. D. 2011. Characterization of mesoscale instabilities in localized granular shear using digital image correlation. *Acta Geotechnica*. 6:205-217.

Richefeu, V., Combe, G., Viggiani, G. 2012. An experimental assessment of displacement fluctuations in a 2D granular material subjected to shear. *Géotechnique Letters*. 2:113-118.

Tordesillas, A., Muthuswamy, M., Walsh, S. 2008. Mesoscale measures of nonaffine deformation in dense granular assemblies. *Journal of Engineering Mechanics*. 134:1095-1113.

Tsallis, C. 1988. Possible generalization of Boltzmann-Gibbs statistics. *Journal of Statistical Physics*. 52:479—487.

Williams, J. R., Rege, N. 1997. Coherent vortex structures in deforming granular materials. *Mechanics of Cohesive-frictional Materials*. 2:223-236.

Unsaturated states of granular media analysed at grain scale by x-ray computed tomography

Ghonwa KHADDOUR, Simon SALAGER, Pascal CHARRIER and Jacques DESRUES

Grenoble-INP, UJF-Grenoble 1, CNRS UMR 5521, 3SR Lab, Grenoble F-38041, France

ghonwa.khaddour @3sr-grenoble.fr, simon.salager@3sr-grenoble.fr, pascal.charrier@3sr-grenoble.fr, jacques.desrues@3sr-grenoble.fr

ABSTRACT

Hydraulic and hydro-mechanical behaviour of unsaturated granular media are strongly influenced by the grain scale nature of these multi-phases materials. Consequently, measurements and observations done at grain level are essential as they lead to a further understanding of the physical mechanisms acting at this scale, which are responsible of the observed global response of the material. X-ray tomography allows sufficiently high spatial resolution, to study most kinds of granular media, and as it is a non-destructive technique, imaging can be done during carrying out in situ experiments.

INTRODUCTION

The microstructural scanning method has proved its validity to distinguish individual sand grains, measure grain displacements and breakage, as well as characterizing air and water distribution at the micro-scale in small samples [1, 2]. Through this 3D imaging technique, a sample can be scanned in one state, and then made to evolve by controlling some relevant variables like suction, in order to capture some of the hydraulic responses and properties, such as retention behaviour, water repartition, pore size distribution or porosity. As an example concerning mechanical behaviour a triaxial test can be implemented, allowing to have global/local information about the kinematic field in the diffuse regime or within localized shear band region, by combining X-ray CT to digital image correlation [4, 5]. This paper aims to present some methodologies applied to achieve the two main goals. First, a characterisation of the links between degree of saturation and suction is done. The experiment is started with the saturated case, then applying suction gradually, until ending up with the dry state [2]. This led to answer some questions related to the four different domains (fully saturated, funicular, pendular and hygroscopic), as transition steps and changes between these domains. A close focus, in this study, was considered in the pendular domain, where water meniscus witness remarkable changes in radius, volume, grain contacts and spatial position. The Second goal is to study water retention states of different granular materials, at several degrees of saturation,

in order to get porosity maps, check degree of saturation values, and to deduce material shape influence on water repartition [3].

EXPERIMENTS

Sampling technique, for both objectives, was chosen in order to obtain a good homogeneity in term of porosity. The samples were cylindrical (10x10 mm), prepared using water pluviation method. A specific pressure plate, well adapted to X-ray scanning, has been developed to precisely control suction in sand samples (imposed both by negative water pressure as well as by positive air pressure) [1]. High resolution (7.5μm/px) X-ray tomography has been reached in this work. By using the physical properties of X-ray, an image of the sample can be developed to display the different densities and compositions within the sample (radiography). In a later step, image processing is applied, and it includes reconstruction, binarization and trinarization. All the data acquired from X-ray scan, were converted into two-dimensional slice images (i.e. reconstructed). Then a process of segmenting/thresholding phase contrast volume images of the sample is done. This process converts grey scale images, obtained from reconstruction, into binary or trinary form. A binarized image, where two phases representing sand grains and voids can be visualized (white=air and black=grains), while a trinarized image, where three phases of grain, water and air, are separated (black=air, blue=water and brown=grains). A reconstructed horizontal slice, a binarized horizontal slice and a trinarized horizontal one are shown in Fig. 1, while an image of the radiogram, a reconstructed vertical slice and trinarized vertical one are shown in Fig. 2.

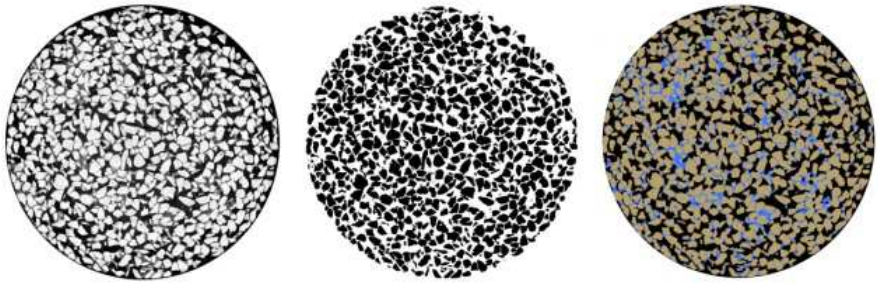

Fig. 1 (Reconstructed-Binarized-Trinarized) horizontal slice of unsaturated Hostun sand

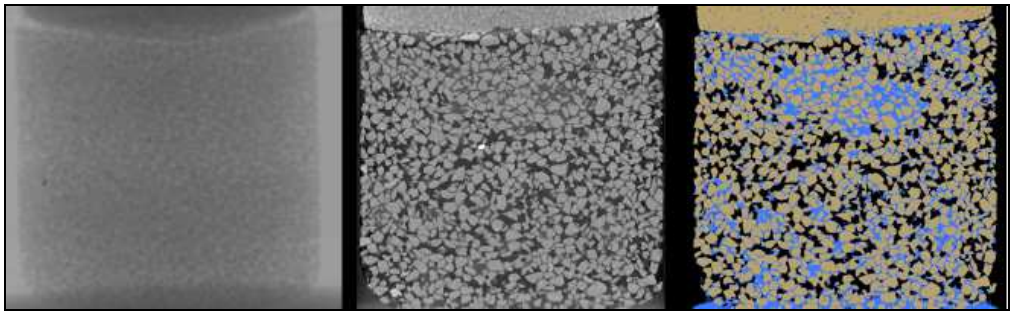

Fig. 2 Radiogram and (Reconstructed-Trinarized) vertical slice of unsaturated Hostun sand

A threshold of the gray value histogram, in some cases, is not sufficient to clearly distinguish the phases, especially if noise and partial volume effect (PVE) are highly presented in the

images. Simultaneous region growing program, is used here, which starts from the seeds at peaks value, Fig. 3, and evolves by considering gray value variance computations inside a spherical selection to correct PVE, and finally smoothing the trinarized images. Fig. 4 shows results obtained for four degrees of saturation and imposed suction.

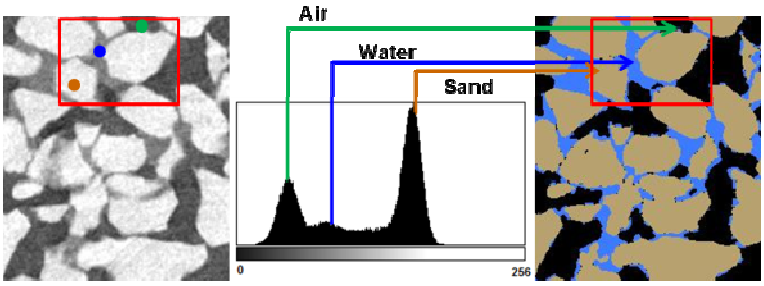

Fig. 3 Trinarisation method applied to Hostun sand sample

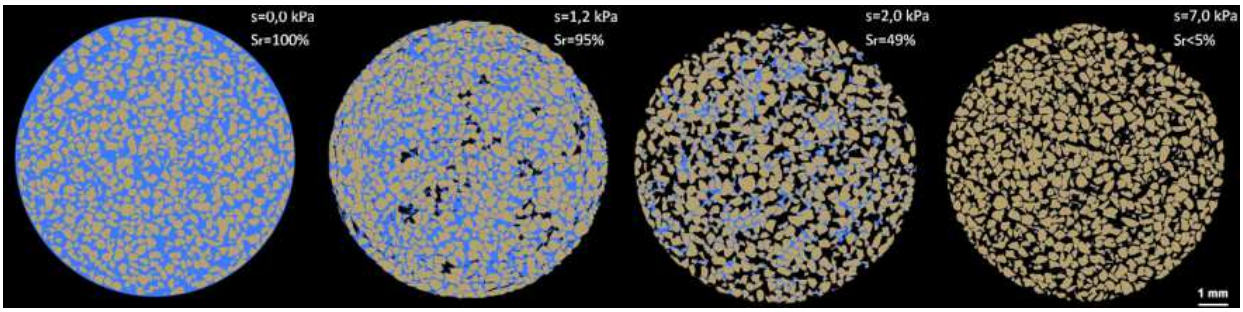

Fig. 4 Different domains (fully saturated, funicular, pendular and hygroscopic) shown in trinarized images of Hostun sand

Later, an innovative code was developed, so that porosity and degree of saturation mapping can be acquired. The program was designed to start with the trinarized images, apply a grid, choose a representative elementary volume (REV), for which local/global values of porosity and degree of saturation were calculated with high precision. These values revealed the link, at the grain scale, between porosity, degree of saturation and suction, Fig. 5, as that high porosity regions are linked to low degree of saturation regions, and vice versa.

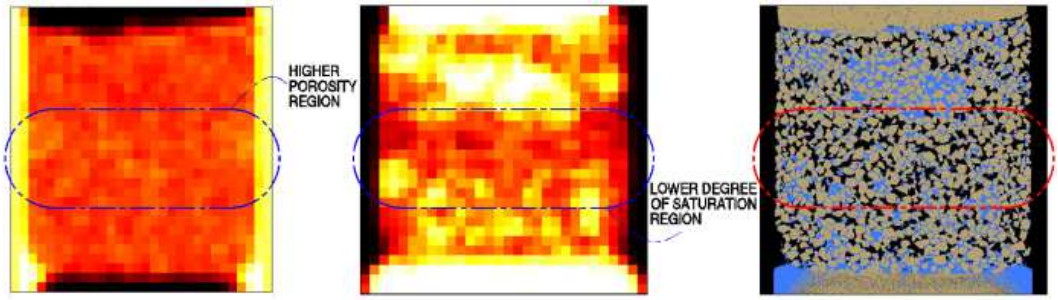

Fig. 5 Porosity map (left), degree of saturation map (centre), and trinarized image (right), for Hostun sand

Fig. 6 shows the relationship between water repartition, material composition and grain size, for Sr=50%, and for the three materials tested. It can be noticed, that grain angularity has an influence on water distribution inside the sample. Increasing the angularity (as for Hostun

sand) leads to have less homogeneous distribution of water than in the case of rounded grains (as in Glass beads).

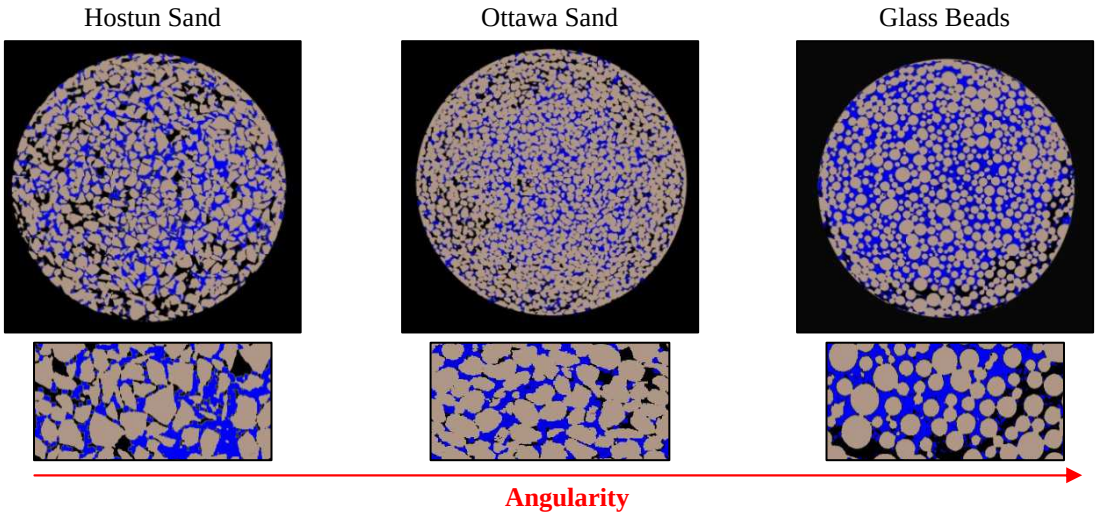

Fig. 5 Trinarised images of (Left to right): Ottawa sand, Hostun sand and Glass beads, (Sr=50%), for a slice at same height of the sample

This ongoing work focuses on the exploration of micro-scale hydraulic mechanisms in unsaturated granular materials. The results shows that not only global water retention curve is obtainable through image processing, but also a local relation between suction, porosity and degree of saturation can be computed for each point in the sample. The methodologies presented in this paper can be used for more expanded analysis that includes the measurement of effective stress or orientation of water meniscus.

REFERENCES

Kim F., Penumadu D., Hussey D. (2011) Water Distribution Variation in Partially Saturated Granular Materials Using Neutron Imaging. Journal of Geotechnical and Geoenvironmental Engineering, in press.

Khaddour G., Andò E., Salager S., Bésuelle P., Viggiani G., Hall S., Desrues J.(2013). Application of X-ray tomography to the characterisation of grain-scale mechanisms in sand. Multiphysical Testing of Soils and Shales , Springer Series in Geomechanics and Geoengineering, Part 4, 195-200, DOI: 10.1007/978-3-642-32492-5_23.

Riedel I., Andò E., Salager S., Bésuelle P., Viggiani G. (2012). Water retention behaviour explored by X-ray CT analysis. Proceedings of E-UNSAT 2012, Napoli.

Andò E., Hall S., Viggiani G., Desrues J., Besuelle P.(2012). Grain-scale experimental investigation of localised deformation in sand: a discrete tracking approach. Acta Geotechnica, 7, 1, 1-13.

Y Higo, F Oka, S Kimoto, T Sanagawa, and Y Matsushima. Study of strain localization and microstructural changes in partially saturated sand during triaxial tests using microfocus x-ray ct. Soils and Founda-tions, Japanese Geotechnical Society, 51(1):95{111, 2011.

Experimental characterization of the evolution of ballast grain shape and roughness

I. Deiros, D. Tunkin, G. Combe* & F. Emeriault
Laboratoire Sols, Solides, Structures, Grenoble, France
ivan.deiros@3sr-grenoble.fr denis.tunkin@3sr-grenoble.fr
gael.combe@3sr-grenoble.fr fabrice.emeriault@3sr-grenoble.fr
and
C. Voivret
SNCF – Innovation et recherche, Paris, France
charles.voivret@sncf.fr

* *Corresponding author*

ABSTRACT

Ballast aggregates have been used since the beginning of modern railway history because of its impressive efficiency as track foundation. However, high speed lines erode the grains much faster than predicted by empirical models used so far. Hence a numerical approach is needed in order to get first a better understanding of the behaviour of ballast and then be able to predict it in an accurate manner. The first step though consists in identifying all the parameters involved in ballast morphology and how they behave along the erosion process. On the macro – scale, morphology is governed by shape parameters; but when focusing on the micro – scale, one of the most important parameters is the description of surface texture, i.e. basically roughness. A literature review is performed in order to select some parameters that are commonly used to assess morphology. Then an experimental study on real ballast grains, using a Micro-Deval device to erode the grains and X-ray tomography and a laser profilometer to scan them, is performed to find out which of these parameters are actually suitable to assess the evolution of the morphology when the grains erode.

INTRODUCTION

Ballast is the crushed rock used for the foundation of a railway track, it forms the trackbed upon which railway sleepers are laid. It is used mainly to bear the dynamic load of trains,

transmitted by the railway ties, acting as a support base for the track structure giving it strength and rigidity but also allowing for flexibility. It is also used to facilitate drainage of water and to keep away vegetation that might interfere with the track structure. Some assays have been developed in order to control its quality but, due to its simplicity and effectiveness, it is an element of the track which has not changed so much in essence over the years. A good ballast aggregate must be: sharp, rough, hard and dense, resistant to impact, resistant to abrasion, homogeneous and dimensionally stable and without fine.

Along their lifespan, ballast grains get eroded mainly due to the cyclic loads caused by the traffic of trains and the maintenance operations. Roughness and sharpness are lost gradually, and, whenever the properties do not fulfil the requirements, the whole ballast must be removed and changed, which involves a great economic investment. Therefore it is important to have a good knowledge about its behaviour in order to assess properly the maintenance costs of the track. Until now, the experience over the years in ballasted tracks and the derived empirical formulas are the only tools we have to predict when the ballast shall be substituted. In conventional lines, these empirical formulas have proven to work well and no further studies have been needed so far. But it is no longer the case since we deal with high-speed lines, where ballast has shown to erode much faster than expected. While it was expected to last for 30 years, some lines in France and Japan had to be substituted after just 15 years. For that and other problems associated, ballast is being questioned as the best solution in this kind of lines, having the main competition with the slab track. Using slab track instead of ballast involves a minor maintenance costs but about twice the initial investment, so there is not a clear optimal solution and the discussion is still alive and far from being conclusive.

Every parameter regarding how grains morphology evolves upon time while the grains wear must be then identified and studied separately in order to understand properly the erosion process. At the macro – scale, cyclic loads induce breakage of sharp corners of the aggregates, smashing of weaker particles, repeated grinding and wearing. All these processes progressively sculpt the grains transforming the shape towards more rounded particles decreasing considerably their performance. At the micro-scale, friction between particles is reduced, decreasing the stiffness of the track to lateral loads, due to the sliding contacts that polish the grains and reduce surface roughness.

Figure 1. **Left: TGV railway track lying over ballasted trackbed. Right: common samples of ballast grains (granite), around 6-7 cm long; the grain on the right is completely new (sharp edges), while the grain on the left has been eroded changing its morphology (rounded edges).**

MORPHOLOGY OF THE BALLAST GRAINS

In order to describe the morphology of a particle in detail there is a large number of quantities, parameters and definitions used in the literature. Some authors (Mitchell and Soga

2005) use three levels to characterize shape and texture at different scales. At large scales, sphericity, elongation and flatness are usually used to provide a general idea of the grain shape. The intermediate scale is focused on describing the roundness of the grain, i.e. how sharp are the angles and borders, and it is usually described using the opposite parameter: angularity. Finally, in order to describe the micro-scale on aggregates, the main parameter to define the surface texture is roughness.

Shape parameters

Shape parameters describe the macro-scale morphology of the grains, i.e. both the general aspect and the angularity of the grains, which corresponds to the large and intermediate levels of the description above.

The main parameter describing the shape of a grain is sphericity, i.e. how close the shape of the grain is compared to that of a sphere, always ranging from 0 to 1, the latter value corresponding to the perfect sphere. Sphericity is defined in the literature in several ways, the most common definition being the ratio between the area of a sphere with the same volume of the particle and the area of the particle. However, since it is not so easy to extract the area of the contour of an irregular grain, other definitions are considered.

Inscribing the grain into a rectangular prism, three characteristic lengths can be defined corresponding to the sides of the cuboid: D_S (shortest), D_M (intermediate) and D_L (longest). Using these three characteristic lengths, sphericity Ψ can be defined (Krumbein 1941), but it can be also complemented with other aspect ratios which help to better understand the general morphology of the particle. Elongation ratio (ER) compares the longest length with the intermediate one, flatness ratio (FR) compares the shortest with the intermediate and flat and elongation ratio (FE) compares the longest with the shortest. Aggregates are considered flat or elongated if their flatness ratio or elongation ratio, respectively, present values lower than 1/3. One last parameter commonly used to describe general morphology is the shape factor (SF), which is a combination of FR and FE (Barksdale 1991). According to the presented definitions, all five described parameters range from 0 to 1, the latter value corresponding to the case of a sphere or a cube.

$$\Psi = \sqrt[3]{\frac{D_S D_M}{D_L^2}} \qquad (1.1) \qquad ER = \frac{D_M}{D_L} \qquad (1.2) \qquad FR = \frac{D_S}{D_M} \qquad (1.3)$$

$$FE = \frac{D_L}{D_S} \qquad (1.4) \qquad SF = \frac{D_S}{\sqrt{D_L D_M}} \qquad (1.5)$$

At a smaller scale, it is interesting to describe the sharpness of the angles of the grain. This is commonly assessed by parameters called roundness or, its antonym, angularity. Roundness is usually defined as the average radius of curvature of all the corners divided by the radius of the largest inscribed circle. According to these definitions, a sphere has a roundness of 1, but not a cube. Since it is not easy to assess the radius of curvature of the corners, the evaluations of roundness is often obtained by using visual guides. In order to properly quantify either roundness or angularity, many methods have been proposed in the literature. For instance, the gradient method gives a finite angularity value to a highly sharp grain and a near zero value to a well rounded grain and interpolates intermediate angularities by comparison with the two extremes. However, when a multi-scale description of the morphology is needed, other methods that can deal with all three levels of description are commonly used. Fourier analysis of the contour can be used when dealing with 2D particles (Wang et al. 2004), obtaining different signatures for different scales depending on the frequency. If a 3D description is

needed there are two methods that can be used to analyse image data: wavelet method (Kim et al. 2002) and spherical harmonic analysis (Garboczi 2002). The second method has been chosen for this project since it was also used to deal with 3D X-ray tomography data.

If the radius R(θ,Φ) is measured from the centre of mass of the grain to the surface, θ angle measured from positive z-axis (0<θ<π) and Φ angle measured from positive x-axis (0<Φ<2π):

$$R(\theta,\phi) = \sum_{n=0}^{\infty} \sum_{m=-n}^{n} a_{nm} Y_n^m(\theta,\phi) \tag{2}$$

Where a_{nm} is a scalar coefficient and Y_n^m (θ,Φ) is an harmonic function of degree n and order m and is given by:

$$Y_n^m(\theta,\phi) = \sqrt{\frac{(2n+1)\cdot(n-m)!}{4\pi(n+m)!}} P_n^m(\cos(\theta))\cdot e^{im\phi} \tag{3}$$

Where P_n^m are the associated Legendre polynomials. The quantification of aggregate form, angularity and surface texture is based on solving the coefficient a_{nm}. Garboczi proposed the use of the following integral form:

$$a_{nm} = \int_0^{\pi}\int_0^{2\pi} d\phi d\theta \sin(\theta)\cdot R(\theta,\phi)\cdot Y_n^m * \tag{4}$$

Where the asterisk denotes the complex conjugate. Three descriptors for the different scales are then proposed (Masad et al. 2005) using the spherical coefficient a_{nm}:

$$Form = \sum_{n=0}^{5} \sum_{m=-1}^{n} |a_{nm}| \tag{5}$$

$$Angularity = \sum_{n=6}^{25} \sum_{m=-1}^{n} |a_{nm}| \tag{6}$$

$$Texture = \sum_{n=26}^{n_{max}} \sum_{m=-1}^{n} |a_{nm}| \tag{7}$$

Table 1 presents the values of the different shape parameters for some typical regular shapes. It can be observed how all the parameters have values close to 1 when the the shape is closer to that of a sphere, with the exception of angularity which gets values close to 0. Besides, while the typical shape parameters do not distinguish between a sphere and a cube, form and angularity indexes (spherical harmonic parameters) do.

	Ψ	ER	FR	FE	SF	Form	Ang.
Unit sphere	1	1	1	1	1	1	0
Unit cube	1	1	1	1	1	1.27	0.33
Cylinder (r=2, h=5)	0.86	0.80	1	1.25	0.89	1.46	0.39
Cuboid (3:1:1)	0.48	0.33	1	3	0.58	2.10	0.77

Table 1. **Values of the shape parameters for some regular shapes: sphericity (Ψ), elongation ratio (ER), flatness ratio (FR), flat and elongation ratio (FE), shape factor (SF) and the spherical harmonics parameters form and angularity indexes.**

Roughness parameters

Surface texture is the repetitive or random deviation from the nominal surface that forms the three- dimensional topography of the surface. Although surface texture can be assessed with

the methods described above, due to the complexity of the method, other much simpler methods are commonly used at the micro-scale. Surface roughness is commonly quantified by scalar parameters which assess the height of the surface relative to a reference line or plane, depending on whether the roughness is evaluated over a height profile (2D) or over the whole surface (3D) (Bhushan 2000). Note that roughness parameters are usually referred with an R in the case of 2D profiles and with an S in the case of 3D surfaces. The mean line (or surface) is defined such that the area between the profile and the mean line above the line is equal to that below the mean line:

$$m = \frac{1}{N}\sum_{i=1}^{N} z_i \tag{8}$$

Where N is the discrete amount of data points and z_i is the height of each data point with respect to the reference plane. If there is no special interest in using a particular reference plane, in order to simplify the calculations, the mean surface is generally used as the reference plane so that m = 0, and this simplification will be taken into account in the following definitions. Amplitude parameters compare the height of the surface with the reference plane (Table 2), with a particular emphasis on:

- Average roughness (R_a/S_a), i.e. the arithmetic mean of the absolute value of vertical deviations from the mean surface.
- Root-mean-square height (R_q/S_q), i.e. the square root of the arithmetic mean of the square of the vertical deviations from the reference surface.

There are other amplitude parameters considering the extreme values like R_t/S_t which computes the distance between the highest asperity and the lowest valley or, in order to minimize the effect of strange data in the extreme values, R_z/S_z computes the distance between the averages of the five highest asperities and the five lowest valleys . Following the same structure of the average roughness and the RMS height, the moments of third and fourth order can be also computed. These two parameters are called skewness (Sk/S_{Sk}) and kurtosis (K/S_{Ku}) and they are usually classified as shape parameters (of roughness) since they describe, respectively, whether the valleys are wider or narrower than the peaks and whether the surface has a more peaky or more wavy roughness.

	2D		3D	
Average roughness	$R_a = \frac{1}{N}\sum_{i=1}^{N}\lvert z_i\rvert$	(9.1)	$S_a = \frac{1}{N\cdot M}\sum_{i=1}^{M}\sum_{j=1}^{N}\lvert z_{ij}\rvert$	(9.2)
RMS height	$R_q = \sigma = \sqrt{\frac{1}{N}\sum_{i=1}^{N} z_i^{\,2}}$	(10.1)	$S_q = \sqrt{\frac{1}{N\cdot M}\sum_{i=1}^{M}\sum_{j=1}^{N} z_{ij}^{\,2}}$	(10.2)
Skewness	$Sk = \frac{1}{\sigma^3\cdot N}\sum_{i=1}^{N} z_i^{\,3}$	(11.1)	$S_{Sk} = \frac{1}{S_q^{\,3}\cdot N\cdot M}\sum_{i=1}^{M}\sum_{j=1}^{N} z_{ij}^{\,3}$	(11.2)
Kurtosis	$K = \frac{1}{\sigma^4\cdot N}\sum_{i=1}^{N} z_i^{\,4}$	(12.1)	$S_{Ku} = \frac{1}{S_q^{\,4}\cdot N\cdot M}\sum_{i=1}^{M}\sum_{j=1}^{N} z_{ij}^{\,4}$	(12.2)

Table 2. **Definitions of the roughness amplitude parameters.**

These amplitude and shape parameters can be complemented by the spacing parameters, i.e. a way to quantify the density of asperities and are mainly represented by peak density (N_p in 2D

and η in 3D). However, the reliability of this parameter depends on how the peaks are defined and the sensibility of the measure device.

Roughness can be assessed in other deeper ways than scalars. Probabilistic analysis has been proposed in the literature (Bhushan 2000) in the form of density functions and spatial functions. Although not included in this study, these functions can be interesting in some specific cases in order to better understand processes involving surface texture.

A unique property of rough surfaces is that, if they are repeatedly magnified increasing observed details of roughness right down to nano-scale, these details often appear quite similar in structure. The fractal approach (Majumdar and Bhushan 1990) has the ability to characterize surface roughness by scale-independent parameters and provides information on the roughness structure at all length scales that exhibit the fractal behaviour. Fractal surfaces have a non-integer dimension associated, called fractal dimension (D), that ranges between 2 and 3 and provides a statistical index of complexity comparing how the details in the surface change with the scale at which the surface is measured, i.e. a ratio of the change in detail to the change in scale (Mandelbrot 1982).

There are several methods to compute fractal dimension but one of the most commons is the box counting method. The computed total area of a surface map increases while a finer mesh is chosen to plot the map so that more details can be included. Following this principle, both the area, calculated with different mesh sizes, and the length of the mesh element in each case are represented in a log – log plot. The fractional part of the fractal dimension is given by the slope of the resultant line, and the total fractal dimension is computed summing up 2 to the fractional dimension. For example, a completely flat surface implies an equal measurement of the area whatever the mesh size one uses, thus the slope of the log – log plot and so the fractional dimension will always be equal to 0 and the fractal dimension equal to 2.0, the same as the traditional dimension of a plane.

EVOLUTION OF THE MORPHOLOGY

Experimental campaign

In order to study the evolution of the different morphology parameters described above during the wearing process, some real ballast grains have been artificially worn and scanned to search for some tendencies in the shape and roughness parameters. New granite ballast grains have been provided by the SNCF corresponding to those actually used in the French high-speed railway network. Five different grains have been selected trying to include different initial morphologies.

Figure 2. **Ballast samples before erosion. From left to right: S10, S11, S12, S13 and S14.**

These five sample, shown in Figure 2 and called S10, S11, S12 S13 and S14, have been eroded twice using a Micro-Deval device, during 3 hours per cycle of erosion, along with

other ballast grains to cover a total of 10 ballast grains and 2 litres of water inside each cylinder (without metal balls). The procedure to erode the grains was chosen with the main objective of being aggressive enough to cause a good amount of wear per cycle on the grains but gentle enough to be able to observe an evolution. During the first cycle of erosion the grains lost around 5-6% of the weight, while in the second cycle the grains lost only a bit more than 3%. Sample S10, the largest one, broke during both cycles losing 11% of the weight in the first cycle and almost 6% in the second. However, the size of the sample is not really determinant in the relative amount of matter lost in the erosion process, but the shape does since some morphologies are more likely to break than others.

Image analysis

Before and after each erosion cycle, the samples have been scanned using X-ray tomography (Figure 3), to obtain a 3D image of the whole grain, and with a laser profilometer (Figure 4) over one flat face to assess the roughness (except for sample S14, which did not have any flat face large enough to be scanned with the laser). Finally, the retrieved data has been analysed using a Matlab code.

The resolution achieved by the tomograph on the performed scans was 0.0513 mm / voxel edge, but in order to be able to faster process the data, a scaling factor was applied reducing the number of voxels to half so the final resolution is 0.1026 mm / voxel edge. This resolution is enough to assess shape parameters since these parameters do not deal with the micro-scale but with orders of magnitude of millimetres or even centimetres.

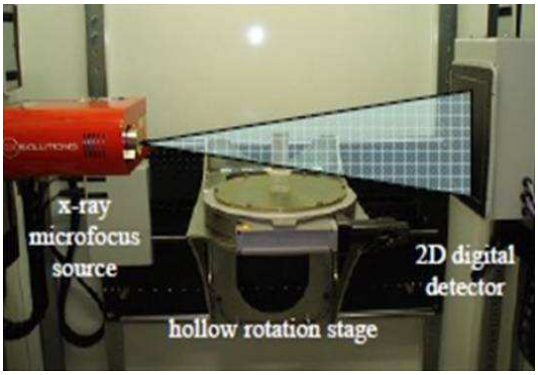

Figure 3. **Operation diagram of the X-ray tomography device. The source, along with the detector film on the opposite, side takes sectional images of the sample placed on a rotating stage allowing a complete 360º turn.**

Table 3 shows the total amount of mass lost after both cycles of erosion, and the reduction in the number of voxels of the 3D reconstructions from the tomographies. The results given by the X–ray tomography are really good and reliable in terms of matter lost. Comparing the weight and the number of voxels lost the difference is insignificant.

Grain	Total mass lost (%)	Total voxels lost (%)	Difference (%)
S10	16.12	15.70	-0.42
S11	8.83	8.39	-0.44
S12	8.13	8.36	+0.23
S13	9.23	8.96	-0.27
S14	7.80	8.21	+0.41

Table 3. **Comparison between the mass lost and the reduction of voxels in the tomographies after both cycles of erosion.**

On the other side, due to some mechanical issues associated with the supporting structure and the screws moving the laser profilometer, the device was not able to offer a better accuracy in

a specific point than ± 0.10 mm, which is pretty low if it is compared to the order of magnitude of roughness. However, since these issues affect all the scans in approximately the same way, it can be assumed, after making some scans of the same areas in different samples, that the accuracy of the device when computing roughness (z-axis) is about ± 0.02 mm, or even better.

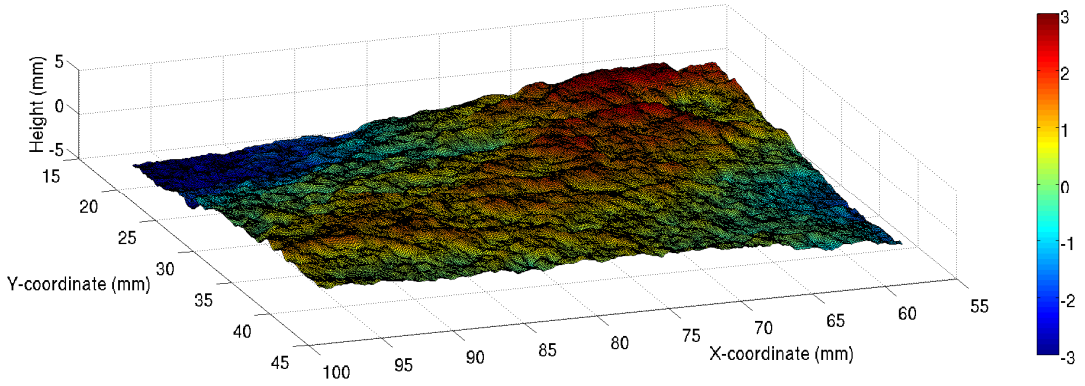

Figure 4. **Surface map of a ballast grain face reconstructed using a square-element mesh (0.1 mm per element side) from the data points retrieved by the laser profilometer.**

Evolution of parameters

It is necessary to remark before presenting the results that the first cycle of erosion was strongly more aggressive than the second one, producing the majority of the changes on the morphology of the grains, especially regarding roughness. Figure 5 shows sample S12 before and after the first cycle of erosion and a comparison of both where the eroded areas are highlighted in red. It is clearly seen how sharp corners disappear first, due to either wear or breakage of weaker parts, reducing considerably the angularity of the grain. It is also shown how roughness is dramatically reduced leaving an already smooth surface after the first cycle of erosion. However, the general shape (elongation, sphericity, etc…) of the grain remains without remarkable changes.

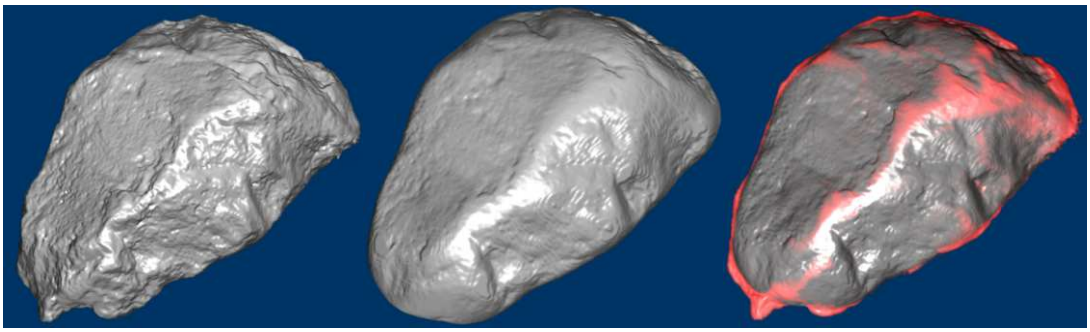

Figure 5. **3D reconstruction of sample S12 from the X-ray tomographies before and after the first cycle of erosion. The lost matter is highlighted in red.**

Hence among all shape parameters considered to describe the form of the ballast grains, only angularity presents a remarkable decreasing tendency in all grains. Figure 6 shows the evolution in percentage of all shape parameters after both cycles of erosion in comparison with their initial values. It is clearly seen how the angularity of all grains decreases in a significant amount. Figure 7 shows the evolution of angularity along both cycles, although the first cycle is aggressive enough to considerably round the edges and reduce angularity, the second cycle still contributes in a significant way to the process.

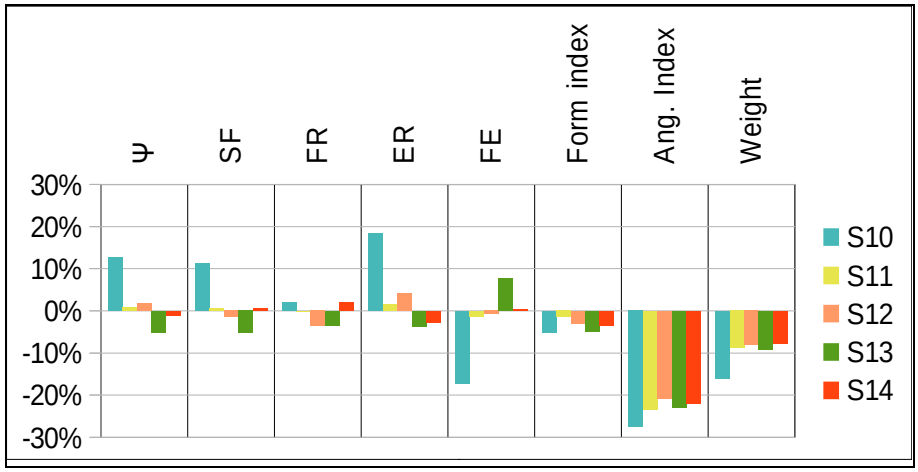

Figure 6. **Evolution in percentage of the different shape parameters (sphericity (Ψ), elongation ratio (ER), flatness ratio (FR), flat and elongation ratio (FE), shape factor (SF) and form and angularity indexes) and weight between the initial values (new grains) and after the second cycle of erosion. S1X corresponds to the name of the different grain samples.**

Form index also decreases in all grains but extremely slow. All the other parameters remain with approximately the same values during both cycles of erosion although they are thought to tend to values close to 1 if the erosion is much more aggressive, since the grains tend to reach a spherical-ellipsoidal shape. However, Micro-Deval was not able to reproduce such a big amount of erosion. Sample S10 presents a larger evolution on its morphology but this is not surprising since that sample broke both in the first and in the second cycle losing up to 16% of the mass. Note that Ψ, SF, FR and ER are, by definition, lower or equal to 1 so they increase if the shape approximates to that of a sphere, while Form index and FE are always larger or equal to 1, decreasing if the grain gets closer to the shape of a sphere.

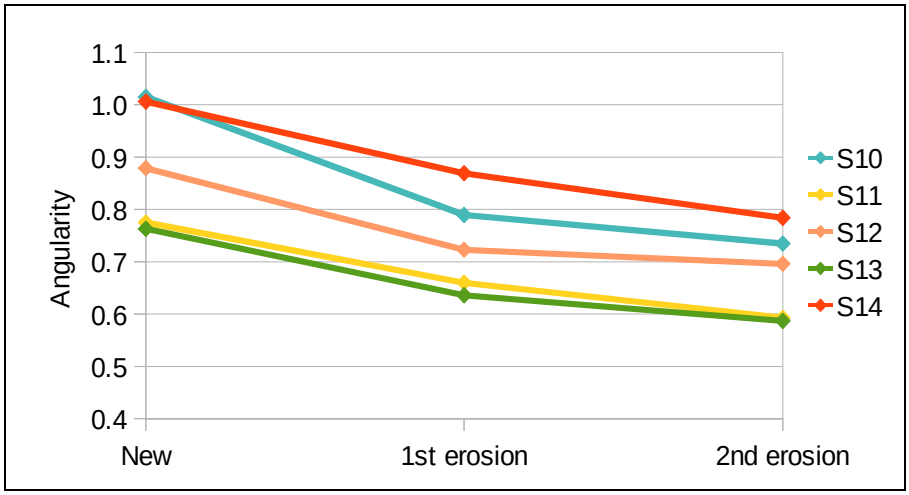

Figure 7. **Evolution of angularity along the two cycles of erosion. Angularity has an inferior limit of 0, corresponding to a perfect sphere. S1X is the name of the different grain samples.**

On the other hand, using a Micro-Deval device, although mitigated by the particular methodology applied, surface texture is polished and smoothed in a very fast way. Micro-scale roughness is virtually lost as a whole in the first cycle of erosion and only waviness, in a half-way between micro and intermediate scales, lasts for a longer time. This waviness has been partially removed before the analysis along with the shape of the grain through least squares correction using 6 degrees polynomial functions.

After the first cycle, some parameters were quickly discarded for different reasons. Skewness and kurtosis present an extremely large variance and instability between scans since they are too sensitive to the accuracy of the measurements. On the other hand, although it is a bit more stable, peak or asperity density is completely influenced by the definition given to the asperities. Thus the low accuracy of the laser in a specific point mentionned before is not enough precise to properly deal with all these parameters.

Figure 8 shows the evolution in percentage of the different amplitude parameters and fractal dimension after the first cycle of erosion. The parameters denoted with an R have been computed as an average of the 2D profiles, while the parameters denoted with an S have been computed over the whole surface after reconstruction with Matlab. As expected, these parameters are clearly reduced during the process. For some reason, sample S13 shows a lower roughness descent although it did not lose less matter than the others, probably because of the influence of larger asperities not compensated with the waviness correction which presents a higher resistance to wear.

Average roughness and RMS roughness are the most commonly used parameters when assessing roughness and the reason is that they behave in a very stable way showing a very small variance. However, extreme values R_t, S_t and even S_z are too susceptible to big defaults on the surface texture or strange measurements of the laser.

On the other hand, fractal dimension shows also a very stable behaviour and its evolution seems to be pretty related to the evolution of the amplitude parameters. Having into account the way fractal dimension is computed, in which the fractional part is obtained from the slope of a log-log plot and then 2 is summed up to get the total fractal dimension, it has been judged more convenient to compute the percentage only considering the fractional part.

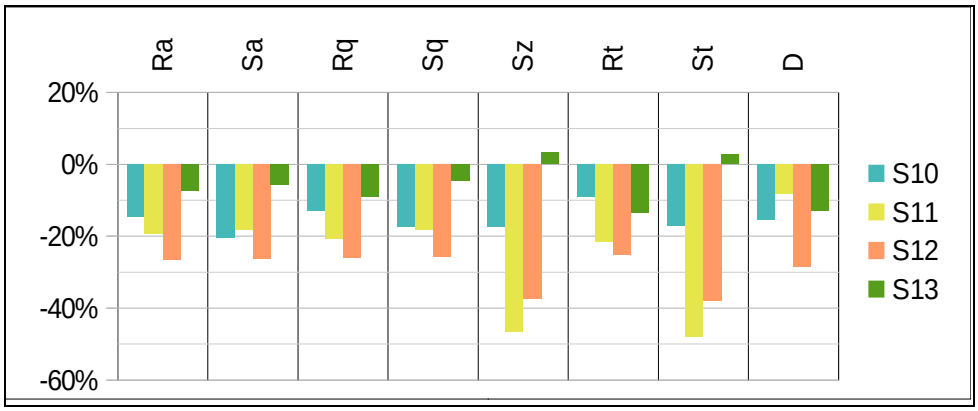

Figure 8. **Evolution in percentage of the amplitude roughness parameters (average roughness (R_a/S_a), RMS height (R_q/S_q), average maximum height (S_z) and maximum height (R_t/S_t)) and fractal dimension (D) between the initial values and after the first cycle of erosion. S1X is the name of the different ballast grain samples.**

CONCLUSIONS

It has been demonstrated, as expected, that for the type of wear applied by the Micro-Deval device (without large breakages) and during a limited time (6h), the smaller the scale the faster the parameters are smoothed.

Hence micro roughness is lost very quickly, even faster than expected so more and shorter cycles should be applied in order to assess more properly its evolution. Although the stability of the parameters is acceptable, since the inaccuracies of the laser affect all scans in the same

way, it is also recommended to improve the precision of the device to be able to get reliable absolute values of roughness. Nevertheless, it can be stated that amplitude parameters, especially the ones not including extreme values, along with fractal dimension are good candidates to assess the evolution of surface texture during wearing processes.

The intermediate scale of morphology, mainly represented by angularity, plays a very important role in the evolution of shape since sharp angles and edges are rounded and weak pointed tips break easily. This tendency has been shown evident in all grains and during both cycles of erosion.

However, large scale morphology has a much slower evolution, depending to a large extent on the grains crushing and breakage of the weaker parts. A much more aggressive wearing must be performed in order to see a significant evolution on the parameters.

ACKNOWLEDGEMENTS

The authors want to acknowledge the Laboratoire 3SR in Grenoble and the French railway company Société Nationale des Chemins de Fer Français SNCF.

REFERENCES

Barksdale, R.D., et al. 1991. Measurement of aggregate shape, surface area, and roughness. *Transportation Research Record* 1301: 107-116.

Bhushan, B. 2000. Surface Roughness Analysis and Measurement Techniques. *Modern Tribology Handbook.* CRC Press, USA, vol. 1, chap. 2 .

Garboczi, E.J. 2002. Three-dimensional mathematical analysis of particle shape using X- ray tomography and spherical harmonics: Application to aggregates used in concrete. *Cement and Concrete Research* 32(10): 1621-1638.

Krumbein, W.C. 1941. Measurement and geological significance of shape and roundness of sedimentary particles. *Journal of Sedimentary Petrology* 11: 64-72.

Kim, H., et al. 2002. Wavelet-based three-dimensional descriptors of aggregate particles. *Transportation Research Record*: *Journal of the Transportation Research Board* 1787(1): 109-116.

Majumdar A., Bhushan, B. 1990. Role of fractal geometry in roughness characterization and contact mechanics of surfaces. *Journal of Tribology* 112(2): 205-216 .

Mandelbrot, B.B. 1982. The fractal geometry of nature. W.H. Freeman and Company, New York .

Masad, E.A., et al. 2005. Computations of particle surface characteristics using optical and X-ray CT images. *Computational Materials Science* 34(4): 406-424.

Mitchell J.K. & Soga K. 2005. Soil composition and engineering properties. *Fundamentals of soil behavior*. 3rd edition. John Wiley & Sons, Inc., Hoboken, New Jersey, chap. 4.

Wang, L.B., Frost, J.D. & Lai, J.S. 2004. Three-dimensional digital representation of granular material microstructure from X-ray tomography imaging. *Journal of Computing in Civil Engineering* 18 (special issue: applications of imaging technologies in civil engineering materials): 28-35.

Vertical cyclic loading on soil reinforcement by the rigid piles: multi-scale experimental analysis

M. Houda, O. Jenck & F. Emeriault
Laboratoire Sols, Solides, Structures, Grenoble, France
moustafa.houda @3sr-grenoble.fr orianne.jenck@3sr-grenoble.fr
fabric.emeriault@3sr-grenoble.fr

ABSTRACT

An original experimental device was developed in laboratory with a reduced scale on the length equal to 1/10, to simulate soft soil improvement by vertical rigid piles. A campaign was performed in order to assess the behaviour of a load transfer platform (LTP) of small thickness, built under a surface rigid slab. Several surface loading conditions, monotonic and cyclic, were applied in order to analyse the impact of vertical cyclic loading (with no development of dynamic effects) and its loading magnitude. The model has an important number of piles, so a pertinent analysis can be done on the model central part. Originality of the model is also the presence of a lateral visualization window and application of a digital image correlation (DIC) method to follow each visible grain of the LTP. Mechanisms developing in the LTP during the cycles can thus be highlighted and understood. The DIC results complete those obtained in the central part by the load and displacement sensors.

INTRODUCTION

Soft soil improvement by rigid piles involving granular platforms is widely implemented across the world due to the low costs, rapid construction, and the resulting small total and differential settlements compared to the traditional soft soil improvement techniques like grout injection, vertical drains or preloading. This technique is different from those using classical piles, where the structure is directly connected to the piles. The load applied by the structure is partially transferred through a Load Transfer Platform (LTP) to the vertical rigid pile grid that assures the load transfer to the substratum below (Figure 1). In the case of a surface slab, loads are also redistributed in this part of the system, especially for thin granular platforms, where full arching cannot develop.

Experimental studies on soft soil improvement by rigid piles have been carried out by several researchers in the past, attempting to analyse the effect of different material

parameters, geometrical configurations and geosynthetic reinforcements, to investigate their respective contributions to the reduction of settlements and to the increase of load transfer onto piles, and to develop corresponding design methods. In particular, Kempfert *et al*. (2004), Heitz *et al*. (2008) and Van Eekelen *et al*. (2012) have based their research works on 1g laboratory models in a three dimensional configuration.

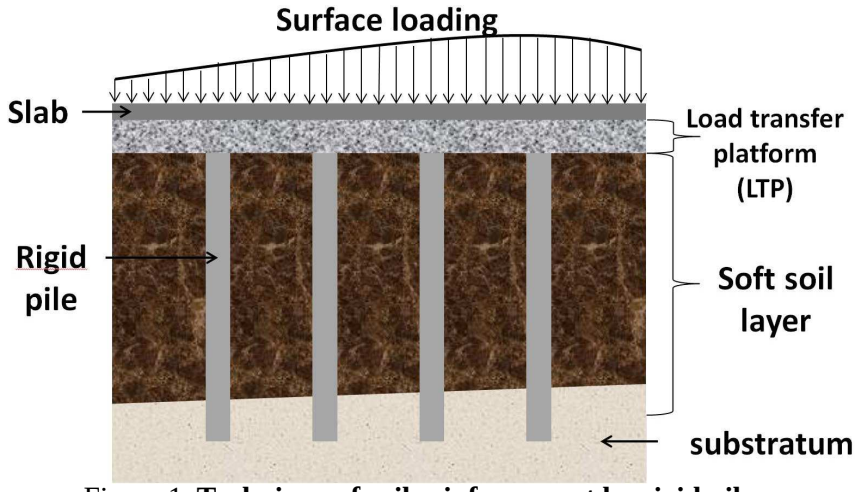

Figure 1. **Technique of soil reinforcement by rigid piles**

Blanc et al. (2013) and Okyay et al. (2013) performed model tests in a centrifuge in order to obtain the same stress level in the model than in the prototype.Other research works aimed to visualize the arching effect inside the LTP using Digital Image Correlation (DIC) methods (Eskişar et al., 2012; Jenck et al., 2014). The majority of these studies were limited to the case of static or monotonic loading, except Heitz et al. (2008) who applied a high number of cycles (up to one million cycles) with high frequencies of 1 or 5Hz simulating the case of a railway. They underlined the effect of the loading frequency on the efficiency and the settlements.
The objective of this paper is to study the effect of vertical cyclic loading on the structure's behaviour using a three-dimensional small scale model simulating the soil reinforcement by vertical rigid piles. A series of model tests are conducted and the behaviour of the system is studied based on the results of force and displacement sensors. The objective of this study includes visualizing the mechanisms in the LTP using a particular Digital Image Correlation (DIC) method called Particle Image Tracking (PIT) technique that enables us to analyse the displacement and rotation fields of the grains composing the LTP.

MODEL TESTS

The tests are performed using a 1g three-dimensional model with a scale factor of 1/10th on length (presented in details in Houda et al., 2013). Four semi-piles are added next to a window allowing the visualization and the analysis of the mechanisms taking place inside the LTP as shown in Figure 2. The soft soil layer has a thickness Hs = 400mm and is overlain by a layer of gravel with a thickness Hg = 50mm (Figure 3). A rigid plate is placed above the LTP in order to model the case of soil reinforcement under "flat slab". Loading on the surface is applied using a membrane under pressure (Pm) which permits to apply monotonic or cyclic loadings.
The instrumentation used in the tests is located in the central zone, far from the boundaries. A force sensor is located at the top of each of the four central piles. Each force sensor has a compression range between 0 to 1000 kg and a diameter equal to the pile's diameter (pile =35mm). Three displacement sensors (D1, D2 and D3) are used to measure the settlements at the LTP base. The general measurement set-up is shown in figures 2 and 3

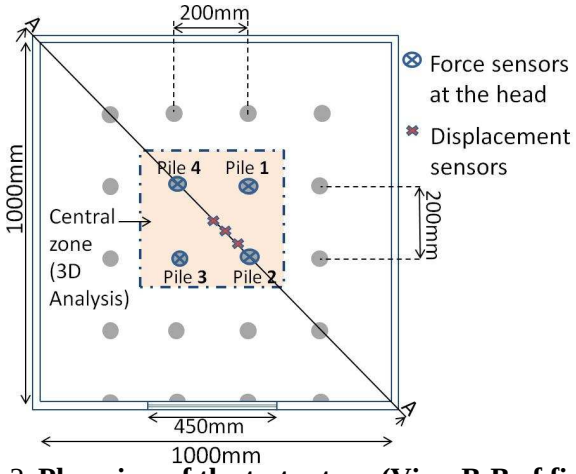

Figure 2. **Plan view of the test set-up (View B-B of figure 3)**

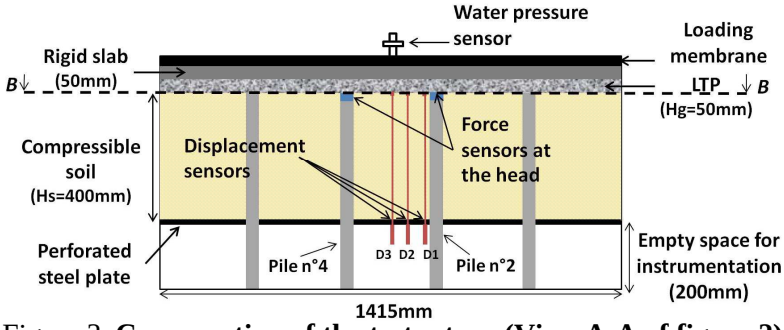

Figure 3. **Cross-section of the test set-up (View A-A of figure 2)**

Finding good simulating materials to represent the soft soil is a challenge for researchers. In this study, a mixture of Fontainebleau fine sand and expanded polystyrene balls (with a small amount of water to avoid segregation) is used to model the soft soil compressibility. The soil has a compressibility index Cc = 2.8 and an initial void ratio $e_0 = 7.2$ (considering the polystyrene balls are void). The corresponding average measured unit weight of the mixture is $\gamma_{soft\text{-}soil}=4.5kN/m^3$. In practice, the thickness of the granular layer usually lies in the range of 0.5m to 1m. In the present study, with a scale factor of $1/10^{th}$ on the length, a 50mm layer of 2-6mm diameter gravel is used to model the LTP (Figure3). The average unit weight after compaction is equal to $\gamma_{gravel} = 14.8kN/m^3$. The friction angle and the cohesion are found from triaxial tests equal to $\varphi = 45°$ and c = 0kPa.

The experimental campaign has been defined to evaluate the effect of low frequency cycles on the system's behaviour. Three types of test are performed in this campaign, with different loading conditions. They are summarized in Figure 4. The repeatability is verified by repeating each test (test A and B). The test "Monotonic 1" consists in applying three increasing levels of static loading Pm = 10, 20 and 30kPa, each loading level is maintained constant during 3 hours. The test "Cyclic 1" consists in applying 50 cycles between Pm = 0 and 10kPa before loading the system up to constant pressure Pm = 20kPa and 30kPa. The monotonic loading test is applied in order to study first the behaviour of the system under monotonic (simple) loading. In test "Cyclic 2", 50 cycles are applied between Pm = 10 and 20kPa before increasing the pressure up to a constant level Pm = 30kPa. The objective of applying two different types of cycles is to study the effect of cycles and their average pressure level on the system's behaviour.

The cyclic loadings always start with unloading and are divided into two stages: the period of each of the 6 first cycles is equal to 50 min (in order to take photographs for further applying

the DIC); then the period of each of the next 44 cycles is reduced to 20 min.The increase of the pressure up to 30kPa after the application of the cycles enables to analyse if the behaviour of the structure changes after a certain history of cyclic loading.

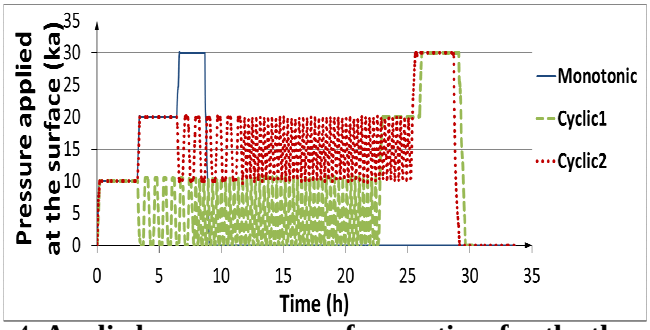

Figure 4. **Applied pressure on surface vs time for the three tests**

MONITORING RESULTS

The effect of applying cyclic loading on the structure's surface is examined by comparing the cyclic test results to the reference "Monotonic" test results. The effect of the stress level at which the cycles are performed is highlighted by comparing tests "Cyclic1" and "Cyclic2".
The distribution of the load at the top of the four central piles, not presented in this paper, is found to be homogenous - the maximum difference between the force measured at top of each pile and the average force does not exceed 10%. It is assumed that the distribution is also uniform on the outer piles (the box is made of smooth metallic walls in order to prevent as much as possible friction with the soft soil and LTP).
Figure 5 shows the evolution of the average force on the head of the four central piles (Figure 2) for the two cyclic tests "Cyclic 1A" and "Cyclic 2A". The force values presented during the cycles are only the values obtained at the end of each cycle (when the applied pressure Pm is maximum). After applying 50 cycles, the average force is found to be larger by 35% and 25% of its value before applying the cycles, in tests "Cyclic1" and "Cyclic2" respectively. This means that during the cycles, more loads are transmitted to the piles so less pressure is applied on the soft soil.

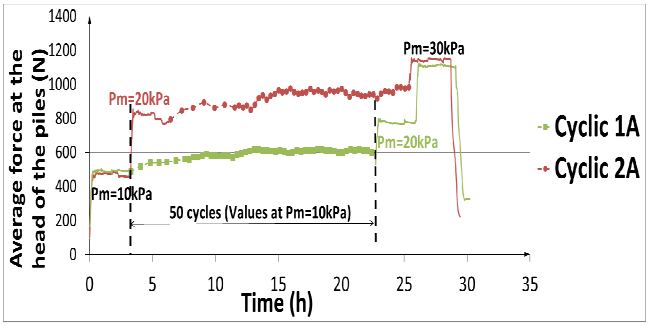

Figure 5. **Average head force vs time**

The efficiency E_i for each pile is defined in Eq. (1) as the ratio of the load measured on the pile i (F_{ti}) to the total load applied on a unit cell around the pile of area A = s^2 = 0.04 m^2. This total load is the summation of the dead load DL, which is the weight of the LPT, the rigid plate and the water inside the loading membrane, plus the live load LL which is the overload at the surface (LL = Pm x A).

$$E_i = \frac{Ft_i}{DL + LL} \quad (1)$$

Figure 6 shows the evolution of the average efficiency (average of the four values of Ei) for the three tests at different steps of the experiment. By comparing the test “Cyclic1” with the reference test “Monotonic 1”, an increase of the average efficiency due to the cycles up to a value around 1 is observed for Pm = 10kPa. This increase reflects an increase of the load transfer onto the piles due to the cycles. After applying the cycles, when increasing the surface pressure up to Pm = 20kPa, the efficiency decreases down to the same value found in the test “Monotonic 1” for the same applied surface pressure. We can observe the same trend for test “Cyclic2” where the cycles lead to an increase of the efficiency up to a value about 1, followed by a decrease down to the same value found in the test “Monotonic” for an applied pressure Pm = 30kPa. These observations demonstrate that the efficiency increase due to the cycles is not preserved when a larger surface pressure is applied. Therefore, the history of the cyclic loading seems to have no more influence on the load transfer when applying higher values of surface pressure.

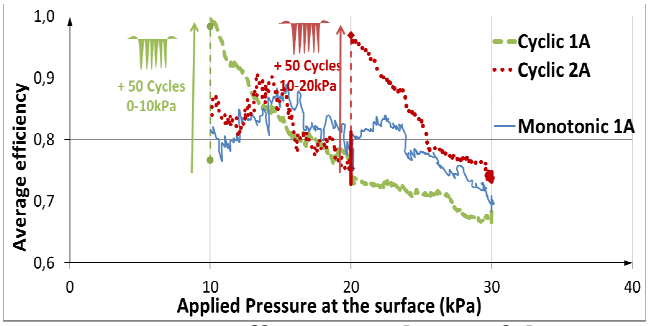

Figure 6. **Average efficiency evolution of the 3 tests**

The comparison between the cyclic tests results in terms of soft soil settlements on Figure 7 (Disp3 is the settlement measured in the centre by the sensor D3 presented in figure 3) shows an accumulation of settlement during the cycles (with a decreasing rate, where approximately 50% of the total settlement accumulation takes place during the first 6 cycles and without reaching stabilization at the end of the 50 cycles). The accumulation due to the 50 cycles in the test “Cyclic1” is about two times larger than the accumulation measured in the test “Cyclic2”. In fact, the settlement increase is equal to 8.5mm during the 50 cycles in test “Cyclic1” and equal to 4.5mm for test “Cyclic2”, which means that when same amplitude cycles are applied at a higher load level, less settlement accumulation is obtained.
It is noteworthy that the accumulation of the settlements happens during the loading phase when the applied pressure is around its maximum. During unloading, the settlement does not present any evolution.
Figure 7 also gives the settlement results for the test “Monotonic”, where no cycles are applied. After applying the cycles in the two tests “Cyclic1” and “Cyclic2”, the increase of the applied load *Pm* up to 30kPa leads to a final settlement Disp3 equal to the value measured in the test “Monotonic”. Therefore, the effect of the cycles in terms of settlement accumulation seems to be erased by the increase of the pressure up to a higher value than that experienced previously (here Pm = 30kPa).

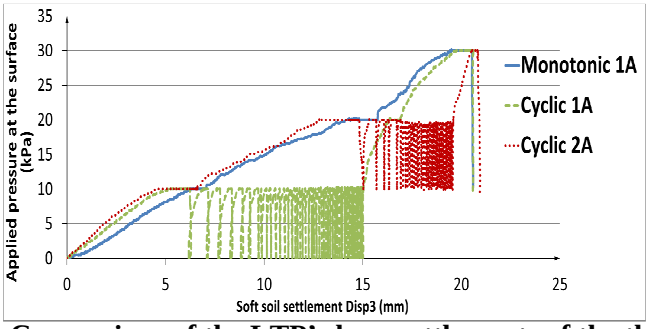

Figure 7. **Comparison of the LTP's base settlements of the three tests**

The experimental results based on the sensors permitted us to measure and analyse the forces at the head of the piles and the settlements at the LTP base. The following part of the paper consists in an image analysis using DIC that permitted us to visualize the displacements fields inside the LTP in order to better understand the mechanisms taking place inside it.

IMAGE ANALYSIS

The model side window and the four semi-piles are designed to visualize the displacement field, permitting a qualitative analysis of the mechanisms taking place inside the soil and especially inside the LTP. Photographs are taken through the window made of Plexiglas (Figure 8).

The image analysis can be achieved with the application of a new approach able to assess the 2D motion of rigid bodies in a granular layer (Combe and Richefeu, 2013). It enables to investigate the mechanism of load transfer by analysing the kinematics of the grains inside the granular layer during monotonic and cyclic loading. This technique is named Particle Image Tracking (PIT), and is based on the Digital Image Correlation (DIC). PIT analysis is performed during the first six cycles of each test. Results of the test "Cyclic 1A" are presented.

In order to represent the vertical displacement field, each grain of the LTP is represented by a polygon (Voronoi cell) and coloured according to its corresponding vertical displacement. Figure 9 represents the vertical displacement field evolution during the first six cycles, taking as a reference state the end of the 3 hours of 10kPa loading. The white cells are the grains "lost" during the application of PIT (because their Zero-mean Normalized Cross-Correlation ZNCC is smaller than 0.7, chosen a quality threshold).

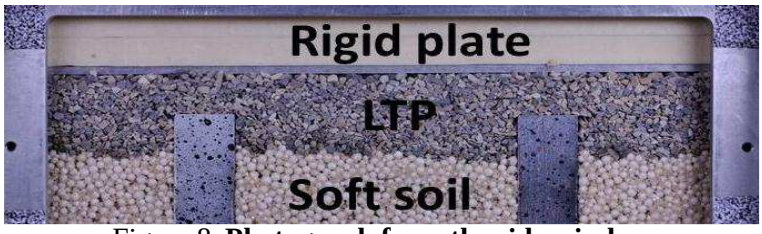

Figure 8. **Photograph from the side window**

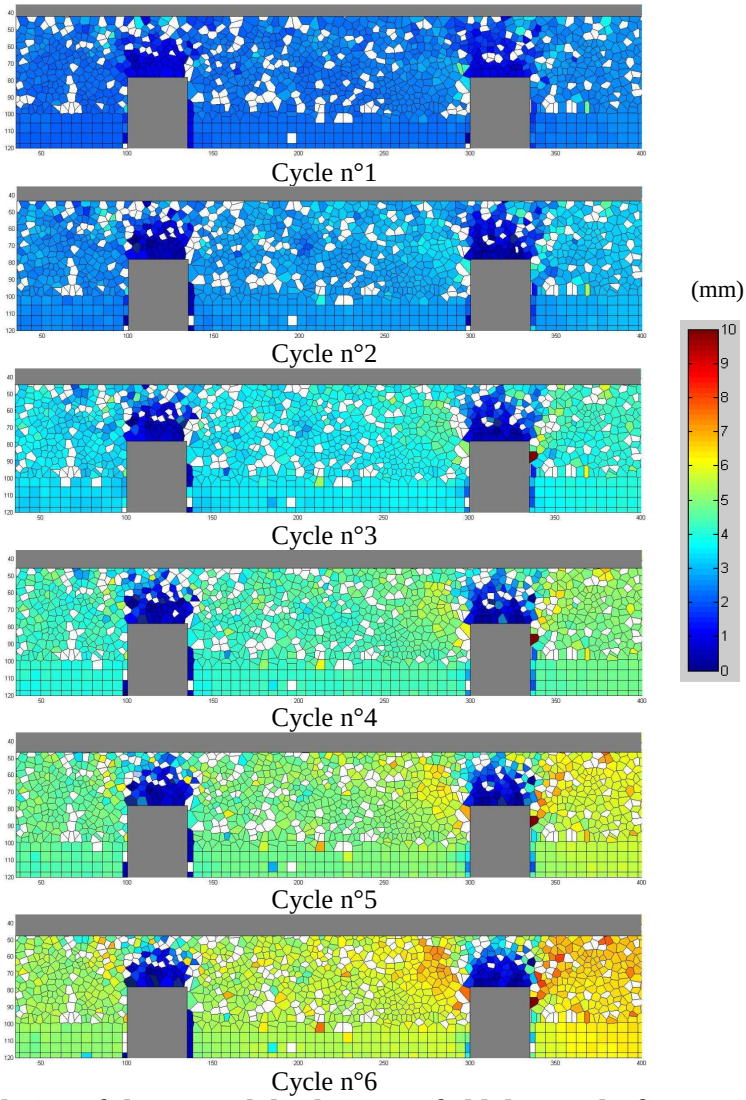

Figure 9. **Evolution of the vertical displacement field during the first six cycles**

The settlement accumulation during the cycles is clearly highlighted between the semi-piles. We also observe that the parts of the LTP directly above the piles present almost no displacement - equal to a maximum of 0.3mm for the grains situated directly above the piles, at the end of the sixth cycle - compared to the maximum displacement between the two semi-piles, at the LTP base, found equal to 5mm at the end of the sixth cycle. These stationary masses above the piles could function as vertical extensions of the piles inside the LTP. As these zones extend almost up to the slab base level, it could explain the high values of the measured efficiency using the force sensors up to the value of 0.98 at the end of the 50 cycles, where the surface loading is transmitted from the slab directly to the pile heads through these stationary zones.

By comparing the settlements in the LTP at different distances from the LTP base, no horizontal line of equal settlement could be observed. Therefore, the upper plan of equal settlement is considered to be the ground slab level.

In fact, the maximum vertical incremental displacement between the semi-piles (Δd) reduces from one cycle to the other (Δd = 1.4mm during 1st cycle; 1mm during 2nd cycle; down to 0.3mm for 6th cycle). This is in good agreement with the results found on the central part of the model, using the displacement sensor, where we observed an accumulation of displacement that follows a similar decreasing rate ($\Delta D3$ = 1.2mm during 1st cycle; 0.9mm during 2nd cycle; down to 0.4mm for 6th cycle (Figure 7)).

The study of the horizontal displacement field during the first six cycles shows that the zone between the two semi-piles, where the vertical displacements are maximum, and the zone above the pile, have almost no horizontal displacements (value less than 5% of the settlement). Figure 10 gives an example of a horizontal displacement field. This figure shows two parts presenting the same horizontal displacement but in two different directions. The accumulation of the horizontal displacement during the cycles was found to be very small (10% of its initial value after 6 cycles) due to the presence of the side walls that prevent the accumulation of horizontal displacements (which is not the case of the vertical displacements where the LTP lays on a compressible layer) and therefore it is not presented in detail in this paper.

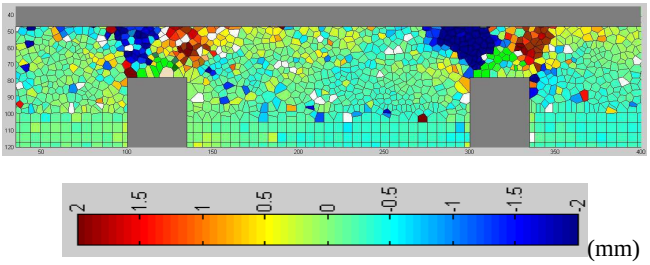

Figure 10. **Horizontal displacements at the cycle n°6 of the test "Cyclic1"**

CONCLUSION

A 1g three-dimensional physical model was developed in order to study the technique of soil reinforcement using rigid piles. A series of tests were performed to investigate the load transfer mechanisms in the LTP under low frequency cyclic surface loading. The tests show an accumulation of the settlement during the cycles with a decreasing rate without reaching stabilization at the end of the 50 cycles. Both instrumentation and image analysis are in good agreement with those results. The application of the cycles leads to an increase of the system efficiency up to a value around 1. The image analysis proves to be effective for the displacement field analysis. It effectively shows stationary masses of soil above the piles, which could work as pile extension up to the slab, explaining the load being transmitted from the slab directly to the pile through these motionless zones. This laboratory model permits us also to perform tests with different LTP thicknesses in order to investigate its effect on the load transfer mechanisms. In this regard, another series of test was undertaken using a LTP thickness of 0.1m. Although the similarity between the model and the prototype is not strictly maintained, the experimental results are useful to gain a better understanding of the mechanisms in the load transfer platform under cyclic loading and can be used to develop or verify the validity of theoretical or numerical methods. It also permits the constitution of an experimental database for performing a parametric study with a continuum numerical modelling with the aim to extrapolate the results to real scale structures.

ACKNOWLEDGEMENTS

The authors are grateful to Technique and Research Department of the French National Federation of Public Works (FNTP) for providing financial support. The authors would like to express their gratitude to J. Canou (ENPC), L. Thorel (IFSTTAR), Ph. Gotteland (FNTP), S. Brûlé and E. Javelaud (Menard) for their advices on this work. Many thanks also go to G. Combe (3SR lab) for his help in the PIT and in the practice of the program "Tracker", as well as G. Vian and J.B. Toni for the technical support.

REFERENCES

Blanc, M., Rault G., Thorel L. & Almeida, M. 2013. Centrifuge investigation of load transfer mechanisms in a granular mattress above a rigid inclusions network. Geotextiles and Geomembranes 36, 92–105.

Combe, G. & Richefeu, V. 2013. Tracker: a Particle Image Tracking (PIT) technique dedicated to nonsmooth motions involved in granular packings powders and grains 2013, July 8–12, UNSW, Sydney, Australia.

Eskişar, T., Otani, J. & Hironaka, J. 2012. Visualization of soil arching on reinforced embankment with rigid pile foundation using X-ray CT. Geotextiles and Geomembranes 32, 44–54.

Jenck, O., Combe, G., Emeriault, F. & De Pasquale, A. 2014. Arching effect in a granular soil subjected to monotonic or cyclic loading: kinematic analysis. 8th Int. Conf. on Physical Modelling in Geotechnics, Perth, Australia 14-17 January 2014.

Heitz, C., Lüking, J. & Kempfert, H.-G. 2008. Geosynthetic reinforced and pile supported embankments under static and cyclic Loading. Proceedings of the 4th European Geosynthetics Conference EuroGeo4, Edinburgh (UK), paper n°215.

Houda, M., Jenck, O., Emeriault, F., Briançon, L. & Gotteland, P. 2013. Development of a three-dimensional small model to simulate soil improved by rigid piles. Proceedings of the 18th International Conference on Soil Mechanics and Geotechnical Engineering, Paris, France.

Kempfert, H.G, Göbel, C., Alexiew, D. & Heitz, C. 2004. German recommendations for reinforced embankments on pile-similar elements. EuroGeo3-Third European Geosynthetics Conference, Geotechnical Engineering with Geosynthetics, 279–284.

Okyay, U.S., Dias, D., Thorel, L. & Rault, G. 2013. Centrifuge Modeling of a Pile-Supported Granular Earth-Platform. Journal of Geotechnical and Geoenvironemental Engineering. doi: 10.1061/(ASCE)GT.1943-5606.0001004

Van Eekelen, S.J.M., Bezuijen, A., Lodder, H.J. & van Tol, A.F. 2012. Model experiments on piled embankments. Part I. Geotextiles and Geomembranes 32, 69–81.

Part Two: Hydro-Mechanical behavior of granular material & soils

Improvement of soils mechanical behavior by biological calcification: application to hydraulic earthen structures

A. Dadda, F. Emeriault, C.Geindreau

Laboratoire Sols, Solides, Structures, Grenoble, France

abdelali.dadda@3sr-grenoble.fr , fabrice.emeriault@3sr-grenoble.fr, christian.geindreau@grenoble-inp.fr

ABSTRACT

The soils improvement with calcite precipitation catalysed by bacteria is a promising technique for the reinforcement of the hydraulic structures, potentially subjected to internal erosion and liquefaction of their foundations. It needs in-situ injection solutions carrying selected microorganisms and chemical reagents in the aimed structure. However, thorough lab study must be completed before applying this technique in a full-scale, to determine the applicability conditions of this process, and to validate its effectiveness in terms of mechanical behaviour. This work examines the microstructural properties changes, and its influence on the mechanical behaviour of biocemented soils. The microstructural properties of biocalcified porous media will be characterized in 3D using nanotomography observations. In this context, the spatial distribution of different phases (pore, calcite) in terms of volume fraction will be investigated; also the orientation of calcite bridges between grains (structural anisotropy) will be quantified, depending to the injection conditions. The structural changes influence on the transport properties (permeability, dispersion) will be also quantified. Triaxial tests of static and dynamic loading; under drained and undrained conditions will be carried out, followed by continuum μCT observations to analyse the mechanical behaviour of treated soils. This tests programme will explore the relationship between microstructure and bio-hydro-mechanical behaviour of bio-calcified porous media, and also will evaluate the effectiveness of the bio-reinforcement method.

INTRODUCTION

The geotechnics is an old discipline but constantly evolving by the time, in the 19th century, Coulomb and Rankin developed a calculation methods based on mathematics and physics. The geology, chemistry and mineralogy are also taking a part in this development from the 20th century. Recently, the use of biological processes in geotechnics, particularly for soil reinforcement found a strong echo in the scientific community. Nowadays, the harnessing of biological processes in geotechnical engineering promises to be the next transformative practice, due to economics and environmental factors (Mitchell & Carlos Santamarina, 2005). Numerous promising methods of bio-reinforcement are introduced in the literature, given their profitability and efficiency, especially at large depths, compared to other techniques (Dynamic compaction, chemical grouting) (Ivanov & Chu, 2008).

The Management of hydraulic structures (dikes, dams) is a major challenge from the perspective of public safety. In France, these structures are mostly more than 50 years and locally present pathologies related to their aging, which can eventually lead to their failure. The evolution of the current regulations requires enhanced monitoring of these structures (particularly vis-a-vis the seismic hazard and the internal erosion) and their treatment in case of proven risks. Biocementation may present an ecological and profitable solution for the stabilization of these structures, but this technique has not been developed yet for in-situ applications. Currently, many research projects are initiated in Europe and internationally to develop a reliable and durable technique. The project « BOREAL » (Bio-renforcement des OuvRagEs hydrAuLiques en remblais) was launched in 2014 in France, in order to extend this new biotechnology application to the reinforcement of hydraulic structures in charge, using the MICP process (Microbial-Induced Calcite Precipitation). This project brings together all the skills needed to overcome technical problems (3SR, LTHE, Micro-bio-geology laboratory of Angers University, CNR, EDF, Soletanche Bachy, geophyConsult and ENOVEO), 3SR will study the mechanical aspects of the biocalcification process at the macroscopic and microscopic scale.

BIOTECHNOLOGY IN GEOTECHNICS

The bio-geo-technology is a branch of geotechnics that uses biological applications to solve geotechnical problems. However, at present this field mainly related to site applications (slopes coverage by vegetated soil), for strengthening against erosion, slipping and reduce water infiltration. These techniques are advantageous economically, environmentally and aesthetically (Karol, 2003). The geo-microbial technology is the new emerging branch of bio-geo-technology, wherein the microorganisms are a major component. At present, there are two major directions in construction microbial biotechnology: (1) the microbial production of construction materials and (2) the applications of microorganisms in construction process. Many different biotechnological products for civil engineering are developing, classified by the results of the microbial treatment (Torgal, et al., 2015) :

- Bio-aggregation of soil or particles is a process to increase size of the fine particles so that water and wind soil erosions, sand movement, as well as dust emission will be reduced.
- Bio-crusting of soil surface is a process to form mineral or organic crust onto soil surface so that that erosion, dust emission, and water infiltration will be reduced.
- Bio-coating of solid surface is a process to form a layer on solid surface so that aesthetics or colonization of surface will be enhanced.

- Bioclogging of soil or porous matrix is a process to fill in the pores and channels in soil/matrix so that hydraulic conductivity of soil or porous matrix will be significantly reduced.
- Biocementation of soil or particles is a process to increase significantly strength of soil or particles.
- Biodesaturation of soil is a process to decrease saturation and liquefaction potential of soil through biogas production in situ.
- Bio-encapsulation of clay/soil/particles is a process to increase strength of soft clayey soil through the formation of strong shell around a piece of soft material.
- Bioremediation of soil is a process to remove pollutants from soil or immobilize pollutant in soil before construction.

Despite the multitude of the bio-geo-technology applications, the latest research focused on two promising applications: Bioclogging and Biocementation. Both processes effectively replace other reinforcement techniques harmful to the environment and / or unprofitable.

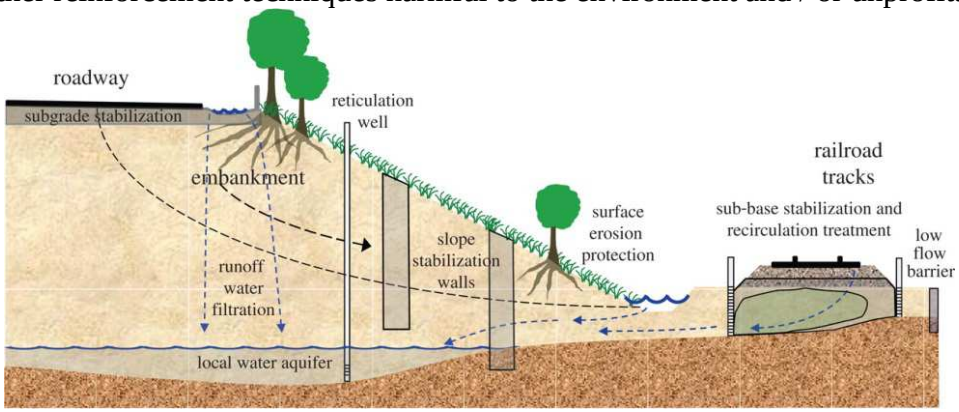

Figure 1. **Schema of the of bio-geo-technology applications multifunctionality in geotechnics** (DeJong, et al., 2011)

La bio-cimentation

Microbial cementation is a process of links creation between the particles which are called "bridges"; these bridges are generated by the injection process of selected micro-organisms and specific additives in the soil. This operation aims to improve the soils strength, it is considered as an effective solution for solving various geotechnical problems:

- Internal erosion of hydraulic structures.
- Liquefaction.
- Landslide slopes.
- Swelling clay soils, etc.

This process is different from the organic-binder where particle formation of bonds is performed by the cellular channels (such as the mycelial fungi, actinomycetes, and heterotrophic bacteria). However, bio-binding does not seem to be suitable for large scale operations, because of their instability and their ability to be degraded by other microorganisms. Therefore, only processes that are induced by microbial activity, such as oxidation, reduction, dissolution and precipitation of inorganic substances in soils can form stable and sustainable linkages between particles (Ivanov & Chu, 2008).

BIOCEMENTATION BY MICP (BIOCALCIFICATION)

The biocementation by the precipitation of calcium carbonate (CaCO3) is induced by bacterial activities in the presence of other substances (calcium and urea). This process is called MICP or biocalcification; it generates three crystalline forms of calcium carbonate (calcite, vaterite, and aragonite). The precipitation in this process occurs preferentially at the inter-granular contacts. Indeed, the bacterial cells are bound in locations of low shear forces produced by the flow injection (Figure 2). This operation increases the strength of the treated soils without significant decrease in hydraulic conductivity (DeJong, et al., 2013).

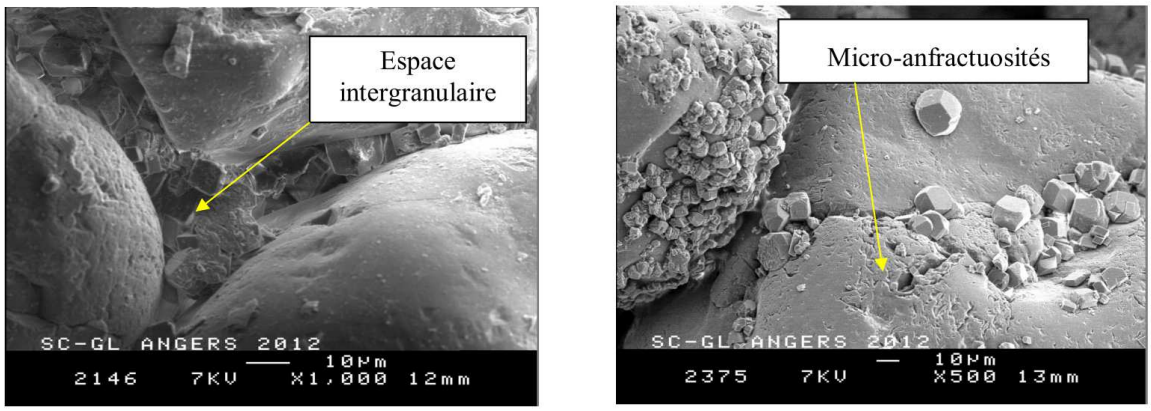

Figure 2. **Biocalcification in inter-granular spaces and in grains cracks** (Girinsky, 2009)

The biochemical reactions of this process is given as follows:

$$(NH_2)_2CO + H_2O \xrightarrow{\text{Urease}} CO_2\uparrow + 2NH_3 \quad (1)$$

$$2NH_3 + 2H_2O \longrightarrow 2NH_4^+ + 2OH^- \quad (2)$$

$$CO_2 + H_2O \longleftrightarrow H_2CO_3 \longrightarrow H^+ + HCO_3^- \longleftrightarrow 2H^+ + CO_3^{2-} \quad (3)$$

$$CaCl_2 + H_2CO_3 \longrightarrow CaCO_3\downarrow + 2HCl, \quad (4)$$

$$2HCl + 2NH_4OH \longrightarrow 2NH_4Cl + H_2O, \quad (5)$$

The total reaction:

$$(NH_2)_2CO + 2H_2O + CaCl_2 \xrightarrow{\text{Urease}} CaCO_3\downarrow + 2NH_4Cl \quad (6)$$

The metabolic activity of microorganisms leads to secrete enzymes such as urease, which is able to hydrolyzing urea in the microbial cells, by decomposing to ammonia (NH_3) and carbon dioxide (CO_2) (Eq .1), These chemicals products diffuse across the cell wall of the microorganism within the surrounding solution (Figure 3). Two reactions occur spontaneously in the presence of water; ammonia is converted into ammonium ions (NH_4^+) (Eq .2), and the carbon dioxide balanced with carbonic acid, carbonate ions and bicarbonate (Eq. 3) depending on the pH value, the enzyme carbonic anhydrase may play a role in the acceleration of this reaction (Dhami, et al., 2014). The increase in pH value is due to the generation of the hydroxide ions (OH^-) during the production of the NH_4^+. The enzymatic activity of bacteria is promoted in alkalinity environment (pH: 8.5-10), producing the required carbonates for calcite precipitation (Eq. 4) (DeJong, et al., 2010).

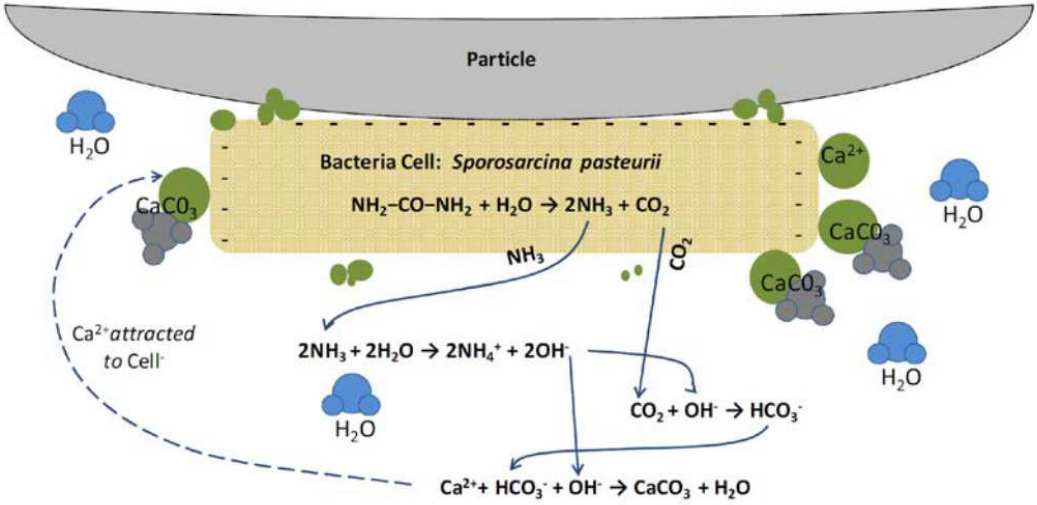

Figure 3. **Representative schema of the chemical reactions during the biocalcification** (DeJong, et al., 2010)

A large family of microorganisms are able to produce urease, most research in biological calcification used *Sporosarcina pasteurii* (formerly *Bacillus pasteurii*), in particular the strain *S. pasteurii* ATCC 11859 (DSM 33), because of its high urease activity (Ferris, et al., 1996), also their ability to grow in basic media (pH greater than 8.5) and in high calcium concentration media (greater than 0.75 M) (Fernando et al. 2015). Other physiologically similar species using for biocementation are the representatives of the genus Bacillus: *B. cereus* (Castanier, et al., 2000), *B. megaterium* (Bang, et al., 2001) and (Dhami, et al., 2014). Some species are also halotolerant (adaptable to very high salt concentrations) as those of the genus *Staphylococcus* (*Staphylococcus succinus* in particular, has great potential urease) (Stabnikov, et al., 2013). However, the strain of *S. succinus* is usually toxic (Zell, et al., 2008).

Today, the MICP process still has many drawbacks: the by-product of the hydrolysis of urea (ammonia) is toxic and harmful to the aquatic environment and atmosphere, and the high pH which increases the risk of corrosion (Pacheco-Torgal & Labrincha, 2013). Therefore, it is necessary to continue research on MICP and on new types of biocalcification in order to overcome these disadvantages.

EVOLUTION OF BIO-CIMENTED SOILS

MECANICAL PROPERTIES

The Biocementation has been used since 1999 to renovate the facades of historic buildings, by recreating a "cullet" composed of calcium carbonate, for sustainable protection of stone attacks and damages. In geotechnics, there are many biological applications of soil reinforcement by biocementation. These methods are not adapted for large scales conditions and for some specific issues (e.g. the mitigation of soil liquefaction).
Laboratory tests were conducted to evaluate the increase of soil mechanical strengthening with biological cementation process. A direct relationship between the amount of precipitated calcite and the shear strength determined by drained triaxial tests. Otherwise, large treatment heterogeneity in the used columns was found (Whiffin, et al., 2007) (Figure 4).

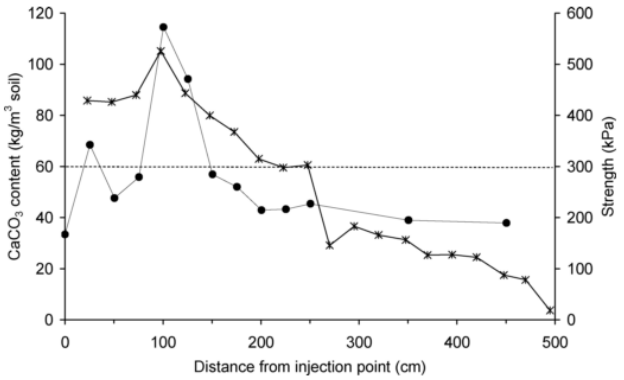

Figure 4. **Calcium carbonate (*) and strength (•) profiles along the column length** (Whiffin, et al., 2007).

In 2006, (DeJong et al) showed that the treatment of sands through this process provides greater shear strength than treatment with gypsum (DeJong, et al., 2006). The biocement degradation was followed by measuring the shear wave velocity (Vs) for both types of treatments. These measurements show the existence of a similar failure behavior between these two types of treatments (rapid degradation is observed in the 1% of axial strain, followed by a progressive deterioration) (Figure 5). Montoya also showed that loose sand after biocalcification acquires the strength of dense sand in triaxial tests (Figure 6) (Montoya, 2008).

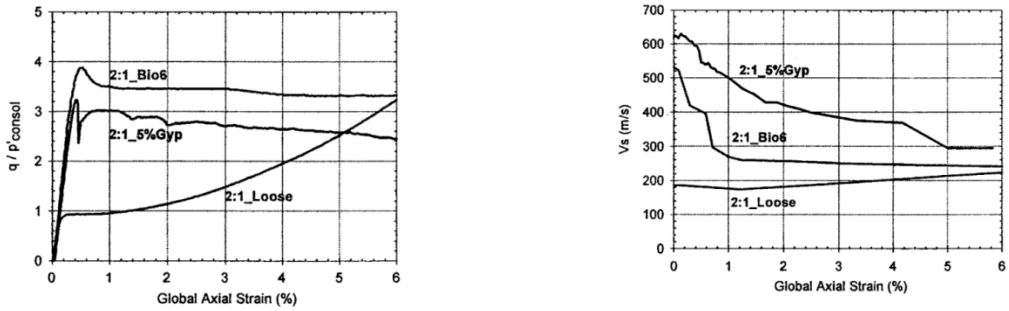

Figure 5. **Comparison of undrained triaxial tests for different states of sand (loose, treated with gypsum and biocalcified)** (DeJong, et al., 2006)

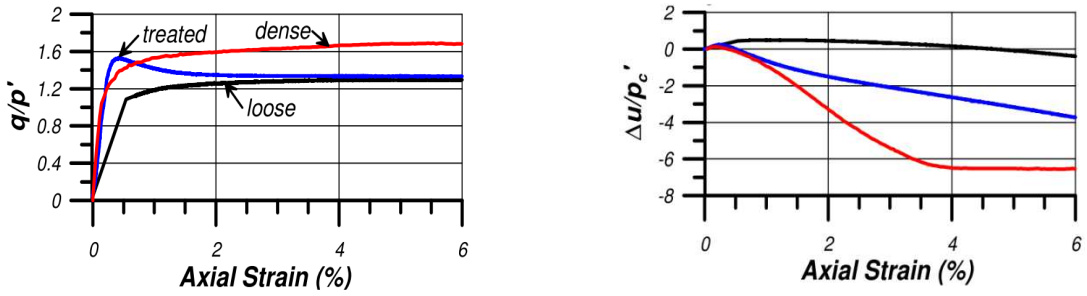

Figure 6. **Comparison of undrained triaxial tests for different states of sand (loose, dense and biocalcified)** (Montoya, 2008)

Various laboratory works also showed a significant increase in the compressive strength of biocemented soils (Chu, et al., 2013) and (Al Qabany & Soga, 2013), without knowing the cement degradation mechanism. Montoya (2012), provides a simplified illustration of the failure mechanism of calcite bridges under loading (Figure 7), which represents a coupling between two bases failure modes (calcite-calcite and calcite-silica) (Montoya, 2012). This mode failure has been shown by microstructural observations on SEM and X-ray tomography (Montoya, 2012).

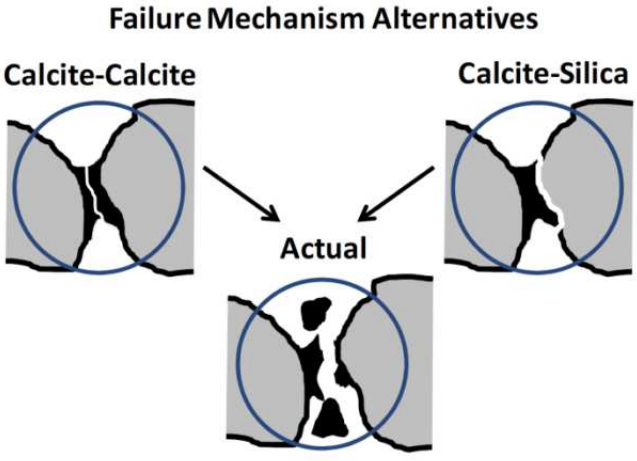

Figure 7. **Illustration schema of calcite bridges failure mechanism** (Montoya, 2012)

Specific problems

Research Works on soil strengthening by biocementation on more specific problems (e.g. Liquefaction) has also been made. Burbank (2011) performs in-situ treatment followed by CPT (cone penetration test) measurements (Figure 8), it also showed a significant increase in the tip resistance relative to the initial state, and estimates an increase in liquefaction resistance of about 3.5% (Burbank, et al., 2011). This resistance is then demonstrated by the use of geotechnical centrifuge test (designed for seismic simulation), which determine that the MICP reduces pore pressure and settlements, therefore reduces the soil liquefaction risks (Montoya, et al., 2013).

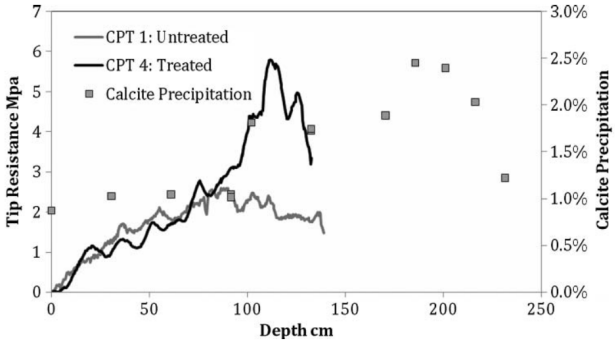

Figure 8. **Tip resistance and precipitated calcite percentage** (Burbank, et al., 2011)

Tests carried out by Soletanche Bachy on biocalcified samples on scale model were qualified as a non-erodible soil up to a minimum speed of around 9 cm/s, as a result of JET erosion test, whereas the untreated original sand was erodible at a speed of 2 cm/s.

CONCLUSION

The soils improvement method by calcite precipitation catalysed with bacteria is a promising technique, in the field of hydraulic structures securing, potentially subject to internal erosion and liquefaction. More advanced works on the biological geotechnical applications is possible through a variety of research, especially in strengthening by biocementation. However, serious challenges remain unsolved, preventing the development of such processes in large-scale. The main challenge in this process is the heterogeneity of the treatment; this phenomenon is related to several factors (the distribution of bacteria and nutrients in the solid skeleton, the viscosity and density of the injected solution, the size of the bacteria compared to the soil pore size, and the existence of a water flow, etc.). Before the application of the process in full scale, a fundamental research is still needed to define the conditions of applicability of this process, to validate its effectiveness in terms of mechanical behavior. Specific tests for each issue will be conducted to a further investigation of microstructural properties changing, and for determining possible links between the microstructural changes and the mechanical behavior.

Most of the research works performed to date have focused on the implementation of biogeochemical processes for soil properties improvement. On the other hand, the achievement of an in-situ treatment is only the first stage of technique development, whether mechanical or bio-geo-chemical durability over the time (e.g. water saturated with carbon dioxide) should be studied.

A complete modeling of the process is essential for future in-situ applications; current models can predict the spatial distribution of calcite, and the mechanical behaviour of treated soil (DeJong, et al., 2013). Nevertheless, to perform a complete model of this process, it is important to precisely characterize: biogeochemical reactions, small-scale biochemical processes (e.g. microbial growth, enzyme levels, gas production, etc.), local changes porosity (and hydraulic conductivity), saturation and degradation processes in treated soils. Spatial variability of microbes on the surface of soil particles, and the identification of the appropriate transition between discrete and continuous scale is particularly challenging, because the biogeochemical processes occurring at the micrometric scale.

REFERENCES

Al Qabany, A. & Soga, K., 2013. Effect of chemical treatment used in MICP on engineering properties of cemented soils. Géotechnique, 63(4), pp. 331-339.

Bang, S., Galinat, J. & Ramakrishnan, V., 2001. Calcite precipitation induced by polyurethane immobilized Bacillus pasteurii. *Enzyme and Microbial Technology,* 28(4-5), pp. 404-409.

Barkouki, T. et al., 2011. Forward and inverse bio-geochemical model- ing of microbially induced calcite precipitation in half-meter column experiments. *Transport in Porous Media,* 90(1), pp. 23-39.

Burbank, M. et al., 2011. Precipitation of calcite by indigenous microorganisms to strengthen liquefiable soil. *Geomicrobiol Journal,* 28(4), pp. 301-312.

Burbank, M. et al., 2011. Precipitation of calcite by indigenous microorganisms to strengthen liquefiable soil. *Geomicrobiol Journal,* 28(4), pp. 301-312.

Castanier, S. et al., 2000. Bacterial carbonatogenesis and applications to preservation and restoration of historic property. Dans: *microbes and art. the role of microbial communities in the degradation and protection of cultural heritage.* New York: Kluwer Academic/Plenum Publisher, pp. 203-218.

Chu, J., Ivanov, V., Stabnikov, V. & Li, B., 2013. Microbial method for construction of aquaculture pond in sand. *Géotechnique,* 63(10), pp. 871-875.

DeJong, J. et al., 2013. Biogeochemical processes and geotechnical applications: progress, opportunities and challenges. *Géotechnique,* 63(4), pp. 387-301.

DeJong, J. et al., 2011. Soil engineering in vivo : harnessing natural biogeochemical systems for sustainable, multi-functional engineering solutions. *the Royal Society Interface Journal,* 8(54), pp. 1-15.

DeJong, J. T., Fritzges, M. B. & Nüsslein, K., 2006. Microbially Induced Cementation to Control Sand Response to Undrained Shear. *Journal of Geotechnical and Geoenvironmental Engineering,* 132(11), pp. 1381-1392.

DeJong, J. T., Mortensen, B. M., Martinez, B. C. & Nelson, D. C., 2010. Bio-mediated soil improvement. *Ecological Engineering,* 36(2), pp. 197-210.

Dhami, N., Reddy, M. & Mukherjee, A., 2014. Synergistic role of bacterial urease and carbonic anhydrase in carbonate mineralization. *Applied Biochemistry and Biotechnology Journal,* 172(5), p. 2552–2561.

Fauriel, S., 2012. Bio-chemo-hydro-mechanical modeling of soils in the framework of microbial induced calcite precipitation. *PhD thesis, Ecole Polytechnique Fédérale de Lausane*.

Fauriel, S. & Laloui, L., 2011. Modelling of biogrout propagation in soils. *2nd International Symposium on Computational Geomechanics,* p. 578–586.

Ferris, F. G., Stehmeier, L., Kantzas, A. & Mourits, F. M., 1996. Bacteriogenic mineral plugging. *Petroleum Technology,* 35(9), pp. 56-61.

Girinsky, O., 2009. Pré-industrialisation d'un procédé de consolidation de sol par bio-calcification in-situ. *Université d'Angers UFR sciences,* pp. 1-368.

Ivanov, V. & Chu, J., 2008. Applications of microorganisms to geotechnical engineering for bioclogging and biocementation of soil in situ. *Environmental Science and Biotechnology Journal,* 7(2), pp. 139-153.

Jonkers, H. et al., 2010. Application of bacteria as self-healing agent for the development of sustainable concrete. *Ecological Engineering,* 36(2), pp. 230-235.

Karol, R. H., 2003. *Chemical Grouting And Soil Stabilization.* New York: Marcel Dekker.

Laloui, L. & Fauriel, S., 2011. Laloui, L. & Fauriel, S. (2011). Biogrout propagation in soils.. *Proceedings of the international workshop on multiscale and multiphysics processes in geomechanics,* pp. 77-80.

Martinez, B., 2012. Experimental and numerical upscaling of MICP for soil improvement. *Doctoral dissertation, University of California.*

Martinez, B., Barkouki, T., DeJong, J. & Ginn, T. R., 2011. Upscaling of microbial induced calcite precipitation in 0.5m columns: experimental and modeling results. *Geo-Frontiers 2011: Advances in Geotechnical Engineering,* pp. 4049-4059.

Mitchell, J. K. & Carlos Santamarina, J., 2005. Biological considerations in geotechnical engineering. *Geotechnical and Geoenvironmental Engineering journal,* 131(10), p. 1222–1233.

Montoya, B., 2012. Bio-Mediated Soil Improvement and the Effect of Cementation on the Behavior, Improvement, and Performance of Sand. *Doctoral dissertation, university of California, Davis, CA, USA.*

Montoya, B. M., 2008. Bio-Mediated Soil Improvement and the Effect of Cementation on the Behavior, Improvement, and Performance of Sand. *UNIVERSITY OF CALIFORNIA,* pp. 1-252.

Montoya, B. M., DeJong, J. T. & Boulanger, R., 2013. Dynamic response of liquefiable sand improved by microbial induced calcite precipitation. *Géotechnique,* 63(4), pp. 302-312.

Pacheco-Torgal, F. & Labrincha, J., 2013. Biotech cementitious materials: Some aspects of an innovative approach for concrete with enhanced durability. *Construction and Building Materials,* Volume 40, pp. 1136-1141.

Reddy, S., Rao, M., Aparna, P. & Sasikala, C., 2010. Performance of standard grade bacterial (Bacillus subtilis) concrete. *Asian Journal of Civil Engineering,* 11(1), pp. 43-55.

Sarda, D., Choonia, H., Sarode, D. & Lele, S., 2009. Biocalcification by Bacillus pasteurii urease: a novel application. *Industrial Microbiology and Biotechnology,* 36(8), pp. 1111-1115.

Stabnikov, V., Chu, J., Ivanov, V. & Li, Y., 2013. Halotolerant, alkaliphilic urease-producing bacteria from different climate zones and their application for biocementation of sand. *World Journal of Microbiology and Biotechnology,* 29(8), p. 1453–1460.

Torgal, F. P., Labrincha, J., Diamanti, M. & Lee, H., 2015. *Biotechnologies and Biomimetics for Civil Engineering.* New York: Springer.

Vahabi, A. et al., 2014. Calcium carbonate precipitation by strain Bacillus licheniformis AK01, newly isolated from loamy soil : a promising alternative for sealing cement-based materials. *Basic Microbiol*, 55(1), pp. 105-111.

Van Wijngaarden, W. K., Vermolen, F., Van Meurs, G. & Vuik, C., 2012. Mathematical model and analytical solution for the fixation of bacteria in biogrout. *Transport in porous media*, 92(3), pp. 847-866.

Wang, J., De Belie, N. & Verstraete, W., 2012. Diatomaceous earth as a protective vehicle for bacteria applied for self-healing concrete. *Biotechnology Methods*, 39(4), pp. 567-577.

Whiffin, V., Van Paassen, L. & Harkes, M., 2007. Microbial carbonate precipitation as a soil improvement technique. *Geomecrobial*, 24(5), pp. 417-423.

Wiktor, V. & Jonkers, H., 2011. Quantification of crack-healing in novel bacteria-based self-healing concrete. *Cement and Concrete Composites*, 33(7), p. 763–770.

Zell, C. et al., 2008. Characterization of toxin production of coagulase-negative staphylococci isolated from food and starter cultures. *International Journal of Food Microbiology*, 127(3), p. 246–251.

Physical effects of liquid-vapor water transition in unsaturated soils

B. Pelizzari, J. Monnet, B. Loret, D. Mahmutovic
Université Joseph Fourier, L3SR, BP53, 38041 Grenoble, France
Benjamin.pelizzari@3sr-grenoble.fr
O. Plé
Université de Savoie, LOCIE - Savoie Technolac 73376 Le Bourget du Lac, France
olivier.ple@univ-savoie.fr
L. Boutonnier
Egis géotechnique, 3 rue du docteur Schweitzer, 38180 Seyssins, France
Luc.BOUTONNIER@egis.fr
J.-F. Daïan
Université Joseph Fourier, LTHE, BP53, 38041 Grenoble, France

ABSTRACT

The retention of water in soil is one of the main concerns of soil mechanics. Suction implies negative water pressure in pores for unsaturated soils. The existence of such pressure implicates that water can sustain tension meaning that its nucleation is avoided through the shape of the soil skeleton. Under these conditions, there is a competition between nucleation and air entry during the desaturation of soils, ruled by Laplace's law and the classical nucleation theory (CNT). Nucleation also rules the gravimetric water content in pores not in direct contact with the boundary condition surrounding the soil. Moreover the overall use of methods such as axis translation modifies the soil water retention through restrained nucleation and increase of the adsorption film thickness. The soil water characteristic curve is hence modified.

INTRODUCTION

The retention of water in unsaturated soil is dictated by the interaction between different phases. The equilibrium of air, water, vapor and soil (or ice) particles leads to the capillary phenomena usually termed as suction. This component, defined by the difference between air pressure (u_a) and water pressure (u_{wl}), is widely used for the description of the mechanical response of soils. The value of suction ranges from 0 to 10 MPa according to most reviews (Fleureau et al. 1993). The French ANR project TerreDurable (Boutonnier et al. 2012) is dedicated to the study of fine grain soil for the construction of embankments, situation where the soil is typically unsaturated

(Pendular to hygroscopic domain). Although some concern have been made regarding such suction values and their actual mechanical effect on soil (Baker & Frydman 2009). This paper presents the mechanical response of water at negative pressure through its capillary pressure and nucleation process. Corresponding physical phenomenon leads to desaturation. Furthermore desaturation at a single pore scale will be examined. Then evolution of porosity and behavior associated is discussed. The absolute pressure is used with a vacuum pressure equal to zero.

THEORICAL BACKGROUND

Suction classical definitions

Suction is given through equation 1:

$$s = u_a - u_{wl} \tag{1}$$

This difference in pressure is attributed to the interface between liquid and water vapor. The progressive decrease of the number of molecules (Fig. 1) per layers leads to disequilibrium of the stress tensor at the interface between liquid and gas. In order to re-equilibrate the tensor, a tensile stress appears in the interface which is curve. Taking into account the interface between water and soil, in accordance with the wetting angle θ of the soil, leads to Laplace's law (equation 2).

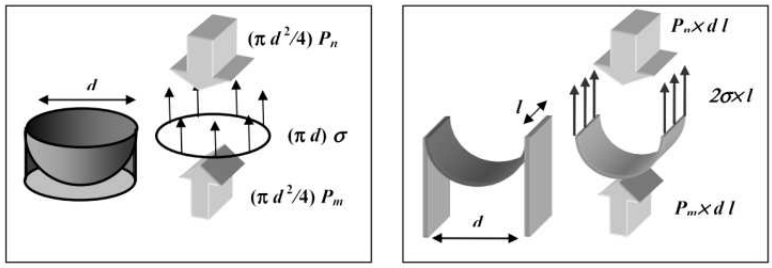

Figure 1. **Measurement and correspondence between suction and pore size**

$$s = \frac{2.\sigma.\cos(\theta)}{r_c} \tag{2}$$

where σ the superficial tension of water (0.728 kN/m) and r_c the radius of the meniscus. This radius can be assimilated as the porosity radius and defines the air entry value of a pore. For soils interacting with water, θ is equal to zero. The chemical equilibrium between liquid water and vapor in the air through the interface leads to Kelvin's law (Eq. 3). That determines the value of suction in reference to the relative humidity of the air (Bear 1972).

$$s = \frac{\rho_{wl}.R.T}{M}.Ln\left(\frac{u_{wg}}{u_{wsat}}\right) \tag{3}$$

where u_{wg} the pressure of the gaseous water, u_{wsat} the saturating vapor pressure, ρ_{wl} water liquid density, R the perfect gas constant, T the temperature in kelvin, and M the molar mass of water; u_{wsat} is a function of temperature and is equal to 2.3kPa at 20°C.

Classical methods to control suction

There are three methods to maintain a fixed level of suction in a soil sample. The first one is axis transla-tion. The soil has to sustain a certain value of air pressure that trigger the air entry for a given pore size. This method is also used to improve the meas-urement of suction as it increases the pressure value of the pore water and hence allows better measure-ment. The second method is the osmotic method. The saturated soil sample is put in a membrane, and then is placed into a liquid with a given concentra-tion of Polyethylene glycol (PEG). This leads to a negative pressure in the pore water due to the differ-ence in concentration between pure and saline water. The last one relies on Kelvin's law. By controlling the ambient humidity of the air surrounding the soil, the suction is controlled. The equilibration of the soil with the relative humidity is rather long. Figure 2 summarizes the measurement methods depending on the pore size.

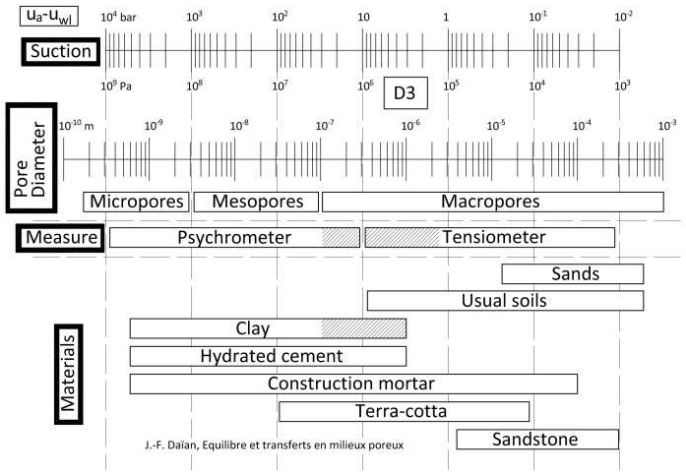

Figure 2. **Measurements and correspondences between suction and pore size (Daian, 2013)**

WATER PHASE CHANGES AND NEGATIVE PRESSURE

Pressure values in water

Suction in the range above 80-100 kPa are often observed, measured and calculated throughout literature. Romero et al. (2011) present values of suction in clayey soil up to 500kPa. Alonso et al. (1990) use constitutive models with admissible suction up to 300kPa. Cui et al. (2005) use values between 100 kPa and 7MPa for their field simulation. Ridley & Burland (1993) developed a tensiometer to measure suction up to 1.2MPa. Delage & Romero (2008) use values of suction control up to 100MPa using vapor control. At 80kPa, clays are nearly saturated and tend to be in the hygroscopic domain (D2) (Boutonnier & Virollet 2003). Considering a volume of water at a temperature of 20°C, the action of increase its suction above 99kPa is equivalent to decrease the water pressure under 1kPa and would produce cavitation, according to the phase diagram of water (Fig. 3).

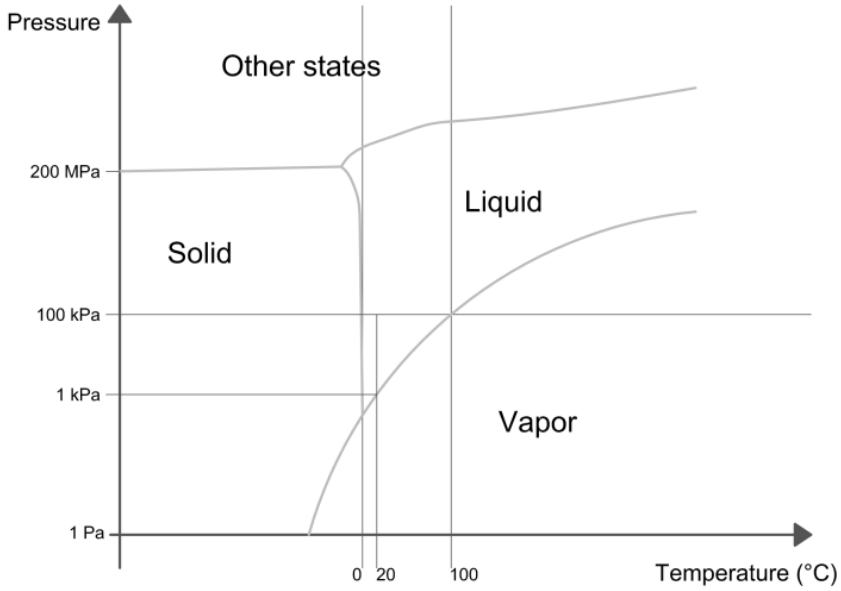

Figure 3. **Phase Diagram of the water substance**

Moreover, another theoretical point concerns suction values above 100 kPa under atmospheric pressure. At such a state, the capillary pressure is negative, and lower than the vacuum pressure, which is theoretically impossible according to the phase diagram (Fig. 3). These concerns have already been addressed by Baker & Frydman (2009).

Van der Waals forces in liquids

When the suction increases, the water pressure de-creases. Ultimately, water has to sustain negative pressure. The fluid is then in tension. The reason of such phenomenon is found in the intermolecular forces. The perfect gas equation (Eq. 4) gives the relation between pressure and temperature with n the specific volume:

$$u_{wg} = n.R.T \tag{4}$$

This equation depends only of the kinetic forces of molecules and their capacity of movement (degrees of freedom). These forces define the pressure of gases in a finite volume. In liquids or solids, other forces alter the equation. Molecules tend to attract each other's in different manners depending of the links between them. These forces can be classified in two sorts, weak and strong bounds. In the case of water, the main link between molecules is generated through van der Waals forces. The equation becomes Equation 5 with u_{wl} the pressure of liquid water:

$$u_{wl} = n.R.T - u_{\text{int}} \tag{5}$$

where u_{int} the internal pressure of the fluid generated by the intermolecular attraction forces. For liquid water at standard conditions for temperature and pressure (20°C, 101.325 kPa), with a density of 1000 kg/m3, the value of u_{wl} is equal to 135 MPa; u_{int} is hence equal to 134.9 MPa. The internal pressure plays the role of a reservoir of tension applicable to the fluid. This explains that a fluid can sustain negative pressures as long as nucleation is not

triggered. The liquid sustains a slight dilatation under negative pressures due to the increase of its intermolecular distance.

Classical nucleation theory (CNT)

Different theories of nucleation are available. In this paper, the Caupin & Herbert (2006) theory has been used. Nucleation corresponds to a new phase. The energy needed to create this phase can be divided in two different parts. The energy to create a given volume of new phase (vapor phase) and the energy needed to create an interface between an existing phase and a new one (Eq. 6):

$$W = \frac{4}{3}\pi r_c^{\,3}(u_{wl} - u_{wsat}) + 4\pi r_c^{\,2}\sigma \tag{6}$$

where r_c is the critical radius of the bubble created, σ the superficial tension of water, u_{wsat} the saturated vapor pressure and u_{wl} the pressure of the liquid. The competition of the interface creation and the vaporization leads to an energy threshold for nucleation (Eq.7):

$$E_b = \frac{16\pi}{3}\frac{\sigma^3}{(u_{wsat} - u_{wl})} \tag{7}$$

$$r_c = \frac{2\sigma}{(u_{wsat} - u_{wl})} \tag{8}$$

The critical radius of the bubble can be extrapolated from Laplace's law (Eq.8). The critical radius represents the minimum size of the bubble. Hence there is a minimum volume of vapor to be created in order to nucleate has shown in figure 4. The nucleation occurs only when enough space is offered for a bubble. This assumption depends of the wetting potential of the surface of the porosity. For a non-wetting defect on the surface, the bubble needs less work to appear since the interface on the defect al-ready exists (Rasmussen et al. 2012). Wetting defects in soils are uncommon.

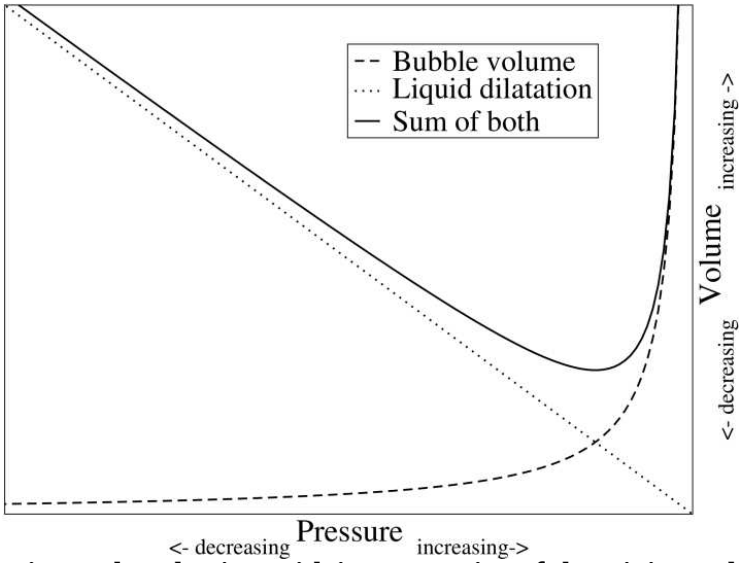

Figure 4. **Dilatation and nucleation, with interpretation of the minimum bubble volume (Daian, 2013)**

DESATURATION OF SOILS

Nucleation versus gravimetric desaturation

When a soil dries, two phenomena are in competition: nucleation and gravimetric desaturation. It can be obtained through different methods, for example, using osmosis. The water content of a pore is governed by two laws: the CNT laws and the Laplace's law with the air entry in the pore. Then two desaturation radii exist (Eq. 2, 8). The values of the corresponding capillary pressures to empty a given porosity are presented in Equations 9 and 10.

$$u_{wl}^{Laplace} = u_a - \frac{2\sigma}{r_c} \tag{9}$$

$$u_{wl}^{CNT} = u_{wsat} - \frac{2\sigma}{r_c} \tag{10}$$

Since u_{wsat} (2.34 kPa at 20°C) is lower than the air pressure, the nucleation occurs always after the air entry in a given pore, of a given size. Figure 5 gives a representation of this phenomenon and shows that when lower values of capillary pressure are reached (s ~ 10 MPa), nucleation and gravimetric desaturation occur nearly simultaneously and cannot be separated. Moreover nucleation cannot occur for value of suction smaller than ~105 kPa.

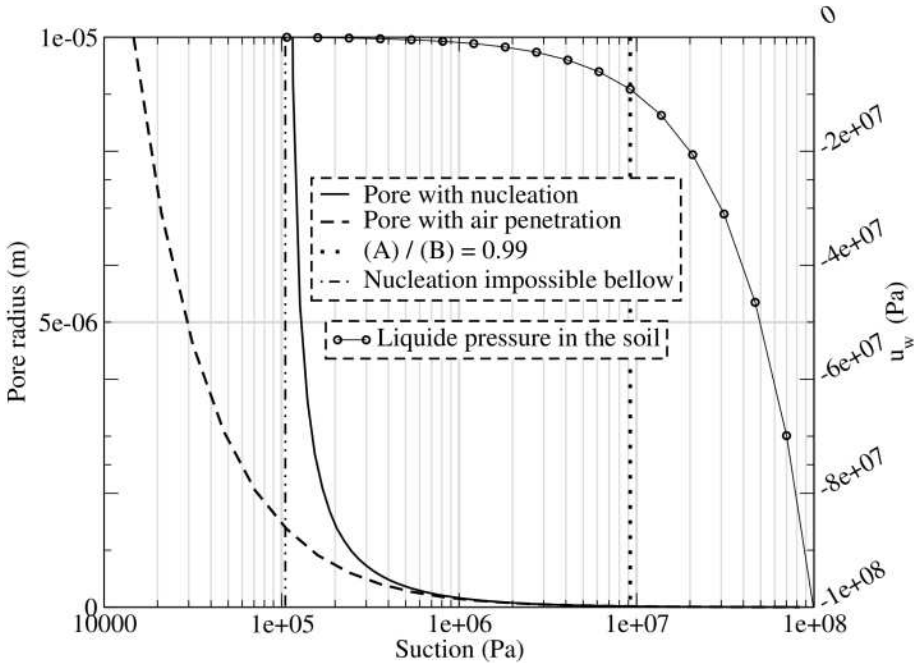

Figure 5. **Nucleation versus air penetration under osmotic depression (u_a = 100kPa)**

Nucleation in saturated hidden pores

The main concern lies in the phase change of water in hidden pores along the desiccation path. Hidden pores are not in direct contact with the exterior. Their internal pressure is dictated by smaller pores in interaction with the boundary conditions of the soil (suction, hydrometric control…). Therefore, hidden pores can sustain water pressure lower than

expected from their air entry suction. Water is trapped until the smaller pore is emptied. Considering a homogeneous water pressure, but taking account of the CNT, nucleation can occur with the following two provisos: Sufficiently low pressure and suitable volume for the bubble. For the given succession of porosity presented (figure 6) Table (1) shows the comportment of the water and its possible nucleation.

Table 1. **Occurrence of nucleation in given pore succession for u_a = 100 kPa**

N°	Size	Suction	$u_{w\ Laplace}$	$u_{w\ CNT}$	R_{nuc}	Nucleation
	µm	MPa	MPa	MPa	µm	
1	0.100	1.46	-1.36	-1.45	0.107	No
2	0.110	1.32	-1.22	-1.32	0.107	Yes
3	0.150	0.97	-0.87	-0.97	0.107	Yes

Figure 6a shows the form of the proposed porosity when empty. Pores of three diameters are defined and numbered from 1 to 3. At atmospheric pressure, the water pressure in the pores is homogeneous and equal to the pressure assigned in the smallest saturated porosity (1). The given values of u_w Laplace and suction for (2-3) represent their non-hidden behavior. The u_w CNT values give the minimal pressure of nucleation for the pore radius. For a pressure at -1.36 MPa, the radius of nucleation is 0.107 µm. Hence the two pores whose radius is larger than this value nucleate. On the other hand, the smaller pore remains saturated as shown in figure 6b.

Effects of Axis translation on nucleation

The main concern on the uses of axis translation is its tendency to modify the phases of water for a given suction. The method is used in most case to enable the direct measurement of suction using a classical tensiometer or to control the overall suction of a sample of soil. The aim is to keep the value u_a - u_w the same but with increased values of u_a hence of u_w. This leads to a modified nucleation, as presented in table (2) and (3). The porosity is kept the same as in table (1) as well as the values of suction.

The table shows that axis translation tends to modify the phases of the water in the soil. In natural conditions, the pores would all be empty due to the cavitation of its water. Using air pressure such as table (2) or (3) leads to an increase of the water content for a given suction. Table (2) would then correspond to figure 4c and table (3) to figure 4d. Hence the water soil characteristic curve is modified from its state in ordinary conditions. Moreover, under these conditions, the nucleation would need more work to occur. Figure 7 shows the modification in minimal diameter required to nucleate a hidden pore.

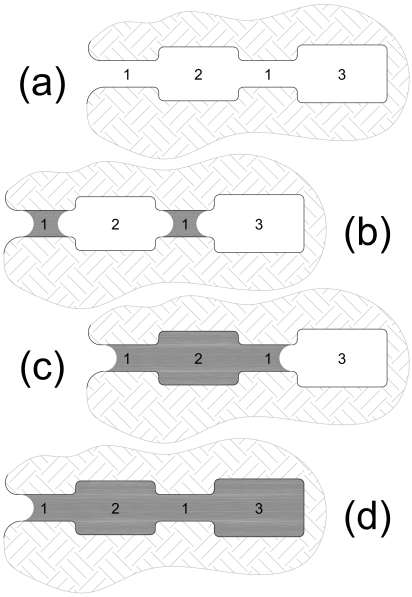

Figure 6. **Example of a succession of porosity: (a), desaturated; (b) and (c), partially saturated; (d), saturated**

Table 2. **Occurrence of nucleation in given pore series for u_a = 250 kPa**

N°	Size	Suction	$u_{w\ Laplace}$	$u_{w\ CNT}$	R_{nuc}	Nucleation
	µm	MPa	MPa	MPa	µm	
1	0.100	1.46	-1.36	-1.45	0.12	No
2	0.110	1.32	-3.32	-1.32	0.12	No
3	0.150	0.97	-0.71	-0.97	0.12	Yes

Table 3. **Occurrence of nucleation in given pore series for u_a = 500 kPa**

N°	Size	Suction	$u_{w\ Laplace}$	$u_{w\ CNT}$	R_{nuc}	Nucleation
	nm	MPa	MPa	MPa	nm	
1	0.100	1.46	-0.96	-1.45	0.152	No
2	0.110	1.32	-0.82	-1.32	0.152	No
3	0.130	0.91	-0.47	-0.97	0.152	No

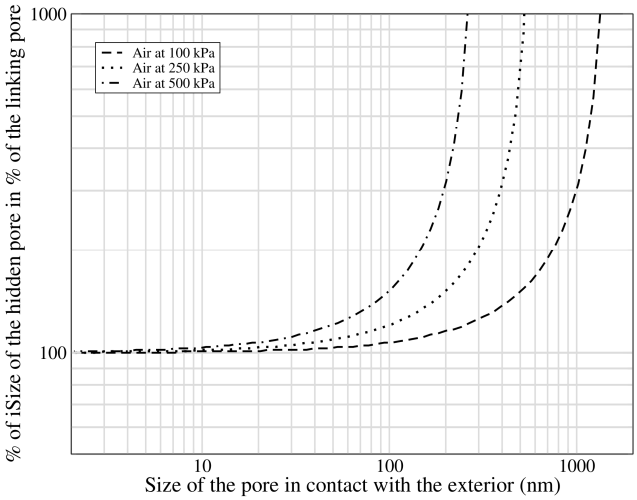

Figure 7. **Minimal size of the hidden pore for nucleation to occur (expressed in percent of the contact pore)**

Adsorption film behavior

Water droplet in contact with a solid behaves differently depending of the wetting capability of the surface. For the soil, the main problem concerns clays. The potential of a surface to attract water can be explained through van der Waals forces. For a wetting solid, gaseous water molecules are attracted by the surface and adopt the configuration of a film (fig.8).

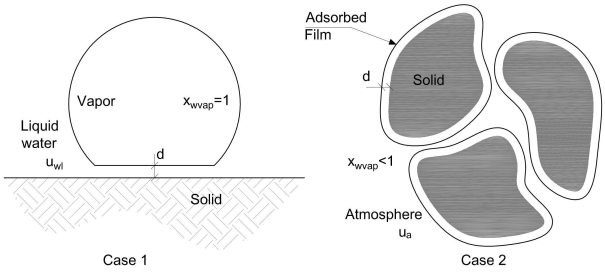

Figure 8. **Definition of the adsorbed film : Case 1: in liquid water with growing bubble (nearly saturated); case 2: in presence of atmosphere (nearly desaturated)**

The potential energy of water adsorbed by a plane surface, ψ_a can be calculated with the addition of non retarded van der Waals forces and leads to Hamaker's potential (Maugis 1980) defined in equation 11.

$$\psi_a = \frac{A}{6\pi}\frac{1}{d^3} \tag{11}$$

with A = 6.10-6 J known as the Hamaker's Constant and d the thickness of the adsorbed film (Frydman & Baker 2009). This potential ψa is in equilibrium with the chemical potential of vapor water in air ψc given in Equation 12. This equation is admissible under the hypothesis that air and vapor behave like perfect gases.

$$\psi_c = \frac{\rho_{wl}\, RT}{M}\left[\ln\left(\frac{u_a}{u_{wsat}}\right) + \ln(x_{wvap})\right] \tag{12}$$

with u_{wsat} the saturating vapor pressure, u_a air pressure, and x_{wvap} the proportion of vapor molecules in one mole of air. Combining the two equations gives the thickness of the film depending of the pressure of vapor as shown in figure 9.

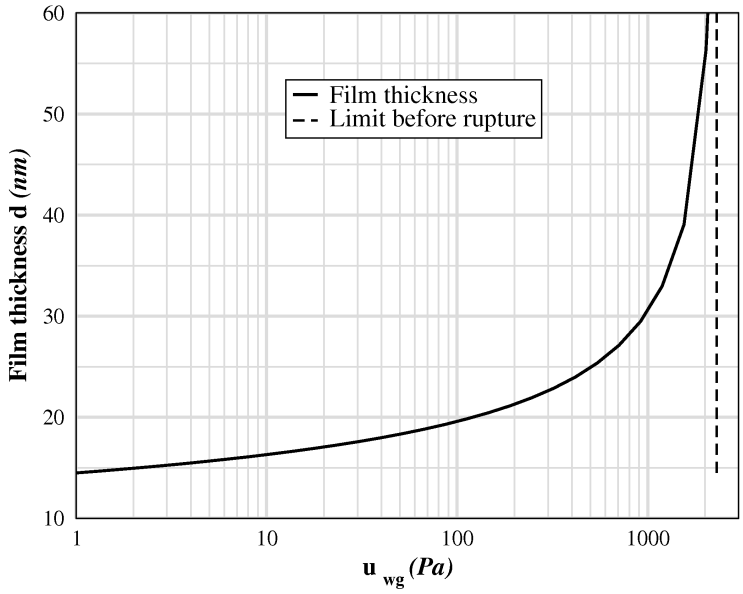

Figure 9. **Film thickness increase versus vapor pressure (x_{vap} =1)**

Equation 12 shows the importance of the air pressure in a soil when analyzing its capacity to retain water at low saturations (pendular domain). As the atmosphere is a mixture of air and vapor, doubling the atmosphere pressure, for example with axis translation, results in doubling the vapor pressure. It corresponds to an isothermal compression of the mix of the two perfects gases. Although, that increase of pressure does not affect the value of the saturated vapor pressure which only depends of temperature. Hence doubling atmospheric pressure leads to doubling the relative humidity (Hr) defined in Equation 13.

$$Hr = \frac{u_a \, x_{wvap}}{u_{wsat}} \tag{13}$$

The changes in relative humidity by an increase of pressure affect the thickness of the film through equation 12 as shown in table (4).

Table (4) displays the increase/variation of the film thickness and relative humidity when the atmosphere pressure u_a increases. Hr_{init} represents the relative humidity when the system is at u_a = 100kPa. u_{wvap} and x_{wvap} are the vapor pressure and proportion of the mix deduced from Hr_{init}. Hr_{AT} and $u_{wvap\ AT}$ are the value calculated when applying axis translation. d is the thickness of the film. Any increase in pressure in a closed container results in an increase of the thickness of the adsorbed film. For soil near desaturation, the use of the axis translation produces an increase in the water gravimetric content.

Table 4. **Thickness of adsorbed layer with axis translation**

u_a	Hr_{init}	u_{wvap}	x_{wvap}	Hr_{AT}	$u_{wvap\ AT}$	d
MPa	%	kPa	%	%	kPa	nm
0.10				10	0.230	21.7
0.25	10	0.230	0.230	25	0.575	25.7
0.50				50	1.150	32.4
0.10				30	6.900	26.9
0.25	30	0.690	0.690	75	1.730	43.4
0.50				100	3.450	-
0.10				45	1.040	30.9
0.25	45	1.040	1.035	100	2.590	-
0.50				100	5.180	-

CONCLUSION

Through classical nucleation theory and the properties of van der Waals forces, the phase's change of water in soil has been described. The existence of water at negative pressure is defined by its intermolecular forces of attraction, but such negative pressure is admissible only until nucleation. Regarding porosity directly in contact with the atmosphere, nucleation is always preceded by air entry. Then, the two phenomena are triggered nearly at the same time for high suction values.

Contrary to the previous statement, most pores are not in direct contact with the ambient air and behave accordingly to smaller pores in contact with the larger pores and the exterior. The CNT shows that those pores nucleate under normal conditions while the smaller pores keep saturated. The use of axis translation generates the presence of water in pores normally filled with vapor, for equivalent values of suction.

For nearly desaturated soil, the behavior of the adsorbed water is defined by the attraction between soil and water molecules. The equilibrium with the vapor pressure in the ambient air defines the film thickness. The use of an isothermal compression through axis translation generates changes in its thickness by an increase of relative humidity.

Those two phenomena lead to a modification of the soil water characteristic curve. The present analyses of the behavior of water in soil need to be ex-tended through another nucleation theory (spinodal theory). Then the growth of the vapor bubble until its interface reaches the soil inner wall shall be ad-dressed. Furthermore, the real prevalence of these phenomena should be quantified.

ACKNOWLEDGEMENTS

The authors would like to thank Vinci Construction Terrassement for financing the ph-D thesis in the context of the French ANR project TerreDurable.

REFERENCES

Alonso, E. E., Gens, A., Josa, A. (1990). A constitutive model for partially saturated soils, Géotechnique, vol. 40 n°3: 405-430.

Baker, R., & Frydman, S. (2009). Unsaturated soil mechanics Critical review of physical foundations. Engineering Geology (106): 26-39.

Bear, J. (1972) Dynamics of fluids in porous media, Elsevier, The Netherlands, 764 p.

Boutonnier, L., & Virollet, M. (2003). Tassements et gonflement instantanés dans les sols fins proches de la saturation. Revue Française de géotechnique(104), 3-19.

Boutonnier, L., Monnet, J., Fleureau, J.M., Fry, J.J., Loret, B., Magnan, J.P., Plé O., Wong, K. (2012) TerreDurable – Terrassements économiques écologiques et durables, Agence Nationale de la Recherche – Programme Bâtiments et Villes durables (ANR-11-VILD-0004).

Caupin, F. & Herbert, E (2006). Cavitation in water: a review. C. R. Physique vol. 7 n°9-10: 1000-1017.

Cui, Y.J., Lu, Y.F., Delage, P., & Riffard, M. (2005). Field simulation of in situ water content and temperature changes due to ground-atmospheric interactions. Géotechnique, vol. 55 n°7: 557-567.

Daian J.F. (2013). Equilibre et transferts en milieu poreux – Première partie état d'équilibre, Doc. Hal-00452876

Delage, P., Romero, E. (2008). Geoenvironmental Testing. Geotechnical and Geological Engineering 26: 729–749

Fleureau, J.M., Kheirbek-Saoud, S., Soemitro, R., & Taibi, S. (1993). Behavior of clayey soils on drying-wetting paths. Canadian Geotechnical Journal, vol. 30, n°2: 287-296

Frydman, S. & Baker, R. (2009). Theoretical Soil-Water characteristic curves based on adsorption, cavitation, and double porosity. International journal of geomechanics, vol. 9, n°6: 250-257

Maugis, D. (1980). Mécanique et thermodynamique de la phase superficielle. Cahier du groupe français de rhéologie, Vol. 5, n°5.

Rasmussen C.J., Gor G.Y. ,& Neimark V. (2012) Monte Carlo Simulation of cavitation in pores with nonwetting defects. Langmuir, vol 28, n°6: 4702-4711.

Ridley, A. M., Burland, J. B. (1993) A new instrument for the measurement of moisture suction. Géotechnique, vol. 43 n°2: 321-324.

Romero, E., Della Vecchia, G. & Jommi, C. (2011). An insight into the water retention properties of compacted clayey soils. Géotechnique, vol. 61 n°4: 313-328.

Micromechanical modeling of internal erosion by suffusion in soils

I. G. Tejada, L. Sibille and B. Chareyre

Univ. Grenoble Alpes, 3SR, F-38000 Grenoble, France
CNRS, 3SR, F-38000 Grenoble, France
ignacio.tejada@3sr-grenoble.fr, luc.sibille@3sr-grenoble.fr, bruno.chareyre@3sr-grenoble.fr

ABSTRACT

Suffusion is the process of migration of fine particles in the bulk of the soil under certain conditions. It is in the end the consequence of many mechanisms at the grain scale that are determined by the features of the soil (size distribution, shape, mass, void ratio) and of the carrier fluid (viscosity, density, hydraulic gradient).

Microscopic modeling (i.e. considering the time evolution of grains according to their mutual interactions and the interactions with the fluid) can reproduce the complex microscopic events that result on suffusion without the need to introduce additional phenomenological terms.

We use a microscopic hydromechanical model that combines the distinct element method with the pore-scale finite volumes method (the DEM-PFV) to go further on the understanding and description of suffusion in soils.

INTRODUCTION

The description of the process of internal erosion in soils is being object of great interest in geotechnical engineering since it is one of the most common cause of degradation of earth dams and dikes. Moreover, its consequences may be specially dangerous since internal erosion is hard to detect in advance.

Internal erosion is referred to as the migration of soil particles caused by internal flow. It includes the phenomena of piping (i.e. a continuous pipe is formed in the soil as a consequence of the erosion of particles), contact erosion (occurring at the interface between a

fine and a coarse soil layers) and suffusion (the migration of the fine fraction that happens in the bulk of the soil). Our research focuses on the latter.

Suffusion is a complex phenomenon owing to the diversity of the mechanisms involved. The potential for internal stability is determined by the size distribution of the material while the onset and development of suffusion is governed by the hydromechanical behavior (Moffat & Fannin, 2006).

Therefore hydromechanical models are used to study this phenomenon. Their objective is to capture the poromechanical effects that are the result of the two-way coupling between the deformation of the solid matrix and the fluid pressure in saturated porous media. To do that they must consider (Herzig et al., 1970) the features of the carrier fluid (flow rate, viscosity, density), the transportable particles (size, shape, mass fraction with respect to the total solid phase) and the coarse skeleton (porosity, diameter of constrictions, size and shape of grains). The hydromechanical models have to be able to reproduce at least three possible microscopic events that result on suffusion: the detachment of fine solid particles from the coarse skeleton, their transport by the fluid and their eventual filtration within the interstitial spaces of the coarse skeleton.

The transport of fine eroded particles is a consequence of the flow. Even when from a macroscopic point of view the Darcy's permeability and the fluxes are supposed to be homogeneous, the reality is that the geometrical randomness of the coarse skeleton at grain scale induces randomness in flow velocities. Therefore the transport of fines cannot be exclusively described by convection mechanisms but some kind of stochastic action is needed.

The detachment of fine particles can be produced by local changes in the flow that introduce perturbations in the local structures, but also by degradation or aging processes. The former may be the consequence of changes in the macroscopic conditions (typically because of variations of the hydraulic gradient).

Filtration may occur at different sites of the coarse skeleton (surfaces, crevices, constrictions and caverns). It may also be a collective event in which several particles contribute to the clogging of a constriction. The fluid pressure and friction may help fine particles be retained, as well as other forces (van der Waals, electrical, chemical) may do when particles are very small (Santamarina, 2003). Among the physical processes that may cause the retention by making fine particles reach the retention sites are sedimentation, hydrodynamical effects (mechanical dispersion), direct interception (when a particle tries to pass through a smaller constriction and gets trapped) and Brownian diffusion.

Suffusion is generally considered as a phenomenon characterized by a low kinetic. However the filtration of particles may clog flow channels, what in the end affects the macroscopic permeability of the medium. Furthermore, in some cases, the deposition of particles may be very localized resulting on barriers to the flow that may be the onset of a second erosion phase, characterized by a high kinetic, and very aggressive for the soil micro-structure. Therefore this second erosion phase may be damaging for the durability of water retaining structures made of soil.

The aim of this research work is to improve the understanding and the description of the suffusion in soils, identifying and analyzing events that occur on the level of the grains.

MODELING SUFFUSION

Macroscopic model

The macroscopic approach to suffusion embraces research topics like solute transport in saturated porous media (Bear & Bachmat, 1991) or erosion problems (Vardoulakis et al., 1996, Papamichos & Vardoulakis, 2005). Macroscopic models of internal erosion regard the continuum as a three-phase medium (solid skeleton, free or transportable particles and fluid) for which the corresponding mass balance equations are established.

In the mass balance some source and sink terms are included to account for the fact that transported fine particles may join the solid skeleton and vice-versa. These phenomenological terms, often called erosion and filtration laws, are the macroscopic approach to deposition, clogging and detachment mechanisms. They are usually inferred from experiments.

Microscopic model

The microscopic approach to suffusion computes the position of grains (either coarse or fine) according to their mutual interaction and their interaction with the fluid, which is in turn affected by the position of the solid particles.

An example of microscopic hydromechanical model is DEM-PFV, a combination of the distinct element method, DEM (Cundall 1970), with the pore-scale finite volumes method PFV (Chareyre et al., 2012, Catalano et al., 2014). The former for the solid phase, and the latter for the flow of an incompressible pore fluid.

The DEM is used to compute the motion of each solid particle of the granular material. Particles are supposed to interact via short-range forces, i.e. only via mechanical contact, and the dynamics of the granular material is governed by Newton's equation of motion for the center-of-mass coordinates and the Euler angles of its particles.

Initially, the DEM was developed without considering the effect of fluids and was therefore restricted to dry granular materials but more recently some coupled models have emerged to consider the effect of fluid flows. Continuum-based models use continuum formulations, coarse-grid meshing and numerical methods such as finite differences or finite volumes for the fluid phase. In contrast, micro-scale models are based on a very fine discretization of the void space to solve the corresponding Navier–Stokes problem. Continuum techniques (like the finite element method) or particle-based methods (such as the Lattice–Boltzmann method (Sibille et al., 2014)) are used to solve the equations. These method have more computational cost than continuum-based models because of the higher number of degrees of freedom associated to the fluid.

Pore-Network models, PN, are a good compromise between micro-scale and continuum-based models, since they overcome the high computational cost of the former, without introducing all the phenomenological assumptions of the latter. Moreover, PN can describe accurately the effects of fluid at a grain scale. In a PN model the void space is represented as a network of connected pores and throats, where the properties of the throats are supposed to reflect the effect of local void geometry on the flow. The pore-scale finite volumes method (PFV) is a PN model for incompressible flow in sphere packings in which the spatial discretization leads to fluid elements whose sizes are of the same order as the size of the solid particles.

OBJECTIVES

Microscopic modeling may provide insight on suffusion since the complex events that occur at the level of the grains can be reproduced. Under this idea, we use a micro hydromechanical model, the DEM-PFV, to study the phenomenon. We use the open-source code *Yade* (Šmilauer et al. 2010).

In particular we start with a microscopic model in which the coarse skeleton is fixed while the particles, driven by a stationary flow, can go through it. This simple case study may be useful to understand the different stages of a suffusion process.

Microscopic modeling of transport of fine particles

Many macroscopic models consider a double scheme of convection diffusion to explain the transport of particles.

The coarse skeleton is in the end a topology of pores connected by throats of different sizes. When the size of a fine particle is smaller than the smallest constriction, the particle can be transported with no limitation. In such case, fine particles are usually assumed to travel at the same velocity of the fluid (although its viscosity may be accordingly corrected). However as the size of a fine particle is close to, but yet smaller than the characteristic size of coarse particles, pores or constrictions, the motion of the particle is marked by many collision and rolling events, what make the mean convective velocity much smaller than that of the flow. As these events are perfectly reproduced in DEM-PFV models, simulations (Fig. 1) may help to measure the value of the convective velocity for different coarse skeletons, fine particles and flows.

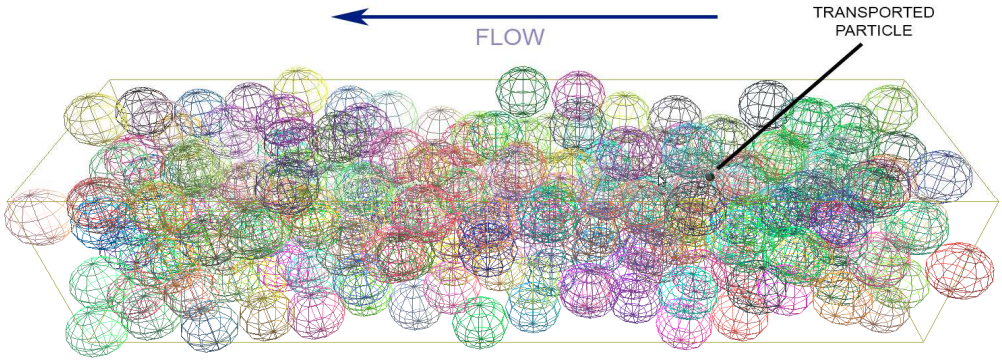

Figure 1. **DEM-PFV simulation of the transport of a small particle through a coarse and dense skeleton produced by a stationary flow**

On the other hand, diffusion terms try to take into account the randomness of the pathlines caused by mechanical dispersion as well as molecular diffusion (in case of very small particles). However Fickean terms works only for normal diffusion, situation that needs to meet some requirements that are not always satisfied (Klafter & Sokolov 2005, Klages et al., 2008). The processes of anomalous diffusion, either subdiffusion or superdiffusion, are those in which the mean square displacement of particles due to random processes does not present a linear relationship with time. The way in which the diffusion process occurs in a granular material can be studied with the DEM-PFV since it allows tracking the motion of transported particles to carry out statistical analyses (Fig.2).

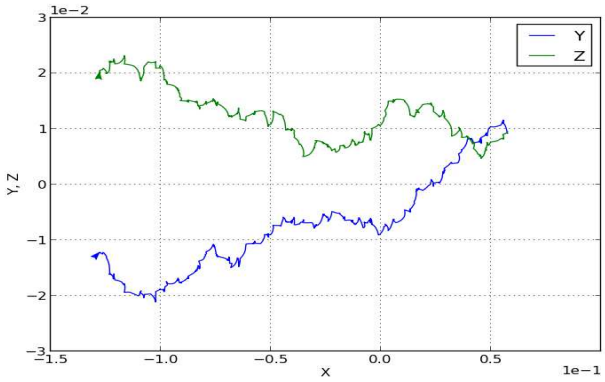

Figure 2. **Pathline of a small particle carried by the flow through a coarse and dense skeleton. X is the direction of the flow (from right to left) while Y and Z are the perpendicular directions.**

Microscopic modeling of filtration

When the size of a fine particle is larger than the smallest constrictions but smaller than the largest ones, the particle may be trapped by direct interception at some point. The probability of such an event depends on the constriction size distribution, the size of the fine particle and the travel distance. On the other hand collective clogging events can occur when many fine particles run into the same pore or constriction, so it is more probable with higher concentration of them. These events of filtration can be modeled with DEM-PFV since different coarse skeletons, fluxes and fine particles can be used (and eventually many of them at the same time).

On the other hand, the macroscopic permeability of the coarse skeleton is intimately joined to the features of the constrictions. Therefore as these are clogged by fine particles that are previously filtrated, the permeability is reduced. The permeability can be computed with DEM-PFV since it solves the equations for the fluid at the pore scale. Furthermore, when the permeability changes so do the fluxes. It could also be the cause of other events involved in suffusion.

Microscopic modeling of detachment

Detachment events are much complex to be reproduced when very idealized models are used. For example a particle that has been trapped by direct interception will not easily detached unless the direction of the fluid were inverted or the coarse particles were slightly displaced. Furthermore, the geometry of particles play important role on the stability of local structures. Nevertheless, if these aspects are thoroughly taken into account, DEM-PFV simulations can help to understand the events of detachment and the influence of aspects as friction or cohesion.

ACKNOWLEDGEMENTS

The authors gratefully acknowledge support from Labex TEC21 - Ingénierie de la complexité, through the program MODERO.

REFERENCES

Bear, J. & Bachmat, Y. 1991. Introduction to Modeling of Transport Phenomena in Porous Media. Kluwer Academic Publishers.

Catalano, E., Chareyre, B. and Barthélémy, E. 2014. Pore-scale modeling of fluid-particles interaction and emerging poromechanical effects . *Int. J. Numer. Anal. Meth. Geomech*. 38:51–71

Chareyre, B., Cortis, A., Catalano, E. & Barthélemy, E. 2012. Pore-Scale Modeling of Viscous Flow and Induced Forces in Dense Sphere Packings . *Transp Porous Med.* 92:473–493.

Cundall, P.A. & Strack, O.D.L. 1979. A discrete numerical model for granular assemblies. *Géotechnique* 29(1): 47-65.

Herzig, J. P., Leclerc, D. M. & Le Goff, P. 1970. Flow of Suspensions through Porous Media-Application to Deep Filtration. *Ind. Eng. Chem*. 62 (5): 8–35.

Klafter, J. & Sokolov, M. 2005. Anomalous diffusion spreads its wings. *Physics World*. August 2005:29-32.

Klages, R., Radons, G. & Sokolov, I. M. 2008. Anomalous Transport: Foundations and Applications. WILEY-VCH .

Moffat, R. A. & Fannin, J. 2006. A Large Permeameter for Study of Internal Stability in Cohesionless Soils. *Geotech. Testing J*. 29(4): 273-279.

Papamichos E. & Vardoulakis I. 2005. Sand erosion with a porosity diffusion law, *Computers and Geotechnics.* 32:47–58.

Santamarina, J. 2003. Soil Behavior at the Microscale: Particle Forces. *Soil Behavior and Soft Ground Construction GSP*. 119 :25-56.

Sterpi, D. 2003. Effects of the Erosion and Transport of Fine Particles due to Seepage Flow. *Int. J. of Geomechs*. 3(1):111-122.

Sibille, L., Lominé, F., Poullain, P., Sail, Y., & Marot, D. 2014. Internal erosion in granular media: direct numerical simulations and energy interpretation. *Hydrol. Process.* DOI: 10.1002/hyp.10351.

Šmilauer, V., Catalano, E., Chareyre, B., Dorofeenko, S., Duriez, J., Gladky, A., Kozicki, J., Modenese, C., Scholtès, L., Sibille, L., Stránský, J. & Thoeni, K. 2010. Yade Documentation (V. Šmilauer, ed.), The Yade Project, 1st ed. http://yade-dem.org/doc/.

Vardoulakis I., Stavropoulou M., Papanastasiou P., 1996. Hydromechanical aspects of sand production problem. *Transport in Porous Media.* 22: 225 -244.

Experimental and Numerical Study of Suffusion in Granular Media

Hashem ABDOU [1, 2], Olivier PLE [3,4], Fabrice EMERIAULT [1, 2]

[1] Univ. Grenoble Alpes, 3SR, F-38000Grenoble, France

[2] CNRS, 3SR, F-38000Grenoble, France

[3]Univ. Savoie Mont Blanc, LOCIE, F-73000 Chambéry, France

[4] CNRS, LOCIE, F-73000 Chambéry, France

ABSTRACT

The phenomenon of suffusion corresponds to the migration of eroded fine particles in a porous media under the action of an internal flow. This mechanism could be the main origin of damage in embankments and earth dams. Many studies were done to understand the phenomenon of Suffusion. These works were based on a reconstituted model soil tested via laboratory experiments. In order to represent as far as possible the in-situ and real scale situation, a new experiment has been developed in 3SR Laboratory called the “Cross Erosion Test” (CET). In this new apparatus, a Plexiglas tank is equipped with two boreholes to induce, during the test, an internal erosion of "suffusion" type in a saturated soil (whether natural or model). The flow rate, velocity, hydraulic gradient and turbidity of the extracted water are measured. Analysing these measured data, we can detect the migration of fine particles and observe the erosion in the test soil. Two aspects are presented: the new experimental apparatus and its first main results and the initiation of the numerical simulation of the internal erosion phenomena using the code of “Comsol Multiphysics 3.4b”.

INTRODUCTION

Suffusion is a process of internal erosion whereby fine grains are removed from a soil due to groundwater flow. This causes a change in the hydraulic and mechanical properties of the soil. A schematic overview is given in Fig. 1. This type of internal erosion is triggered in soils which are subjected to a large hydraulic gradient, i.e. levees or earth dams. This type of internal erosion is still an active research topic, e.g. (Fannin & Moffat 2006, Bonelli & Marot 2008, Bonelli & Brivois 2008, Monnet et al. 2012, Beguin et al. 2010, Papamichos et al.

2001, Vardoulakis et al. 1996). However, most of these authors are focused on characterizing the effects of suffusion in laboratory tests.

In the current paper, we will study the effects of suffusion in a granular medium: we first present a new experimental device named Cross Erosion Test (CET) (Nguyen, 2013), which is devoted to the measurement of the initiation of the suffusion. Then principles of numerical modeling, using the finite element code of Comsol multiphysics (3.4b) will be presented.
The principle of the test is to inject clear water into the soil sample by using a first borehole then extracting the water charged with particles in another borehole. In this test, the erosion is estimated based on the measurement of the evolution of the total mass of particles that are collected over time. This technique can be transposable, in-situ, to determine the risks of suffusion in earth dams, dikes and other earthworks.

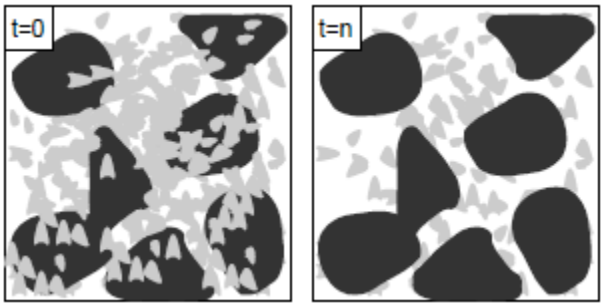

Figure 1. ***Schematic representation of suffusion, from Roosenbrand (2011)***

DESIGN OF THE CROSS EROSION TEST

Test principle

CET was developed in 3SR laboratory. This test requires two boreholes to achieve the "suffusion" (Figure 2). In the first borehole, clean water is injected with an imposed hydraulic head. Hydraulic head and flow rate are measured. The device is designed to maintain input parameters as constant as possible. The soil volume is contained in a Plexiglass tank, 55 cm high, 50 cm wide and 40 cm deep. A plastic tube of 6 cm in diameter is used to inject clean water. An electric pump is used to extract water and eroded particles in a second tube or borehole. The diameter of the opening of the aspiration filter of the pump is equal to 1.5 mm. The distance between the injection borehole and the pump is equal to 45 cm. In order to measure the injection flow rate and the extracted flow rate, two flow meters are placed respectively at the input and the output water. Two pressure sensors are used for measuring the injection pressure and the pump pressure. An endoscopic camera placed at the bottom of a glass tube fixed after the pump allows to obtain a continuous recording of the extracted water charged with the eroded particles (Ple et al. 2012, Nguyen et al. 2013). That leads us to qualify the eroded mass. The collected images are processed by spectral analysis (ImagJ or Fiji). Measuring the volumetric flow rate of the exit water and the hydraulic head of injection allows us to control the hydraulic conditions of internal erosion. The theoretical initiation of internal erosion is determined by Terzaghi critical gradient (Terzaghi et al. 1996):

$$i_{cT} = \frac{\gamma'}{\gamma w} \qquad (1)$$

Where γ' is the buoyant unit weight of the soil sample and γ_w is the unit weight of water. The hydraulic gradient during the test (i_{exp}) is defined by the difference in hydraulic head between the upstream and downstream divided by the length of the liquid path (Monnet et al. 2012):

$$i_{exp} = \frac{\Delta h}{h} \quad (2)$$

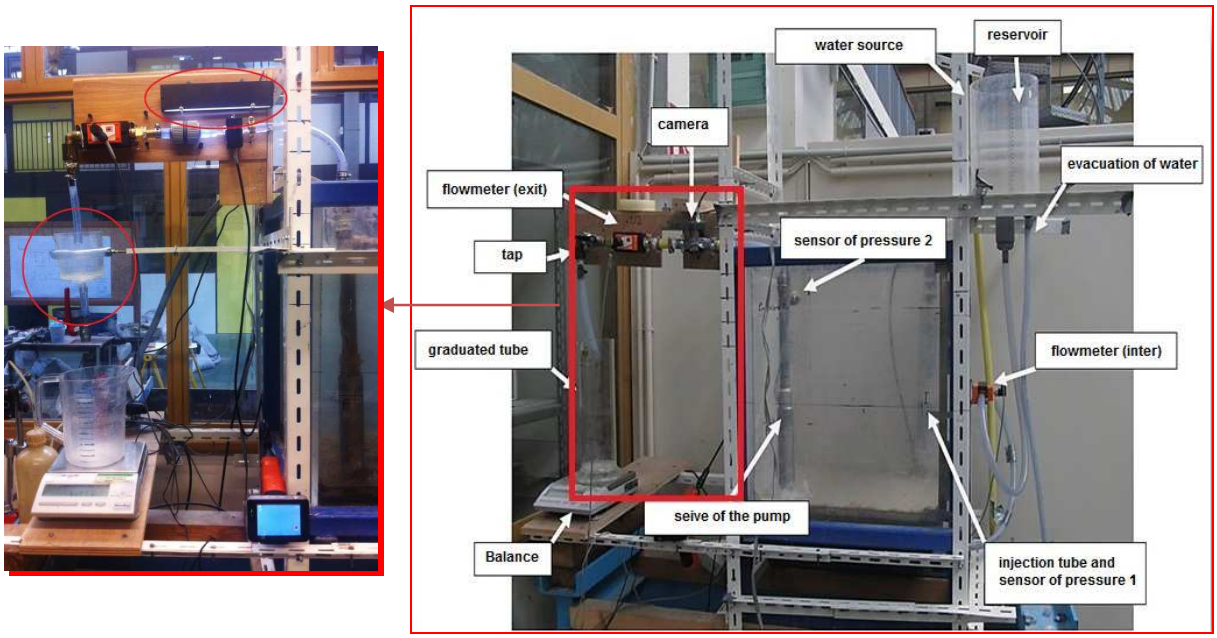

Figure 2, ***schema of CET***

Preparation of the Soil Sample

The main objective of CET is to characterize the susceptibility of a soil to suffusion. This test is developed to be applied to a wide range of soils including the soil of the dikes of Isère and Drac rivers in Grenoble (Monnet et al. 2011). According to the report of AD Isère Drac Romanche (IMS-RN, 2006), most of the dikes along Isère consist in sandy gravels and gravely sands, with little amount of silt (see figure 3). The grain size distribution curves of these soils are discontinuous and sensitive to the internal erosion.

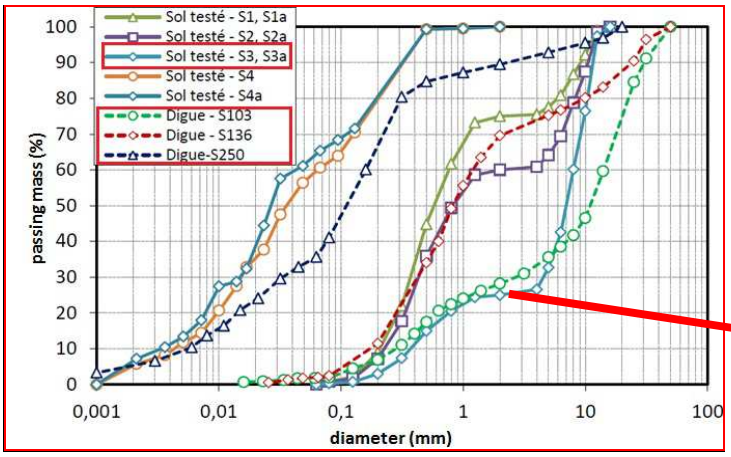

Figure 3. ***Grain size distribution curves of Isère dikes***

Figure 4. ***Grain size analysis of the reconstituted soil***

For the soil sample S3, as a result of the PhD thesis of Duc Manh Nguyen (Nguyen, 2013), this type of soil did not show any suffusion but self-filtration. We will retest the same soil with same hydraulic conditions during the test but with a better reconstitution of the soil sample in the laboratory to fit the same grain size distribution curve of the natural soil and the same granular materials (see figure 4). The susceptibility to the suffusion will be tested. The soil (S3) used in the experiment is a reconstituted soil with sand (0/2 mm) 25% in weight, gravels (2/20 mm) 70% in weight and 5% of Silt (see Figure 4). The properties of S3 are given in table- 1.

k (m/s)	n	ρ_d (kg/m3)	d_{10} (mm)	d_{15} (mm)	d_{30} (mm)	d_{50} (mm)	d_{60} (mm)	d_{85} (mm)	C_u
2.04 E-4	0.36	1688	0.38	0.5	4.57	7.02	7.99	11.04	21.03

Table 1. ***Properties of the soil S3***

Concerning the procedure defined for filling the tank with the soil sample, dry soil is deposited into layers of 3 cm to 4 cm and then the soil is compacted with a small compaction device. The sample is then saturated under a small hydraulic head (2 cm) on the top of the soil sample (see fig. 5).

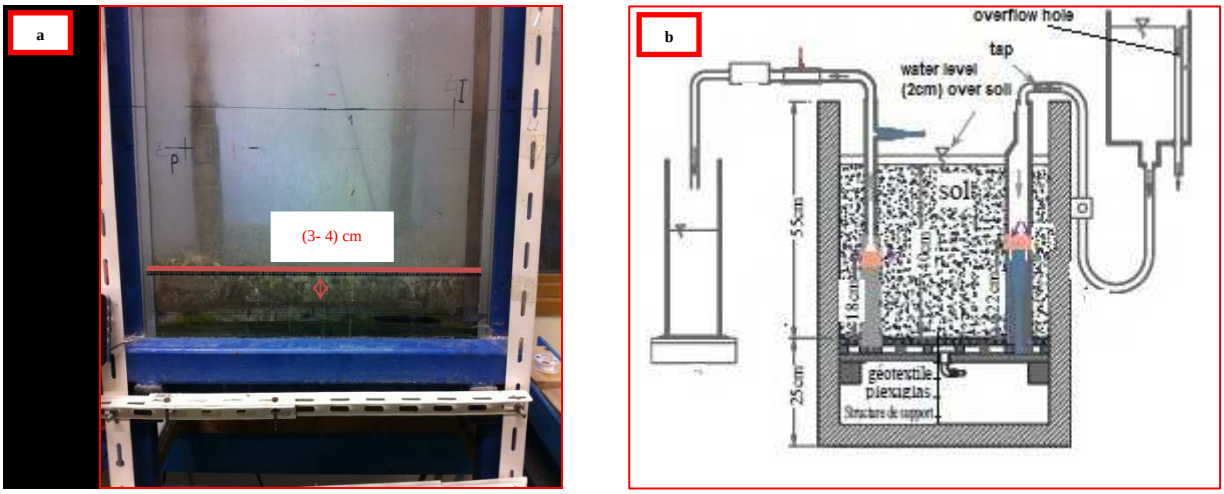

Figure 5. ***Installing and saturating of the soil sample***

THE FIRST TEST RESULTS

Evolution of the hydraulic gradient

During the test, the injection hydraulic head is variable (from 0.46 m to 0.58 m). The corresponding frequency of the pump ranges thus between 27 Hz and 51 Hz. As shown in figure 6, the frequency is increased and results in an increase of the hydraulic gradient and the velocity of the flow. Suffusion is detected for the first time by the camera with a hydraulic gradient of 0,45 m/m corresponding to a frequency of 27 Hz. However, for each stable value of the frequency, we can clearly notice that an increase of hydraulic gradient (i_{exp}) and a simultaneous decrease of the velocity occur. This means that the permeability decreases and therefore clogging at the level of the inspiration filter tend to appear due to particle transport. As we can notice in Figure 6, frequency increases the effect of clogging (drop in the measured velocity). Nevertheless, when the frequency is further increased, the particles which may have

clogged the filter are removed by the effect of increasing the flow rate and then suffusion resumes.

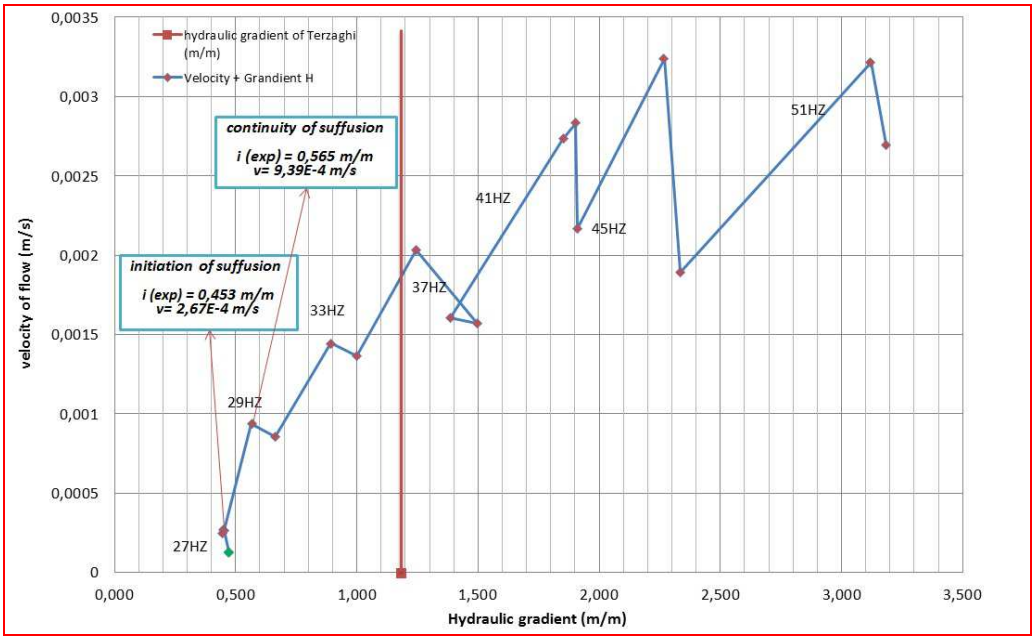

Figure 6. ***Velocity of the exit flow in function of the hydraulic gradient S3***

Evolution of cumulative eroded soil mass

According to many experimental studies, the coefficient of uniformity of the particle size distribution is a major criterion to estimate the internal stability of a soil (Kenney & Lau 1985, Wan & Fell 2008). The coefficient of uniformity is defined as D_{60}/D_{10}, where D_{60} and D_{10} are respectively the diameter of the particles at 60% and 10% passing mass. A soil presenting a large value *Cu* means that there is a broad range of particle diameters.

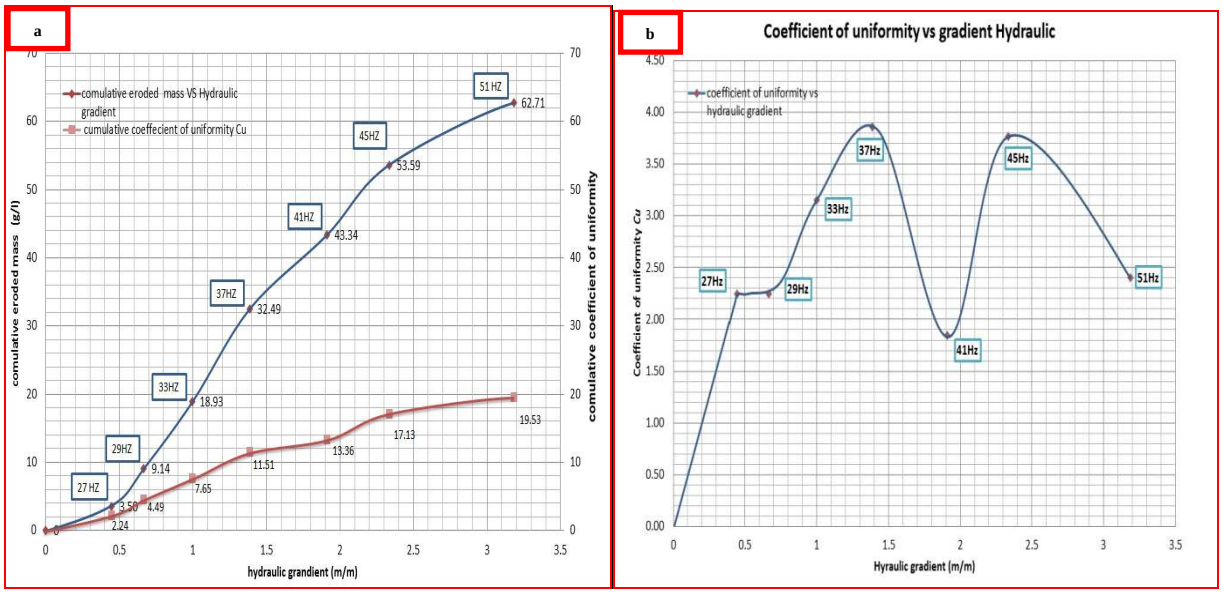

Figure 7. ***The mass of the eroded particles and coefficient of uniformity in function of the hydraulic gradient- S3***

For each frequency, eroded particles were collected and then a sieve size analysis was conducted (see fig. 8). The maximum measured particle diameter is totally related to the

opening size of the aspiration filter of the pump (1.5 mm). Using the grain distribution curves of eroded particles, the coefficient of uniformity *(Cu)* of each curve was measured.

Figure (7-a) explains also the relationship between the cumulative coefficients of uniformity (C_u) mentioned above and the hydraulic gradient for the different frequencies. The individual relationship between the coefficient of uniformity and hydraulic gradient is shown in Figure (7-b). This plot indicates that coefficient of uniformity reaches a peak (3.86) at a hydraulic gradient (i_{exp}) of (1.4 m/m) for the frequency 37 Hz and then the curve tends to decrease that means finer particles tend to appear for a frequency of 41 Hz. However, for the frequency 45 Hz, the coefficient of uniformity increases which indicates those coarser particles are affected by the increase of the hydraulic gradient. This non uniform evolution of C_u may be due to the effect of clogging and its destruction by a further increase of the frequency and thus hydraulic gradient.

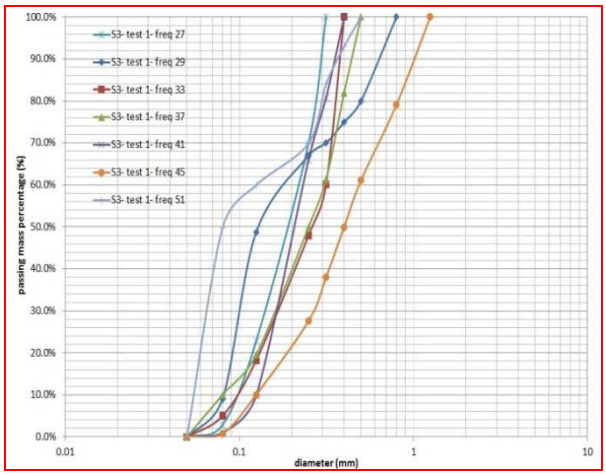

Figure 8. ***Grain size distribution curves of eroded particles***

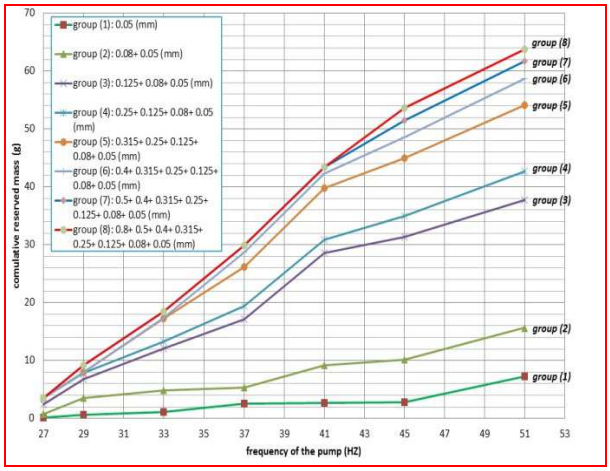

Figure 9. ***Cumulative reserved eroded mass in function of the frequency of the pump.***

Figure 9 illustrates the relationship between the cumulative reserved eroded mass of different group of diameters and the different frequencies of the pump. When frequency increases, the diameter of particles increases. As shown by the figure, there is a gap between group (2) and group (3) that means that the diameter (0.125 mm) reserves the maximum amount of cumulative eroded soil mass (difference between group (2) and (3)) for the different increase of frequency (22.3 g at 51 Hz). However, for the frequency 51 Hz, (0.8 mm) and (0.5 mm) were not observed (group (6), group (7) and group (8) return approximately the same cumulative reserved eroded mass) and finer particles tend to appear, which must be related to the effect of clogging.

INITIATION OF A NUMERICAL MODELING

In this part we will present a first numerical approach to the internal erosion. The modeling is performed by using the finite element code in Comsol Multiphysics 4.3b (Nguyen et al, 2013). A 3D model of the CET experiment has been created to understand and predict what happens during the test. This simulation allows us to anticipate the problem and take into account the hydraulic phenomena and then to predict the hydraulic conditions that cause the initiation of the internal erosion. Moreover, this modeling also provides a good representation of the CET experience to quantify the influence of each parameter (see fig. 10).

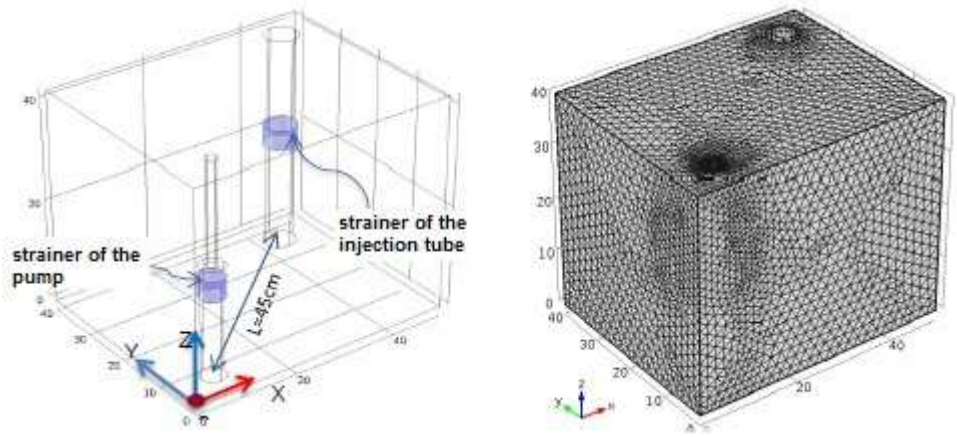

Figure 10. ***The geometry of the model CET***

The fluid flow is assumed to follow Darcy's law. Permeability is assumed to follow the Kozeny-Carman equation. The eroded particles and the fluid have the same speed. The erosion is described by the classical law of Vardoulakis and improved by Bendahmane (Vardoulakis, I. 2004, Bendahmane 2005). This law directly connects the variation of the porosity to the velocity of the fluid flow. The equations of the problem are written as following:

Darcy's low:

$$q = -\frac{K}{\mu}\nabla p \tag{3}$$

Mass conservation of the fluid:

$$\frac{\partial(\rho f.n)}{\partial t} + \nabla(\rho f.u) = Qm \tag{4}$$

Erosion low:

$$\frac{\dot{m}}{\rho s} = \lambda(1-n)\|v\| \qquad : v = \frac{q}{n} \tag{4}$$

Where q (m/s) is the velocity of Darcy, v (m/s) is the velocity of fluid flow in the pores of the soil, K (m^2) is the intrinsic permeability of the soil, μ (Pa.s) is the fluid viscosity and ∇p (Pa) is the gradient of the fluid pressure between upstream and downstream. Q_m (kg/(m^3.s)) is the term of the mass source, n is the porosity of the soil, u ≠ v (m/s) is the velocity of the flow. ρ_s (kg/m^3) is the density of the grains of the soil and ρ_f (kg/m^3) is the density of water. λ (1/m) is the empirical coefficient of Papamichos et al. (2001).

In Comsol 4.3b, Darcy's law and the mass conservation of fluid are integrated in the Darcy mode (dl) to describe the fluid flow in a saturated soil and the equation of the erosion law will be solved by using the technique of partial differential equations (pde).

This approach is carried out at a macroscopic scale by taking into account the erosion and transport of fine particles in a porous medium. The fluid pressure is considered as a dependent variable. The hydraulic head and the velocity of flow are variable with time and space. The mass conservation equation will be coupled with the erosion law. These equations combined with the flow in a porous medium equation can track the change of porosity and the average concentration of eroded particles. The results also can determine the total mass of eroded particles.

CONCLUSION

The aim of this paper is to investigate the susceptibility of a soil to the suffusion by using a new laboratory technique named the Cross Erosion Test. For soil S3, suffusion was detected by the camera and by controlling the hydraulic conditions of internal erosion. Suffusion was detected for the values of hydraulic gradient (i_{exp}): 0.45, 0.56 and 0.99 which is less than the value of the critical hydraulic gradient of Terzaghi (i_{cT} = 1.18).). Frequency increase leads to an increase in hydraulic gradient and velocity of flow. Continuous suffusion phenomenon was observed.

The observed increase of the coefficient of uniformity is due to an increase of hydraulic gradient but for a certain frequency the coefficient of uniformity tends to decrease with increasing the hydraulic gradient, this may indicate that clogging phenomenon occurs. For the frequency 51 Hz, (d_1= 0.8 mm) and (d_2= 0.5 mm) were not observed and finer particles tend to appear. This indicates that the inspiration filter of the pump (1.5mm) is clogged by coarser particle that may be disrupt the flow rate.

For the numerical model, a 3D modeling is performed to reproduce the hydraulic conditions of the experiment. The erosion law must be verified by comparing the numerical results and the experimental results. To solve this problem, the finite element method can be applied with either a 2D or 3D model. The fluid pressure is considered as a dependent variable. The hydraulic head and the velocity of flow are variable with time and space.

ACKNOWLEDGEMENTS

The authors are grateful for the effort and support of Mr. Michel PINHAS, the director of AD Isère Drac Romanche (Association Départementale Isère Drac Romanche).

REFERENCES

Beguin, R., Faure, Y-H., Guidoux, C., Philippe, P. (2010, juin 7). "Érosion interne provoquée par une interface granulaire au sein des ouvrages en terre". *JNGG*.

Bendahmane, F. (2005). "Influence des interactions mécaniques eau-sol sur l'érosion interne". *Université de Nantes*.

Bonelli S., Brivois O. (2008). "The scaling law in the hole erosion test with a constant pressure drop". *International Journal for Numerical and Analytical Methods in Geomechanics, 32*, 1573-1595.

IMS-RN. (2006). *Diagnostic des digues du DracDu pont du Rondeau au pont des Martyrs (5930 m).* Association Départementale Isère Drac Romanche, Grenoble.

Kenney, T.C. et Lau, D. (1985). "Internal stability of granular filters". *Canadian Geotechnical Journal, 22(2),* 215–225.

Monnet, J., Ple, O., Broucke, M., Nguyen, D.M. (2011). "Internal Erosion Test: Design and Preliminary Results". *International Journal of Civil Engineering and Building Materials, 1*(2), 60-67.

Monnet, J., Ple, O., Nguyen, D.M,. (2012). "Characterization of the Susceptibility of the Soils to Internal Erosion". *4th International Conference on Geotechnical and Geophysical Site Characterization (ISC'4).* Porto de Galinhas, Pernambuco, Brazil.

Monnet, J., Ple, O., Nguyen, D.M,. (2012). "Internal Erosion in Dikes alongside Roads and Railways". *Advances in Transportation Geotechnics II, 2*, 919-923.

Monnet, J., Ple, O., Nguyen, D.M, Plotto, P. (2011, Mai 29-31). "Caractérisation des sols à l'érosion interne - L'essai d'érosion transverse". *Rencontres AUGC*, p. 10.

Monnet, J., Ple, O., Nguyen, D.M, Plotto, P. (2011, april 26-29). "The cross erosion test, preliminary results". *European working group on internal erosion in embankment dams & their foundations*, p. 8.

Monnet, J., Ple, O., Nguyen, D.M, Plotto, P. (2012). "A new test for the characterization of suffusion into embankment and dam ". *International Conference on Scour and Erosion (ICSE).* Paris.

Monnet, J., Ple, O., Nguyen, D.M. (2013). " Identification du risque d'érosion interne sur les digues de l'Isère et du Drac". *the 18th International Conference on Soil Mechanics and Geotechnical Engineering (ICSMGE).* Paris, France.

Nguyen, D. M. (2013). *Méthode Hydro-Géomécanique de caractérisation de la susceptibilité des sols à l'érosion interne.* PhD, Grenoble.

Nguyen, D.M, Monnet, J., Ple, O. (2013, Mai 29-31). " Caractérisation des sols à l'érosion interne : L'essai d'érosion transverse (Cross Erosion Test)". *Rencontres AUGC*, p. 8.

Nguyen, D.M, Ple, O., Monnet, J. (2013). "Experimental Study of Suffusion in Granular Soils". *Advanced Materials Research, 684*.

Papamichos, E., Vardoulakis, I., Tronvoll, J. Skjerstein, A. (2001). Volumetric sand production model and experiment. *Int. J. Numer. Anal. Methods Geomech., 25*(8), 789-808.

Ple, O., Monnet, J., Nguyen, D.M. (2012). "Apparatus design for suffusion characterization". *International Journal of Emerging Technology and Advanced Engineering, 2*(3), 430-435.

S. Bonelli, D. Marot. (2008). On the modelling of internal soil erosion. *The 12th International Conference of International Association for Computer Methods and Advances in Geomechanics*. Goa, India.

Terzaghi, K., Peck, R.B., Mesri, G. (1996). *Soil mechanics in engineering practice* (Third Edition ed.). John Wiley & Sons Inc. Publishers.

Vardoulakis, I. (2004). Fluidisation in artesian flow conditions: Hydromechanically stable granular media. *Géotechnique, 54*(2), 117-130.

Vardoulakis, I., Stavropoulou, M., Papanastasiou, P. (1996). Hydromechanical aspects of sand production problem. *Transport in Porous Media, 22*, 225-244.

Wan C.F., Fell R. (2008). "Assessing the potential of internal instability and suffusion in embankment dams and their foundations". *J. Geotech. Geoenviron. Engrg., 134(3),* 401-407.

Pore-scale simulations of two-phase flow in granular materials

C. Yuan, B. Chareyre & F. Darve
Laboratoire Sols, Solides, Structures, Grenoble, France
chao.yuan@3sr-grenoble.fr bruno.chareyre@3sr-grenoble.fr
felix.darve@3sr-grenoble.fr

ABSTRACT

A pore-scale model is presented for simulating two-phase flow in granular materials. The solid phase is idealized as dense random packings of polydisperse spheres, generated with the discrete element method (DEM). The pore space is conceptualized as a network of pores connected by throats, which is obtained by using regular triangulation. Theoretical formulas for calculating geometrical properties and entry capillary pressure for given pores are developed by extending the Mayer and Stowe-Princen (MS-P) theory of drainage. Such relationships are employed in the network for defining as local invasion criteria, so that the drainage can be represented by the replacement of W-phase when the threshold value is reached. Different side boundary conditions and the events of W-phase entrapment are considered during the coupling procedures. This pore-scale model is verified by comparing simulation results with experimental data of quasi-static drainage experiments in a synthetic porous medium. The simulated $P^c - S^w$ curve in primary drainage is in agreement with the experimental one.

INTRODUCTION

Understanding transport properties of multiphase flow in porous media is of great importance for many areas of engineering and science, such as oil recovery, agriculture irrigation and environmental restoration. Although most of these problems describe such flow process at the macro-scale, pore-scale modeling provides an important means to improve our understanding of the insight physical processes. In order to simulate large domains, one often represent the porous medium by a pore-network, in which the void space of the medium is represented by a lattice of wide pores connected by narrow throats. Using appropriate physical laws that govern the transport and arrangement of fluids in system, network can then be made to replicate experimental measurements at the microscopic scale (Fatt 1956, Ma et al. 1996, Mayer & Stwoe1965). However, most of those networks are based on regular and structured topology, which can not describe the irregular and unstructured characteristics of porous

medium. Recently, more and more researchers focus their interest on models of realism, in which the topology of networks are based on real porous medium. This approach is pioneered by Bryant and Blunt (Bryant & Blunt 1992, Bryant et al. 1993), who constructed the network based on a measured random packing of equal spheres (Finney pack). With the help of powerful measuring methods and computational techniques, more and more accurate topologically equivalent skeletons are built(Øren et al. 1998, Dong & Blunt 2009).

The method considered in this study is similarly devoted to the pore-scale modeling of the transport process of multiphase flow, but important differences are also noticeable in the geometrical idealization of the pore space and network modeling. These difference are mainly due to the spherical geometry of the solid particles and to the pore space decomposition technique. This study represents a first step in the direction of developing a fully coupled, computationally efficient model combining two-phase flow and deformation in porous media. In particular, we will focus our effort on the faithful approximation of the capillary pressures applied by the fluid-fluid interface on solid grains and of the arrangements of phases displacements, with the aim of incorporate these pressures and arrangements in the discrete element method (DEM) computation.

PORE-SCALE NETWORK

We propose a pore-scale network model to process the decomposition of the porous media. The solid phase is idealized as dense random packings of polydisperse spheres, generated with DEM (Smilauer et al.2010). The decomposition of the pore space is obtained in three dimensions by a using Regular Triangulation method, in which the void of porous media is conceptualized as a network of pores connected by throats. A similar network was introduced recently for the so called the Pore-scale Finite Volume scheme (PFV) for one-phase flow. It is able to reflect in a natural way the deformation of the porous material system. Here it will be discussed briefly; a more detailed description can be found in Chareyre et al. (2012) and Catalano (2012).

Regular Triangulation (or referred as weighted Delaunay triangulation) generalizes classical Delaunay triangulation to weighted points, where weights account for the size of the spheres (Edelsbrunner &Shah 1996). The dual Voronoi graph of regular triangulation is entirely contained in voids between solid spheres. Such network scheme can ideally be assigned to solve the flow path problem within the porous sample. A typical network of Regular Triangulation is shown in Figure 1. Based on this decomposition, a “pore” is bounded by four solid spheres with respective radius $R\{r_1, r_2, r_3, r_4\}$, which are arranged forming a simple tetrahedron packing order. Pore body volume is defined to be the irregular cavity within the tetrahedron (see Figure 2(a)). The shape of pore throat is considered to be the cross section extending within tetrahedral facets, thus the volume of throat is assumed to be 0. Specifically, the geometry of entry pore throat is a critical cross-sectional area quantified by the multiphase contact lines (shown in Figure 2(b)).

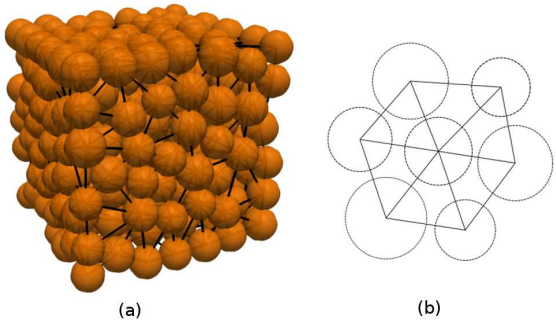

Figure1. **Definition of pore network for packing of spheres, generated by regular triangulation in 3D(a) and 2D(b).**

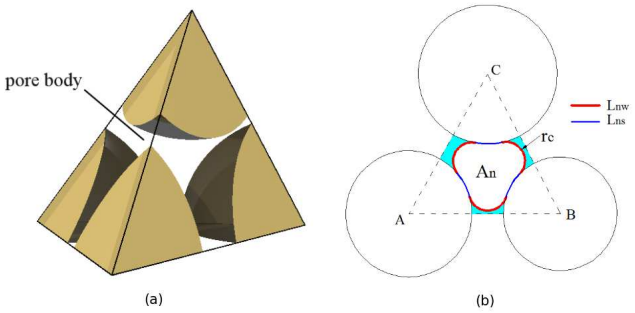

Figure 2. **Pore geometry. (a)A pore defined by tetrahedral element of the finite volume decomposition. (b)Definition of pore throat geometry.** r_c is the curvature of meniscus; L_{nw} is the length of contact line between nonwetting and wetting phases; L_{ns} is the length of contact line between nonwetting and solid phases.

Since each pore is a tetrahedron, it has four neighbors, resulting in a lattice of connectivity four. Although the similar network can be found in other models (Mason 1971, Gladkikh & Bryant 2003), those decomposition techniques are limited by solid particle size, in which the triangulation can only be assigned in packing of equal spheres. In this model, the network definition applies polydisperse sphere packings. The only restriction on this geometrical description is that the center of one sphere should not lie inside another sphere. As such, contact or even moderate overlaps between adjacent spheres are allowed.

DRAINAGE MODEL

Local rules

The phenomena of multiphase flow in porous media can be divided into quasi-static regime and dynamic ones. For two-phase flow, or referred as drainage and imbibition, in the absence of gravity, the conventional immiscible displacement can be described by two dimensionless numbers, the viscosity ratio M and the capillary number C_a,

$$M = \frac{\mu_{inv}}{\mu}, C_a = \frac{\mu v}{\sigma} \tag{1}$$

where μ_{inv} is the viscosity of invading phase, μ is the viscosity of receding phase, v is the receding phase average or macroscopic velocity and σ is the interfacial tension between two

fluid phases (Lenormand et al. 1988, Lenormand 1990). The limit of "quasi-static" flow is defined by C_a closed to 0.

The model we propose is aiming to simulate the primary drainage phenomenon of air-water system, or typically, more generally nonwetting-wetting (NW-W) systems. We hypothesize the drainage process is in a quasi-static regime, in which dynamic effects is in absent and the flow is dominated by capillary forces. Thus, we can neglect the effects of phases viscosity during the process. The porous within a fluid phase is uniform in every connected domain.

The drainage process is controlled by the capillary pressure P^c, i.e., the pressure difference between NW-phase and W-phase. The invasion of one pore is controlled by the associated pore throats. Because the entry capillary pressure of pore body is smaller than that of pore throat, after the invasion of throat, the body is filled by NW-phase spontaneously. In principle, the receding W-phase can be present in the involved domain in the form of disconnected pendular rings left behind. The relationship between the capillary pressure and volume of liquid bridge can be found in our previous research (Scholtes et al. 2009). However, in this model, we assume this volume is negligible. So there is no saturation associated with corner W-phase. Thus the state of a local pore unit is in binary condition, i.e., the pore is either filled with W-phase or with NW-phase.

A relationship between capillary pressure P^c, interfacial tension, σ, and curvature of the NW-W interface, *C*, is given by the Young-Laplace equation,

$$P^c = \sigma C \tag{2}$$

The curvature *C* is fixed by the boundary conditions of NW-phase, W-phase and solid particle surface. For simplicity in the simulation, the solid particle media and pore-network are assumed to be fixed. Commonly in a regular interface, *C* can be acquired from the principal radii of the meniscus (r_1 and r_2) by

$$C = (\frac{1}{r_1} + \frac{1}{r_2}) \tag{3}$$

However, in complex pore geometry, *C* are difficult to define. So a more clearly knowledge of connection among P^c, *C* and pore geometry is required.

Determination of entry capillary pressure

The drainage process is assumed in quasi-static regime, so P^c is applied into porous media to result in from one equilibrium state to another. The NW-phase invasion is locally controlled by entry capillary pressure P_e^c of pore throat. The determination of P_e^c is based on MS-P (Mayer-Stowe-Princen) method, which follows the balance of forces for NW-W interface of pore throat (Princen 1969, Mayer&Stowe 1996).

$$\sum F = F^p + T^\sigma \tag{4}$$

where, F_p is the capillary force acting on pore throat section domain; T^σ is the total tension force along multi-phase contact lines. The same strategy for solving P_e^c can also be found in Ma et al. (1996), Prodanovic & Bryant (2006) and Joekar-Niasar et al. (2010). For completeness, we recall the generic aspect of the MS-P method hereafter.

As described in the previous section, the geometry of pore throat has a mixed cross-sectional shape extending in the facet of tetrahedral pore. Figure 2(b) shows the schematic cross section of a local pore throat formed by solid phase surface and NW-W interface. In local drainage of pore unit, when NW-phase invades pore body, W-phase will remain in the corners of throats along the fictious tube. The longitudinal curvature of the resulting interface inside the tube is zero (Joekar-Niasar et al. 2010). The critical curvature of three menisci extending within throat section, i.e., the curvature of contact lines between NW-phase and W-phase, are equal. Let that radius be denoted by entry capillary radius r_c. Then, following Young-Laplace equation, P_e^c can be written:

$$P_e^c = P^n - P^w = \frac{\sigma^{nw}}{r_c} \tag{5}$$

in which, P^n and P^w are pressure of NW-phase and W-phase; σ^{nw} is NW-W interface tension.

According to the geometry of pore throat we defined in Figure 2(b), the forces acting on interface can be written:

$$F^p = P_e^c A_n \tag{6}$$

$$T^\sigma = L_{nw}\sigma^{nw} + L_{ns}\sigma^{ns} - L_{ns}\sigma^{ws} \tag{7}$$

where, A_n is the area of pore throat section; L_{nw} and L_{ns} are total length of NW-W contact lines and NW-Solid contact lines, respectively. The multiphase interfacial tensions, σ^{ns}, σ^{ws} and σ^{nw} have a relationship with contact angle θ, defined by Young's equation,

$$\sigma^{ns} - \sigma^{ws} = \sigma^{nw}\cos\theta \tag{8}$$

Then Eq.7 will be read,

$$T^\sigma = (L_{nw} + L_{ns}\cos\theta)\sigma^{nw} \tag{9}$$

In a local pore geometry, Eq.6 and Eq.9 can be expressed by the functions of r_c, so the equilibrium state in Eq.4 can be implicitly described by r_c:

$$\sum F(r_c) = F^p(r_c) + T^\sigma(r_c) = 0 \tag{10}$$

Function of $\sum F(r_c)$ is monotonic; the value boundary of r_c can be obtained by following the geometry of pore throat. Therefore, r_c can be solved by numerical technique. Finally, P_e^c can be determined by Eq.5.

Drainage and entrapment of W-phase

Each tetrahedral pore has four neighboring pores, thus the coordination number in 3-D is four. In order to explain the invasion logic of our model, herein we project the system of 3-D network to a 2-D lattice mapping (see Figure 3). Pore bodies and throats are represented by squares and line bondings respectively. Different flags are assigned to the pores for tracking the flow path, which can dynamically record the pore states and the connectivity of different regions with the reservoirs. A search algorithm is employed for updating those states during invasion.

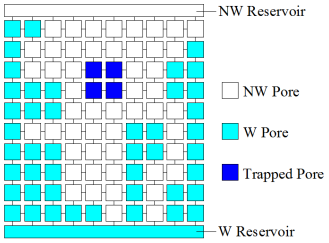

Figure 3. **Demonstration of NW-phase invasion and W-phase trapping in network (in 2D mapping for clarify).**

Initially, the porous media is saturated, and the top and bottom boundaries are connected to NW and W reservoirs, respectively. The effect of gravity is ignored. Drainage starts by increasing the capillary pressure P^c, in which we increase the local pressure of NW reservoir P^n and keep local pressure of W reservoir P^w constant. A search is executed on the pore throats which are connecting with NW reservoir, to locate the easiest entrance for invasion. The first phase displacement, or referred as Haines jump, happens when local P^c surpasses the minimum threshold, e.g. the local entry capillary pressure $P_e^c(i)$ of pore unit *i*. After pore *i* being drained, a second judgment is performed on the neighbor pore of *i*, e.g. pore *j*. If P^c is also larger than $P_e^c(j)$, pore *j* will be drained as well. Such NW-phase percolation will be performed until no more pores can be drained. Then a new equilibrium is achieved, and the state flags are updated for next step of drainage. So the Haines jump events maybe not only displace the W-phase pore-by-pore, but could also involve pore clusters. Such discontinuous changes of the W-phase content can also be verified by experimental tests (Prodanovic & Bryant 2006).

As the NW-phase is invading, the W-phase maybe forms clusters which are disconnected with the W reservoir. We propose the model being in a quasi-static regime, so the entrapped W-phase will remain stationary even if local P^n is growing. The evacuation of pore unit is hypothesized to be binary; therefore, the trapped W-phase will be the only factor that affects residual saturation. In order to identify these entrapment events, a dynamic search rule is employed during each step of drainage by assigning a Trapped Pore flag (as seen in Figure 3).

In the model, W-phase is assumed to be incompressible, so the geometry of trapped cluster will remain unchanged ever since it forms. According to Equ.(2), P^c will also remain the same because of unchanging of NW-W interfacial curvature. Therefore, P^w of trapped W-phase will grow along with the increasing of local P^n. Since the disconnections of different regions may happen on time sequential, P^w of trapped clusters will show diversity.

Boundary conditions

In our model, the evolution of NW-phase invasion is considered to be a finite-size problem, thus we only focus our interest on the case of non-periodic boundary condition (NPBC). Although the Regular Triangulation operation in PFV scheme is able to achieve the network with periodic boundary condition (PBC), the related study will be deferred to our further publication. In NPBC scenario of PFV model, the boundaries are in the form of spheres with near-infinity radii for obtaining the triangulation procedure. Thus, there are no new special cases of plane geometry that are introduced in the model, and all equations and algorithms presented in previous sections can be utilized for boundaries.

We assign top and bottom boundary layers of pore units connecting with NW and W reservoirs, respectively, in which case the state flags of those pores will not change during invasion. Correspondingly, the calculation of saturation will not involve the volume of these boundary pores.

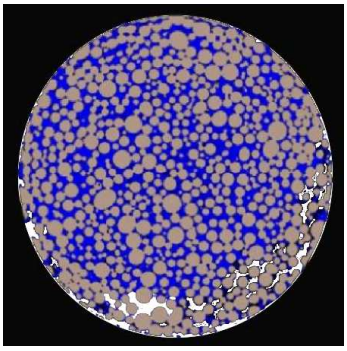

Figure 4. **Experimental scan through the cross-section of glass beads column by G. Khaddour. Brown (gray) circle regions are glass beads, blue (dark) regions are water, and white regions are air. See color version of this figure in the HTML.**

Another consideration in NPBC is the connectivity of side boundary pores, i.e., the sides are assumed to be open or closed. In the usual case, the porous medium is located in a regular container in the experimental test, so the side pore throats are open, or referred as a permeable boundary condition. The pores contacting with side boundary of container can be drained much easier than inside ones, in which case early Haines jumps can be observed in side domain, because the side boundary pore, which is composed by solid particles and smooth container wall, has relatively larger pore throat and the P_e^c trend to be smaller. This priority of invasion event has been verified by experiment test (Khaddour 2012). As shown in Figure 4, the NW-phase firstly penetrates into the void between glass beads and the container, and then invades the pores composed by glass beads. It is worthwhile to note that this percolation sequence is only adapted to spherical granular material test. If the drainage experiment is operated with irregular shape porous media, the composition of side pores will be different, and the priority of invasion needs further discussion. In some special cases, the side pore throats are closed, corresponding to an impermeable boundary condition, which means there is no fluid exchange between the side voids and the porous media. The different side boundary conditions can significantly influence the drainage patterns and residual saturation (Chandler et al. 1982). Therefore, to accommodate different scenarios, we perform both of situations, named open-side drainage and close-side drainage. In open-side drainage, NW-phase can go through the space between porous medium and side boundary of container (corresponding to a permeable boundary condition); while in close-side drainage, the Haines jump can only happen inside the porous medium (corresponding to an impermeable boundary condition). The calculations of saturation are adapted to different scenarios as well.

Implementation

The network by using Regular Triangulation, which is based on PFV scheme (Chareyre et al. 2012), has been implemented in C++. The C++ library CGAL (Boissonnat et al. 2002) is used for the regular triangulation procedure. Geometry for determination of entry capillary pressure and local drainage rules are also implemented in this model with C++. This pore-scale network is freely available as an optional package of the open-source software Yade (Smilauer et al. 2012).

The CGAL library insures exact predicates and constructions of network. The only nontrivial operation is the computation of entry phase curvature needed to define the NW-W phase contact lines and pore throat areas to determine acting forces in Equ.(10). As mentioned in previous section, open-side and close-side drainage modes are assigned according to optional side boundary conditions.

COMPARISON WITH EXPERIMENT

Numerical setup

In this section, we verify the pore-network model by comparing the simulation results with experimental data of quasi-static drainage experiment in a synthetic porous medium (Culligan et al. 2004). The medium consisted of packed glass beads, which are contained in a column of 70 mm in length and 7 mm in diameter. The particle size distribution (PSD) of glass beads is given in Table.(1), with a porosity of 0.34. Drainage is carried out by pumping water out of the porous medium with a certain flow rate to maintain the system to equilibrate. A 5 mm section of the column is imaged by using X-ray micro-tomography to obtain capillary pressure-saturation ($P^c - S^w$) relationship.

Weight(%)	Diameter(mm)
30	1.0-1.4
35	0.850
35	0.600

Table 1. **Particle size distribution of porous medium**

In the simulation, it's unachievable to assign the pore-network (Regular Triangulation) in geometry of circular column, so we compromise by implementing model in cuboid packings. Following the experimental scene, the simulation packing is connected to the NW reservoir on the top, and to the W reservoir at the bottom. However, the scanned domain emulated by our model is only a small part of a large column, in which case the assumption of connection between pore units of top layer and NW reservoir boundary is still ambiguous. Because for low capillary number, flow in porous medium is dominated by capillary forces, leading to capillary fingerings regime in the column. Thus in the scanned domain, the scope of connectivity between pores of top layer and NW reservoir is unclear. We can assume only some big pores connecting with invading phase reservoir or all of them involving this connection. Both of the hypotheses are reasonable if we only plan to simulate part of the volume or sections of experimental tests, but the results will be significantly different. The similar numerical comparison and conclusions can also be found in Joekar-Niasar et al. (2010). To extricate this predicament, we implement the simulation in a slightly larger size of container. The scanned region of data analyzed in experiment are 4.522 mm, 5.117 mm and 4.964 mm in the x, y and z direction, and the average grain size for the distribution of beads is 0.8675 mm. We assign the simulation in a cuboid packing with 7 mm in side length, in which 800 spheres are distributed randomly, assuming the pores of top boundaries are all connected with invading phase reservoir. But the quantitative study of $P^c - S^w$ relationship is only manipulated on the cuboid sub-domain with 5 mm in side length. The connectivity between sub-domain and reservoir is locally determined by the pore geometry. According to the setup of experiment, we suppose the NW-phase can invade from side boundary, thus open-side drainage mode is assigned.

In the research, we couldn't manage to achieve the original positioning data of glass beads in benchmark experiment. But the porous medium with target PSD and porosity can be easily emulated by using our DEM software by the growth of spheres after randomly positioning, using the radius expansion-friction decrease (REFD) growth algorithm of (Chareyre et al. 2002). So we compromise to simulate a series of repeated test on different randomly positioning packings with the consistent PSD and porosity of the experiment. In order to compare conveniently with all simulation cases, the simulation results and experiment data are both normalized to be dimensionless quantities. We represent the capillary pressure P^c by,

$$P^* = \frac{P^c \overline{D}}{\sigma^{nw}} \tag{10}$$

in which, $\overline{D}$=0.8675 mm is the average size for PSD, σ^{nw} = 7.28 × 10−2N⁄m is the W-phase (water) surface tension in contact with NW-phase (air) in 20 ^{o}C. We also assume the material of solid particles is perfectly wetting, so the contact angle θ in simulation is 0.

Comparison results and discussion

Using the technique described above, we compute the primary drainage process of 100 randomly positioning packings with the same PSD and porosity. Figure 5 presents the results of these simulations, in which we gather all scattered (S^w, P^*) points of each simulation in one image. As shown in Figure 5, although all packings share the same macro-mechanics parameters, the $P^c - S^w$ curves still have a distinct variety because of micro setup, i.e., sphere positioning. Especially, the residual saturation has a great difference. This erratic dispersion can be reduced by enlarging the simulation scales. The (P^c, S^w) variables associating with the representative elementary volume will be deferred to our further publication. We compare the average results from 100 repeating simulations with the experimental data. It shows satisfactory agreement between predicated capillary curve and obtained experimentally by Culligan et al. (2012). The unremarkable difference is mainly caused by the different specimen shapes, i.e., the simulation using cuboid column packing and experiment using circular column one.

We capture one test from the series of simulation and cut a slice to observe the characteristics of invasion as shown in Figure .6. By increasing P^c, the invasion starts from the pores with larger throat, in which the entry capillary pressure is smaller (see slice (a)). As described in previous section, the P_e^c of side pore throats usually relative smaller than that of inside pore throats, so the NW-phase invade from side pores first (as shown in Figure 6(a) and (b)). By comparing slices (b) and (c), we can find out that at certain circumstances even a slight changing in P^c can cause a notable NW-W interface movement. So such event, i.e., Haines jump, can involve a cluster of pores, causing a obvious discontinuous decrease of W-phase content. In slice (d) showing the finish of test, even under a large P^c, there is no changing in saturation, which means such W-phase is entrapped by NW-phase.

In the model, it's assumed that the W-phase transport by film flow or evaporation is negligible, so even if we keep increasing local P^c, the trapped W-phase will stay stationary. As explained in previous section, the trapping events happen in sequentiality, and the W-phase is supposed to be incompressible, thus the inner wetting pressure P^w of different trapped cluster show a diversity as shown in Figure 7. From the pressure distribution, we can

determine the order of occurrence of disconnections, in which the larger trapped P^w means the earlier happening of entrapment.

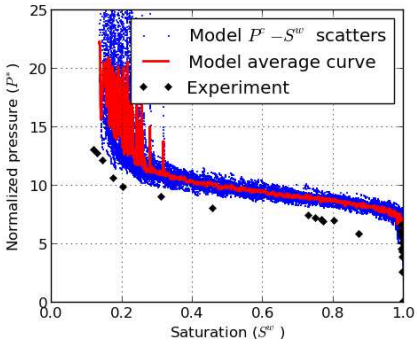

Figure 5. **Comparison between simulation and experiment for primary drainage $P^c - S^w$ curves. The No. of observations of simulation is 100.**

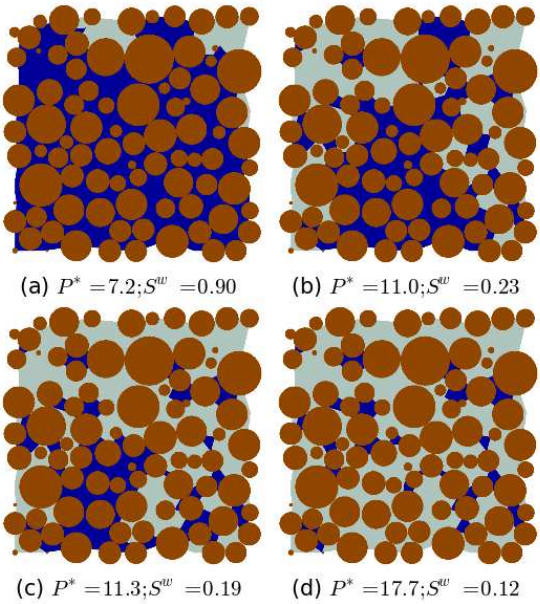

Figure 6. **The process of drainage (800 particles), NW-phase invade from top. Brown (gray) is solid phase, blue (black) is W-phase, and light cyan (white) is NW-phase, see color version of this figure in the HTML.**

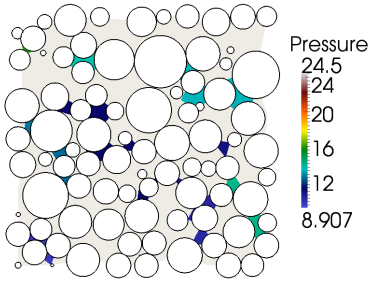

Figure 7. **Distribution of capillary pressure. White circle is solid, light region is NW-phase pressure P^n, dark regions are W-phase pressures P^w, see color version of this figure in the HTML.**

CONCLUSION

A pore-scale network model of quasi-static two-phase flow in dense sphere packings has been proposed. The model can satisfactorily replicate the phenomenon of primary drainage in synthetic porous medium. The pore space is efficiently represented by means of a Regular Triangulation and the entry pore throat geometry is mathematically determined by the equilibrium of the pore system. The key methods of this model are the calculation of the entry capillary pressure applied by the fluids and the prediction of the displacements of phases. Expressions of the local capillary force and tension force induced on the NW-W interface of pore throat have been derived, which are based on Young-Laplace equation and local pore geometry. The definition of entry capillary pressure is based on MS-P (Mayer-Stowe-Princen) method, which follows the balance of forces for NW-W interface in quasi-static regime. The drainage process is represented by the invasion of NW-phase when the threshold value is reached.

One key feature of the model is its capability to entrap the receding W-phase, indicating the residual saturation. A dynamic search algorithm is applied to identify whether local disconnection causes large clusters of wetting pores to get disconnected with wetting phase reservoir. Another key feature is its optional side boundary condition. To accommodate different experimental situations, the pore throats of side boundary can be considered open or closed, corresponding to the permeable or impermeable boundary conditions. For validation purpose, the model has been used for simulating primary drainage experiments carried out in a glass bead packing. The simulated $P^c - S^w$ curve is in agreement with experiment one, which means the capability of the pore-scale network model for simulating a real porous medium can be verified.

ACKNOWLEDGEMENTS

The authors want to acknowledge G. Khaddour and S. Salager for discussions and sharing us the experimental images, and G.Viggiani for suggesting this cooperation work.

REFERENCES

Bear, J. 1972. Dynamics of fluids in porous media., American Elsevier, New York.

Boissonnat, J., Devillers, O., Pion, S., Teillaud, M. & Yvinec, M. 2002. Triangulations in cgal, *Computational Geometry: Theory and Applications* 22: 5–19.

Bryant, S. & Blunt, M. 1992. Prediction of relative permeability in simple porous media, *Phys. Rev. A* 46 : 2004–2011.

Bryant, S., King, P. & Mellor, D. 1993. Network model evaluation of permeability and spatial correlation in a real random sphere packing, *Transport in Porous Media* 11 (1): 53–70.

Catalano, E. 2012. A pore-scale coupled hydromechanical model for biphasic granular media, *Ph.D. thesis*, Grenoble INP.

Chandler, R., Koplik, J., Lerman, K. & Willemsen, JF. 1982. Capillary displacement and percolation in porous media, *Journal of Fluid Mechanics* 119: 249–267.

Chareyre, B., Briancon, L.& Villard, P. 2002. Theoretical versus experimental modelling of the anchorage capacity of geotextiles in trenches., *Geosynthetics International* 9 (2): 97–123.

Chareyre, B., Cortis A., Catalano E., & Barthelemy E. 2012. Pore-scale modeling of viscous flow and induced forces in dense sphere packings, *Transp. Porous Med.* 92: 473–493.

Cundall, P. & Strack, O. 1979. A discrete numerical model for granular assemblies, *Geotechnique* (29): 47–65.

Culligan, K., Wildenschild, D., Christensen, B., Gray, W., Rivers, M., & Tompson, A. 2004. Interfacial area measurements for unsaturated flow through a porous medium, *Water Resour. Res.* 40 (12).

Dong, H. & Blunt, M. 2009. Pore-network extraction from micro-computerized tomography images, *Phys. Rev. E* 80: 036307.

Dullien, F. 1992. Porous Media: Fluid Transport and Pore Structure, Academic, San Diego, Calif.

Edelsbrunner, H. & Shah, NR. 1996. Incremental topological flipping works for regular triangulations, *Algorithmica* 15 (6): 223–241.

Fatt, I. 1956. The network model of porous media, *Trans AIME* 207: 144–181.

Gladkikh, M. & Bryant, S. 2003. Prediction of interfacial areas during imbibition in simple porous media, *Advances in Water Resources* 26 (6): 609 –622.

Hilpert, M. & Miller, C. 2001. Pore-morphology-based simulation of drainage in totally wetting porous media, *Advances in Water Resources*. 24 (34): 243 – 255.

Joekar-Niasar, V., Prodanovic, M., Wildenschild, D. & Hassanizadeh, S. 2010. Network model investigation of interfacial area, capillary pressure and saturation relationships in granular porous media, *Water Resour. Res.* 46.

Khaddour, G. 2012. Microscopic mechanisms related to water retention in sand, *Master's thesis*, Universite Joseph Fourier Grenoble.

Lenormand, R. 1990. Liquids in porous media, *Journal of Physics: Condensed Matter* 2 (S): SA79.

Lenormand, R., Touboul, E., & Zarcone, C. 1998. Numerical models and experiments on immiscible displacements in porous media, *Journal of Fluid Mechanics* 189: 165–187.

Ma, S., Mason, G. & Morrow, N. 1996. Effect of contact angle on drainage and imbibition in regular polygonal tubes, *Colloids and Surfaces A: Physicochemical and Engineering Aspects* 117 (3): 273 – 291.

Mason, G. 1971. A model of the pore space in a random packing of equal spheres, *Journal of Colloid and Interface Science* 35 (2): 279 – 287.

Mayer, R. & Stowe, R. 1965. Mercury porosimetrybreakthrough pressure for penetration between packed spheres, *Journal of Colloid Science* 20 (8): 893 – 911.

Øren, P., Bakke, S., & Arntzen, O. 1998 Extending predictive capabilities to network models, *SPE Journal* 3 (4): 324–336.

Princen, H. 1969. Capillary phenomena in assemblies of parallel cylinders: Ii. capillary rise in systems with more than two cylinders, *Journal of Colloid and Interface Science* 30 (3): 359 – 371.

Prodanovic, M. & Bryant, S. 2006. A level set method for determining critical curvatures for drainage and imbibition, *Journal of Colloid and Interface Science* 304 (2): 442 – 458.

Scholtes, L., Hicher, P., Nicot, F., Chareyre, B. & Darve, F. 2009. On the capillary stress tensor in wet granular materials, *Int. J. Numer. Anal. Meth. Geomech.* 33 (10): 1289–1313.

Stark, CP. 1991. An invasion percolation model of drainage network evolution, *Nature* 352 (6334): 423–425.

Smilauer, V., Catalano, E., Chareyre, B., Dorofeenko, S., Duriez, J., Gladky, A., Kozicki, J., Modenese, C., Scholtes, L., Sibille, L., Stransky, J. & Thoeni, K.. 2010. Yade Reference Documentation, *Yade Documentation*. http://yade-dem.org/doc/.

Numerical modelling of the localized fluidization in a saturated granular medium using the coupled method DEM-PFV

Marcella Toraldo
University of the study of Salerno, Italy
CNRS, 3SR, F-38000 Grenoble, France
m.toraldo@studenti.unisa.it - marcella.toraldo@3sr-grenoble.fr

Bruno Chareyre, Luc Sibille
Université Grenoble Alpes, 3SR, F-38000 Grenoble, France
CNRS, 3SR, F-38000 Grenoble, France
Bruno.chareyre@3sr-grenoble.fr luc.sibille@3sr-grenoble.fr

ABSTRACT

We present the numerical results of the progressive fluidization of a saturated granular medium under the effect of a localized upward flow injected from its base. The numerical model used, is based on the coupling between a discrete element model (DEM) for the solid phase and a finite volume method defined at pore scale (PFV) to solve the interstitial fluid flow. By simulating an increase of the injected flux, different regimes are successively observed in the sample: a static bed regime, a dilatation one, a fluidized cavity (that does not open op to the top surface of the granular bed), and finally the fluidization of the total height of the granular specimen inside a fluidized chimney.

INTRODUCTION

The purpose of this study is to simulate numerically the localized fluidization in a saturated granular medium using the coupled method DEM-PFV implemented in YADE code. The numerical model DEM-PFV (Catalano *et al.*, 2014; Sari *et al.*, 2011; Tong *et al.*, 2012), is a micro-hydromechanical model for granular materials that combines the discrete element method for the modelling of the solid phase and a pore-scale finite volume formulation for the flow of an incompressible pore fluid. The numerical results of the progressive development of a fluidized zone, under the effect of a localized upward flow injected at the bottom of the bed, are presented in this paper. Gradually, increasing the injected flux, different regimes are successively observed in the sample: static bed, dilatation, fluidized cavity that doesn't open

up to the top surface of the granular bed, and finally fluidization of the total height of the granular specimen inside a fluidized chimney. The simulations are conducted by increasing the injected flux by steps and computing, in the simulation time, values of excess of pressure at the injection point, height of the fluidized zone and height of the specimen. The possibility to represent the results in terms of dimensionless parameters has been investigated by performing simulations with samples constituted with different particle sizes. The two dimensionless graphs are obtained. The first shows the evolution of the normalized excess of pressure with the normalized flux and permits to evaluate the ranges of normalized values of flux for which the different regimes occur. The second shows the evolution of the normalized height of the cavity with the normalized flux and allows to compare the numerical results obtained with some previous experimental results from the literature.

THE SIMULATION

Characteristics of the sample

The sample of dimensions 0.60×0.32×0.10 m (width × height × depth) is constituted by 2000 spherical particles with a mean radius of 0.01125 m, representing the solid phase (Figure 1). All the geometrical and mechanical characteristics of the specimen are reported in the Table 1.

Table 1. Geometrical and mechanical characteristics of the sample

Characteristics of the sample		
Width (w)	[m]	0.60
Height (H_0)	[m]	0.32
Depth (d)	[m]	0.10
Spheres nb.	[-]	2000
Mean radius (r_m)	[m]	0.01125
Porosity (n)	[-]	0.38
Density of the solid phase (ρ_s)	[kg/m^3]	2600
Dynamic viscosity (μ)	[Pa.s]	0.01
Contact friction	[°]	10
Normal contact stiffness ($k_n/2r_m$)	[Pa]	400000
Ratio shear/normal stiffness (k_s/k_n)	[-]	0.5

With respect to the boundary conditions imposed, the sample is constrained only on the bottom edge and not on the top. Periodic conditions are imposed on vertical sides for the particles and for the fluid. It means that, under the action of the flow, the particles at the top of the sample are free to move and those going out from one of the vertical face of the box, come back into the opposite face. This saturated sample is used to investigate, at pore scale, the effects of the fluidization resulting of the injection of an upward flux at the middle of the bottom face of the specimen (Figure 1). In particular, excess of pressure at the injection point, height of the fluidized zone, and height of the specimen are numerically determined in the simulation time from the imposed values of flux.

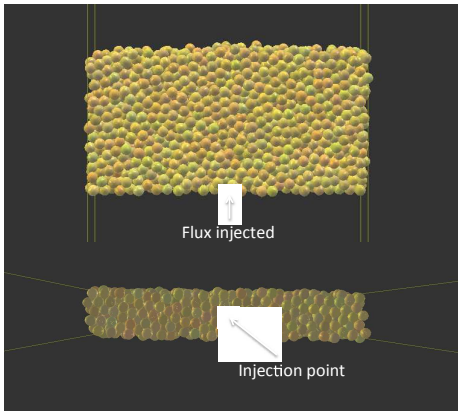

Figure 1. Injection point - the upward flux is injected in the middle of the bottom of the sample

UPWARD INJECTED FLUX

The simulations are conducted increasing the upward injected flux from an initial value of 0.0001 m^3/s, till 0.0261 m^3/s with increments of 0.001m^3/s (27 steps). The Figure 2 shows the evolution of the imposed flux (q) and of the computed excess of pressure (p) at the injection point. The excess pressure is given by the difference between the total pressure (p^{tot}) and the hydrostatic pressure: $p = p^{tot} - \rho \cdot g \cdot z$. Each step needs of a large number of iterations depending on the flow rate value in order to reach an established state of the sample. For low values of injected flux, the pressure presents a peak just after the increase of the injected flux but reaches quickly a constant value considered as the established regime. However for larger values of injected flux the pressure needs more time to reaches an established regime. Therefore, the larger the flux is, the higher the number of iterations is to reach an establish regime and to characterize the sample behaviour for this flux.

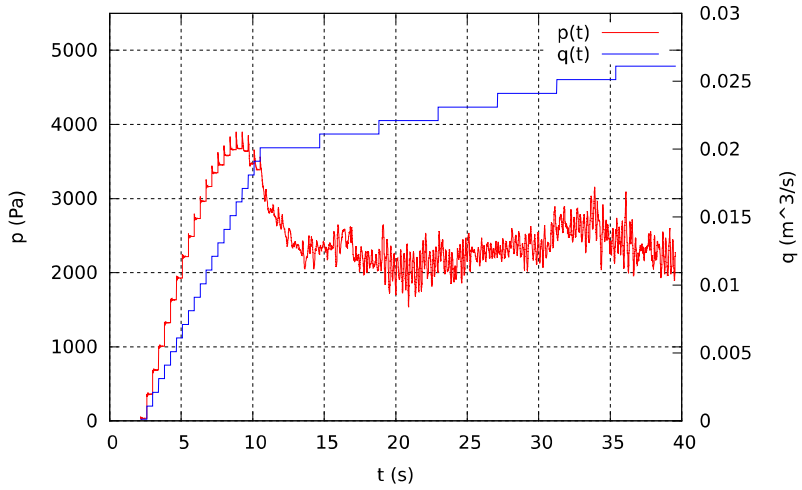

Figure 2. Evolution of the pressure in the time when the flow rate is increased from 0.0001 m^3/s, till 0.0261 m^3/s with increments of 0.001m^3/s (27 steps)

THE NUMERICAL RESULTS

The regimes

The numerical results obtained show a progressive development of a fluidized zone in a bed of grains, immersed in a liquid, under the effect of a localized upward flow injected at the bottom of the bed. It is seen that, gradually, by increasing the injected flux, four regimes are successively observed in the sample depending on the flow rate transiting through the injection point: (i.) Static regime: the granular layer remains immobile during the entire sequence with an imposed flow rate; (ii.) Dilatation regime: the sample dilates but does not develop a fluidized zone; (iii.) Cavity regime: a fluidization zone develops just above the injection point (Figure 3) and like a bubble, moves up and down along the central part of the sample but does not reach the top of the sample. Only the grains into the cavity are in movement; (iv.) Chimney regime: the fluidization zone quickly reaches the top of the sample thereby creating a chimney of fluidized grains

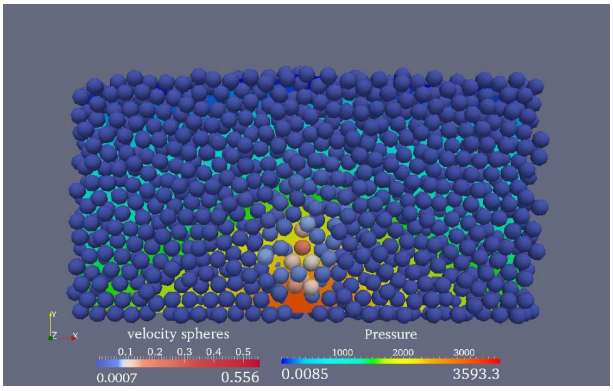

Figure 3. Development of the fluidized zone (t=13 s)

These regimes can be characterized by an estimation of the position, along the vertical axis, of the fluidized zone (height of the cavity). It will be zero in static regime and in dilatation regime, between zero and the height of the sample (H) in cavity regime and almost equal to H in chimney regime. Numerically, it is possible to represent the fluidized height in the time, through the highest position of the particles having a velocity higher than a threshold value (v_{lim}) opportunely chosen. The following graphs (Figures 4 and 5) show the evolution of the height of the cavity (h_f), of the height of the sample (H) and of the excess of pressure (p) for each injected flux step. These values correspond to average values over a given time period once the established regime has been reached. To discriminate the different regimes let us denote the following critical flow rate values: (i.) Q_{dil}: flow rate value from which there is a sample dilatation; (ii.) Q_{cav}: from this flow rate value the sample reaches the cavity regime ($h_f > 0$); (iii.) Q_{chim}: the height of the cavity reaches the height of the sample.

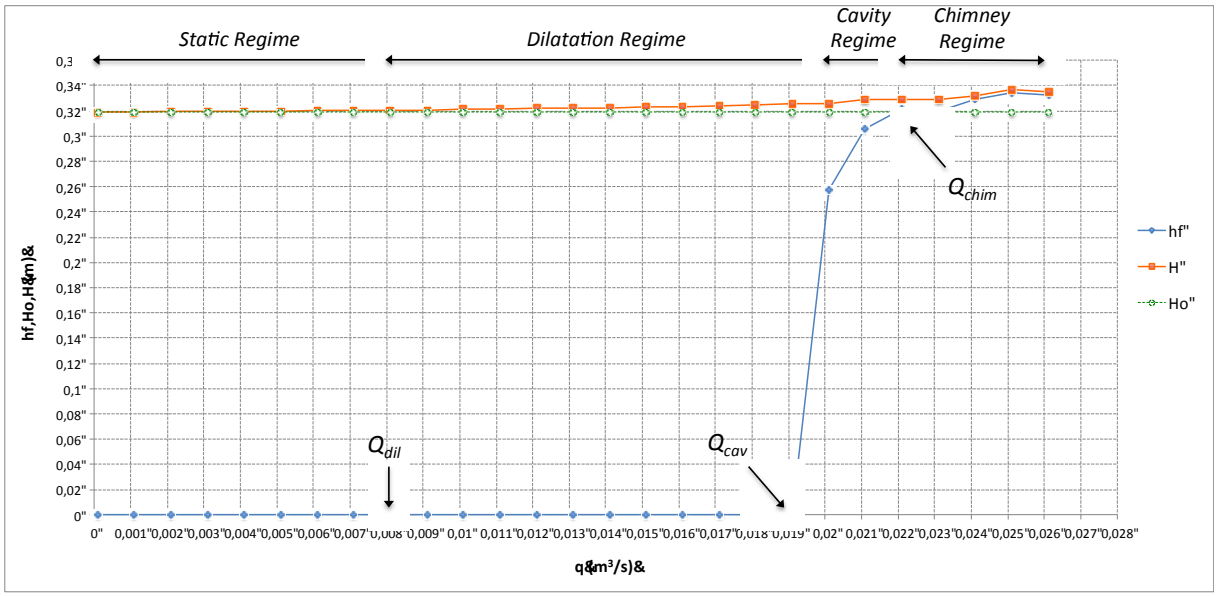

Figure 4. Evolution of the average value of the height of the cavity (h_f) and of the sample height (H) versus the injected flux (q) from 0.0001 m^3/s, till 0.0261 m^3/s

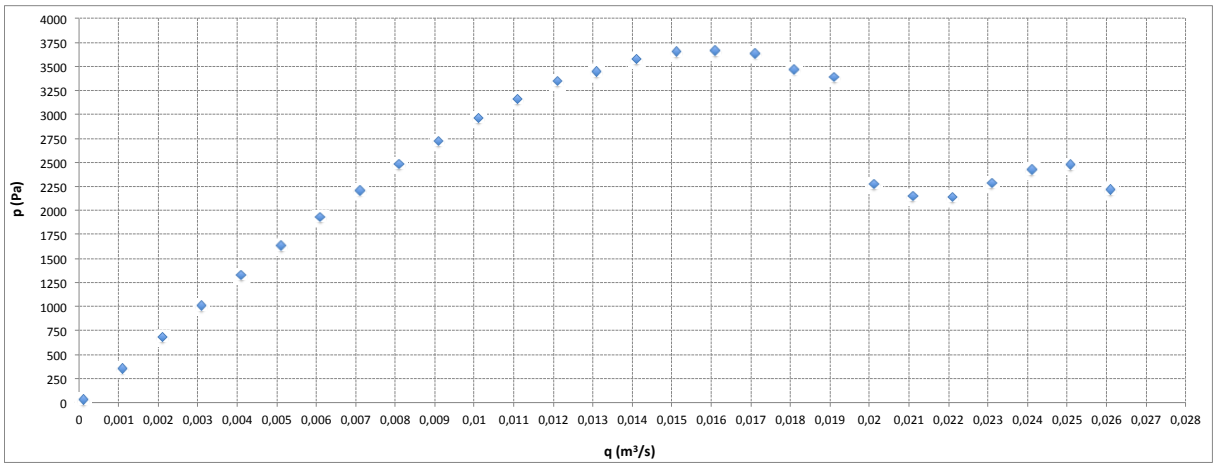

Figure 5. Evolution of the average value of the excess pressure (p) versus the injected flux (q) from 0.0001 m^3/s, till 0.0261 m^3/s

Interesting considerations can be done comparing the Figures 4 and 5. (i.) Static regime: for $0.0001 \leq q < 0.009$ m^3/s, the particles are statics and the pressure linearly grows with the flow. (ii.) Dilatation regime: for $0.009 \leq q \leq 0.016$ m^3/s, due to the decompression of the sample the pressure increases more slowly with increasing flow rate till a maximum value of 3671 Pa. It means that the hydraulic conductivity of the granular assembly, increase due to an increase of the porosity. For $0.016 < q < 0.019$ m^3/s the height of the sample increases more rapidly by increasing the flow rate causing an additional decompression of the sample; the pressure decreases until 3386 Pa. (iii.) Cavity regime: for $0.019 < q < 0.022$ m^3/s, with the formation of the fluidized zone the pressure drops quickly. (iv.) Chimney regime: for $q > 0.022$ m^3/s: when the fluidized zone reaches the top of the cavity, a convective motion is triggered, causes compression and decompression of the sample and consequently oscillatory pressure trend.

DIMENSIONLESS GRAPHS AND COMPARISON WITH THE EXPERIMENTAL RESULTS

Three samples (A,B,C) with different numbers of particles are considered (Table 2).

Table 2. Geometrical and mechanical characteristics of the samples A, B, and C

Characteristics of the samples				
		A	B	C
Width (w)	[m]	0.60	0.60	0.60
Height (H_0)	[m]	0.319	0.317	0.321
Depth (d)	[m]	0.10	0.10	0.10
N° spheres	[-]	2000	3000	4000
Mean diameter (d_m)	[m]	0.0225	0.0197	0.0179
Density of the solid phase (ρ_s)	[kg/m^3]	2600	2600	2600
Dynamic viscosity (μ)	[Pa.s]	0.01	0.01	0.01
Contact friction	[°]	10	10	10
Normal contact stiffness ($k_n/2r_m$)	[Pa]	400000	400000	400000
Ratio shear/normal stiffness (k_s/k_n)	[-]	0.5	0.5	0.5

For each sample, the injected flux is increased from an initial value of 0.0001 m^3/s till 0.0261 m^3/s with increments of 0.001m^3/s (27 steps), and the excess pressure in the middle of the bottom face of the sample is computed. Bigger is the number of the particles, smaller is their mean radius, smaller is the permeability of the sample; and bigger is the pressure computed at the bottom for a given value of injected flux. In the same way, the critical values the injected flux, for which the fluidized zone develops and reaches the top of the sample, are also different for the three specimens. By scaling the pressure, the flux and the height of the fluidized zone using respectively the coefficients α, β and δ, we define the following normalized parameters p/α, q/β, and h_f/δ.

$$\alpha = \rho_s \cdot g \cdot \frac{H_0^2}{D}\left[Pa\right]; \qquad \beta = \frac{\rho_s \cdot g \cdot H_0^2 \cdot D^2}{\mu}\left[\frac{m^3}{s}\right]; \qquad \delta = H_0\left[m\right].$$

Then two normalized graphs are plotted. The first (Figure 6) shows the evolution of the normalized excess of pressure (p/α) with the normalized flux (q/β). In this way it is possible to have ranges of normalized injected flux for which the four different regimes are observed: the static layer, the dilatation, the development of the fluidized cavity and the fluidization of the total height. The second dimensionless graph (Figure 7) shows the evolution of the normalized height of the cavity (h_f/δ) with the normalized flux (q/β) and permits to compare the numerical results obtained with the previous experimental ones conducted by Philippe and Badiane (2011, 2013), using a physical model. The scaled curves relatives to the numerical simulations of the samples A, B and C are not far from the scaled curve relative to the experimental results. The difference can be explained by the fact that the permeability of the numerical model may be slightly different from the one of the physical model (nothing has been done to tune the numerical permeability) leading to slightly different values of flux.

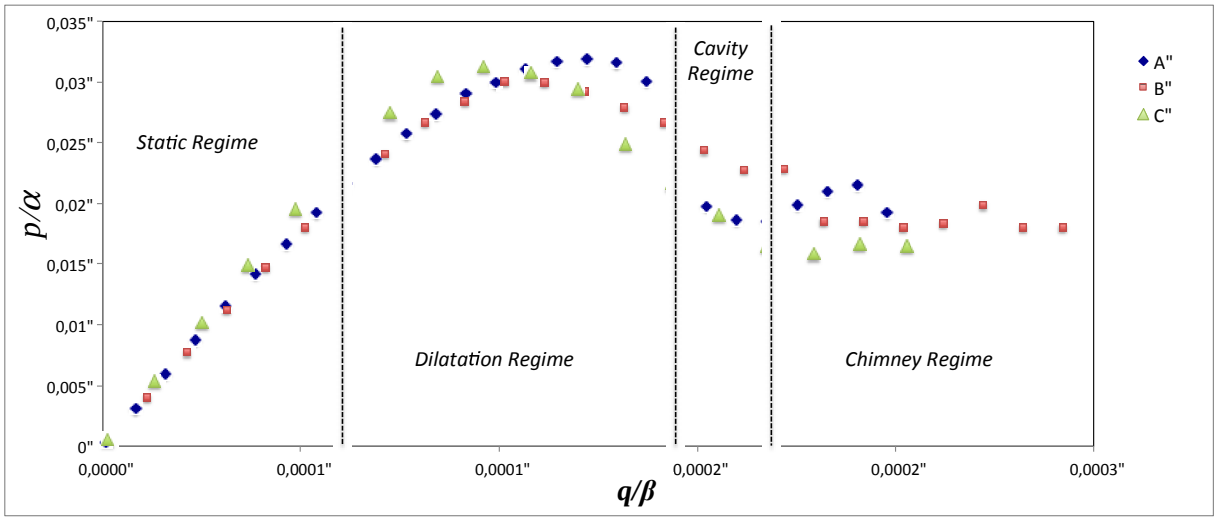

Figure 6. Evolution of the normalized excess of pressure (p/α) with the normalized flux (q/β)

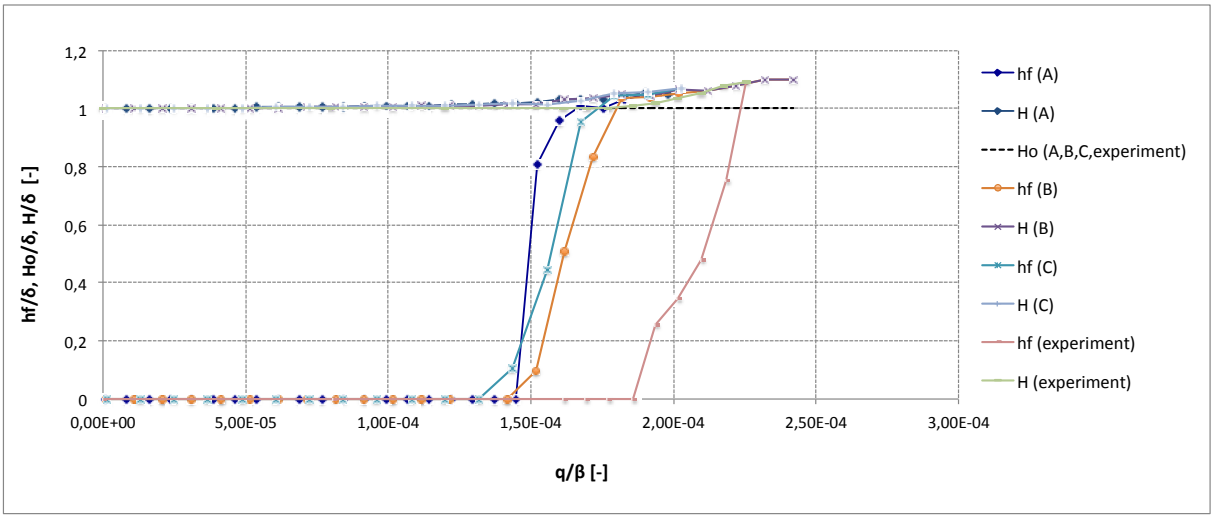

Figure 7. Evolution of the normalized height of the cavity (h_f/δ) with the normalized flux (q/β)

CONCLUSION

Numerical simulations of the localized fluidization in a saturated granular medium have been presented. The numerical results show the progressive development of different regimes inside the sample, depending on the increasing injected flux transiting through the injection point, in agreement with the experimental results. The qualitatively comparison of the phenomenon observed experimentally and simulated numerically is satisfactory; the comparison via dimensionless graph shows that the numerical results are not far from those obtained by Philippe and Badiane (2011, 2013) using a physical modelling. It means that the coupled model DEM-PFV used in this study, is able to simulate the phenomenon in object. However the work is not finished, more investigations are needed to better analyse quantitatively the problem using smaller particles, and computing stress and deformation in the sample. In addition, in the current configuration of the numerical model the size of the injection hole is dependent on the size of the particles. We think this particular configuration has an effect on the scaling of the parameters of the problem (such as the introduction of the

size of the particles in the scaling of the pressure). This should be corrected by defining an injection hole independent of the particle size.

REFERENCES

P. Philippe and M. Badiane (2013). Localized fluidization in a granular medium. *Physical Review* E 87; DOI:10.1103/PhysRevE.87.042206

P. Philippe and M. Badiane (2011). Chimney of Fluidization and "Sandboil" in a Granular Soil. S. Bonelli et all (eds.), *Advances in Bifurcation and Degradation in Geomaterials* -Proceedings of the 9th International Workshop on Bifurcation and Degradation in Geomaterials- Springer Series in Geomechanics and Geoengineering 11: 125-129; DOI:10.1007/978-94-007-1421-2_16

E. Catalano, B. Chareyre and E. Barthélémy (2014). Pore-scale modeling of fluid-particles interaction and emerging poromechanical effects. *International Journal for Numerical and Analytical Methods in Geomechanics* 38:51–71; DOI: 10.1002/nag.2198

H. Sari, B. Chareyre, E. Catalano, P. Philippe and E. Vincens (2011). Investigation of internal erosion processes using a coupled DEM-fluid method. *II International Conference on Particle-based Methods* – Fundamentals and Applications PARTICLES 2011 E. Oñate and D.R.J. Owen (Eds.)

A.-T. Tong, E. Catalano and B. Chareyre (2012). Pore-Scale Flow Simulations: Model Predictions Compared with Experiments on Bi-Dispersed Granular Assemblies. *Oil & Gas Science and Technology* – Rev. IFP Energies nouvelles 67(5):743-752; DOI: 10.2516/ogst/2012032

Description of the mechanical degradation of soils subjected to an internal erosion process by suffusion

R. Aboul Hosn, L. Sibille, B. Chareyre
Univ. Grenoble Alpes, 3SR, F-38000 Grenoble, France
CNRS, 3SR, F-38000 Grenoble, France
rodaina.aboulhosn@3sr-grenoble.fr
luc.sibille@3sr-grenoble.fr
bruno.chareyre@3sr-grenoble.fr
and
N. Benahmed
IRSTEA d-Aix-en-provence, Aix-en-provence, France
nadia.benahmed@irstea.fr

ABSTRACT

Seepage-induced erosion, resulting from soil particle migration, is widely observed in both natural soil deposits and artificially engineered fill structures. It is considered as one of the causes for the dysfunctions of earthen structures, as dams. This of which could have catastrophic consequences. In this paper we will present a particular case of internal erosion called suffusion. A literature review on some experimental as well as numerical approaches is presented. Furthermore, the methodology to be followed in our study in order to analyze the process of suffusion is explained.

Keywords: Suffusion, DEM, granular material, micro-structure

INTRODUCTION

The description of internal erosion, in particular ‘‘suffusion’’ phenomenon, constitutes a strongly coupled fluid-solid problem. During the suffusion process, fine particles are detached from the soil structure by interstitial flow leaving behind the granular skeleton. Thus by modifying the microstructure of soil through the evacuation or displacement of fines, suffusion can induce locally some mechanical degradations of the soil, which under a constant external mechanical load may present some deformations. These deformations may lead on one hand to the modification of the pore spaces, thus resulting in obvious changes in the porosity and the hydraulic conductivity, and on the other hand, suffusion may lead to the loss of the mechanical resistance of the soil thereby leading to rupture.

The hydrological mechanisms of internal erosion has been widely investigated. Changes in the hydraulic gradient and in the hydraulic conductivity, as well as the loss in fine particles, were the primary concerns. Experimental researches have also indicated that changes in the fine content may either cause a decrease or an increase in the soil strength. Therefore the soil behavior seems to be dependent on the range of fine contents, which may possibly explain the changes in the soil strength after internal erosion.

In this paper, we will present some of the studies, experimental and numerical, done to analyze the process of suffusion and to understand the behavior of soils in such cases. Moreover, the methodology that will be followed in our research work is presented.

LITERATURE REVIEW

Internal erosion occurs due to different factors which can have major consequences on the mechanical properties of soil such as gradation, permeability, volumetric changes and shear strength. Different studies based on experimental as well as numerical approaches have been done to analyze soils sensibility to erosion. Some of these approaches are presented in this section.

Key factors leading to internal erosion

1. Soil gradation :

It is assumed that depending on the soil gradation different soil behavior will be noticed. For this purpose an experimental study done by Xiao & Shwiyhat (2012) investigated the influence of gradation on suffusion. They showed that gap-graded soils tend to produce more pronounced physical and geomechanical changes than poorly graded soils in which they present greater erosion rates, permeability and volume reduction. With the progress of erosion, subsequent clogging occurs leading to a decrease in the permeability rate until suffusion and particle migration stopped.

2. Hydraulic gradient:

Different studies have been done to investigate the influence of the hydraulic gradient on the suffusion process. Two values for the hydraulic gradients were identified by Chang & Zhang (2011) and Ke & Takahashi (2012): the initiation hydraulic gradient and the skeleton hydraulic gradient. The first corresponding to the onset of erosion (the mass of the eroded soil as well as the permeability start to increase slightly, but an equilibrium state can still be reached easily) and the second corresponding to the sudden increase in the erosion rate, soil permeability and deformations where sudden strain jumps were noticed due to the rearrangement of coarse particles to reach rapidly a new equilibrium position.

Chang & Xu (2012) realised that, from an initial state, with the increase of the hydraulic gradient until the initiation of internal erosion, the fine grains filling the voids start to erode, however at this stage the structure is still stable. But, with the progressive increase in the hydraulic gradient and the increase in erosion, the granular structure loses its lateral support and the force chains buckle which leads to sudden deformations.

DEGRADATION OF THE MECHANICAL PROPERTIES OF SOIL

a. Experimental approaches:

Several experiments have been established to describe the response of eroded soil samples. Analyzing post-erosion curve gradations, Chang & Zhang (2011), Ke & Takahashi (2014a, 2014b) showed that these curves move downward due to the fines loss (figure 1). Such new gradation can have major consequences on the soil behavior.

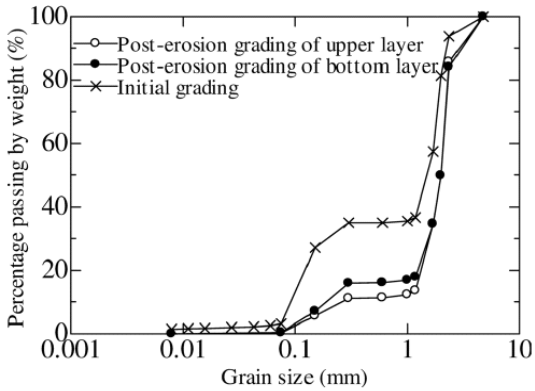

Figure 11: Post-suffusion grain size distribution
(Ke & Takahashi, 2014a, 2014b)

There are several experimental strategies that can be followed to investigate the influence of fines loss. One method is to develop a triaxial erodimeter apparatus, which can perform both erosion and triaxial tests. Another way is by preparing samples with different initial fines content and consider them representive of soils subjected to different degrees of erosion rates (i.e. without performing any real erosion process) then perform classical triaxial tests to check their mechanical behavior.

Ke & Takahashi (2014a), performed real erosion tests by following the first strategy. They used a newly developed triaxial apparatus and performed erosion tests on samples wth different initial fines content and they noticed that as the initial percentage of fines increases, both the percentage of cumulative fines loss and volumetric strain increases. Analyzing the stress-strain curves and the volumetric strain, they noticed that a percentage of fines corresponding to 25% shows a special behavior, in which it had almost same deviatoric stress as other samples of different fines content, but larger volumetric strains. They concluded in that case that the fines content of 25% signifies that fines almost occupy the voids of coarse grains and begin to separate the sand grains. Moreover, samples with higher initial fines content lead to an increase in the hydraulic conductivity as well as volumetric strains. In addition, specimens with the lowest fine content, which had the least void ratio, showed the

highest drained strength and least volumetric strain. On the other hand, Benahmed et al. (2014), followed the other strategy to analyze the process of erosion. It was noticed that even when the fine content is less than a threshold value, this doesn't cancel the role of fines which can still participate slightly in the strength of the soil sample. Moreover, it was noticed that samples with the higher fines content exhibited a slight increase in the shear strength. Concerning the volumetric strain, it was found very sensitive to the percentage of fines, in which the mixture becomes less contractive as the fines content increases. In addition little influence of fines was noticed on the critical strength. Furthermore, Benahmed et al. (2014) highlighted the importance of the intergranular void ratio for characterizing the triaxial response of soil samples with different fines content. It was found that the intergranular void ratio serves as a suitable parameter to describe the critical state.

Furthermore, analyzing the mechanical behavior of eroded soil, Chang & Zhang (2011) and Ke & Takahashi (2012) showed how the shear strength is significantly affected. It was concluded that after the internal erosion, the soil resistance decreases as shown in Figure 2.

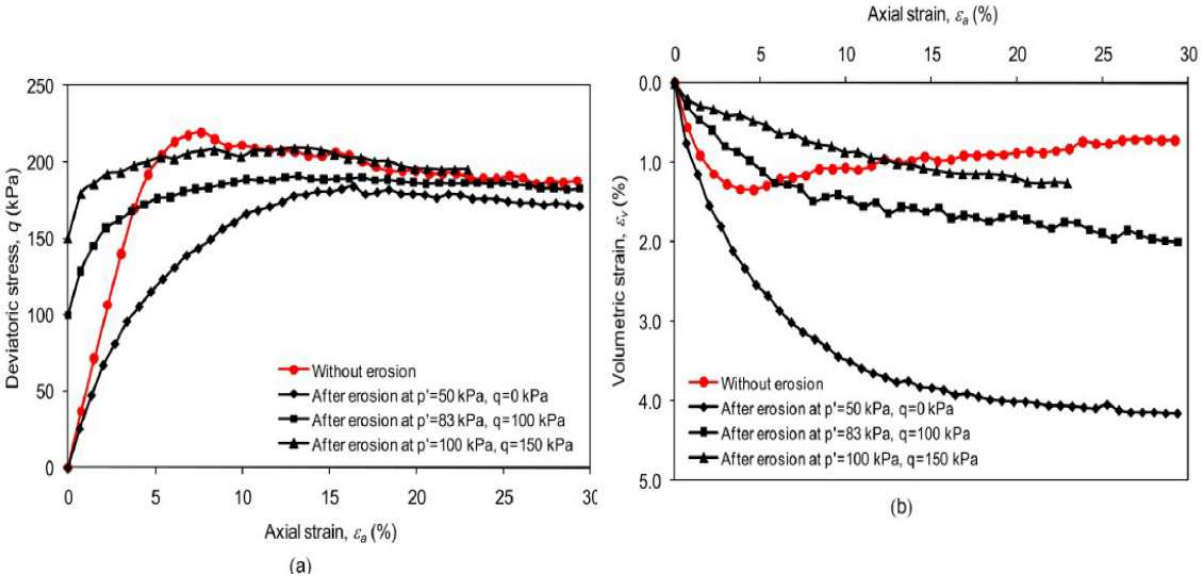

Figure 12: Stress-strain relationships without and with internal erosion under different initial stress conditions *(Chang & Zhang, 2011)*

b. Numerical approaches :

In addition to experimental approaches, several numerical approaches were also done to study the relation between the removal of soil particles and its consequences on the mechanical behavior. The studies presented here are based on the discrete element method (DEM).

Wood et al. (2008) and Scholtès et al. (2010) succeeded in presenting numerical approaches to analyze suffussion. Figure 3 shows that depending on the soil stress states from which internal erosion initiated, the soil either shows contractive behavior and stabilizes or dilative behavior and fails. The shear stress level at critical state appears to give the two different behaviors.

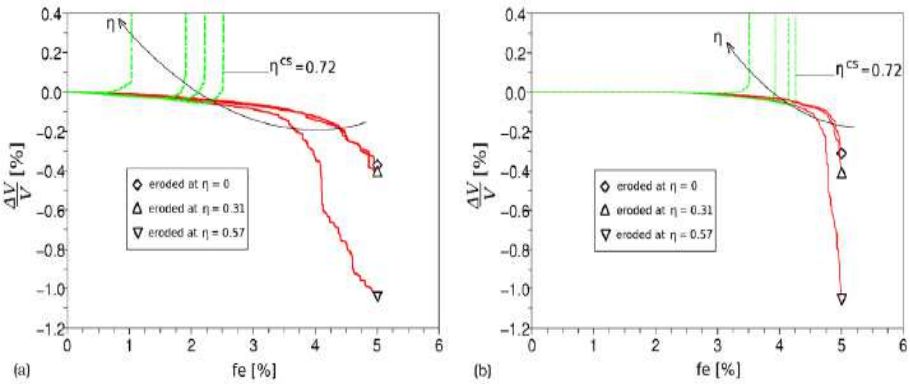

Figure 13: Volumetric strains as a function of extracted mass fe for particle removals performed at different mobilized frictions η = q/p. (a) size criterion only, (b) combined size and loading criteria. *(Scholtès, Hicher, & Sibille, 2010)*

It was also noticed, that the internal erosion process leads to the decrease in the shear strength, due to the decrease in the internal friction angle. (Figure 4)

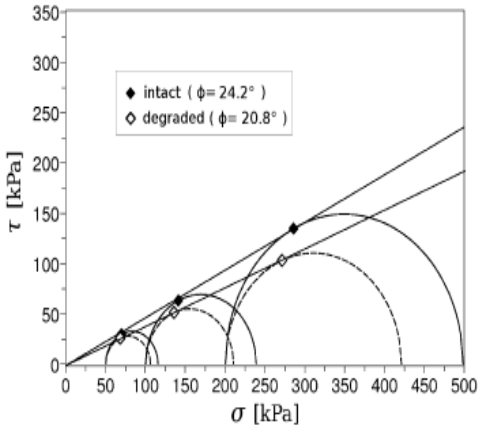

Figure 14: Mohr–Coulomb failure envelopes corresponding to the DEM numerical sample before and after particle extraction. *(Scholtès, Hicher, & Sibille, 2010)*

THE METHODOLOGY OF OUR STUDY

As can be deduced from the literature mentioned above, an abundance of work has been done to describe the degradation of the mechanical properties of soils subjected to suffusion. It was shown that such a description is complex because it depends on the granulometry, the micro-structural arrangement and other parameters. However, the phenomena of suffusion introduces heterogeneities in the soil structure, this which constitutes an obstacle in the interpretation of results. Futhermore, so far there are no clear relations established between the mechanical properties of the granular structure and a representative parameter of the degree of evolution of internal erosion by suffusion.

In an attempt to shed the light on these points, we planned to describe the mechanical response of a soil subjected to the process of suffusion taking into consideration the degradation of the microstructure through the following steps:

- First we will describe the degradation of the mechanical properties of soil and identify a relation with an appropriate parameter of the suffusion process. This will be done in the case of a homogeneous medium. For the experimental study, soil samples are created in the laboratory presenting a similar microstructure to that of the eroded soils by suffusion, except that these samples are considered homogeneous. These data will serve as a reference to the numerical approach which is based on DEM. Two options will be tested, either to reproduce numerically the experimental creation mode of the samples or to introduce in a numerical model a kinetic extraction of solid grains mimicking an erosion process by suffusion. From this first step, we will focus on analyzing the mechanical response of the initial state of the granular assembly, during degradation and after degradation. An initial law of degradation of the mechanical properties should be deduced from this first step.

- The second step will focus on taking into account the heterogeneities induced by suffusion in order to interpret the laboratory test results conducted on soil samples being effectively subjected to a process of erosion by suffusion. We will study the feasibility of achieving such laboratory tests and in case of difficulty we will depend on data from recent literature. Concerning the numerical modeling, either we maintain the DEM to reproduce the degradation in a heterogeneous manner or an alternative way may be to introduce the law of degradation in a finite element model and to work on the degradation parameter in a heterogeneous manner. This step will permit us to validate and refine the description of the degradation of these mechanical properties in real cases of erosion.

- The final step is to take into account the complete coupling from the fluid flow to the degraded mechanical behavior via the introduction of a law of erosion.

CONCLUSION

Experimental and numerical approaches were presented in this paper in order to study the effects of internal erosion by suffusion. It was noticed that gap-graded soils tend to produce more pronounced physical and geomechanical changes through high erosion rates. Moreover, fines content and the hydraulic gradient are considered key factors in this problem. It was shown that the mechanical behavior is significantly affected by the loss of fine particles. Finally, the methodology that will be followed in our study was presented which will allow us to describe the mechanical degradation of the soil subjected to suffusion.

ACKNOWLEDGEMENTS

The authors want to acknowledge the University of Grenoble Alpes, for providing the grant for our thesis.

REFERENCES

Benahmed, N., Nguyen, T. K., Hicher, P. Y., & Nicolas, M. (2014). An experimental investigation into the effects of low plastic fines content on the behaviour of sand/silt mixtures. *European Journal of Environmental and Civil Engineering*, (August), 54, 1–20. doi:10.1080/19648189.2014.939304

Chang, D. S., & Xu, T. H. (2012). Laboratory Investigation of Initiation and Development of Internal Erosion in Soils under Complex Stress States, 895–902.

Chang, D. S., & Zhang, L. M. (2011). A Stress-controlled Erosion Apparatus for Studying Internal Erosion in Soils. *Geotechnical Testing Journal*, *34*(6), 103889. doi:10.1520/GTJ103889

Ke, L., & Takahashi, A. (2012). Strength reduction of cohesionless soil due to internal erosion induced by one-dimensional upward seepage flow. *Soils and Foundations*, *52*(4), 698–711. doi:10.1016/j.sandf.2012.07.010

Ke, L., & Takahashi, A. (2014a). Experimental investigations on suffusion characteristics and its mechanical consequences on saturated cohesionless soil. *Soils and Foundations*, *54*(4), 713–730. doi:10.1016/j.sandf.2014.06.024

Ke, L., & Takahashi, A. (2014b). Triaxial Erosion Test for Evaluation of Mechanical Consequences of Internal Erosion. *Geotechnical Testing Journal*, *37*(2), 20130049. doi:10.1520/GTJ20130049

Scholtès, L., Hicher, P.-Y., & Sibille, L. (2010). Multiscale approaches to describe mechanical responses induced by particle removal in granular materials. *Comptes Rendus Mécanique*, *338*(10-11), 627–638. doi:10.1016/j.crme.2010.10.003

Šmilauer, E. Catalano, B. Chareyre, S. Dorofeenko, J. Duriez, A. Gladky, J. Kozicki, C. Modenese, L. Scholtès, L. Sibille, J. Stránský, and K. Thoeni, Yade Documentation (V. Šmilauer, ed.), The Yade Project, 1st ed., 2010. http://yade-dem.org/doc/.

Wood, D. M., Maeda, K., & Nukudani, E. (2008). Discrete element modelling of soil erosion, 491–496. Fourth International Conference on Scour and Erosion 2008

Xiao, M., & Shwiyhat, N. (2012). Experimental Investigation of the Effects of Suffusion on Physical and Geomechanic Characteristics of Sandy Soils. *Geotechnical Testing Journal*, *35*(6), 104594. doi:10.1520/GTJ104594

A hydromechanical coupled FEMLIP model in a visco-elasto-plastic framework

Zhaohua Li, Frédéric Dufour, Félix Darve
Laboratoire Sols, Solides, Structures, Risques, Grenoble, France
zhaohua.li@3sr-grenoble.fr, frederic.dufour@3sr_grenoble.fr, felix.darve@3sr-grenoble.fr

ABSTRACT

In this report, a unified model, presenting solid and fluid states of soil by using appropriate constitutive laws and a transition criterion in between, is recalled and expanded in the domain of unsaturated soil. Moreover, a stress-strain relationship is obtained from modified Van Genuchten's water retention curves, and applied into the finite element method with Lagrangian integration points. With some improvements, the new finite element formulation is applied to solve coupled hydro-mechanical problems involving large displacements after failure.

INTRODUCTION

Up to now, almost all the models for geomaterials are focused on non-associated elasto-plastic behaviour, that is to say, they are valid only for the solid state before failure. However, plastic failure breaks the static equilibrium, saturated geomaterials exhibit consequently a fluid-like behaviour in post-failure stage. In order to simulate completely properties of soil, a unified solid-fluid model with a transition in between has been proposed recently [1, 2], a non-associated elasto-plastic model called “PLASOL” [3] and a Bingham's viscous law are used in the model to describe the behaviors of geomaterials in pre-failure and post-failure stages, and Hill's second order work criterion [4] is chosen as the solid-fluid transition criterion. Since quite a number of natural risks, such as landslides, occur induced by the rainfall, in the report, this unified model is expanded by using Bishop's effective stress, expecting to propose a more reliable model for unsaturated soil. In addition, as its capacities of tracking internal variables during material movement and solving large transformations, the finite element method with Lagrangian integration points (FEMLIP) is taken into account as an appropriate framework. With the visco-elasto-plastic stress-strain relation and the suction-water content relation derived from modified Van Genuchten's water retention curves, a new finite element formulation incorporating hydro-mechanical coupling is developed.

A UNIFIED SOLID-FLUID MODEL IN CONSIDERATION OF AN HYDRO-MECHANICAL COUPLING

the existing unified model

For modeling completely the elasto-plastic behaviour in solid stage and the viscous behaviour in fluid stage of soil, an interesting unified model has been proposed [1 ,2].

Firstly, a non-associated elasto-plastic model called PLASOL is chosen, to simulate the behaviour before failure. This model, proposed by Barnichon [3], uses the Van Eekelen plastic criterion [5] as plastic limit, which allows to avoid geometric singularities and to describe two main features of geomaterials: 1) strength increases progressively with the confining pressure. 2) the friction angle under extension triaxial stress loading is higher than that under compression triaxial stress loading. To calibrate a given elasto-plastic soil, this model requires 13 parameters.

Secondly, as the most conservative criterion in bifurcation domain of soils verified up to now, Hill's second order work [4], written as follows, is used to judge the loss of stability for geomaterials.

$$d^2w = d\sigma_{ij}\, d\varepsilon_{ij} \tag{1}$$

if $d^2w > 0$, for any loading direction it is considered stable, otherwise, a diffuse or localized failure can be reached in the directions related to its negative values.

Lastly, in post-failure stage, the studied geomaterial is considered as exhibiting a viscous behaviour, obeying the Bingham's law expressed as follows:

$$\text{if } J_{2\sigma} > s_y : \dot{e} = \frac{1}{2\eta}\left(s_{ij} - s_y \frac{s_{ij}}{J_{2\sigma}}\right) \qquad \text{else: } \dot{e} = 0 \tag{2}$$

where $J_{2\sigma}$ is the second invariant of stress tensor, s_y is the yield stress, η is the dynamic viscosity, s and $\dot{e}$ are respectively the deviatoric stress and strain rate tensor. It should be noted that, the instantaneous satisfaction of both $d^2w < 0$ and $J_{2\sigma} > s_y$, is considered as a failure, while once $J_{2\sigma} < s_y$ in fluid state, the studied medium turns back to an elasto-plastic solid state.

Bishop's effective stress

By introducing the Bishop's effective stress [6], expressed as follows, the unified model above-mentioned is expanded into the unsaturated domain.

$$\sigma' = \sigma - u_a m + \chi(u_a - u_w)m \tag{3}$$

where σ' is effective stress, σ (expressed as 6 dimensional vectors), u_a and u_w are respectively total stress, air pressure and water pressure, m^T = (1, 1, 1, 0, 0, 0) and $s = u_a - u_w$ is the suction. In our framework, phases are assumed immiscible, grains and liquid are

incompressible, and air pressure is considered identical in the void volume determined by the degree of saturation and porosity and equal to Ptam.

The expression of χ that Arairo W. and Prunier F. [7] proposed is taken into account, by determining two parameters a_χ and n_χ, χ is expressed as follows, and it is located always between 2 boundary water retention curves for a given suction.

$$\chi = (1+(\frac{a_\chi s}{P_{atm}})^{n_\chi})^{\frac{1}{n_\chi}-1} \tag{4}$$

Hydraulic model

Linking degree of saturation or water content to suction, the water retention curves (WRC) show the basic hydraulic properties of soil. By establishing the relation between the degree of saturation and the porosity, WRCs of Van Genuchten-Mualem [8] has been improved and it is given by:

$$Sr_v = Sr_{res} + (Sr_{sat} - Sr_{res})\left(1+\left(\frac{a_v s}{P_{atm}}\right)^{n_v}\right)^{\frac{1}{n_v}-1} \tag{5}$$

where the index v means respectively drying and wetting process, being d and w, Sr_{res}, Sr_{sat} and Sr_v are respectively the residual, saturated and current degrees of saturation, a_v and n_v are two parameters, the former is a function of the porosity [7]:

$$a_v = \frac{P_{atm}}{s_{aev}}\left(\frac{n_v-1}{n_v}\right)^{\frac{1}{n_v}}\frac{-n_v}{(n_v-1)^2}\left(\left(\frac{2n_v-1}{n_v}\right)^{2-\frac{1}{n_v}}-\left(\frac{2n_v-1}{n_v}\right)-\frac{(n_v-1)^2}{n_v}\right) \tag{6}$$

where s_{aev} is the air entry value (AEV), P_{atm} is the atmospheric pressure.

Hence, $\frac{\partial Sr}{\partial s}$ and $\frac{\partial Sr}{\partial n}$ are obtained:

$$\frac{\partial Sr}{\partial s} = (Sr_{sat}-Sr_{res})(1-n_v)\frac{a_v}{P_{atm}}(1+(\frac{a_v s}{P_{atm}})^{n_v})^{\frac{1}{n_v}-2}(\frac{a_v s}{P_{atm}})^{n_v-1} \tag{7}$$

$$\frac{\partial Sr}{\partial n} = \lambda(Sr_{sat}-Sr_{res})(1+(\frac{a_v s}{P_{atm}})^{n_v})^{\frac{1}{n_v}-2}(\frac{a_v s}{P_{atm}})^{n_v-1}\frac{s}{s_{aev}^2}(\frac{n_v-1}{n_v})^{\frac{1}{n_v}-1}\frac{s_{aev0}}{n_0}((\frac{2n_v-1}{n_v})^{2-\frac{1}{n_v}}-n_v) \tag{8}$$

where s_{aev0} is a reference AEV for a reference porosity n_0, and λ a constant material parameter.

FINITE ELEMENT IMPLEMENTATION

Two types of particles

In this paper, the finite element method with Lagrangian integration points (FEMLIP) is chosen as a unified method for coupled hydro-mechanical problems. On one hand, this method is based on FEM. It means that it shares the full continuous approach and the dissociation of the mesh nodes, as FEM; on the other hand, it is developed from the particle-in-cell method [9], the fixed Eulerian mesh and the discretisation of the material points are carried forward. In FEMLIP, the medium is discretized into finite elements for the velocity field. Then the solved velocity field on nodes of the fixed mesh is transferred to material points, in which all material variables are refreshed and carried during the whole computation process [10, 11]. Differing from classic Lagrangian FEM, the material points, playing a role as integration points, are allowed to move across the mesh between time t and time t + δ t, as illustrated in figure 1:

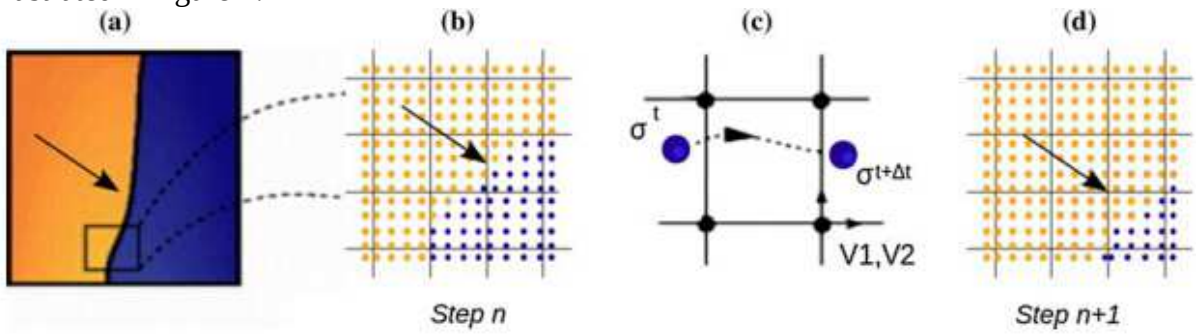

Figure 1: **Schematic presentation of FEMLIP**

Benefiting both the advantages from the Eulerian FEMs and the Lagrangian FEMs, FEMLIP is appropriate to deal with 1) the small deformations of elasto-plastic behaviour before failure, 2) the large deformations upon failure, 3) the large displacements of visco-elastic behaviour after failure.

In order to simulate incompressible fluid and avoid mesh locking problems, the element with 4 corner nodes and 1 central node is used in FEMLIP to reduce the kinetic stress, accordingly, the mixed formulation is chosen for eliminating the numerical effect of the infinite viscous compressible modulus [12].

For simulating compressible geomaterials without hydro-mechanical coupling, the mixed formulation can be simplified as $AV = F$. Here, we just present an oedometric test calculated respectively by the iterative method under the mixed formulation and by the direct method under the formulation above, to ensure the first step of the hydro-mechanical coupling implementation.

The test is simulated by a 1×1 m² weightless square sample discretized in 4×4 elements. Lateral boundaries and inferior boundary are fixed and the sliding along the lateral boundaries is allowed. A vertical velocity of 0.05 m/s is exerted on the superior boundary. With elasto-plastic parameters enumerated in table 1, and an elastic time-step introduced by F. Dufour[12] $\Delta t_e = 10^{-3} s$, two numerical solutions are compared in figure 2. The dotted lines present the p-q stress path of an oedometric test, simulated with an iterative algorithm under the mixed

formulation, the continuous lines, with an archetypical direct algorithm. A perfect superposition is observed, in elastic, strain hardening and elastic rebound domains.

Table 1: Elasto-plastic parameters of oedometric test:

E(MPa)	ν	$\varphi_{e0} = \varphi_{c0}(^\circ)$	$C_0(kPa)$	$\varphi_{ef} = \varphi_{cf}(^\circ)$	$C_f(kPa)$	$\psi_e = \psi_c(^\circ)$	B_p	B_c	$\eta(Pa.s)$	$K_v(Pa.s)$
2,5	0,2	1	1	28	10	5	0,01	0,02	2×10^{15}	2.7×10^{15}

Consequently, on one hand, for dealing with a compressible material without hydro-mechanical coupling, a direct method without iterations is feasible by FEMLIP; on the other hand, by means of implementing the hydro-mechanical coupling, the mixed formulation can be held to calculate water pressure. We will take into account this question in next section.

In this scheme, we distinguish material points in 2 types. Ones don't involve or track hydraulic variables, for these particles suction and all the other hydraulic variables are always nil, by switching off the shape function of water pressure. It means that the finite element formulation integrated by these particles is expressed as $AV = F$. The others involve the hydro-mechanical coupling, in which the water pressure is refreshed and the suction-water content relationship is calculated in every computational time step. The corresponding formulation is in the mixed form, an appropriate iterative method is thus required.

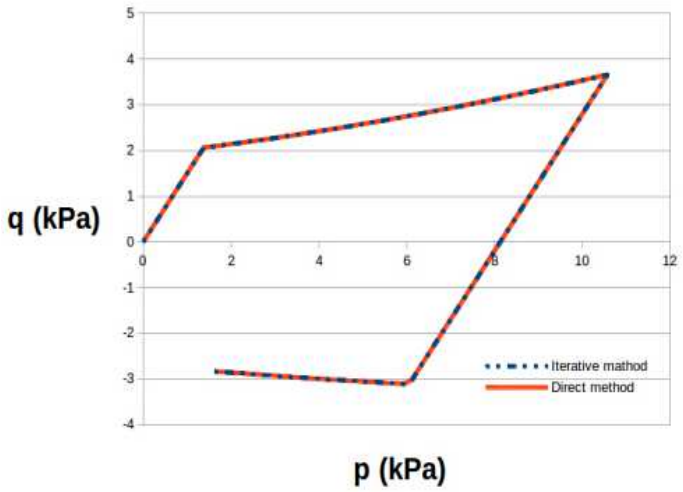

Figure 2: Comparison of numerical results by 2 different numerical methods for an oedometric test

Tensorial equations in FEMLIP

In order to implement the unified model established above into FEMLIP, an adapted incremental stress-strain relationship is needed. Firstly, on basis of Bishop's effective stress, the stress-strain relation in FEMLIP frame is expressed as follows:

$$\bar{\sigma} = D^{ve}\,\dot{\varepsilon} - \Delta t_e\,\chi\,\dot{s}\,m - \chi\,s^t\,m + \overline{\sigma^t} \tag{9}$$

where D^{ve} is the visco-elastic 6x6 matrix and $\bar{\sigma}$ is net stress.

Secondly, knowing that $\theta = n \cdot Sr$, the suction-water content relationship is derived from the modified Van Genuchten-Mualem water retention curves.

$$d\theta = Srdn + ndSr = (Sr + n\frac{\partial Sr}{\partial n})dn + n\frac{\partial Sr}{\partial s}ds = -(1-n)(Sr + n\frac{\partial Sr}{\partial n})m^T d\varepsilon + n\frac{\partial Sr}{\partial s}ds \tag{10}$$

For the sake of simplification, some assumptions can be considered under certain conditions:

- The grains and the water are supposed incompressible.
- The pores of the medium are connected to the outside air, the flow of pore air can be neglected.
- The isothermal conditions are considered to avoid the influence of heat transfer and temperature field.
- The liquid flows obey the generalized Darcy's law.

With these assumptions, the equilibrium equation of momentum and the continuity equation of water flow provide the simplest form of the governing equations, written as:

$$\int_V (\partial\varepsilon^T \sigma^t)dV - \int_S (\partial u^T f^t)dS - \int_V (\partial u^T b^t)dV = 0 \tag{11}$$

$$div(\frac{-k}{g}(\Delta u_w - b_w)) + \frac{\partial}{\partial t}(\rho_w \theta) = 0 \tag{12}$$

where σ is the Cauchy total stress tensor, b is the body force vector and f the distributed or concentrated surface force, S and V are respectively the boundary related to the surface force and the studied volume, the subscript t means at time t when the quantities are computed. g stands for the gravity acceleration, ρ_w is the water density, b_w is the body force vector of pore water, u_w is the pore water pressure, and k the permeability tensor of unsaturated soil. With adapted shape functions and the stress-strain relationship obtained above, discretised finite element equations are obtained as follows:

$$AV^{t+\Delta t_e} + \frac{L}{\Delta t_e}U_w^{t+\Delta t_e} = F^{t+\Delta t_e} \tag{13}$$

$$L'V^{t+\Delta t_e} + (\frac{S}{\Delta t_e} + R)U_w^{t+\Delta t_e} = Q_{ext}^{t+\Delta t_e} + \frac{S}{\Delta t_e}U_w^t \tag{14}$$

where

$$A = \sum \int_V (B^T D^{ep} B)dV$$

$$L = \sum \int_V (B^T \chi m \Delta t_e N_w)dV$$

$$F^{t+\Delta t_e} = \sum \int_V (N^T b^{t+\Delta t_e} - B^T \bar{\sigma}^t)dV + \sum \int_S (N^T t^{t+\Delta t_e})dS$$

$$L' = -\sum \int_V (N_w^T (1-n)(Sr + n\frac{\partial Sr}{\partial n})m^T B)dV$$

$$S = -\sum \int_V (N_w^T n \frac{\partial Sr}{\partial s} N_w)dV$$

$$R = \sum \int_V (B_w^T \frac{k}{\rho_w g} B_w) dV$$

$$Q_{ext}^{t+\Delta t_e} = -\sum (\int_{S_w} (N_w^T q^{t+\Delta t_e}) dS_w - \sum \int_V (B_w^T \frac{k}{\rho_w g} b_w) dV$$

N and N_w are respectively shape functions of velocity and water pressure.

Hence, a new system of equations for calculating the velocity and the water pressure is obtained.

CONCLUSION

This report presents a solid-fluid unified model for geomaterials with a transition criterion in between, and develops it by using Bishop's effective stress. In addition, a visco-elasto-plastic stress-strain relation based on the model, and a suction-water content relation derived from modified Van Genuchten's water retention curves are introduced for solving fully coupled hydro-mechanical problems. For validating the implementation, an oedometric test is simulated as a benchmark. By improving the fluid-like model in post-failure stage, and by incorporating inertial force, a more complete and realistic model is expected.

REFERENCES

Prime N, Dufour F, Darve F. Unified model for gromaterial solid/fluid states and the transition in between. Journal of Engineering Mechanics 140(6), 2013

Prime N, Dufour F, Darve F. Solid-fluid transition modelling in geomaterials and application to a mudflow interacting with an obstacle. Int. Journal for Numerical and Analytical Methods in Geomechanics 2014. Vol 38, p. 1341-1361

Barnichon JD. Finite element modelling in structural and petroleum geology. Ph.D. Thesis 1998. University of Liege

Hill R. A general theory of uniqueness and stability in elastic-plastic solids. Journal of the Mechanics and Physics of Solids 1958. Vol.6 p.236-249

Van Eekelen H A M. Isotropic yield surface in three dimensions for use in soil mechanics. International Journal for Numerical and Analytical Methods in Geomechanics 1980. 4(1), 89-101

Bishop AW. Principle of effective stress. Teknisk Ukeblad 1959; 106(39): 859-863

Arairo W, Prunier F, Djéran-Maigre I, Darve F. A new insight into modelling the behaviour of unsaturated soils. Int. Journal for Numerical and Analytical Methods in Geomechanics 2013. Vol 37, p. 2629-2654

Van Genuchten MT. A closed-form equation for predicting the hydraulic conductivity of unsaturated soils. Soil Science Society of America Journal 1980. 44:892-898

Sulsky D, Zhou SJ, Schreyer HL. Application of a particle-in-cell method to solid mechanics. Computer Physics Communications 1995. 87:236-252

Moresi L, Dufour F, Muhlhaus H-B. A Lagrangian integration point finite element method for large deformation modelling of viscoelastic geomaterials. Journal of Computational Physics 2003. 184:476-497

Moresi L, Dufour F, Muhlhaus H-B. Mantle convection modeling with viscoelastic/brittle lithosphere: numerical methodology and plate tectonic modeling. Pure and Applied Geophysics 2002. 159(10):2335-2356

Dufour F. Développements de la méthode des éléments finis avec des points d'intégration Lagrangiens: Applications à la géomécanique. Ph.D. Thesis 2002. Ecole centrale de Nantes

FEMxDEM Multiscale modeling applied to granular materials

A.Argilaga, J.Desrues, S. Dal Pont, G. Combe and D. Caillerie

Grenoble-INP, UJF, CNRS UMR5521, Laboratoire 3SR

albert.argilagaclaramunt@3sr-grenoble.fr

ABSTRACT

The multi-scale FEM-DEM approach is an innovative numerical method for geotechnical problems, using at the same time the Finite Element Method (FEM) at the engineering macro-scale and the Discrete Element Method (DEM) at the scale of the microstructure of the material. The link between scales is made via computational homogenization. In this way, the continuum numerical constitutive law and the corresponding tangent matrix are obtained directly from the discrete response of the microstructure.

In the proposed paper, a variety of operators, rather than the tangent consistent operator usually adopted for the Newton-Raphson method, is tested in a challenging attempt to improve the convergence performances. Other techniques intended to increase the performance of the code, as for example REV variability, are presented. The independence of the DEM computations is exploited to develop a parallelized code. Some key issues related to parallelization will be presented and discussed. Some results are given exhibiting the above findings with emphasis on aspects related to strain localisation.

INTRODUCTION

The numerical homogenization performed in a material point allows us to use the microscale REV behavior as a constitutive law (Miehe, 2003). In order to apply this multiscale model to a general nonlinear problem, an iterative procedure is used, being Newton Raphson the iterative scheme. A linearized expression of the function object of minimization is needed by the Newton Raphson method. However, our numerical approach doesn't provide an analytical expression of its derivative: the identification of the operator used in the linearized expression is part of the present work.

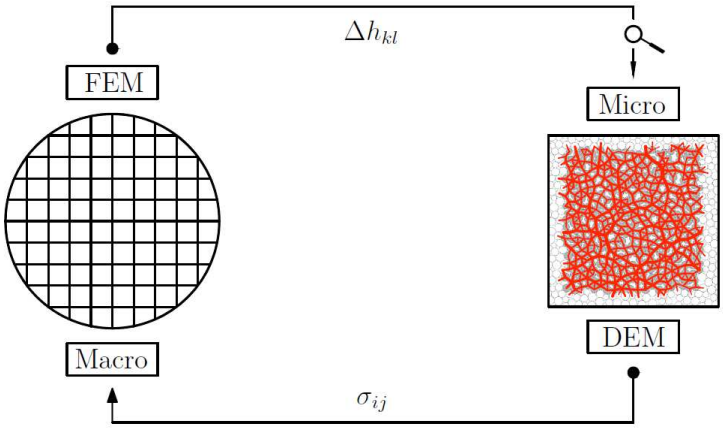

MICROSCALE: DISCRETE ELEMENT METHOD

The Discrete Element Model (DEM) is a code modelling an assembly of grains with frictional smooth contacts. The DEM code used in this work was developed by Gaël Combe and co-workers in 3SR laboratory (Combe, 2003); it consists of a 2D model with spherical grains and works in the following manner:

• REV generation: an assembly of grains is generated in a structured mesh, each grain is given a radius following some random distribution with minimum and maximum values not exceeding the rank [0-0,5]. After this generation the assembly is shaken in order to break the mesh patterns and a velocity is given to each grain in a random direction. For this step, a contact dynamics (CD) algorithm is used, this algorithm is more efficient than DEM for low number of contacts.

• Isotropic compression (Fig. 1): after the REV generation, the grains are very disperse in the space with almost no contacts among them. Different ways of compacting the assembly exist; the one used in this work is an isotropic compression. In order to do this, the four walls bounding the REV are moved towards the centre, decreasing the void ratio of the sample and creating new grain contacts. The friction between grains is set to zero during this step in order to get a high compacity. Doing the same with friction among grains, will result in a much higher void ratio, or even a foam, i.e. an appropriate configurations for industrial applications (Combe, 2003).

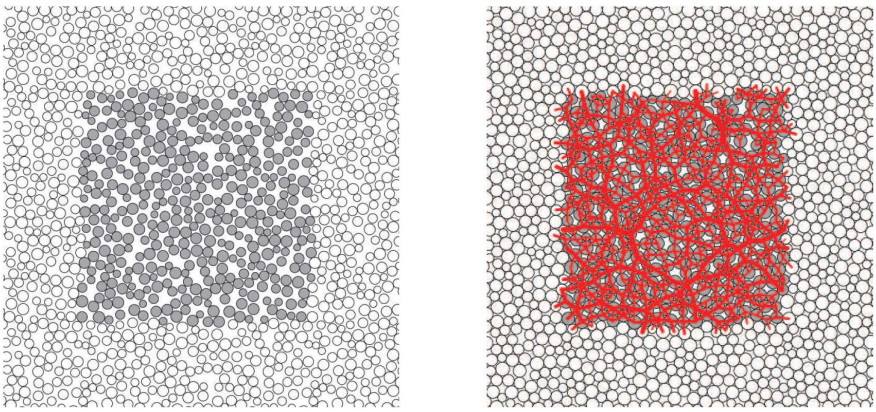

Figure 1. **DEM sample before and after isotropic compression, red lines represent force network.**

• Periodic Boundary Conditions (PLC). For the two scale problems of the present work, the REV is assumed to be periodically distributed in a near neighbourhood. PLC are used in the model to represent an infinity of periodic REV's with the computational cost of only one. In addition, the PLC gives a smoother result compared to rigid wall conditions, being this result comparable to a REV with a bigger number of grains. The inconvenient of the PLC is that they impose some restrictions to the orientation of the shear bands, that may result in a not very realistic structure behaviour (Combe, 2003).

MACROSCALE: ISSUES RELATED TO THE ITERATIVE PROCESS

Because of the non-linearity coming from the large strains in the macroscale, the problem will be solved applying the strain-stress load step by step. In each step, the behaviour of the model is still nonlinear due to the nature of the constitutive law. In order to find the solution in each time step, an iterative scheme will be used: Newton Raphson method is the natural candidate. The constitutive law used in the microscale presents stress softening, i.e. convergence problems are very likely to be encountered.

This issue is well-known in the literature, e.g. De Borst (1987) underlines localization phenomena and the related mesh dependency issues in FEM. Crisfield and Wills (1988) show that Newton's method oscillates between localised and non-localised states in some integration points during the iterative process. They also treat instability problems related to snap-back, snap-through and propose different techniques consisting in changing the minimum pivot value in order to trigger the localisation.

In a numerical model, the state is likely to be homogeneous unless perturbations are introduced in an explicit way. An homogeneous state may induce the calculation to evolve into an homogeneous non stable state after the bifurcation while in reality this situation is much less likely to happen due to microscale heterogeneities, manufacturing imperfections or other kind of geometrical and load perturbations: this will lead to a more localized behaviour than the one predicted in the numerical model. Shi and Crisfield (1992) tried to reproduce all the possible bifurcations in order to be aware of the ones giving the weaker response: the minimum pivot and the determinant of the tangent operator are indicators related to bifurcation triggering. Gastebled and May (2000) show that in local bifurcation negative pivots appear and disappear in successive iterations leading to a very slow convergence.

Similarly, Crisfield and Wills (1988) observed oscillations between localised and non-localised states.
Local bifurcation must be clearly separated from structural bifurcation and a full bifurcation test concerning local and structural bifurcation may be performed (Fig. 2).
Paulino and Liu (2001) suggest that in Boundary Element Problems (BEP), the Continuum Tangent Operator (CON) gives better results than the Consistent Tangent Operator. This result suggest the use of different operators for nonlinear materials, even in FEM.

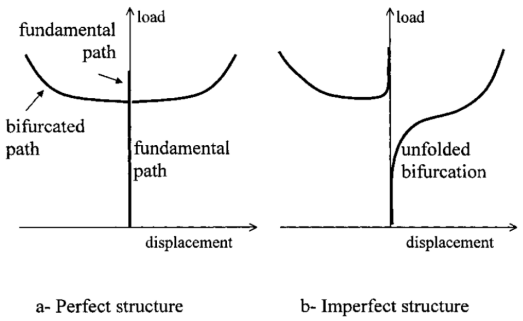

Figure 2. **Bifurcation unfolding. (Gastebled and May, 2000)**

OperatorS CHOICE

The operator in the linearized expression of the constitutive law used in the Newton method is discussed in the following. It is expressed as a third order tensor using the following notation (Eq. 1). In this section the different kind of operators tested are:

Consistent Tangent Operator (CTO)
Auxiliary elastic operator (AEO)
Upper bound Kruyt operator (UKO)
Upper bound Corrected Kruyt Operator (UCKO)

$$\sigma_{ij} = C_{ijkl} \cdot \epsilon_{kl}$$

$$\begin{pmatrix} \sigma_{11} \\ \tau_{12} \\ \tau_{21} \\ \sigma_{22} \end{pmatrix} = \begin{pmatrix} C_{1111} & C_{1112} & C_{1121} & C_{1122} \\ C_{1211} & C_{1212} & C_{1221} & C_{1222} \\ C_{2111} & C_{2112} & C_{2121} & C_{2122} \\ C_{2211} & C_{2212} & C_{2221} & C_{12222} \end{pmatrix} \cdot \begin{pmatrix} \epsilon_{11} \\ \gamma_{12} \\ \gamma_{21} \\ \epsilon_{22} \end{pmatrix}$$

Equation 1. **Cauchy expression and notation.**

CONSISTENT TANGENT OPERATOR (CTO)

The Consistent Tangent Operator is obtained using a perturbation method (Fig. 3) and integrating over the time step: it consists of applying a small perturbation[1] in all the degrees of freedom of the problem (which are four) and computing the homogenized stresses for each degree of freedom, so that all the 16 coefficients are obtained. The second and third rows of the operator are identical by definition of the constitutive law (stresses)[2], while the second and third columns are different as they come from different perturbation calculations (strains). As

[1] Small enough to be considered infinitesimal compared to the magnitude of the loading step.
[2] Small strain approximation is taken into account, so the strain tensor becomes symmetric.

the method requires to recompute 4 times in each time step the additional perturbations, this approach is 5 times more time consuming than a single computation method.

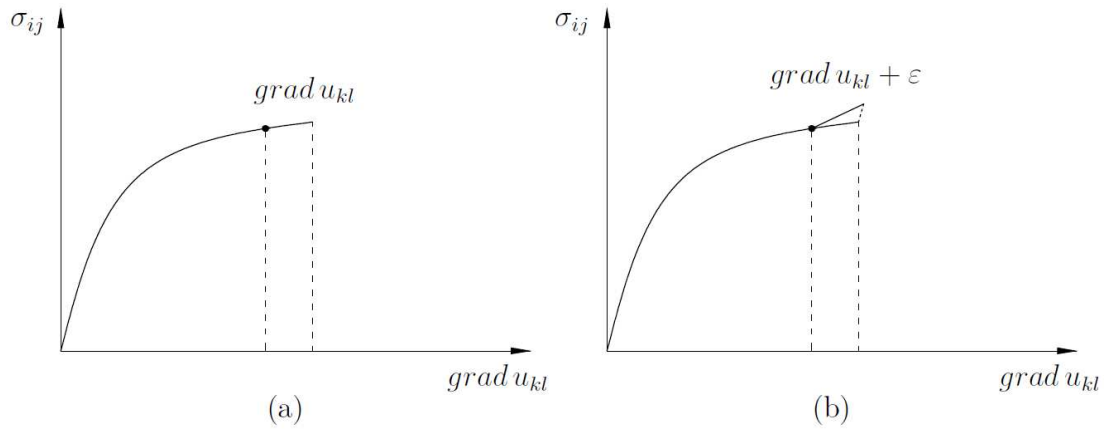

Figure 3. **Perturbation over one loading step.**

The CTO is claimed to provide quadratic convergence. In general, the convergence obtained using it in a FEMxDEM model is not quadratic unless the state is nearly elastic (Fig. 4). The reason why quadratic convergence is lost is the non-continuity of the derivative of the constitutive law. Quadratic convergence can be observed if a very small step is performed, small enough so no grain sliding happens in any REV of the model. Usually this quadratic velocity will be lost in a FEMxDEM model for higher deformations. In this particular case, the constitutive law is smooth enough to provide a continuous derivative. Performing such small step makes no sense since the aim of using DEM is to bring something else than elasticity to the constitutive law. Considering time steps big enough to change the grain contact network, Newton's method will present linear convergence at its best. This linear convergence is lost as the loading path approaches a bifurcation. After bifurcation phenomena, identified as a stress peak in a biaxial test, the convergence rate will remain sub-linear because of the big deformations in some REVs[3], not leading to smooth constitutive laws.

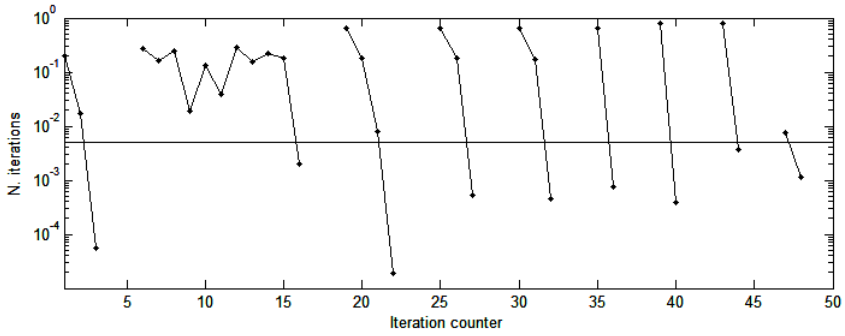

Figure 4. **Convergence using Tangent Operator.**

From a theoretical point of view a negative stiffness coefficient is not possible because of thermodynamic considerations, see Pasternak et al. (2014). Therefore, materials exhibiting negative stiffness are unstable. However, if only some part of the global structure presents negative stiffness and the surrounding is stiff enough, it can "absorb" the instabilities and the structure can be stable (Pasternak et al., 2014). This can be applied to the present case, a multiscale model where the integration of the material points can result in negative stiffness

[3] Inside the shear band.

coefficients but the surrounding materials points with positive stiffness are still able to absorb the instability.

It is observed that in a large system, the use of CTO in the multiscale implementation, results into a divergence bifurcation. It is known from FEM applications using phenomenological laws that the solution can be found after bifurcations. However, the time cost of the FEMxDEM model forces us to stop the simulation before a solution is found, i.e. better numerical approaches are needed.

AUXILIARY ELASTIC OPERATOR (AEO)

In order to solve the post localization convergence problems found using the CTO, other operators are tested. Looking at the history of the operator in a single Gauss point, it can be seen that the non positiveness is restricted to some of the time steps being the operator positive defined in the rest. This issue can be related to the DEM behaviour which gives negative stress only when a series of grains slide, which happens in a systematic way during a constant charging path. In order to provide a smoother evolution of the operator, a time average over several well-converged loading steps in the beginning of the numerical simulation is performed. This provides a regular and positive defined operator, which will be used for the given Gauss point for the rest of the simulation. This operator has a disadvantage as it is not tangent to the law beyond the elastic phase. Consequently, Newton method will never present quadratic convergence. As the operator is unchanged, it doesn't take into account the heterogeneities coming from a shear band. Nevertheless, no perturbations are needed after obtaining the averaged operator and it is 5 times less time-demanding per iteration than the CTO. The improvement with respect to the CTO is that it actually allows going further in the computation after the bifurcation, being able to find a solution for relatively large values of strain and plasticity (Fig. 5).

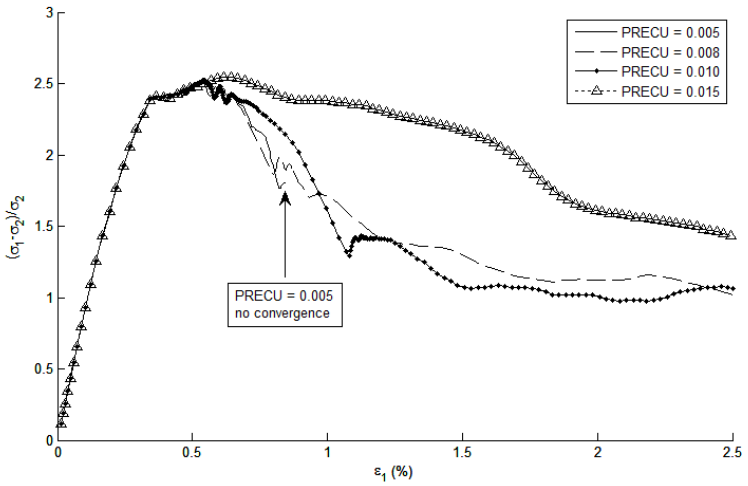

Figure 5. **Strain-stress curves for different biaxial tests using AEO.**

UPPER BOUND KRUYT OPERATOR (UKO)

The elastic operator proposed by Kruyt and Rothenburg, (1998) is tested. Kruyt proposes two extremum principles in order to obtain the upper and lower bound of the elastic moduli of a granular assembly. In this work, we will refer to the operator related to the upper bound of the elastic moduli. This operator has been already used in a multiscale FEMxDEM approach by Guo and Zhao (2014). UKO is obtained assuming homogeneous strain field over the REV and performing a summation over all the contacts, taking in consideration the orientation and stiffness of the contacts (Eq. 2). Cohesion forces are not taken into account. As it consists of an elastic definition, the resulting operator is positive defined (in contrast to the CTO which can have negative eigenvalues due to the softening behaviour). Not being a CTO, quadratic convergence cannot be expected. The positive definition of this operator makes it more robust, especially in a softening branch. In addition, no perturbation is needed for obtaining the coefficients, so, a priori, the computational cost is 1/5 compared to any perturbation-based methods. After each iteration, the operator is obtained performing a summation over the contacts without any additional calculation. Consequently the additional computational cost is minimal compared to the DEM part.

$$L_{ijkl} = \frac{1}{S}\sum_{c\in S}(k_n n_i^c l_j^c n_k^c l_l^c + k_t t_i^c l_j^c t_k^c l_l^c)$$

Equation 2. **Cauchy expression and notation.**

UPPER BOUND CORRECTED KRUYT OPERATOR (UCKO)

As already said in the previous section, the UKO comes from an extremum principle which provides the upper bound of the elastic moduli, the extremum principle providing the lower bound (Kruyt and Rothenburg, 1998) is not convenient to be used in the present implementation since it is not a straight forward procedure. It would mean an increase of the complexity and computational time expenses of the code. Using statistical and thermodynamics principles, Kruyt shows that the elastic moduli can be obtained as the average of the upper and lower bounds if the coordination number is high enough (this is the present case). Being aware of this linearity between upper, lower bounds and actual elastic moduli, and in order to obtain the most accurate approximation of the elastic moduli without increasing the computational time, the UKO is compared to the CTO in the pre-peak part, and a correction coefficient is applied to UKO in order to obtain an approximation of the CTO: the UCKO.

STRAIN LOCALIZATION CATALYSIS: GEOMETRICAL DEFECT

One of the challenges for the Newton method is to reach the required precision criteria when approaching a bifurcation. Beyond the peak stress, Newton method often increases its efficiency reducing the number of iterations per step. This can be seen in the previous biaxial tests as a higher number of iterations around the stress peak are required. One possible way of minimizing this the number of iterations around the peak is to trigger one of the solutions by different means, for instance by introducing a defect in one of the elements that will break the homogeneity of the sample. The biaxial geometry (Fig. 6) is used. In the plot (Fig. 6), the second invariant of strain is shown at the end of a biaxial compression test with constant lateral pressure (2,5% of axial strain). The figure on the left consists of an initially homogeneous sample presenting a shear band at the end of the test. The figure on the right consists of the same configuration but with a geometrical defect introduced in one of the elements. The defect consists of a notch in the central node of an element located in the stress boundary condition contour. The notch has a depth of 10% of the element side length (finite value). In the results, it can be observed that the defect will not trigger a different localization mode; the localization will be exactly the same as in the homogenous case as well the stress-strain curve. The identical stress-strain curve can be put down to the fact that the perturbation induced by the notch is outside the localization which governs the homogenized behaviour at the end of the test. The interest of this experiment is the fact that a finite perturbation of the initial homogeneous state will not make any difference to the homogenized evolution of the test, the reason of this can be explained by the initial bias shear strain of the REVs which has more influence to the homogenized behaviour than the geometrical defect in the element.

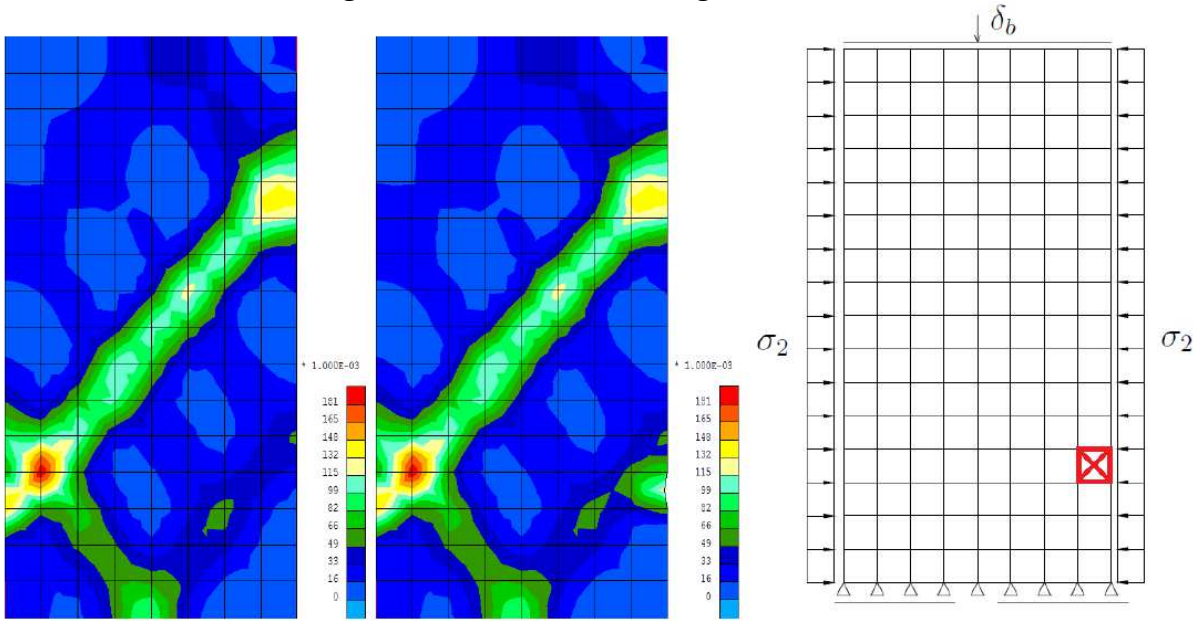

Figure 6. **Second invariant of strain for the end of a biaxial test homogeneous and with a geometrical defect in one element as a localization catalytic.**

STRAIN LOCALIZATION CATALYSIS: DEM PARTICLE FRICTION

In this case, the catalyser for the strain localization is a reduction on the interparticle friction coefficient in one of the elements, from μ=0.5 to μ =0.3 in element number 4 (Fig. 7). The weakened element is now located in the place where the band is supposed to appear because the sign of the bias shear stress of the VERs. Comparing the first map of the second invariant of strain with the second one, it can be affirmed that the weakened element triggers a localization of the strain in a way that for the same axial strain value (2,5%) the sample has a higher strain localization: 26.4% vs 18.1% for the maximum value of second invariant of strain inside the shear band leading to a faster computation and possibly better emulation of real materials with heterogeneous microscale distribution.

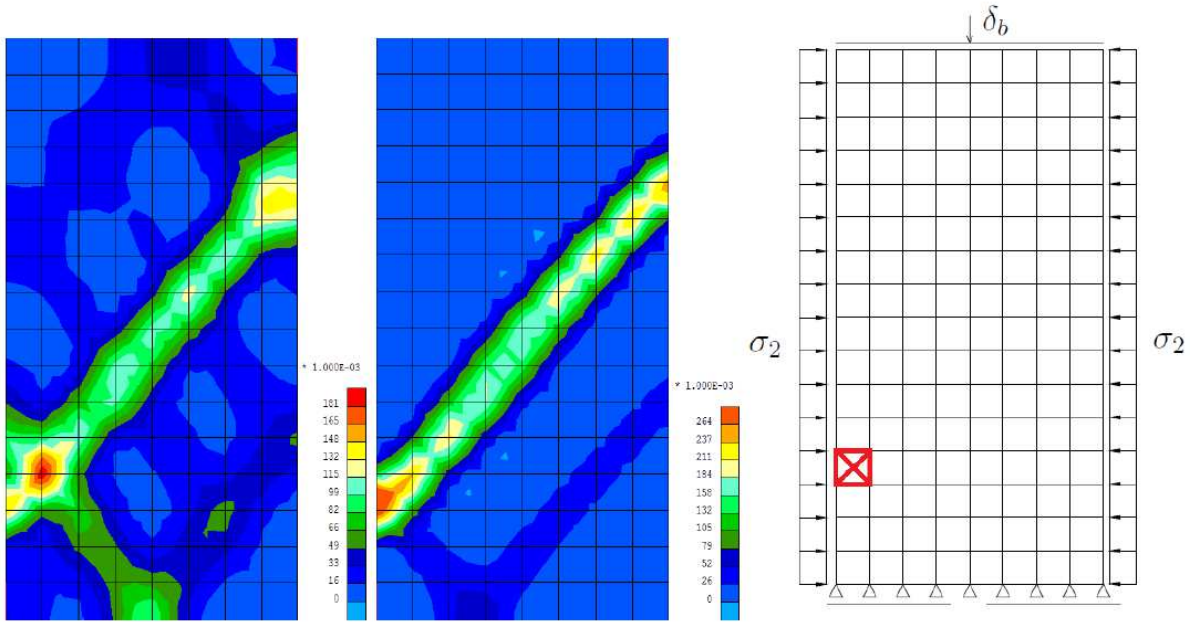

Figure 7. **Second invariant of strain for the end of a biaxial test homogeneous and with different REV in one element as a localization catalytic.**

The strain stress curves present differences after the bifurcation takes place, the homogeneous sample has a peak stress as the end of the elastic part but after several steps the stress increases again, while the sample with a different element presents a more smooth behaviour and reaches softening faster than the homogenous one for strain higher than 1%. At 2,5% of axial strain the homogeneous sample hasn't reached the residual shear stress, in the other hand, the heterogeneous sample reaches the residual stress value near 1,5% of axial strain due to the faster localization process.

REV VARIABILITY

It is proved that breaking the homogeneity of the sample will help to trigger the strain localization reducing the computational time and leading to a faster softening. Following this research direction, a new simulation is prepared, this time introducing a series of different elements (11 elements, 8.5% of the total) along an arbitrary orientation, the RVEs in the elements have the same differential property as in the previous subsection: a reduced contact friction coefficient μ=0.3. The result is a faster computation compared to the case with a single different element and a slightly higher value for the maximum strain localization: 27.3% vs 26.4% for one single different element and 18.1% for an homogenous sample. The localization happens in a faster way than in the homogenous sample or one different element sample, in the other side, the peak stress is lower than in the previous cases 14% lower with respect to the homogenous case and 11% lower with respect to the case with one different element, which may be due to the proportion of weakened elements over the total (8,5%), or weakened elements inside the shear band (62.5%), making an average friction coefficient 25% lower along it.

This test shows that introducing a series of elements with a different property inside the sample can induce strain localization reducing the computational time. However, introducing a big number of elements with a different property can also change the average value of the given property; if this is the case, a comparison with the homogenous state is not representative anymore. In order to perform a proper study about the effect of heterogeneity introduced by element variability a new series of simulations are prepared: the same sample is filled with 28 different elements, half of them with a decreased contact friction in the VER and the other half with increased contact friction leading to a zero bias concerning the reference value of contact friction μ=0.5. This non-biased group of elements is randomly distributed along a diagonal orientation in order to break the sample spatial homogeneity.

In order to capture the effect of the root mean square variability of this zero biased group of heterogeneous elements, a parametric study is carried with the values δ=0.2/0.1/0.05/0.025, being δ the variability of the contact friction coefficient. The second invariant of strain (Fig. 8) shows a more regular and straight shear band for the lower values of δ (closer to homogeneous state), with maximum values of shear strain similar for all cases, from less to more homogenous: 24.3%, 22.3%, 21.7% and 25.2%.

The way the heterogeneous elements affect the global behaviour is the following: the elements with less contact friction in the VERs than the average will present sliding contacts earlier; the elements with higher contact friction in the VERs will be able to withstand more strain without sliding so inducing the strain localization in the already weakened elements. This autocatalytic process will trigger a strain localization earlier than in the case closer to the homogeneous state. Looking at the strain-stress curves (Fig. 8), it can be seen that the pre-peak elastic behaviour starts to plastify earlier for the higher values of δ, presenting a smoother behaviour, more similar to real materials than the simulations with lower values of δ that present a more brittle end of the elastic part. The average peak values for the stress are slightly lower for the cases with higher δ. The early elastic part and the residual shear stress part for large strain are similar or identical in all simulations; the main effect of this element variability is on the localization process. It's worthy remarking that even the case with smallest δ has a typical heterogeneous material behaviour making a difference with the case

presented in previous subsections where the value of $\delta = 0$ concluding that any small finite[4] heterogeneity is able to trigger the localization effect earlier than the numerical rounding which is responsible of the break of homogeneity in homogeneous cases.

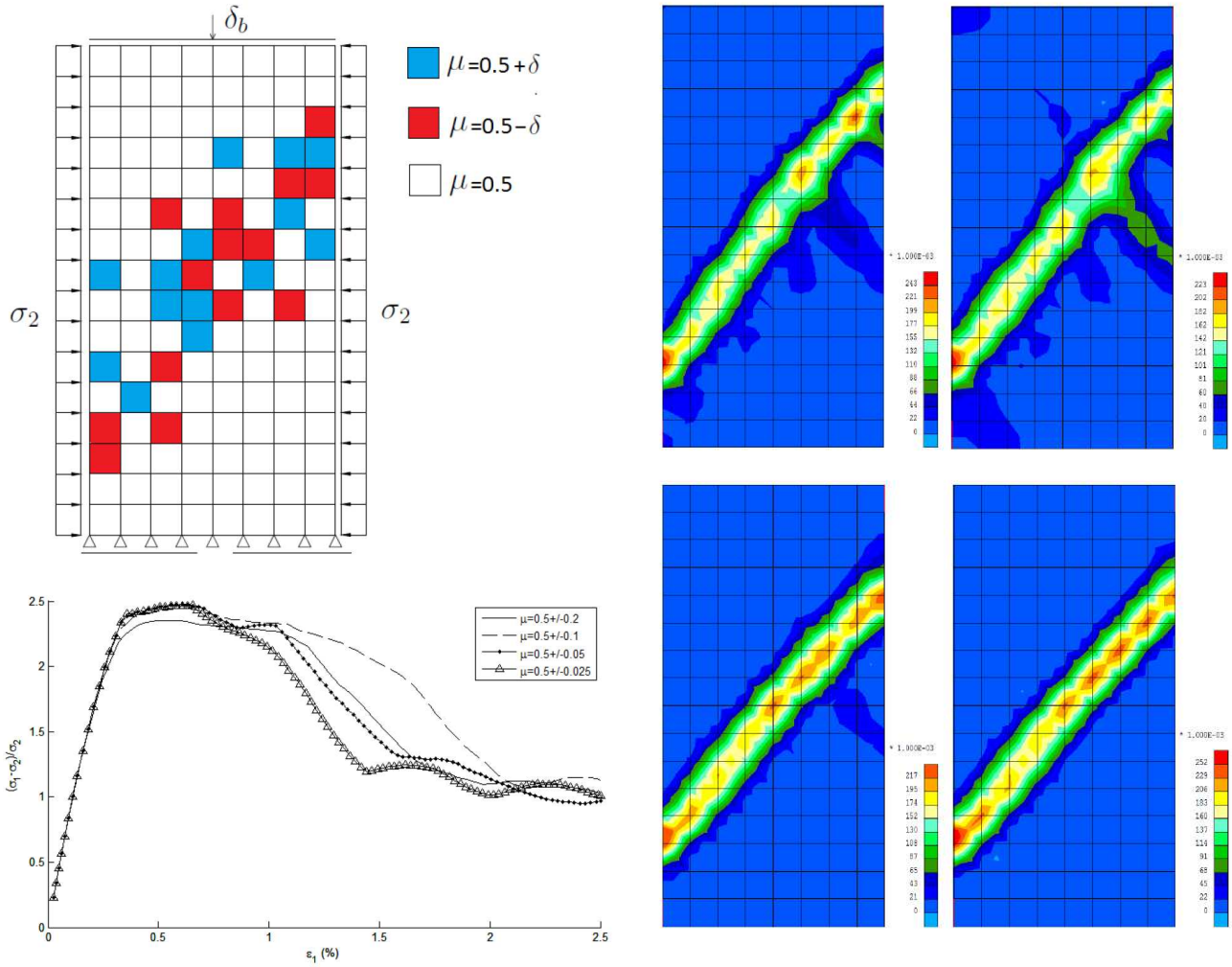

Figure 8. **Biaxial test geometry and REV distribution over the elements. Second invariant of strain for the end of a biaxial compression test. Strain stress curves.**

As commented before, any help to the localization will help the Newton iterative scheme to go straight to the solution resulting in a faster computation, accurate data of computation time is obtained from the present parametric study, the hardware used is an intel core i7 2620M processor[5], in which the four simulations will run at the same time, one in each one of threads, the results are presented together with the homogenous case ($\delta = 0$) (Fig. 9) showing a decrease of the computation time as the sample increases the inhomogeneity: from 54h for the homogeneous case to 41h for $\delta = 0.1$ representing a reduction of 24% of computation time with respect to the homogenous case.

[4] In contraposition to infinitesimal.

[5] Other parameters as the RAM memory are not relevant since this multiscale model is intensive in processor time (integration of the constitutive law), but not in memory usage (the solver deals with a small finite element rigidity matrix, easily factorisable).

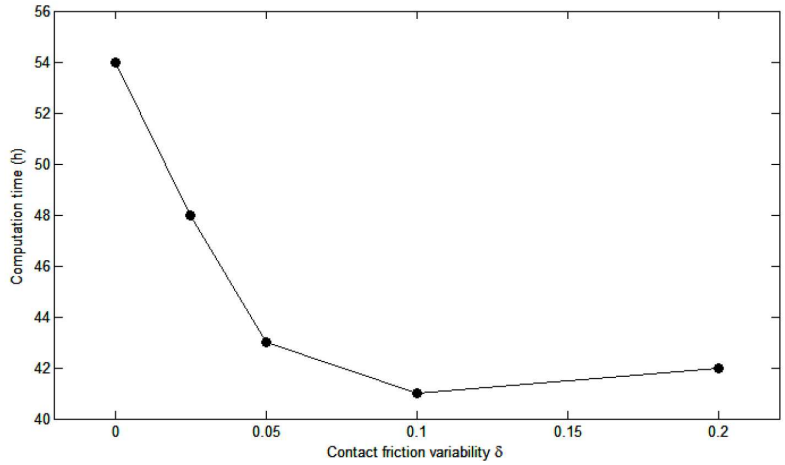

Figure 9. **Computational time for parametric study of REV variability.**

PARALLELIZATION

Introduction

Since the invention of computers till the last decade the increase of performance was mainly due to the increase of clock speed of the processor. Nowadays this scenario has changed, because of physical and energy dissipation limitations the clock speed cannot or is not practical to be increased anymore, so the strategy is to increase the number of processors in the same micro sharing the same memory and being able to perform different computations in parallel. To take profit of these new architectures the old computing paradigms must be adapted to be able to split the computation load in parallel regions.

Numerous examples of FEM parallelisation exist in the literature: early works (Farhat and Crivelli, 1989) already focus on nonlinear FEM problems with shared memory architectures achieving improvements by reducing the overhead required by the element-by-element concurrent computations, Pantalé (2005) presents a study of the effect of different strategies on the speed up in an object oriented FEM code, Nakajima (2005) uses an hybrid MPI/OpenMP implementation applied to a 3D FEM linear elastic problem being able to solve a configuration with 2.2E9 DOF using the Earth Simulator[6] and achieving peak performance of 3.80 TFLOPS. Guo et al. (2014) uses an hybrid MPI/OpenMP implementation in order to parallelize an unstructured finite element model applied to fluid mechanics.

Element loop vs solver, speedup

FEM problems can be parallelized both in the gauss point integration loop and the solver. For the gauss point integration loop, little changes are required since each of the gauss points is independent thus each one can be computed by different processors. For the solver part, the global stiffness matrix can be split into different parts, each one can be solved individually and finally solve a system of equations with the solution of each part. Obviously this parallelisation needs deeper modifications of the original code since the splitting of the global matrix is not automatic. Depending on the problem, the ratio between the time spent on the

[6] Was a highly parallel vector supercomputer system in Japan for running global climate models and problems in solid earth geophysics, it was the fastest in the world between 2002 and 2004 with a capacity of 35,85 TFLOPS.

elements and the solver can vary. Typically, problems with analytical laws and fine meshes are solver intensive meaning that most of the computation time is spent on the solver, on the other hand, double scale problems with coarse macroscale mesh are element intensive meaning that most of the computation time is spent on the integration of the gauss points in the element loop.

This implies, according to Amdahl (1967), a theoretical possible speedup as given in (Eq: 3). The gauss point parallelization is less and less efficient as we increase the number of elements because the time devoted to the solver increases exponentially[7], with the size of the global stiffness matrix. For a big number of processors the speedup factor tends to an asymptotic value linked to the time devoted to the non-parallelizable part (Fig. 10). The mean weakness of multiscale problems as FEMxDEM is the computational expenses related to the integration of the microscale. For less than 512 elements the speedup presents an almost linear relation with the number of processors if this number is less than approx. 50 (Fig. 10).

$$S(n) = \frac{T(1)}{T(n)} = \frac{1}{B + \frac{1}{n}(1 - B)}$$

Equation 3. **Amdahl speedup expression.**

In the previous lines we showed that the element loop parallelization speedup becomes asymptotic with respect to the number of processors (Fig. 10) meaning that the problem switches from element intensive to solver intensive. In this case, the parallel architectures will be less efficient because the time devoted to the element loop tends to zero. This situation is equivalent to the classical FEM using analytical laws thus becoming FEMxDEM an appropriate approach to model real scale problems in equality to pure FEM schemes

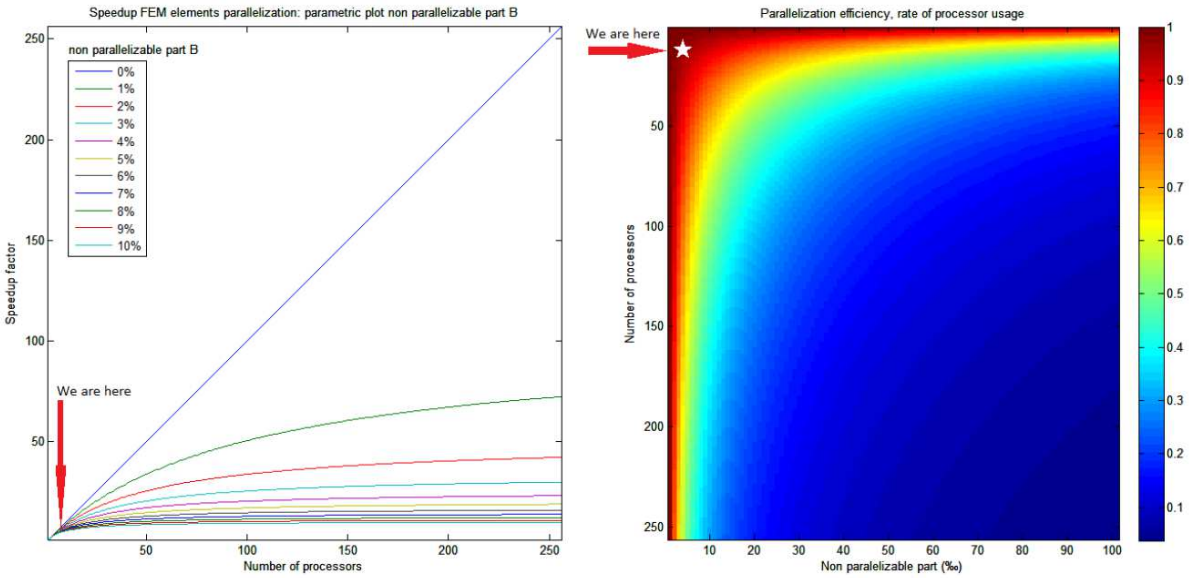

Figure 10. **Plot of theoretical speedup factor using Amdahl formula. Parametric study for different values of B (non paralelizable part) from 0% to 10%. And Parallelization efficiency depending on B (non parallelizable part) and n (number of processors or threads available.**

[7] Quadratic in 2D problems. if Gauss Seidel resolution is considered, in the present case LU factorisation is used, probably decreasing the computation time for bigger matrices.

CONCLUSIONS

The homogenization of a DEM REV serves as a constitutive law for a FEM scheme; this allows us to model granular materials such as, sand, rock or concrete without using phenomenological laws in the first gradient Cauchy expression. The code is not intended to model clay due to the different nature of its microscale.

A very rigorous work has been done concerning the Newton method operator in order to obtain a more efficient iterative method, different operators than the tangent consistent one have been tested. Other techniques have been applied intended to improve the performance of the method, such as geometrical defects or REV variability in an attempt to bring heterogeneity to the initial state.

The code has been parallelized in the element loop, the parallelisation of the element loop can provide a major improvement of the performance, up to 99% of time saving based on elements-solver load ratio for a 512 element sample, for the moment there is no interest on the parallelization of the solver, this scenario can change if in the future, taking advantage of the parallel architectures, the number of elements is increased to higher values.
After the parallelisation of the code, and when used in a high number of parallel cores machine, it switches from element intensive to solver intensive, meaning that it becomes as powerful as analytical law FEM codes.

The definition of the model includes a second gradient constitutive relation.

REFERENCES

Amdahl, G. M., 1967. Validity of the single processor approach to achieving large scale computing capabilities. In: Proceedings of the April 18-20, 1967, spring joint computer conference. ACM, pp.

Bigoni, D. & Hueckel, T. 1991. Uniqueness and localisation – I. Associative and non-associative elastoplasticity. *Int. J. Solids Structures* 28(2): 197-213.

Crisfield, M., Wills, J., 1988. Solution strategies and softening materials. Computer methods in applied mechanics and engineering 66 (3), 267$^{\perp}$ 289.

Cundall, P.A. & Strack, O.D.L. 1979. A discrete numerical model for granular assemblies. *Géotechnique* 29(1): 47-65.

De Borst, R., 1987. Computation of post-bifurcation and post-failure behavior of strain-softening solids. Computers & Structures 25 (2), 211$^{\perp}$ 224.

Farhat, C., Crivelli, L., 1989. A general approach to nonlinear fe computations on shared-memory multiprocessors. Computer Methods in Applied Mechanics and Engineering 72 (2), 153_171.

Gastebled, O., May, I., 2000. Bifurcation in the numerical simulation of softening mechanisms. Computers & Structures 78 (6), 745⊥ 755.

Guo, N., Zhao, J., 2014. A coupled fem/dem approach for hierarchical multiscale modelling of granular media. International Journal for Numerical Methods in Engineering.

Kruyt, N., Rothenburg, L., 1998. Statistical theories for the elastic moduli of two-dimensional assemblies of granular materials. International journal of engineering science 36 (10), 1127⊥ 1142.

Miehe, C. and Dettmar, J. (2003), A framework for micro-macro transitions in periodicparticle aggregates of granular materials, Comput. Methods Appl. Mech.Engrg. 196, 225-256.

Nakajima, K., 2005. Three-level hybrid vs. _at mpi on the earth simulator: Parallel iterative solvers for _nite-element method. Applied Numerical Mathematics 54 (2), 237_255.

Pantalé, O., 2005. Parallelization of an object-oriented fem dynamics code: in_uence of the strategies on the speedup. Advances in Engineering Software 36 (6), 361_373.

Pasternak, E., Dyskin, A. V., Sevel, G., 2014. Chains of oscillators with negative stiffness elements. Journal of Sound and Vibration.

Paulino, G. H., Liu, Y., 2001. Implicit consistent and continuum tangent operators in elastoplastic boundary element formulations. Computer methods in applied mechanics and engineering 190 (15), 2157⊥ 2179.

Combe G., Roux J.-N., 2003. Discrete numerical simulation, quasistatic deformation and the origins of strain in granular materials 3ème Symposium International sur le Comportement des sols et des roches tendres, Lyon, 22-24 Septembre 2003, In di Benedetto et al., pp 1071-1078,

Shi, J., Cris eld, M., 1992. A simple indicator and branch switching technique for hidden unstable equilibrium paths. Finite elements in analysis and design 12 (3), 303⊥ 312.

Buried explosions in dry and saturated sand

E. Roger, B. Loret
Laboratoire Sols, Solides, Structures, Grenoble, France
Eve.roger@3sr-grenoble.fr

ABSTRACT

The aim of this work is to get in numerical simulations the same aerial pressures and impulses as in experiments of buried explosions in dry and saturated sand. A soil model with a non linear elasticity and a viscoplasticity of Perzyna has been developed. Water content has been taken into account through the stiffening of the soil. The model was written in a user routine and incorporated in LS Dyna to run Eulerian simulations. Small scale experiments have been carried out to obtain data for simulations with the model. Pressure gauges were located at various heights above the buried explosion and the propagation of the shock wave was followed with a high speed camera and the technique of shadowgraphy. The density and the water content of the soil were controlled before each shot. The comparison between the simulations and the experiments provide similar results.

INTRODUCTION

To reproduce the effects of a buried explosion, various phenomena must be taken into account in soil modeling: a very large soil compression (since stresses of several gigapascal are reached in the soil close to the explosive) but also tension (which provokes the soil raise and the soil projections). If a structure stands above the buried detonation, the impulse corresponds to the momentum which is transferred by the explosion. It is composed by the shock wave generated by the detonation and by the soil projections because of the kinetic energy they drive. Their contributions can be very important in particular when it deals with fine grained soils.
The model which is described in the following has been developed for a sand which can be saturated. As a matter of fact, various authors noticed that water in soil increases the impulse.
The strain rates generated in soils by explosions are very important (with values between 1000 and 10000 s^{-1}). Dynamic soil modeling is less studied in saturated soils than in dry soils. However modeling a soil at these strain rates requires to take into account viscoplasticity.

CONSTITUTIVE SOIL MODEL

A viscoplastic model with a non linear elasticity has been developed from a model of Tong and Tuan (2007). An isotropic hardening was considered.
The constitutive model is derived from the Drucker Prager model and is constituted of 3 yield surfaces: a cap surface f_1 (equation 1) which can hardening when stresses increase and which has an elliptic form, a failure surface f_2 (equation 2) which allows to limit shear and a surface f_3 (equation 3) with an elliptic form defined by a cutoff value to control tension. The three yield surfaces are continuous to have a whole yield surface with a continuous normal (figure 1).

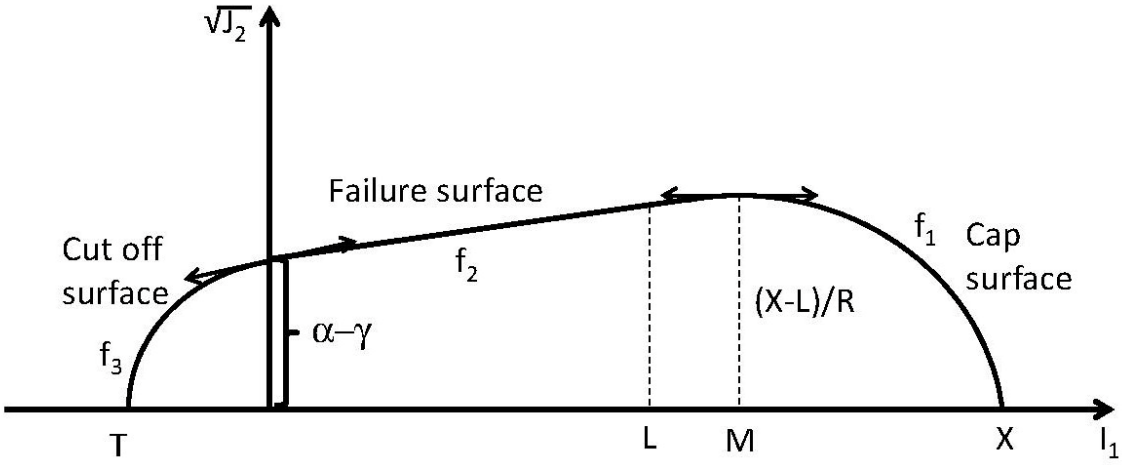

Figure 1. **Yield surface constituted of 3 parts: a tensile part defined by a cutoff value T, a failure surface and a cap surface which can harden**.

$$f_1\left(I_1,\sqrt{J_2}\right)=\sqrt{J_2+\frac{1}{R^2}\left(I_1-M\right)^2}-\frac{1}{R}\left(X-M\right) \qquad (1)$$

$$f_2\left(I_1,\sqrt{J_2}\right)=\sqrt{J_2}+\alpha-\gamma\exp\left(-\beta I_1\right)+\theta I_1 \qquad (2)$$

$$f_3\left(I_1,\sqrt{J_2}\right)=\sqrt{J_2+\frac{B^2}{A^2}\left(I_1-\left(A-T\right)\right)^2}-B \qquad (3)$$

$$A=T\,\frac{Tdf_2/dI_1(0)-f_2(0)}{2Tdf_2/dI_1(0)-f_2(0)} \qquad (4)$$

$$B=\frac{A^2}{A-T}\sqrt{1-\frac{(A-T)^2}{A^2}}\,\frac{df_2}{dI_1}(0) \qquad (5)$$

In above equations, I_1 is the first stress invariant such as I_1= - tr σ, J_2 is the second stress invariant, X corresponds to the intersection between the cap surface and the I_1 axis, M is the

point of the cap where the tangent is horizontal, L is the value of I1 such as $f_1(L)=f_2(L)$ and α, β, γ and θ are parameters defined by the material. T is the tensile limit.

The hardening law is the following:

$$X(k) - X(0) = \frac{1}{D}\left(\left| 1 - \frac{k}{w} \right|^{-1} - 1 \right) \text{ , k= - tr } \boldsymbol{\varepsilon}_{vp} \quad (5)$$

This law is function of the viscoplastic volumetric strain, of a parameter w which can be considered as the volumetric fraction of void in the soil, and D which is a parameter linked to the material.
In a whole, the material requires 12 parameters.

SOIL STIFFENING DURING EXPLOSION

Soils are constituted of three phases (solid grains, water and void). In quasi static regime, water is considered as incompressible and if the soil is compressed, water and air are going to be progressively evacuated from the solid skeleton. This hypothesis is not valid anymore during shocks. For large dynamic compressions like buried explosions, the soil behaves as a undrained medium because water is trapped in the soil and does not have the time to escape. For stresses in the order of magnitude of gigapascal, elastic moduli which vary but not in a significant way during quasi static tests, greatly increase (Zakrisson et al. (2012), Fox & Lee (2014)).
These two aspects have been taken into account in the elastic part of the model. The elastic moduli increase with the average of stresses.

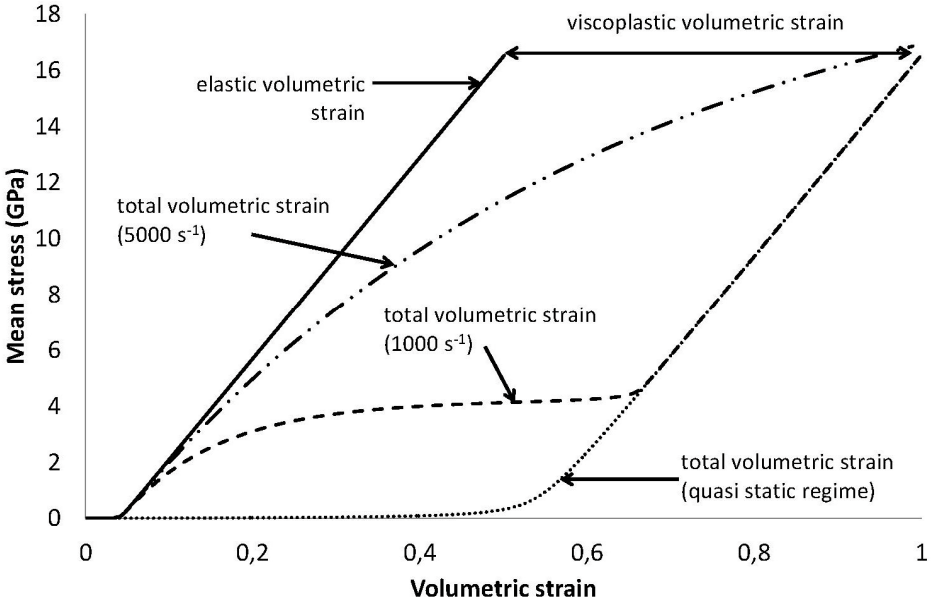

Figure 2. : **Mean stress in relation to the volumetric strain during an isotropic compression test for a quasi static regime and for a strain rate of 1000 s^{-1}.**

When stresses are very large, the bulk modulus K tends toward the grain modulus if the soil is dry (30 to 40 GPa), and toward a modulus which depends both on the grain modulus and on the water modulus weighted by the volumetric fraction of water otherwise. Figure 2 presents

the increase of mean stress in relation to the elastic and the total volumetric strains for an isotropic compression test in a quasi static regime. During an explosion, the soil undergoes strain rates between 1 000 and 10 000 s^{-1}. When the soil contains water, its mechanical behavior depends on the strain rate of the test. In figure 2, the total volumetric strain in an isotropic compression test is compared between a quasi static regime and a strain rate of $1000s^{-1}$. Inertia is visible on the curve, underlining the effect of viscoelasticity.

SMALL SCALE EXPERIMENTS

Small scale experiments have been carried out in dry and saturated sands. They deal with a small quantity of explosive buried at various depths. Pressure gauges were mounted on a shaft at various heights above the location of the buried detonation. Figure 3 shows typical pressure results for a buried detonation.

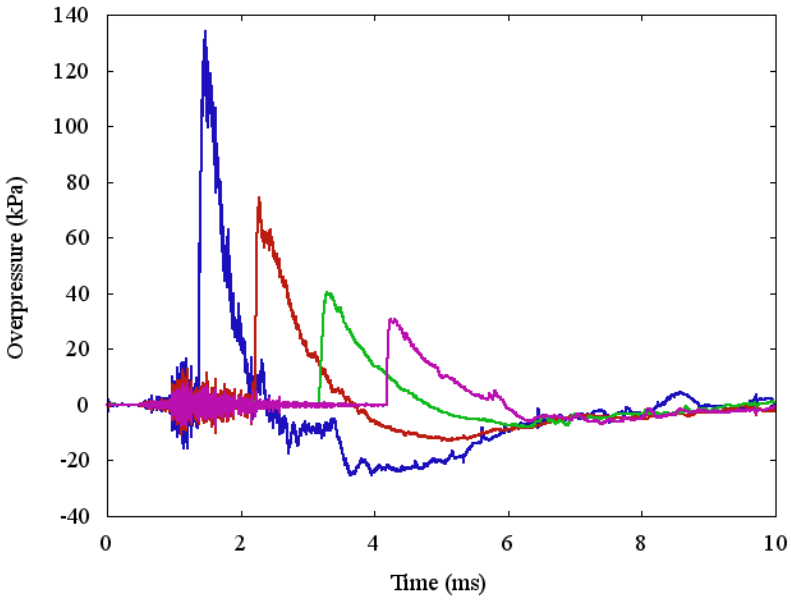

Figure 3: **Typical pressure curves obtained at various heights above a buried detonation**

The four pressure curves on figure 3 have the same shape: first the pressure increase within a microsecond. The pressure intensity is all the more important since the location of the measure is close to the explosive. The pressure decreases then exponentially and takes values below the atmospheric pressure which is due to the mitigation waves which follow the shock wave. Finally the pressure tends to the atmospheric pressure.

A reflective panel was placed in the background of the test to follow the shock wave with a high speed camera. As a matter of fact, the shock wave which is produced by the detonation drives a difference of density which is naturally visible. On the reflective panel, its reflection is emphasized. This technique is called shadowgraphy. On top of clearly following the propagation of the shock wave, the soil raising (which is originally above the buried explosive) and the soil projections can also be distinguished.
Water content and soil density were controlled before and after each shot with two techniques. First a gammadensitometer was used: a probe is placed in the soil and sends two nuclear sources. The fast neutrons are slowed down when colliding with hydrogen atoms. Since water is the main source of hydrogen in the soil, the water content can be obtained. Gamma rays are spread when colliding with grains. The dispersion is measured by the probe and related to the

soil density. Traditional laboratory tests constitute the second sets of soil controls: a soil sample with a known volume is weighted to get its density, and is oven dried for the water content. Both methods provide similar results.
The soil crater produced by the detonation is scanned to get its dimensions.

COMPARISON BETWEEN NUMERICAL SIMULATIONS AND EXPERIMENTS

The model was written in a user routine and incorporated in LS Dyna. Axisymmetric Eulerian simulations reproducing the small scale experiments were run with the same dimensions. The pressures and the time of arrival of the shock wave were compared in figures 4 and 5 for three depths of burial. In the figures, the deepest detonation corresponds to DOB 3.

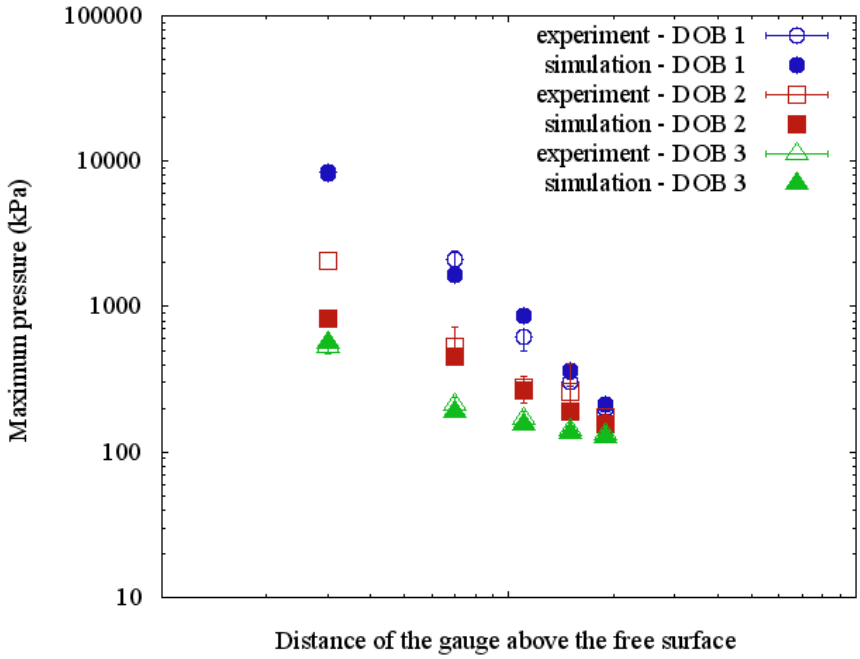

Figure 4: **Comparison between numerical simulations and experiments of pressures for three depths of burial (DOB)**

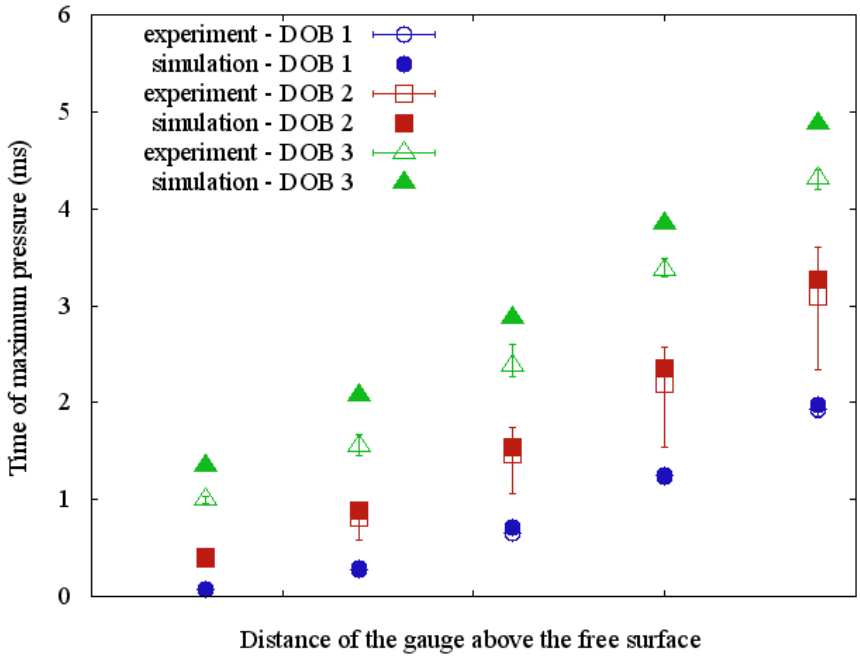

Figure 5: **Same as figure 4 but for times of arrival of the shock wave**

The pressures obtained in simulations and experiments are similar. As for the times of arrival of the shock wave, a small delay exists for the deepest detonations. In fact, since this delay remains the same for all the gauges, it may be due to the soil preparation, and in particular to the grains which are placed above the explosive.

CONCLUSION

To simulate the effects of buried explosions, a soil model has been developed with a non linear elasticity to make the soil resist to the large stresses generated by detonations. The water content was taken into account because of its important contribution to the impulse. Small scale experiments were carried out to get data for the simulations. The pressures due to the detonations of explosives buried at three different depths were recorded at various heights, in dry and saturated sands. Numerical simulations were run to reproduce these experiments. Similar results were obtained.

REFERENCES

Hallquist J.O., LS-DYNA Keyword user's manual, Version 971/Rev 5, Livermore Software Technology Corporation, 2010

Tong, X. & Tuan, C. Y. 2007, Viscoplastic Cap Model for Soils under High Strain Rate Loading, Journal of Geotechnical and Geoenvironmental Engineering, Vol. 133, No. 2, 206-214.

Zakrisson, B. et al. 2012, Modelling and simulation of explosions in soil interacting with deformable structures, Central European Journal of Engineering, Vol. 2, No. 4, 532-550.

Fox, D. M., Lee, J. S. 2014, The influence of water, dry sand, and unsaturated sand constitutive behavior on the blast response of a rigid target, International Journal of Impact Engineering, 65: 163-173.

DEM simulations of unsaturated soils interpreted in a thermodynamic framework.

C. Chalak, B. Chareyre & F. Darve
Laboratoire Sols, Solides, Structures, Grenoble, France
caroline.chalak@3sr-grenoble.fr bruno.chareyre@3sr-grenoble.fr
Felix.Darve@inpg.fr

ABSTRACT

This work deals with the study of the behaviour of unsaturated soils at the grain scale. A solid and verified thermodynamic framework that allows to fill the gap between thermodynamics and the DEM modelling is introduced. The study reduces as a start to a simple system of two particles of different radii connected by a microscopic pendular incompressible liquid bridge in perfect wetting conditions. The energy supplied to the system is determined and is divided into two parts: a) the energy due to the change of the matric suction in the system and b) the energy resulting from the movement of the particles with respect to each other. The internal energies were also calculated. The results obtained from the first law of thermodynamics show that the interfaces between the different phases present in the medium have significant importance in the macro formulation of energies and must be taken into account.

INTRODUCTION

The macro behavior of unsaturated soils is dictated by the interactions between particles subjected to capillary effects which makes their study in the framework of continuum mechanics no longer sufficient. A micromechanical study where new features due to capillary forces in the medium must be taken into account to better describe how these materials behave is then required.

A micromechanical thermodynamic framework is introduced in the following work. The advantage of such study is that at the level of the microstructure of the soil, it is accounted for all the elements present in the medium, including the interfaces that separates the different phases in the medium.

One of the first to highlight the importance of the interfaces in the formulation of free energy and their influence on the effective stress tensor was Coussy (Dangla & Coussy (2002)).

Other studies also following a thermodynamic approach such as Gray et al. (2002) and Nikooee et al.(2013) have introduced balance laws for interfaces.

Nikooee et al. (2013) proposed a new formulation for the effective stress tensor assuming that the deformation in the soil can result a change in the curvature of fluid-fluid interfaces and alter their free energies . This assumption leads to a separate term in the formulation of the effective stress tensor taking into account the amount of wetting non-wetting interfaces and dependent on the derivative of the Helmholtz free energies on the Lagrangian strain tensor. Solid-wetting and solid-non wetting interfaces were neglected in the case of rigid grains.

The main purpose is to test the importance of these interfaces and the energy that must be associated to, in order develop new micro-macro constitutive relations suitable to better describe the mechanical behavior of these materials and fill the gap between the thermodynamics and the DEM modeling.

PENDULAR REGIME : NUMERICAL MODEL

At low water content, water bridges are formed between neighboring particles and the regime to which this study is limited is called pendular because in this case the capillary force resultant from the presence of these meniscii can be linked to the geometry of the grains and to the capillary pressure inside the medium by the capillary theory. At higher saturation, things become more complex.

The DEM model for the pendular regime model is inspired by the work of Scholtès et. al. (2012). The grains are rigid spherical grains connected by liquid bridge in perfect wetting conditions.

$$\Delta u = \gamma C \qquad (1)$$

The shape of the liquid bridge is given by Laplace equation that is the exact numerical solution and gives a relationship between the curvature of the bridge and the matric suction in the medium.

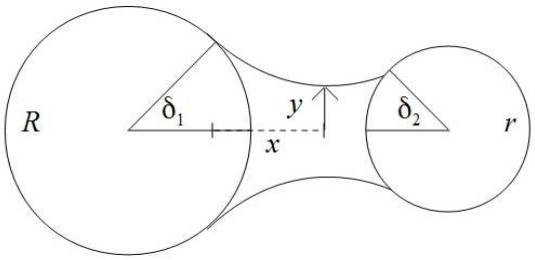

Figure 1. **Illustration of a liquid bridge between 2 spherical particles.**

Solving Laplace equation allows to calculate the capillary force and the geometric properties of the meniscus (volume and interfaces).

The capillary force is calculated at the gorge:

$$F_{cap} = \Pi\, s\, y_0^2 + 2\,\Pi\, \gamma\, y_0 \tag{2}$$

The volume of the bridge is:

$$V = \int \Pi\, y^2(x)\, dx - V_1 - V_2 \tag{3}$$

V1 and V2 are the volumes of the spherical caps covered by both filling angles.

$$A_{wn} = \int 2\,\Pi\, y(x) \sqrt{1 + y'^2(x)}\, dx$$

The wetting-non wetting interface is:

(4)

The solid-wetting interface is:

$$A_{sw} = 2\,\Pi\, R^2 (1 - \cos\delta_1) + 2\,\Pi\, r^2 (1 - \cos\delta_2)$$

(5)

The solid-non wetting interface is:

$$A_{sn} = 2\,\Pi\, R^2 (1 + \cos\delta_1) + 2\,\Pi\, r^2 (1 + \cos\delta_2) \tag{6}$$

The bridge breaks when no physical solution is possible.

ENERGY BALANCE OF A WATER BRIDGE

It is important for any model to verify the laws of thermodynamics that control the interaction between the elements of the system. In this section, the energy balance for a two spheres system connected by a bridge is examined, assuming a linear contact law between the grains and using the pendular bridge model presented in the section above.

We consider a model system of solid, wetted by water in the presence of gaz at atmospheric pressure. The system is inspired by the work of Morrow (1970) (Fig. 2). The solid phase is represented by 2 spherical grains of equal or different sizes. Water can leave or enter the bridge through a passage into one of the particles. The change in the volume of water and surface areas is assumed to be reversible. The walls of the piston have no contribution to the energy of the interfaces and the movement of pistons occurs in a way to keep equilibrium in the sample.

This work extends the work of Morrow (1970) to moving particles. In the 2 grains system presented here, one of the particles is fixed and the other can be either fixed or moving at a given velocity *v*.

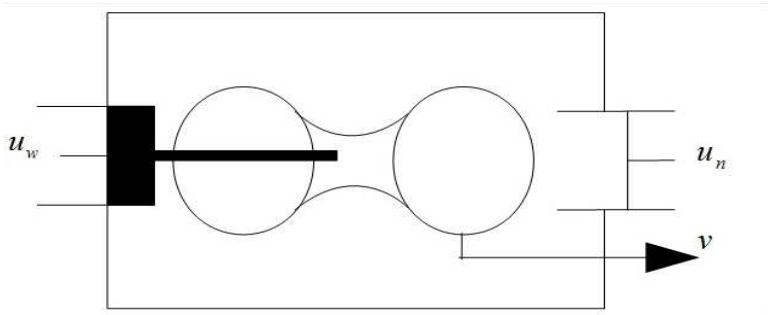

Figure 2. **Idealized system inspired by the work of Morrow (1970)**

The conservation of energy is checked for the system. For the first law of thermodynamic to be verified, the sum of all the internal energies of the components of the system must be equal to the external work supplied to the system.

$$W_{ext} = \Delta E_i \tag{7}$$

External work

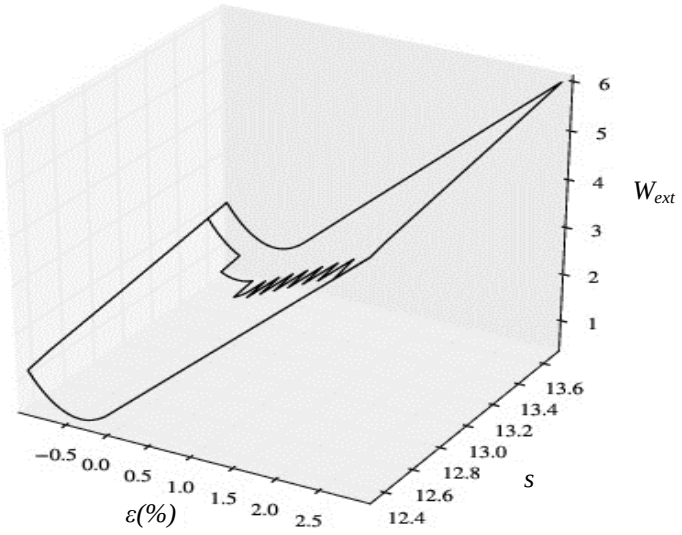

Figure 3. **The paths of external work supplied to the system.**

Different paths of external work are applied either by applying an incremental relative displacement to the particles (keeping the suction constant) or by changing the matric suction s in the medium (keeping both grains fixed) or by changing both together at time.

Figure 3 shows the plot of the external work per volume as function of the suction and the strain, and the different paths applied to the system. It is noticed that the total energy supply

to move the system from a state to another is path independent. Therefore it must be possible to define a formulation for the stored energy depending only on the current configuration.

External work is calculated as the sum of 2 components: a part related to the work done on the system by moving the piston connected to the bridge to provoke a change in the volume of water -dV and one related to the movement of grains.

$$W_{ext} = \int (F_{el} + F_{cap})\, d\alpha - \int s\, dV \tag{8}$$

W_{ext} is the total external work, s is the matric suction, V is volume of meniscus, F_{el} is the contact force , F_{cap} the capillary force and α is the relative displacement between the grains.

Internal energy

The change in the total internal energy of the system is divided into 4 components, the change in the energies of the three phases present in the system and the change of the energy of the interfaces.

$$\Delta E_i = \Delta E_s + \Delta E_w + \Delta E_n + \Sigma \Delta E_{A_j} \tag{9}$$

w denotes for wetting, n for non wetting and s for solid. A_j denotes for the three interfaces present in the system.

The pressure of the gaz in the system is equal to the atmospheric pressure which means that the change in the potential of the gaz phase is negligible. The change in the internal energy of the water is also null as it is an incompressible fluid.

The energy of the solid phase is equal to the elastic energy:

$$\Delta E_s = \Delta E_{el} = \Delta(0.5\, k_N\, x_N^2 + 0.5\, k_T\, x_T^2) \tag{10}$$

k_N and k_T are relatively the normal and shear stiffnesses.

The change in the interfacial energy is calculated based on the work of Morrow(1970).

$$\Delta E_{cap} = \Sigma \gamma_i \Delta A_i \tag{11}$$

In this case, the particles are dry, connected by a water bridge. Three types of interfaces is present in the system, the wetting- non wetting, the solid-wetting and the solid-non wetting interface.

$$\Delta E_{cap} = \gamma_{wn} \Delta A_{wn} + \gamma_{sw} \Delta A_{sw} + \gamma_{sn} \Delta A_{sn}$$

(12)

The equilibrium at contact line gives a relationship between γ_{sw}, γ_{sn} and γ_{wn}. In perfect wetting condition this relationship is:

$$\gamma_{wn} = \gamma_{sw} - \gamma_{sn} \tag{13}$$

For rigid particles $\Delta A_{sw} = -\Delta A_{sn}$; Replacing it in the previous equation, the total change in capillary energy is:

$$\Delta E_{cap} = \gamma_{wn}(\Delta A_{wn} - \Delta A_{sw}) \tag{14}$$

ΔA_{sw} , ΔA_{wn} and $\Delta A_{wn} - \Delta A_{sw}$ are plotted in figure 4 as function of strain and suction to evaluate how each of the interfaces contributes in the total interfacial free energy.
The plots show that the variation of ΔA_{sw} and ΔA_{wn} is of the same order of magnitude, and the difference $\Delta A_{wn} - \Delta A_{sw}$ that is proportionnal to the interfacial energy is much smaller than the value of the change of each individual interface. That means that all interfaces vary significantly with suction and deformation and neglecting the energy of one of the interfaces can lead to an overestimation of the free interfacial energy with a significant error.

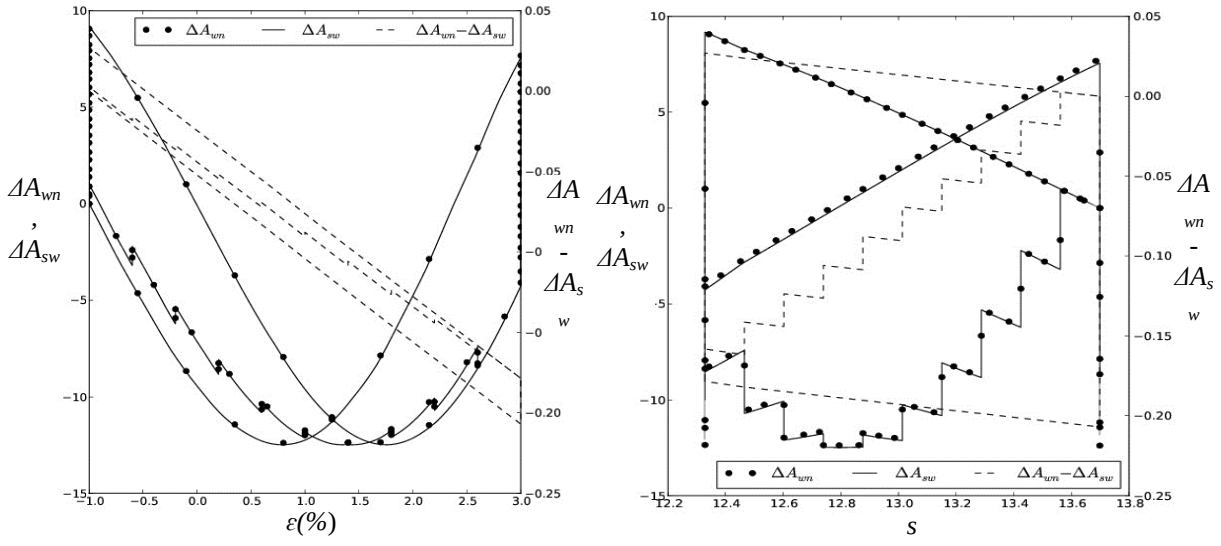

Figure 4. **The plots of the change of the interfaces ΔA_{sw} , ΔA_{wn} and $\Delta A_{wn} - \Delta A_{sw}$ with strain and suction**

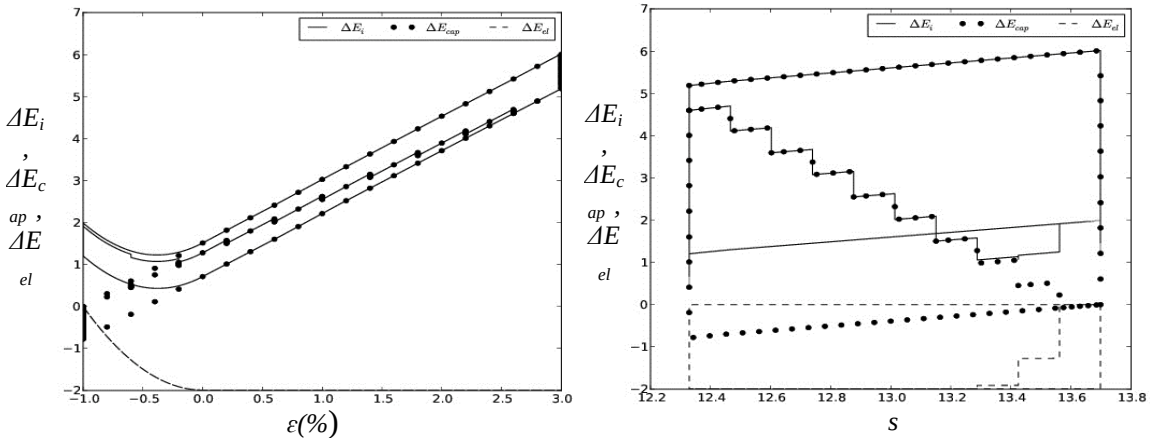

Figure 5. **The plots of the elastic and interfacial energies and the total internal energy stored in the system as function of strain and suction**

The change in internal free energy components and the total free energy that is the sum of both previous components are represented in figure 5 as function of strain and displacement.

FIRST LAW OF THERMODYNAMIC

The external work supplied to the system and total internal energy are plotted as function of strain and suction in figure 6 taking into account the energy of interfaces. The external work is equal to the internal energy stored in the system and the numerical error doesn't exceed 2 percent.

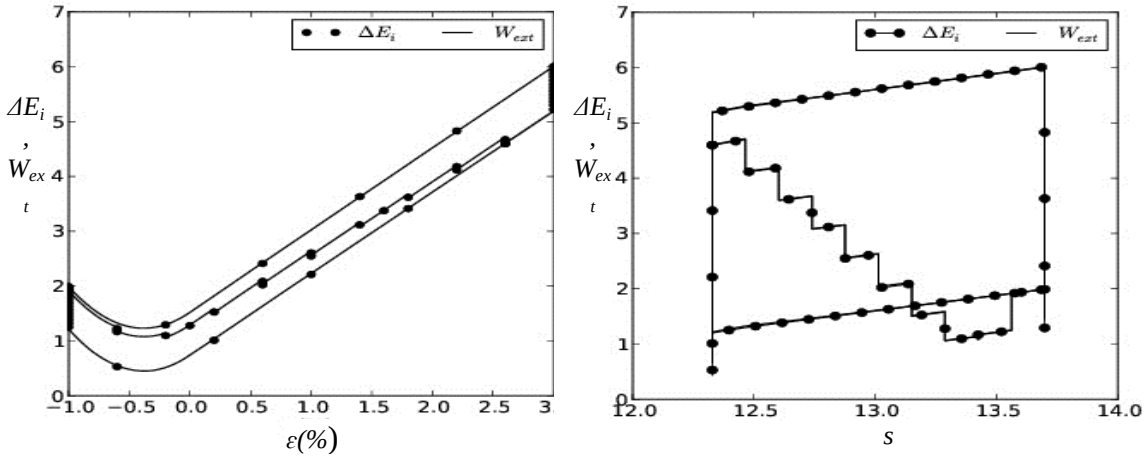

Figure 6. **The plots of the external work and the total internal energy stored in the system as function of strain and suction**

Figure 5. shows also that the interfacial energy may be significant. When the grains for example are distant, the elastic energy is equal to zero while the external work is not null since the grains are moving. If only the elastic energy was taken into account, the energy balance of the system is not verified and there are obviously missing terms that must be taken into account. These terms are equal to the energy of the interfaces in the system.

CONCLUSION

The energy balance for 2 grains connected by water bridge was verified in this work. It has been shown that the energy balanced is not verified without the energy of interfaces that play an important role in the behaviour of unsaturated soil and their energy must be taken into account. The variation of each of the interfaces was also checked and it has been shown that all interfaces must be taken into account to estimate correctly the total interfacial energy in the system.

REFERENCES

Dangla, P., & Coussy, O. (2002). Approche énergétique du comportement des sols non saturés. *Mécanique des sols non saturés*.

Gray, W. G., Tompson, A. F., & Soll, W. E. (2002). Closure conditions for two-fluid flow in porous media. *Transport in Porous media*, *47*(1), 29-65.

Morrow, N. R. (1970). Physics and thermodynamics of capillary action in porous media. *Industrial & Engineering Chemistry*, *62*(6), 32-56.

Nikooee, E., Habibagahi, G., Hassanizadeh, S. M., & Ghahramani, A. (2013). Effective stress in unsaturated soils: A thermodynamic approach based on the interfacial energy and hydromechanical coupling. *Transport in porous media*,*96*(2), 369-396.

Scholtès, L., Nicot, F., Chareyre B. & Darve, F. (2012). Discrete modelling of capillary mechanisms in multi-phase granular media. *arXiv preprint arXiv:1203.1234*.

Part Three: Hydro-Mechanical behavior of rocks

3D HM-DEM model for Hydro-Fracturing

E. Papachristos, F.V. Donzé & B. Chareyre
Laboratoire Sols, Solides, Structures, Grenoble, France
efthymios.papachristos@3sr-grenoble.fr,, frederic.donze@3sr-grenoble.fr, *bruno.chareyre@3sr-grenoble.fr*
and
L.Scholtès
*Lab*oratoire *GeoRessources,Vandoeuvre-lès-Nancy, France*
luc.scholtes@univ-lorraine.fr

ABSTRACT

Numerical methods used to study hydraulic fracturing in low permeability rock masses need to take into account the interaction between the progressive failure mechanism of the intact rock matrix and the pre-existing natural fractures. A fully coupled hydro-mechanical 3D discrete elements model dealing with such interaction is presented here. The ultimate objective is to grasp the role of the rock-matrix failure on the propagation of the main fluid driven fracture under different stress fields and pre-existing fracture orientations. The proposed method provides the spatiotemporal distribution of the induced crack events which can be tracked during the simulations, making possible the identification of the local mechanisms leading to macro-failure in the rock matrix or reactivation of the discontinuity planes. A hydro-fracking experimental test was simulated and, is presented in this paper as part of the validation process of the model.

INTRODUCTION

With the expansion of shale gas and geothermal reservoirs exploitation, the technique of Hydraulic Fracturing (HF) has been widely used over the past years (McClure, 2012; Britt, 2012). Despite recent advances in micro-seismicity analysis or numerical modeling (Nagel et al., 2013), the way progressive failure of rocks affects the fluid flow depending on the in situ stress conditions or the rock heterogeneities is not fully controlled yet (Zoback, 2010).

In this work we focused on setting up a three-dimensional discrete elements model to study fluid driven fractures propagation. The intact rock is modeled by a discrete element method (DEM) able to reproduce fracture initiation and propagation (Scholtès and Donzé, 2013, Garcia et al., 2013). The pre-existing fractures are explicitly modeled and can be individually defined or be part of a discrete fracture network (DFN) (Harthong et al., 2012). Their mechanical response is fully coupled with the fluid within a HM-DEM framework. The

fluid flow and it's interaction with the intact matrix and the pre-existing discontinuities is modeled through a Pore-scale Finite Volume (PFV) scheme (Chareyre et al., 2012, Catalano et al., 2014), specially enhanced for fractured rock modeling.

In order to validate the hydraulic fracture initiation and propagation, a comparison is made with a hydrofracking test performed in sandstone specimens (Stanchits et al., 2013). The overall response of the specimen to the mechanical and hydraulic loading is compared.

NUMERICAL MODEL

DEM model

A 3D coupled discrete element model was used for this study. This model is implemented in YADE OPEN DEM (Kozicky & Donzé 2008, 2009), an extendable open-source framework. A detailed description of the model can be found in several references (Šmilauer et al., 2010, https://yade-dem.org/doc/) and only a short description will be given here. The DEM model considers a set of discrete spherical elements interacting through cohesive-frictional brittle bonds with the possibility for near neighbor interaction. Scholtès and Donzé (2013) showed the advantage of such feature to obtain realistic brittleness ratios and nonlinear failure envelopes for various rock types. The cohesive-frictional bonds behave according to an elastic-brittle constitutive law. For the elastic domain, constant shear and normal stiffnesses are computed depending on the size of the discrete elements and the desired macroscopic parameters. Linear elasticity holds until shear or tensile local bond failure occurs. The failure criteria are expressed using a modified Mohr-Coulomb criterion based on three parameters, a friction angle φ and two stress-like values defining the maximum admissible forces F_s^{max} and F_n^{max} are derived. After brittle rupture, frictional interaction occurs between strictly contacting discrete elements. Such interaction presents no tensile strength, and a purely frictional shear resistance that depends on the friction angle φ. Overall, the DEM model for the rock matrix includes six parameters (Scholtès & Donzé, 2013).

DEM modeling of pre-existing rock discontinuities

Due to the spherical shape of the discrete elements, planar discontinuity surfaces cannot be described without being dependent of the discretization. For this reason, the present model uses the smooth-joint model (SJM) proposed by Mas Ivars et al. (2011). The SJM is applied to all interactions located across pre-existing discontinuity surfaces. The SJM modifies the orientation of the interaction according to the orientation of the pre-existing discontinuity. A frictional elastic-plastic behavior is prescribed along the discontinuity surface, with very small influence of the roughness generated by the spherical elements. The SJM's behavior is characterized by four parameters: normal and tangential joint stiffnesses, a local joint friction angle ϕ and a dilation angle ψ. It is important to note that ϕ corresponds to the resulting macroscopic friction angle of the simulated discontinuity surface, unlike the matrix, where the internal friction angle of the medium does not correspond to the friction angle φ defined at the bond scale (Scholtès & Donzé, 2012).

Fluid Modelling based on a PFV scheme

The numerical approach for simulating the rock mass behavior under fluid injection uses a pore-scale finite volume (PFV) scheme which enables the model to simulate the fluid flow through the rock-matrix as well as through the fractures (see Chareyre et al., 2012,

Catalano et al., 2014). This scheme offers the possibility to set up a complete hydromechanical coupling by means of fluid forces applied on the discrete elements and pore fluid deformation as a function of the displacement of the latters. The pore network model is built through a weighted Delaunay triangulation over the discrete element packing. The discrete elements form the vertexes of the tetrahedrons which represent an elementary pore unit. The Voronoi diagram defines a pipe network that connects the pores one with each other. The permeability of these pipes is defined either through a parallel plate model for pre-existing fractures and induced cracks or through a pipe model for the rock matrix.

The fluid flow formulation characterizing the flow through cracks or pre-existing joints, is based on the cubic law. Considering a normalized width per length unit, the fluid discharge can be expressed such as,

$$q_{ij} = \frac{(a_0+a)^3}{12\mu}\Delta P \quad (1)$$

Where q_{ij} is the discharge from pore *i* to pore *j*, μ the dynamic viscosity, ΔP the pressure variation, a_0 is the residual fracture aperture and *a*, the aperture that corresponds to the relative displacement between interacting discrete elements acting at the edge of the neighboring pore cells.

If the flow from pore *i* to pore *j*, takes place through facets without cracks, i.e. inside the rock matrix, the discharge is given by,

$$q_{ij} = \alpha \frac{R_h^2 A_{ij}}{\mu}\frac{\Delta P}{L_{ij}} \quad (2)$$

with α being a scaling factor, A_{ij} the area of the facet, R_h^2 the hydraulic radius and L_{ij} the inter-pore length.

The model enables one to use either incompressible fluid (Chareyre *et al.*, 2012) or compressible fluid (Scholtès *et al.*, 2014).

NUMERICAL SETUP

The mechanical properties of the rock matrix were chosen to ensure the simulated behavior to be representative of Colton sandstone. The properties of the medium are summarized in Table 1. The mechanical properties of the interaction making the joint planes were selected to simulate non-cohesive fracture surfaces (cohesive and tensile strength set up to zero), with a friction angle equal to 30° and a dilation angle ψ of 5°.

Table 1 – Rock properties

Parameters	Values
Density [kg/m^3]	2500
E [Pa]	20.4×10^9
ν [-]	0.2
UTS[MPa]	3
UCS[MPa]	30
Rock matrix permeability [m^2]	4×10^{-16}
Fracture aperture (zero confinement) [m]	0.001

RESULTS

Hydraulically driven fracture propagation experiment

The model was used to simulate a laboratory experiment carried out by (Stanchits et al., 2013) on a Colton sandstone block. The objective was to investigate the hydraulic fracture initiation by means of acoustic emissions and volumetric measurements. Among the different tests, the fracture was hydraulically induced in an anisotropic stress field by injecting a highly viscous fluid (2.5 kPa.s) into a vertical borehole. The experiment was monitored such that the injection pressure, acoustic emissions (AE) and volumetric deformations were recorded during the test. The tested rock block was about 279.4 mm × 279.4 mm × 381 mm in size (Figure 5a). The hydraulic fracturing test was conducted by injecting the fluid into the borehole at a flow rate of $0.83\text{x}10^{-7}$ m^3/s. The borehole was drilled up to the center of the specimen and two longitudinal scribes were made along the slot to facilitate the initiation of the hydrofracturation along a preferential direction (perpendicular to the minor principal stress). The vertical normal stress (along the borehole or y-axis) represented the major principal stress with a magnitude of σ_v = 4000 psi. The intermediate principal stress of σ_H = 2000 psi was horizontal in the y-direction; the minor principal stress of σ_h = 1000 psi was in the x-direction. The stress state was maintained during the experiment (Figure 5b). The experimental results of the fluid injection test into the Colton sandstone block, i.e. borehole pressure, volume of the injected fluid, lateral deformation of the specimen and AE measurements, are shown in Figure 5b. The injection resulted in the fluid pressure increase until the breakdown pressure of about 4700 psi was reached. Then, fluid injection was interrupted few seconds after breakdown, resulting in high pressure decay. Post-mortem observations showed that, as expected, the vertical HF propagated in the x- direction perpendicular to the minor principal stress with a pancake like shape. A major finding of this study is that hydraulic fracturing initiated significantly earlier than the pressure breakdown as emphasized by AE measurements.

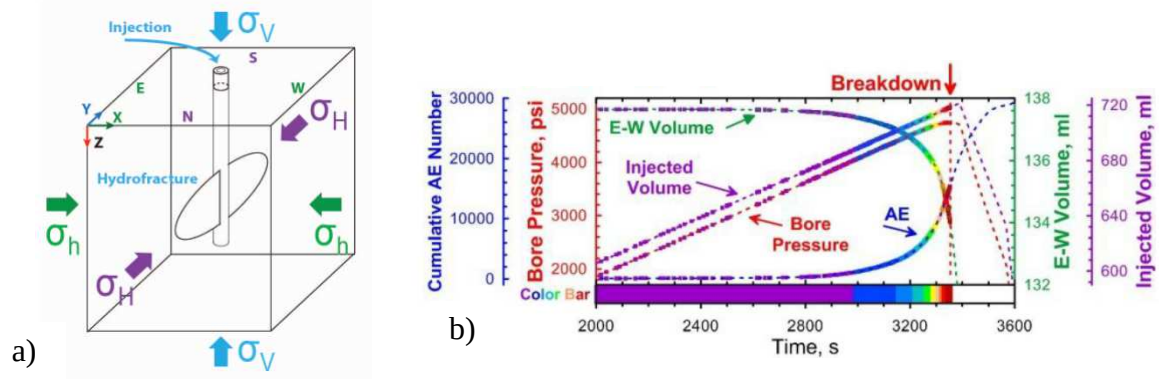

Figure 1 – On the left (a), a schematic which represents the experimental test. On the right (b) the recorded data during the injection test. It shows the evolution of the volumetric deformation along the axis of the applied σ_{min} (E-W Volume), the cumulative injected volume (Injected Volume), the corresponding pressure in the borehole (Bore Pressure) and the recorded acoustic emissions (AE) (from Stanchits et al., 2013).

Hydraulically driven fracture propagation model results

This experiment was simulated numerically in order to verify the ability of the model to reproduce the fracture path, injection pressure and the progressive failure in relation to the AE data. The simulations were run by injecting a compressible fluid with a viscosity significantly lower than in the experiments (25 Pa.s). Besides this lower fluid viscosity, the difference to the experiment lies in the fact that the injection was done in a pre-existing penny shaped crack of 50 mm diameter, located at the center of the numerical model In addition, injection was not interrupted after the breakdown as in the experiments. The resulting micro-crack pattern within the simulated block is presented in Figure 6 (bottom) and its spatial distribution is compared to AE hypocenters recorded in the experiment (top). As observed for the AE in the experiment, micro-cracks coalesced to form a vertical hydro-fracture, which propagated from the borehole towards the model boundary perpendicularly to the minor principal stress direction (x axis). The localization and the time evolution of the simulated micro-cracks are in reasonably good agreement with the AE events. However, micro-cracking and AE measurements, even though correlated, cannot fit exactly (Figure 7). Indeed, several micro-cracks can be part of a unique acoustic event, leading to an earlier activity in terms of micro-cracking. Because of that, the evolution of the micro-cracking over time is slightly different from the AE measurements and their spatial distribution is more diffuse. Note that current works are currently carried out to relate micro-cracking to acoustic events (Raziperchikolaee et al., 2014). The evolution of the borehole pressure and as well as the micro-cracking evolution are presented in Figure 7. Despite the assumptions made in the simulation, the pressure breakdown value is comparable to the one obtained experimentally. The overall evolution of the pressure matches fairly well the laboratory data. The pressure linearly increased up to the peak then decay progressively. Nonetheless, the pressure increase exhibits an earlier and more pronounced departure from linearity compared to the experiment.

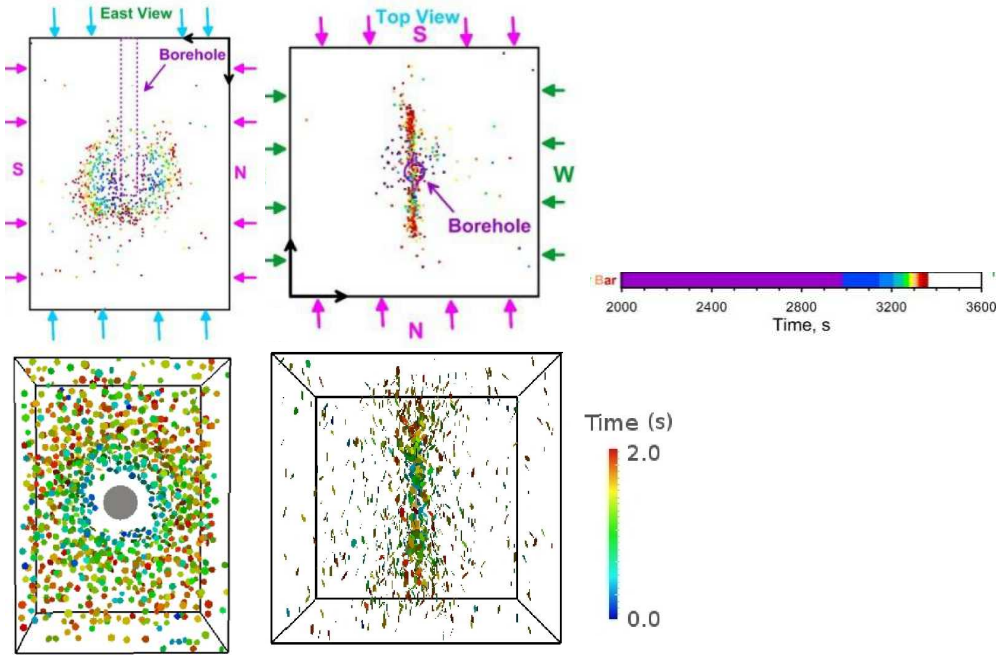

Figure 2 – On the top, two orthogonal projections of AE hypocenters from the experiment (Stanchits et al, 2013) are presented. On the bottom, two orthogonal projections of cracks inside the numerical model are shown.

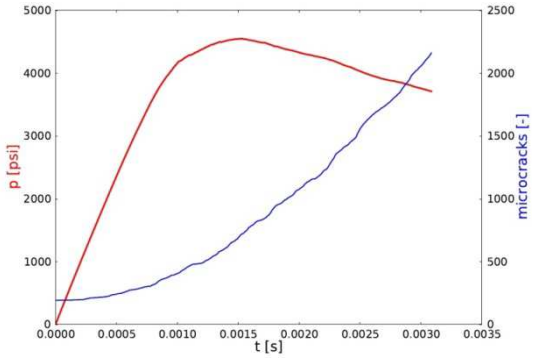

Figure 3 – Crack and pressure history (time in seconds).

CONCLUSION

A 3D coupled DEM model, able to deal with fluid driven fracture propagation in rock with pre-existing and newly created fractures is presented. The model is using explicit dynamic DEM to simulate the rock phase of the system and an enhanced pore-scale finite volumes scheme able to deal with porous matrix and fractures, to represent the fluid phase. The coupling between the fluid phase and the fractures (newly or pre-existing) is based on the initial aperture, residual aperture and the relative displacement of the elements involved in the cracks.

Hydraulic fracturing in homogeneous, non-homogeneous or jointed medium can be considered by the model. Different stress fields defined by magnitudes and orientations of the principal stresses can be also considered. The first code predictions shows a good agreement with laboratory data.

ACKNOWLEDGEMENTS

This work has been supported by TOTAL; grant number FR00006191.

REFERENCES

Britt, L. (2012). Fracture stimulation fundamentals. Journal of Natural Gas Science and Engineering, 8, 34-51.

Catalano, E., Chareyre, B., & Barthélémy, E. (2014). Pore-scale modeling of fluid-particles interaction and emerging poromechanical effects. International Journal for Numerical and Analytical Methods in Geomechanics, 38(1), 51-57.

Chareyre, B., Cortis A., Catalano, E., Barthélémy E. (2012). Pore-scale modeling of viscous flow and induced forces in dense sphere packings. Transport in Porous Media, 94(2), 595-615.

Garcia, X., Nagel, N., Zhang, F., Sanchez-Nagel, M., & Lee, B. (2013, January). Revisiting Vertical Hydraulic Fracture Propagation Through Layered Formations–A Numerical Evaluation. In 47th US Rock Mechanics/Geomechanics Symposium. American Rock Mechanics Association.

Harthong, B., Scholtès, L., & Donzé, F. V. (2012). Strength characterization of rock masses, using a coupled DEM–DFN model. Geophysical Journal International, 191(2), 467-480.

Kozicki, J., & Donzé, F. V. (2008). A new open-source software developed for numerical simulations using discrete modeling methods. Computer Methods in Applied Mechanics and Engineering, 197(49), 4429-4443.

Kozicki, J., & Donzé, F. V. (2009). Yade-open dem: an open-source software using a discrete element method to simulate granular material. Engineering Computations, 26(7), 786-805.

McClure, M. W. (2012). Modeling and characterization of hydraulic stimulation and induced seismicity in geothermal and shale gas reservoirs (Doctoral dissertation, Stanford University).

Mas Ivars, D., Pierce, M. E., Darcel, C., Reyes-Montes, J., Potyondy, D. O., Young, R. P., & Cundall, P. (2011). The Synthetic Rock Mass Approach for Jointed Rock Mass Modelling. International Journal of Rock Mechanics and Mining Sciences, 48(2), 219-244.

Nagel, N. B., Sanchez-Nagel, M. A., Zhang, F., Garcia, X., & Lee, B. (2013). Coupled Numerical Evaluations of the Geomechanical Interactions Between a Hydraulic Fracture Stimulation and a Natural Fracture System in Shale Formations. Rock mechanics and rock engineering, 46(3), 581-609.

Raziperchikolaee, S., Alvarado, V., & Yin, S. (2014). Microscale modeling of fluid flow-geomechanics-seismicity: Relationship between permeability and seismic source response in deformed rock joints. Journal of Geophysical Research: Solid Earth, 119(9), 6958-6975.

Scholtès, L., Chareyre, B., Michallet, H., Catalano, E., & Marzougui, D. (2014). Modeling wave-induced pore pressure and effective stress in a granular seabed. Continuum Mechanics and Thermodynamics, 1-19.

Scholtès, L., & Donzé, F. V. (2013). A DEM model for soft and hard rocks: Role of grain interlocking on strength. Journal of the Mechanics and Physics of Solids, 61(2), 352-369.

Scholtès, L., & Donzé, F. V. (2012). Modelling progressive failure in fractured rock masses using a 3D discrete element method. International Journal of Rock Mechanics and Mining Sciences, 52, 18-30.

Šmilauer, V., Catalano, E., Chareyre, B., Dorofeenko, S., Duriez, J., Gladky, A., Kozicki, J., Modenese, C., Scholtès, L., Sibille, L., Stránský, J. & Thoeni, K., Yade Documentation (V. Šmilauer, ed.), The Yade Project, 1st ed., 2010. http://yade-dem.org/doc/ .

Stanchits, S., Surdi, A., Gathogo, P., Edelman, E., & Suarez-Rivera, R. (2013, January). Monitoring the Early Onset of Hydraulic Fracture Initiation by Acoustic Emission and Volumetric Deformation Measurements. In 47th US Rock Mechanics/Geomechanics Symposium. American Rock Mechanics Association.

Zoback, M. D. (2010). Reservoir geomechanics. Cambridge University Press.

Doublescale modelling of hydromechanical coupling and anisotropy in localization problems[8]

B. van den Eijnden, P. Bésuelle, R. Chambon
Laboratoire Sols, Solides, Structures, Grenoble, France
bram.vandeneijnden@3sr-grenoble.fr, pierre.besuelle@3sr-grenoble.fr, r.chambon@3sr-grenoble.fr
F. Collin
Université de Liège, B-4000 Liège, Belgium
f.collin@ulg.ac.be

ABSTRACT

A new approach is investigated for the modelling of the hydro-mechanical behaviour of Callovo-Oxfordian claystone, a potential host rock for radioactive waste repositories in France. This approach is a double-scale finite element method with a micro and a macro scale. At the micro level a representative elementary volume (REV) is used to model the material behaviour. The global response of this REV serves as an implicit constitutive law for the macro scale. On the macro scale, a poro-mechanical continuum is defined with fully coupled hydro-mechanical behaviour; the microscale contains a model that takes into account the material micro structure and fluid/solid interaction to provide the material responses and associated stiffness matrices. Computational homogenization is used to retrieve these stiffness matrices from the micro level. This double scale approach is applied in the simulation of a biaxial deformation test and the response at the macro level is related to the micro-mechanical behaviour. Hydromechanical coupling is studied as well as material anisotropy.

INTRODUCTION

The principle of deep geological repositories for the disposal of high-level and intermediate-level long-lived radioactive wastes relies among others on the low permeability of the host rock. As the permeability is influenced by mechanical alteration of the material, the coupling between hydraulic and mechanical behaviour of the host rock is an important factor in the

[8] Originally published as a conference paper : van den Eijnden et.al. (2014)

study of radioactive waste disposal. This behaviour on the engineering scale is controlled by micromechanical material behaviour. In this context a double-scale hydromechanical model was developed in which a macro scale is defined at engineering level and a micro scale at the material level [Frey et.al. 2012]. The micro scale computations provide the local material behaviour for the macro scale. This requires the microscale computations to capture the micromechanical phenomena of the material by means of a representative elementary volume (REV). Homogenization of the REV response to enforced deformation provides the constitutive relations for the macro scale computation.
This paper gives a summary of the doublescale coupled model. The scale transition by computational homogenization for hydromechanical coupling is discussed after which an example is given of the application in the modelling of hydromechanical coupling in a biaxial compression test with localization. The final sections discuss material anisotropy as an effect of the microstructure. Although anisotropy is present in both mechanical and hydraulic responses, a restriction to dry simulations is made for the study of anisotropy. The results of these numerical experiments form the basis of the concluding remarks.

MACRO SCALE BALANCE EQUATIONS

On the macro level, a poromechanical continuum is defined under quasi-static assumption. This allows decomposing the constitutive relation in a classical first gradient part (derived from the micro scale), and a second gradient part that links a double stress Σ_{ijk} to the second gradient of displacement. The classical balance equations for this continuum in domain Ω can be written using the principle of virtual work by any two kinematically admissible virtual fields of displacement u_i^* and fluid pressure p^* [Collin et.al. 2006] as

$$\int_\Omega \left(\sigma_{ij}\frac{\partial u_i^*}{\partial x_j} + \rho g_i u_i^*\right) d\Omega - \int_\Gamma (\bar{t}_i u_i^*) d\Gamma = 0 \tag{1}$$

$$\int_\Omega \left(m_j \frac{\partial p^*}{\partial x_j} - \dot{M} p^*\right) d\Omega - \int_\Gamma \bar{q} p^* d\Gamma = 0 \tag{2}$$

with σ_{ij} the Cauchy total stress at the macro level, ρ the density, g_i the gravitational acceleration, $\bar{t}$ the boundary traction, $\dot{M}$ the time derivative of the fluid mass per unit volume, m_i the fluid mass flux and $\bar{q} = m_i n_i$ the fluid flux over a boundary with outward normal vector n_i. In the following, the influence of gravitational acceleration will not be considered. The field equations 1,2 are solved by finite element discretization by a Newton- Raphson scheme [1]. Therefore a linearization of the field equations that approximates the constitutive behaviour for small increments $\delta[.]$ around the updated configuration is needed to give an estimate of the next test solution. This linearization is given by the consistent tangent stiffness matrix (CTSM) in (3) by the 7×7 matrix relating the seven unknowns in (1) and (2) to σ_{ij}, m_i and $\dot{M}$.

$$\begin{bmatrix} C_{ijkl} & A_{ijl} & B_{ij} \\ D_{ikl} & E_{il} & G_i \\ H_{kl} & K_l & L \end{bmatrix} \begin{bmatrix} \frac{\partial \delta u_k}{\partial x_l} \\ \frac{\partial \delta p}{\partial x_l} \\ \delta p \end{bmatrix} = \begin{bmatrix} \delta\sigma_{ij} \\ \delta m_i \\ \delta \dot{M} \end{bmatrix} \tag{3}$$

To obtain objective (mesh independent) results for localization problems, an enriched macroscale continuum is needed that introduces an internal length in the constitutive law. Therefore a local second gradient continuum [Mindlin,1964,Germain,1973,Collin et.al. 2006] is used, that allows to decompose the constitutive relation in a classical one (stress-strain

relation) for which the double-scale model is associated, and a second gradient part that links a double stress $\boldsymbol{\Sigma}_{ijk}$ to the second gradient of displacement. This extends field equation (1) to

$$\int_{\Omega}\left(\sigma_{ij}\frac{\partial u_i^*}{\partial x_j}+\Sigma_{ijk}\frac{\partial^2 u_i^*}{\partial x_j\,\partial x_k}\right)d\Omega-\int_{\Gamma}\left(\bar{t}_i u_i^*+\bar{T}_i\frac{\partial u_i^*}{\partial x_j}n_j\right)d\Gamma=0 \tag{4}$$

where $\bar{T}_i$ is the external double traction. To avoid difficulties with higher order shape functions, constraints on the second gradient of the displacement field are enforced by a field of Lagrange multipliers [Matsushima et.al. 2002]. The second gradient constitutive relation used here is elastic and isotropic, containing one parameter D^{SG} [Besuelle et.al. 2006] that implicitly controls the width of possible localization bands. This constitutive relation acts only on the mechanical part of the macroscale model since the assumption of separation of scales between macro and micro levels allows the microscale REV to represent the local behaviour in macro scale material points.

MICROSCALE MODEL

On the micro scale, a model for hydromechanical coupling [Frey et.al. 2012] is used. This model is constituded by deformable solid grains and damageable interfaces. A linear-elastic constitutive law is used for the solids, thereby concentrating possible degradation in the interfaces. Cohesive forces T_n and T_t between the solid grains act normally and tangentially to the interface orientation as a function of the history of relative displacement Δ between the opposite interface boundaries. Two separate damage laws are used to describe these forces (Figure 1).

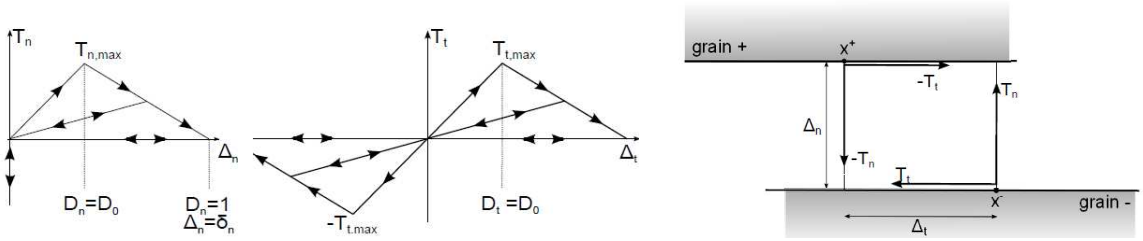

Figure 1: Damage law for interface cohesive forces. Normal cohesive forces T_n and tangential cohesive forces T_t are a function of respectively relative normal and tangential displacements Δ_n and Δ_t between the opposite interface boundaries.

In addition to controlling the material damage the interfaces form a pore channel network that is fully saturated. Fluid transport is controlled by the conductivity of the channels formed by the interface openings and the fluid pressure distribution. Fluid pressure and pressure gradient within the interfaces lead to fluid normal forces and drag forces acting on the solids. In this way, hydromechanical coupling is controlled by the interface openings. Fluid compressibility k^w is taken into account by defining the fluid density ρ^w as a function of fluid pressure p:

$$\dot{\rho}^w=\frac{\rho^w}{k^w}\dot{p},\quad \rho^w(0)=\rho_0^w \tag{5}$$

Laminar flow between smooth parallel plates is used as the model for hydraulic flow in the interfaces, which leads to a cubic relation between the interface hydraulic conductivity κ and interface normal opening Δ_n. Once the fluid problem is solved, the fluid effort on the grains is calculated and the mechanical system is solved, leading to new configuration with new channel conductivities. In this way the coupled problem is solved in an iterative way. Details

on the micro model and a full developement of the numerical procedures is given by [Frey et.al. 2012].

MICRO-TO-MACRO TRANSITION

Considering a balanced REV with periodic boundary conditions, the macro responses σ_{ij}^{M}, $\dot{M}^{M}$ and m_i^M are found by homogenization over REV domain V:

$$\sigma_{ij}^{M} = \frac{1}{V_\Omega}\int_\Omega \sigma_{ij} dV \tag{6}$$

$$M^{M} = \frac{1}{V}\int_\Omega \rho^{w} dV \tag{7}$$

$$m_i^M = \frac{1}{V_\Omega}\int_\Omega m_i dV = \frac{1}{V_\Omega}\int_\Omega \bar{q} x_j dS \tag{8}$$

The macro pressure p^M is defined as to the average of the micro fluid pressure p. The macroscale constitutive behaviour is the incrementally nonlinear relation between the seven unknowns in Equations (1-2) and the seven REV response variables of Equation (6) is given by the 7×7 CTSM in Equation (3). For purely mechanical problems first order computational homogenization by static condensation [Kouznetsova et.al. 2001] is often used to derive the CTSM. An extension of this method for the specific HM-coupled micromechanical model presented above is used here [van den Eijnden et.al 2013]. This method contains a two-step homogenization that first reduces the fluid degrees of freedom from the micro scale global system of equations and second condenses of the remaining equations into (3).

STRAIN LOCALIZATION IN BIAXIAL COMPRESSION

Biaxial compression is a commonly-used modelling exercise to study localization problems. Here a biaxial test on a $0.5m \times 1.0m$ sample with drainage on top and bottom under a compressive loading rate of 10^{-8} m/s is modelled using a 10×20 element mesh. A second gradient parameter D^{SG} is chosen such that mesh independent results are obtained for the element size and classical constitutive relation that are used here. A $1 \times 1mm^2$ microscale REV with a periodic microstructure consisting of 4 grains is chosen (Figure 2).
A minimum permeability is guaranteed by defining a minimum hydraulic opening of the interfaces of $2.0\mu m$. The normalized reaction force on the sample and the fluid pressure in the center of the sample during compression are given in Figure 3.

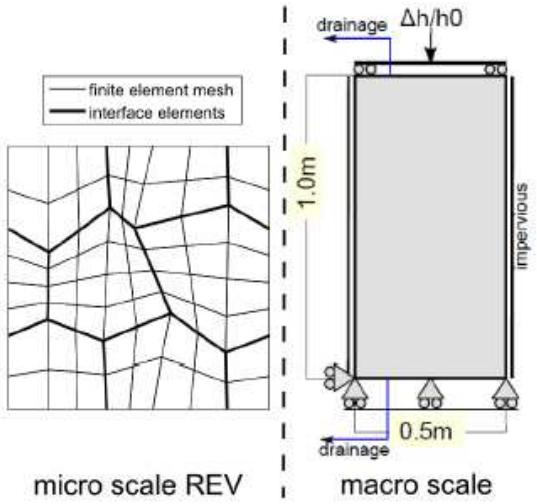

Figure 2: Left; microstructure with interfaces and macroscale boundary conditions. Right; reaction force to loading and pore pressure at sample center.

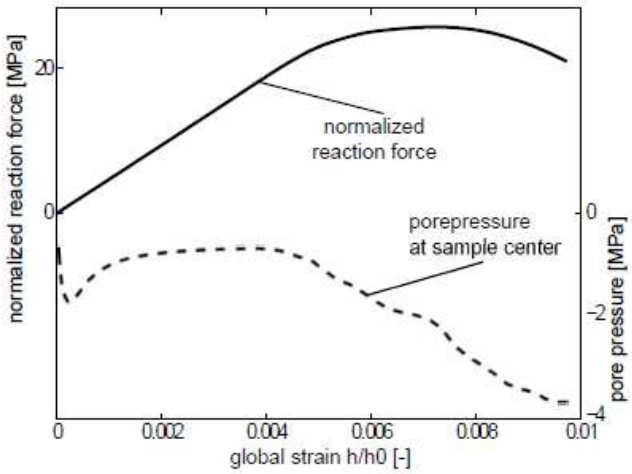

Figure 3: Reaction force to compression normalized against sample width and porepressure at sample center.

The efficiency of computational homogenization depends on the number of iterations needed at the micro level, but also on the complexity of the microstructure (number of degrees of freedom, matrix sparcity etc.) and a proper quantification of the gain in computation time is difficult. However, it is the authors experience that, at least for small microstructures, computational homogenization by static condensation is more efficient than numerical perturbation.

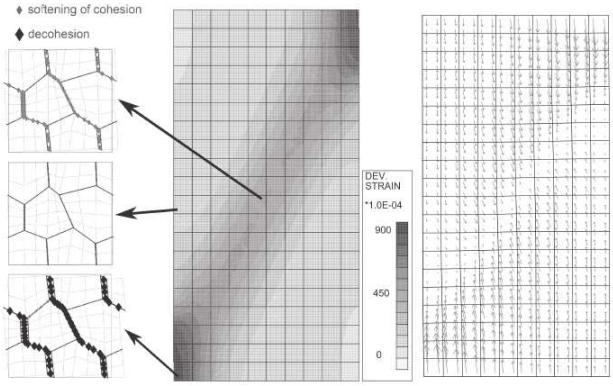

Figure 4: Left: Macro deviatoric strain with deformed microstructures after 1.0% vertical compression. Macro strains are coupled with interface damage and decohesion. Right: Fluid flow at end of test, strongly related to the volumetric strain rate.

Strain localization in a single band (Figure 4:Left) takes place as an effect of evolving damage of the interfaces. After 1.0% axial compression, no solutions can be found as the microstructure in several integration points complete decohesion of the interfaces takes place in the corner elements. Because most of the deformation of the microstructure is through sliding and normal opening of interfaces, the macro scale behaviour is mainly dilatant. This dilatancy leads to a pore volume increase in the localization band. As can be seen from Figure 4:Right the fluid flow tends to be controlled by pore volume change, following the strain localization in the band.

MATERIAL ANISOTROPY

The microstructure in Figure 2 is constructed from hexagonal grains by a small displacement of the interface position. This introduces a strong anisotropy in the material response as an effect of both the low number of interfaces and the limited modes of interface damage patterns. A more isotropic response can be obtained by a microstructure with a better distribution of grain (-interface) orientations and a higher number of grains. In addition, variation of the constitutive parameters at the microscale will influence the way in which this microstructure geometry influences the macroscale behaviour. In the following, only the grain geometry is addressed and microscale constitutive laws are kept homogeneous and isotropic. Moreover, only mechanical behaviour is studied. The initial interface loading stiffness is chosen to be high with respect to grain elasticity, which results in an initially isotropic response. Therefore only softening and damage of the interface cohesion will lead to anisotropy in the macro response.

Creating random microstructures

Microstructures are generated by Vorono tesselation around randomly generated points, repeated in rectangular periodic domains. The obtained Voronoï diagrams are subjected to a shape optimization based on minimum cumulative interface length. In this way, short interfaces can be avoided. Anisotropy is controlled by stretching the rectangular periodic REV into a square domain, resulting in elongated grains with preferential orientation. Figure 5 shows a 40-grain microstructure that is created following this procedure. This microstructure will be used in the following analysis.

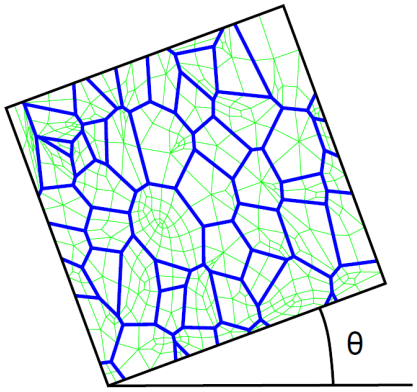

Figure 5: A 40-grain microstruture with a horizontal bedding plane for REV orientation $\theta = 90^{\circ}$.

Macroscale response to REV biaxial compression

The global REV response to biaxial compression under 12 MPa confining pressure for different orientations θ is studied here. Figure 6 shows the stress-strain curves for different orientations. Initial stiffness is isotropic and corresponds to the stiffness of the grains. The peak stress clearly shows the anisotropy in the structural response of the REV. Figure 7 shows the peak reaction force as a function of the REV orientation. Such anisotropic response in peak strength is in line with observations in shales, see for example Niandou et.al. (1997).

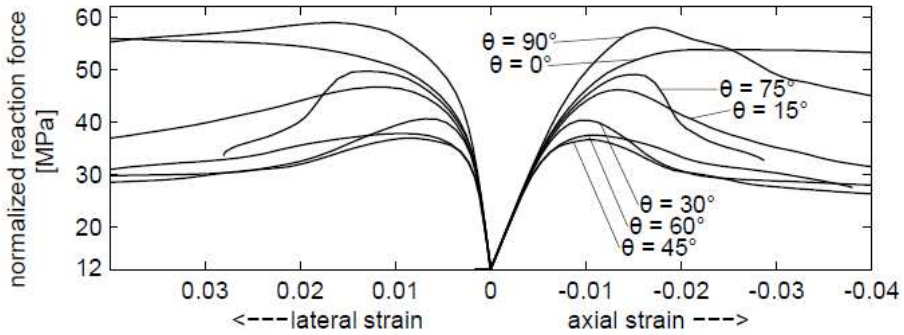

Figure 6: Stress-strain response of an individual integration point.

Figure 7: Stress-strain response of an individual integration point.

The origin of the anisotropy can be found in the microstructure by looking at the softening and damage of the interfaces. Figure 8 shows deformed microstructures after 6% axial compression for different orientations θ. The damage patterns corresponding to a low peak strength show a shear failure of the microstructure along the preferential direction of the bedding plane. The damage patterns for $\theta = 0°$ and $\theta = 90°$ do not follow the preferential direction of the bedding plane. Instead the damage pattern is inclined with respect to the bedding and shows conjugate failure. These more irregular damage patterns lead to a higher strength.

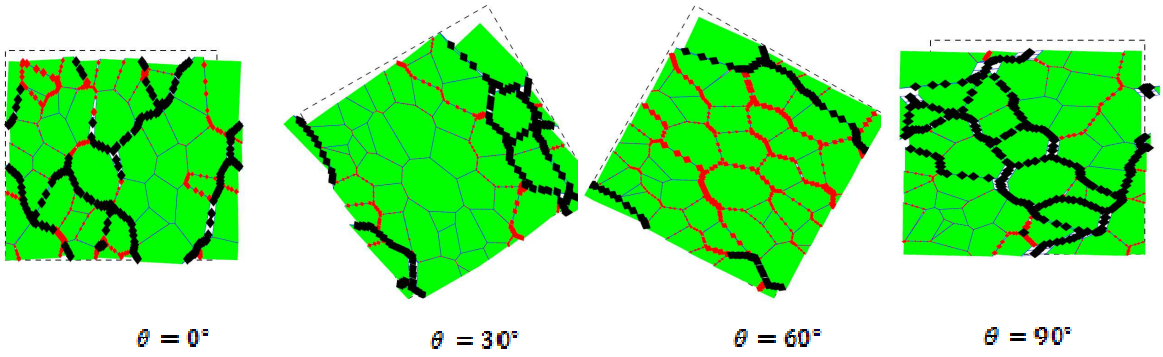

Figure 8: Deformed microstructure after 6% compression. Interface softening ($D_0 < D < 1$) and decohesion ($D = 1$) is given by the symbols ♦ and ◆ respectively.

LOCALIZATION UNDER DOUBLESCALE BIAXIAL COMPRESSION

The REV with microstructure shown in Figure 5 is now used in a doublescale simulation of a biaxial compression test under 12 MPa confinement stress. The local second gradient model discussed in Section 2 is used for enhancement of the finite element method in order to obtain objective results for localization phenomena. Its parameter D^{SG} is chosen such that both mesh dependency and macroscale snapback are avoided for the same mesh as used in Section 5.

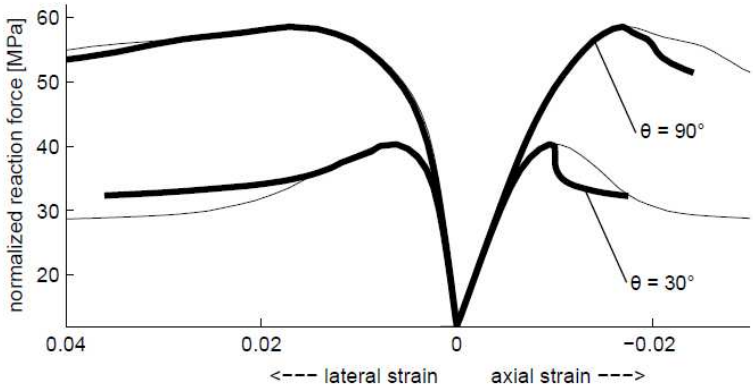

Figure 9: Normalized reaction forces for doublescale biaxial compression tests with REV orientation $\theta = 30°$ and $\theta = 90°$.

Two different REV orientations are used; $\theta = 90°$ and $\theta = 30°$. Figure 9 shows the structural response to biaxial compression under $12MPa$ confining stress, together with the response its homogeneous equivalent from the results in section 6. The response in the postpeak regime is influenced by localized deformation, which leads to a stronger softening for the structural response. The deformed mesh at the end of the test is shown in Figure 10 together with the deformed microstructures inside and ouside the localized zones.

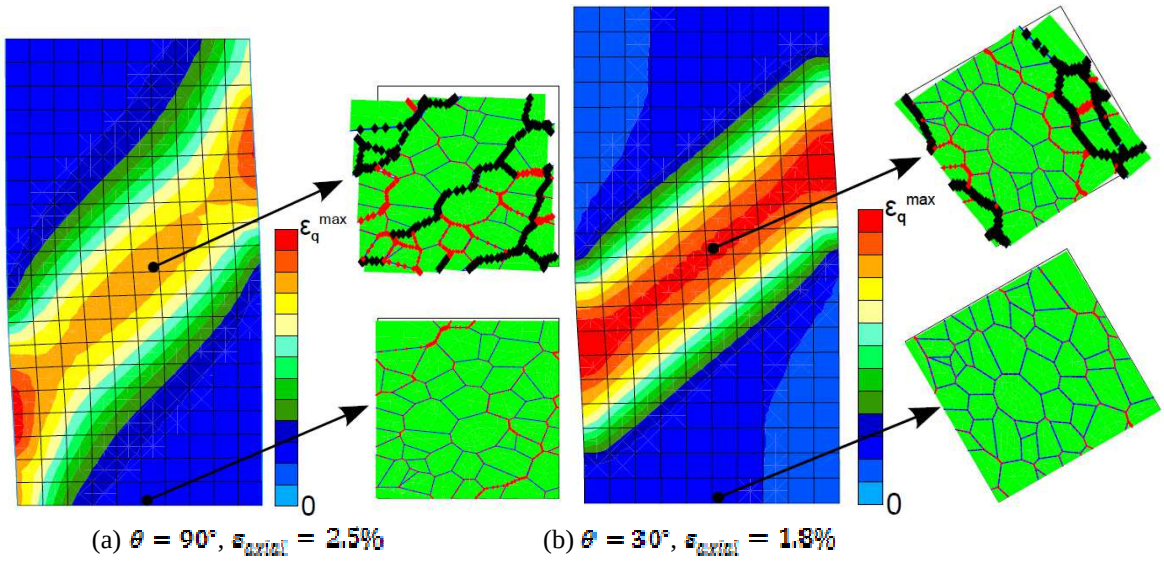

(a) $\theta = 90°$, $\varepsilon_{axial} = 2.5\%$ (b) $\theta = 30°$, $\varepsilon_{axial} = 1.8\%$

Figure 10: Left: Macroscale deformed mesh with Von-Mises equivalent strain. Right: deformed REV with interface softening ♦ and decohesion ◆ inside and outside the localization band.

From these doublescale tests the following observations are made with respect to anisotropy and localization:

• The orientation of the damage patterns at the microscale can be parallel or conjugate with respect to the localization pattern at the macro level, depending on the microstructure orientation.

• There is a possibility of obtaining different damage patterns at the micro scale between the homogeneous solution and the localized doblescale solution. These differences can be observed in the deformed microstructures for $\theta = 90°$ in Figures 9 and 1. The additional constraint on rotation for the homogeneous (integration point) deformation.

• Both the width and the orientation of the localization band change with a the REV orientation θ. In addition, the orientation and width of the localization band change during deformation. The strong decrease in reaction force for $\theta = 30°$ for example corresponds to a thin band that becomes thicker when the softening rate reduces.

CONCLUDING REMARKS

Modelling localization in a biaxial compression test with the presented FE ^{2} method demonstrates that the double scale model for hydromechanical coupling can be used for true doublescale computations. The use of computational homogenization for hydromechanical problems proves to be an efficient technique for homogenization from microstructure to macro continuum. Although the complexity of the microstructural REV remains low and the micromechanical constitutive laws are simplistic, the model is able to capture complex nonlinear material behaviour. Anisotropic macroscale behaviour is demonstrated to be easily obtained through the control of grain shape and orientation. Some effects of the anisotropy on the macroscale postpeak behaviour were demonstrated. Although complex nonlinear and anisotropic behaviour can be obtained, the macroscale response remains a superposition of the micromechanical constitutive laws and additional physical phenomena need to be introduced at the microscale in order to appear in the macroscopic response. Further developments of the microscale model including plastic and frictional behaviour will allow the modelling of a more advanced macro response.

ACKNOWLEDGEMENTS

The support from the French national radioactive waste management agency (Andra) is gratefully acknowledged.

REFERENCES

Bésuelle, P., R. Chambon, & F. Collin (2006). Switching deformation modes in post-localization solutions with a quasibrittle material. *J. Mech. Mat. Str.* 1, 1115 – 1134.

Collin, F., R. Chambon, & R. Charlier (2006). A finite element method for poro mechanical modelling of geotechnical problems using local second gradient models. *Int. J. Numer. Meth. Engng.* 65, 1749–1772.

Eijnden, B. v. d., F. Collin, P. Bésuelle, & R. Chambon (2013). A double scale modelling approach for hydromechanical coupling. *In proceedings of the Third International Symposium on Computational Geomechanics (COMGEO III).*

Eijnden, B. van den, Bésuelle, P., Collin, F. & Chambon, R. (2014) Doublescale modelling of hydromechanical coupling and anisotropy in localization problems. *In Geomechanics from Micro to Macro, Chapter 137.*

Frey, J., C. Dascalu, & R. Chambon (2012). A two-scale poromechanical model for cohesive rocks. Acta Geotechnica 7, 1–18.

Germain, P. (1973). La méthode des puissances virtuelles en mécanique des milieux continus. Journal de Mécanique 12.

Kouznetsova, V., W. Brekelmans, & F. Baaijens (2001). An approach to micro-macro modeling of heterogeneous materials. Computational Mechanics 27, 37–48.

Matsushima, T., R. Chambon,&D. Caillerie (2002). Large strain finite element analysis of a local second gradient model: application to localization. Int. J. Numer. Meth. Engng. 54, 499–521.

Mindlin, R. (1964). Micro-structure in linear elasticity. Archive for Rational Mechnaics and Analysis 16, 51–78.

Niandou, H., J. Shao, J. Henry, & D. Fourmaintraux (1997). Laboratory investigation of the mechanical behaviour of tournemire shale. International Journal of Rock Mechanics and Mining Sciences 34 (1), 3 – 16

DEM Hydromechanical Modeling of Fractured Fault Zones

A. Tsopela & F.V. Donzé
Laboratoire Sols, Solides, Structures, Grenoble, France
alexandra.tsopela@3sr-grenoble.fr
Frederic.Donze@hmg.inpg.fr

ABSTRACT

In the present work, an effort has been made towards the hydromechanical modeling of fractured fault zones. The software used for this purpose is the 3DEC code developed by Itasca and based on the Distinct Element Method. Two main models were considered, one simple example with a single fracture and one study case that concerned the Tournemire site located in Aveyron, France. The first case was considered in order to perform a parametric study and test the influence of some important parameters of the model, serving as a guideline for the sequential hydromechanical calculations in the case of the Tournemire model. It was shown that the joint aperture and the fluid bulk modulus control dramatically the calculation. In the Tournemire case an attempt was made to include in the model the main features of the site (natural fractures, fault core, tunnel). Three hydromechanical simulations were performed involving hydraulic loading through an injection point. Different fault core permeabilities and stress conditions were tested and different patterns of fluid propagation, pressure distribution and fault displacement were derived depending on the fault permeability. The obtained results show that the displacement magnitudes are small due to the insitu stress field that seems to control the hydromechanical behavior of the fault zone.

INTRODUCTION

Field observations of maturely slipped faults show a generally broad zone of cracking and granulation. However large shear deformation in individual earthquakes appears to take place with localization to a zone smaller than 1-5 mm wide within a finely granulated fault core (Rice et al., 2009). Fluid pressurization, a possible mechanism of fault weakening, exerts a critical control on earthquake rupture in the upper crust. One cause for this control is the presence of high fluid pressures inside the fault zone. However the precise mechanisms

relating high fluid pressures and fault rupture remain unclear. There is a need to use 3D hydromechanical models to show that effective stress changes induced by transient regime of fluid pressure along a fault zone with spatially variable material properties (conditions representative of natural faults) can be sufficient to produce large slip in the fault core, and fracturing in the surrounding damage volume. This can also appear interesting in petroleum and geothermal applications given the increasing need in understanding the behavior of reservoir systems for the exploration, production and CO_2 storage. Therefore, understanding the fault architecture and the hydromechanical properties are of high importance in the framework of this problem. Discrete element method, continuum based numerical methods and finite element methods have been applied to simulate hydro-mechanical process in fractured rocks (Lemos 1988; Jing et al 1995). The first step when DEM is applied is to set up a geomechanical model describing the geometry of fracture and rock blocs formed by them. In the present work a specific case study has been considered, the Tournemire site (Aveyron, France), where the Tournemire Research Laboratory is located in the railway tunnel excavated in 1885 and operated by the French Institute of Radioprotection and Nuclear Safety (IRSN). Based on field data at the Tournemire site preliminary coupled hydromechanical calculations are attempted for a 3D model with the characteristics of the Tournemire site, using the Discrete Element Method and more specifically the 3DEC software by Itasca. The calculations consist in realizing "injection experiments" for the investigation of the influence of fluid propagation and fluid pressure increase inside the different parts of the fault zone, and the mechanical response of the system provided the decrease of effective stress.

SITE DESCRIPTION

The Tournemire URL is located in an argillaceous formation, which is 250 m thick and corresponds to sub-horizontal consolidated argillaceous and marly layer (Matray et al., 2007). The maximum horizontal stress is σ_H = -4.0 MPa with an orientation N162±15E, the minimum horizontal stress is σ_h = -2.1 MPa with an orientation N72±15E and the vertical stress σ_v = -3.8 MPa (Rejeb and Cabrera, 2006). The insitu pore pressure is equal to 0.4 – 0.2 MPa according to insitu measurements. The Tournemire massif is traversed by a kilometric extension fault, the Cernon fault, roughly oriented West–East, and by two faults of hectometric extension, the principal and secondary fault, oriented N170–180°E. The secondary fault zone is the one where the injection is going to take place in the area shown in Fig.1. The fault zone consists of an impermeable core (or multiple cores), a damaged zone characterized by fracture permeability and a mineralization zone with calcified fractures characterized by lower density compared to the damaged zone (Henry, 2013). The mechanical properties of the formation are E_1 = 27.68 GPa, E_2 = 9.27 GPa, v_1 = 0.17, v_2 = 0.20, G_{12} = 3.94 GPa, where 1 and 2 correspond to directions parallel and normal to the bedding respectively.

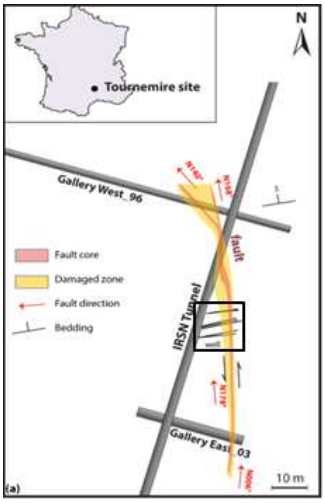

Figure 15: Horizontal view of the tunnel, galleries and the secondary fault

3DEC CODE

As mentioned above, the distinct-element code 3DEC (Itasca Cons. Group, 2013) was selected as the numerical tool for the simulation of the injection into the fault zone. The discontinuous medium, such as a fractured rock mass is modeled as a 3D assemblage of discrete deformable or rigid blocks whereas the discontinuities are treated as distinct boundary interactions between blocks. In the case under consideration, the constitutive model selected for the joints is the Coulomb slip model and for the intact material (blocks) the model used is the transversely isotropic elastic model. In fluid flow analysis, joints are conductive and treated as two-dimensional elements, while individual blocks are considered impermeable. The discharge rate for a given joint is calculated according to the modified cubic law (Itasca Cons. Group, 2013). The hydraulic loading is performed through an injection source controlled in terms of pressure (point source injection). In the study that follows, a personalized hydromechanical calculation was used for the case under consideration and consists in fixing the number of the mechanical and hydraulic cycles according to a maximum unbalanced force threshold. For each mechanical cycle, the unbalanced force is calculated, if it is below the maximum unbalanced force, the number of hydraulic cycles is increased and the procedure is repeated until a prescribed maximum number of hydraulic cycles is reached.

PARAMETRIC STUDY - CASE OF A SINGLE FRACTURE

In order to estimate the effect of different parameters that need to be defined for the actual 3D case representing the Tournemire site, a parametric study on a simple example of a rectangle containing one fracture will be performed, aiming to the determination of an optimized set of parameters that will be used as a guideline for the hydromechanical simulation of the Tournemire case, given its high computational cost.

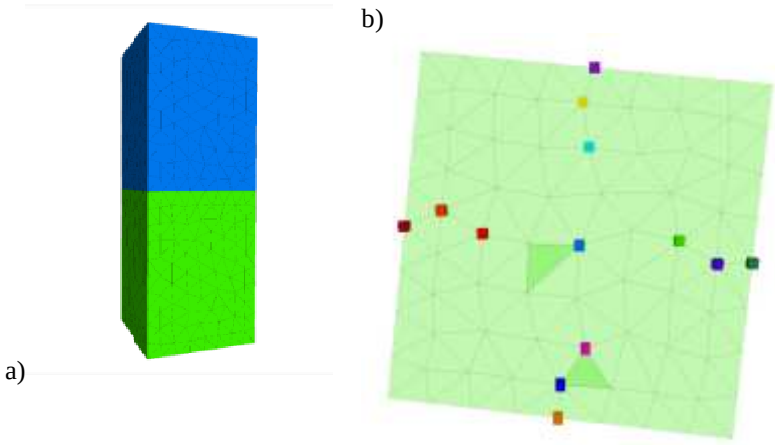

Figure 16: a) Single fracture model, b) pore pressure monitoring locations

In this model, an injection is taking place at (0, 0, 0), which is the center of the discontinuity with an increasing pressure rate until the pressure of 3 MPa is reached. At this point the pressure remains constant until equilibrium is reached and the pore pressure is equal to 3 MPa through the whole plane of the discontinuity. For this purpose, the pore pressure was recorded in 13 points of the joint plane as shown in Figure 2. The injection is controlled by a loop that is run for 40 times with the pore pressure at the injection point starting from 1×10^6 Pa and increasing at each step by 2×10^5 Pa until the value of 3×10^6 Pa is reached from which point the pore pressure remains constant for the rest of the steps. For each step, a duration of 10 seconds is achieved, the target time. The number of mechanical and hydraulic cycles is determined at each step depending on the maximum unbalanced force. The parameters that were tested are the fracture hydraulic aperture, the fracture normal and shear stiffness, the constitutive behavior of the intact material and the fluid bulk modulus.

According to the parametric study, it was shown that the aperture of the joint consists of a first order parameter affecting the calculation time and stability of the system. As the aperture increases, the calculation time increases because of the decrease of the fluid timestep. However, for higher values of aperture, the system appears more stable as concluded by the pore pressure and the unbalanced force values recorded. Another parameter that plays a key role during the simulation is the fluid bulk modulus. It was found that for lower values of fluid stiffness the calculation is really faster and more stable comparing to higher values, including the realistic fluid bulk modulus which is equal to 2 GPa approximately. It is mentioned that it could be possible to use a low value of fluid bulk modulus (2 MPa) in case we are mainly concerned about the pore pressure in the model without taking into account the injected volume of fluid that needs to be huge due to the fluid's high compressibility given a pressure controlled injection. Finally, the joint's normal and shear stiffness can also affect the calculation as for high values the calculation time is small and the solution is more stable comparing to the results obtained for lower stiffness values as during the calculation the aperture stays closer to its initial value. It was also shown that for lower values of stiffness (10^9 Pa/m and below) the constitutive behavior of the intact material can also affect the calculation as it can restrain or not further opening of the fracture. Therefore in the case of a transversely isotropic model, the orientation of the fractures is also an important factor. For the 3D case that follows, the above were taken into account and due to the extremely high calculation times, the values of the parameters were selected mainly according to the calculation time. The values can be unrealistic for some parameters, like the fluid bulk

modulus but such assumptions could be reasonable given the objective and type of the simulation.

TOURNEMIRE STUDY CASE

MODEL SETUP

The area of the site that was attempted to be modeled in 3DEC is the area where the injection took place, included in the black box in Fig. 1. For the construction of the model, its axes were selected to be parallel to the fault direction due to a limitation regarding the geometrical domain where the DFN will be included. As mentioned above, the direction of the secondary fault is very close to the maximum horizontal stress direction. It was therefore assumed for the sake of simplicity that the maximum horizontal stress (σ_H) axis is parallel to the fault and parallel to the x-axis of the 3DEC model. The principal stresses are therefore expressed according to the 3DEC axes as follows: σ_H - σ_{xx}, σ_h - σ_{yy}, σ_v - σ_{zz}. The center of the model is at (0,0,0) and the dimensions of the model were chosen to be 20m in the x-direction, 30m in the y-direction and 20m in the z-direction. For the modeling of the area under consideration in 3D, the intact rock is implemented as blocks; the fault core is implemented as a persistent discontinuity, parallel to the x-axis and the natural fractures are implemented as a stochastic Discrete Fracture Network (DFN). The joint representing the fault core in the model is located where the green block starts (Fig. 3a). It is noted at this point that the East damaged zone was not included in the current model in order to keep the model as simple as possible. However it was proven necessary to take the model into account as it has an effect on the stress distribution during the calculations for the initial mechanical equilibrium of the model.

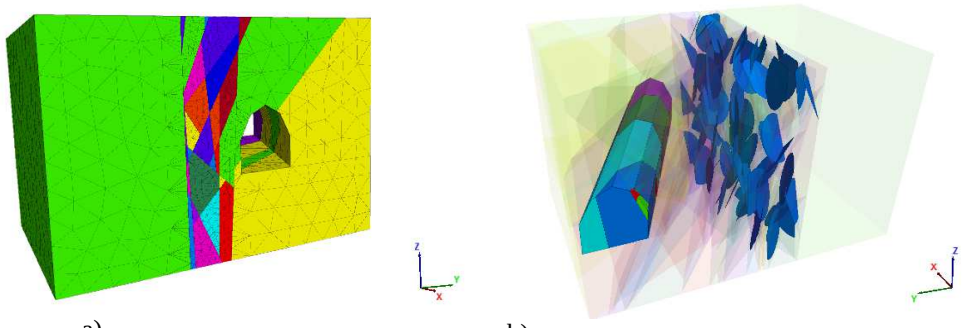

a) b)

Figure 17 : a) 3DEC model for the Tournemire case, b) DFN and tunnel of 3DEC model.

As far as the initial and boundary conditions are concerned, an insitu stress field is applied to the model equal to [σ_{xx}, σ_{yy}, σ_{zz}, σ_{xy}, σ_{xz}, σ_{yz}] = [-4.0MPa, -2.1MPa, -3.8MPa, 0, 0, 0] and the boundary displacements are fixed. An insitu pore pressure equal to 0.4MPa is applied to the model without any hydraulic boundary conditions. The mesh in the model varies from 0.5m to 2m (average dimension of the finite-difference elements) for the DFN region and the rest of the model respectively. For the implementation of the stochastic DFN the size is controlled by a power law distribution with a scaling exponent α = 1.5, the orientation follows a Fisher distribution with a dispersion value k = 10, dip angle = 90°, dip direction = 30°. The position follows a uniform distribution and the resulting connectivity is equal to 3.
The behavior of the intact material is transversely isotropic with the properties mentioned in the site description section. It is noted that in 3DEC, direction 1 is the x- or y-direction and

direction 2 is the z direction. Regarding the properties of the joints in the 3DEC model, the joint representing the fault core is characterized by lower mechanical properties than the natural fractures of the damaged zone and it is less permeable. Taking this and the results from the single fracture example into account, the values for the mechanical and hydraulic properties of the joints in the model are summarized in the table below (Table 1):

	Fault core	**DFN**
Normal stiffness (Pa/m)	10^{10}	10^{11}
Shear stiffness (Pa/m)	10^{10}	10^{11}
Cohesion (Pa)	0	10
Friction angle (°)	20	30
Tensile strength (Pa)	0	10
Initial aperture (m)	varying	10^{-5}
Residual aperture (m)	varying	10^{-6}
Maximum aperture (m)	varying	10^{-4}

Table 1 : Mechanical and hydraulic properties of the fault core joint, the DFN and he joints created by the DFN.

PRELIMINARY RESULTS

Based on mesoscale field experiments carried out at the Tournemire site a coupled hydromechanical calculation is attempted for the model described above. A number of experiments have already been performed by realizing pressure controlled water injections in different parts of the formation and the fault zone.

Two different configurations were considered by changing the permeability of the joint representing the fault core zone. For the first case, the hydraulic aperture of the joint representing the fault core, is equal to 10^{-6} m and does not vary during the calculation. For the second case the aperture is increased up to 0.5×10^{-5} m for the initial aperture at zero stress, 0.5×10^{-6} m for the residual aperture and 0.5×10^{-4} m for the maximum aperture. For both cases, 40 injection steps are performed for 10 seconds each. The pressure rate is equal to 0.2 MPa starting from 1 MPa until the value of 3 MPa is reached where for the rest of the injection steps the pressure remains constant. The evolution of the pore pressure distribution and the failure indicator of the sub-contacts on the fault core joint (gray plane in Fig 4) are shown below.

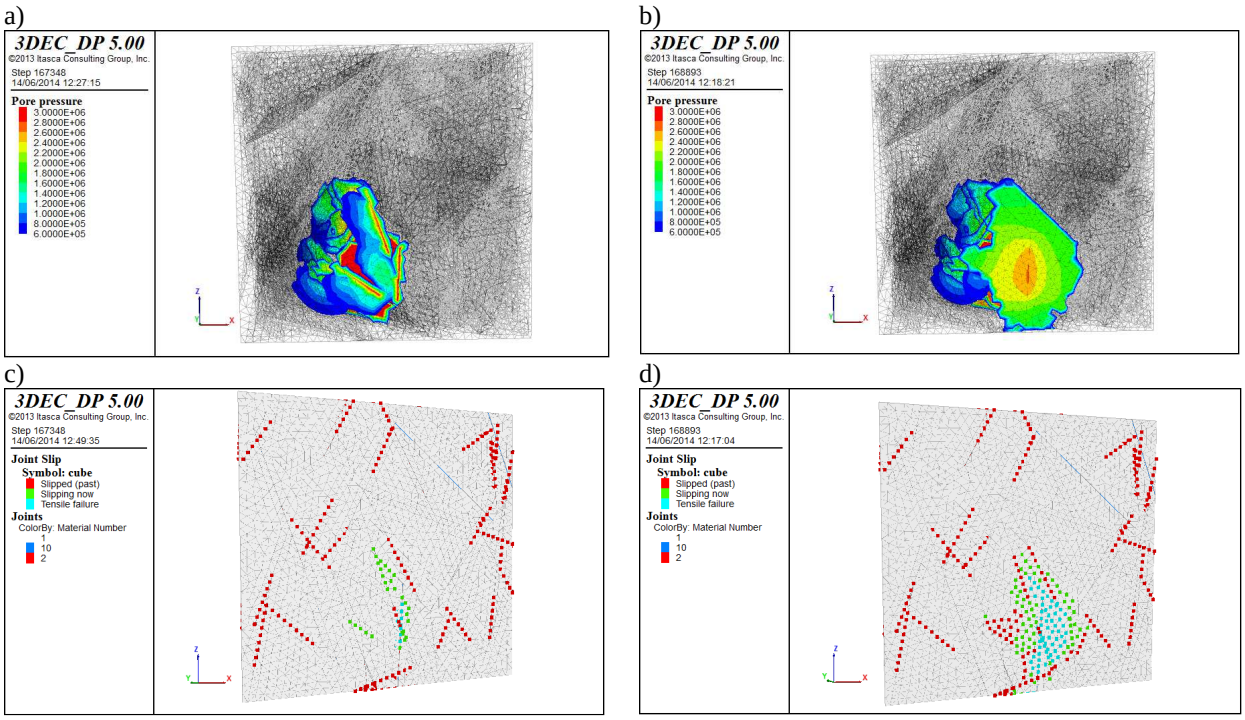

Figure 18 : Lower permeability case: a) Pore pressure distribution, c) failure indicators on the fault core joint. Increased permeability case: b) Pore pressure distribution, e) failure indicators on the fault core joint.

The failure indicators show whether a sub-contact has failed in tension (blue), has already slipped (red) or is slipping (green). It is noted that before the beginning of the flow calculation the sub-contacts of the fractures were set to tensile failure for the initiation of flow and as soon as the injection begins it is illustrated that they have already slipped. By observing the figures obtained at the end of the calculation regarding the failure indicator and by correlating them to the plot showing the evolution of the pore pressure in the fault core joint (Fig. 4), for the first case we can state that rovided the connectivity of the fracture network, the fluid is mostly propagating through the fractures, however due to the low permeability of the fault core zone, there are only particular parts of the fault core that are slipping or have failed, located at the intersections with fractures. In addition, due to the permeability contrast (cubic law), it can be observed that at the intersections of the fracture network with the fault core joint, within the area surrounding the injection, the fluid pressure is high because as the aperture is 10 times smaller the fluid cannot easily propagate through the fault core causing an increase in pressure.

In the second case the fluid is able to propagate in the fault core joint due to the aperture increase. It is shown that at the intersection of the fault core and the fracture and a specific part around it, the material has failed in tension for pore pressure values around 2.2 MPa, which is lower than the pressure causing tensile failure in the fractures due to the decreased mechanical properties of the fault.

Regarding the displacement of the fault core joint, the x-, y- and z-displacements were recorded for five different points on the joint throughout the calculation.

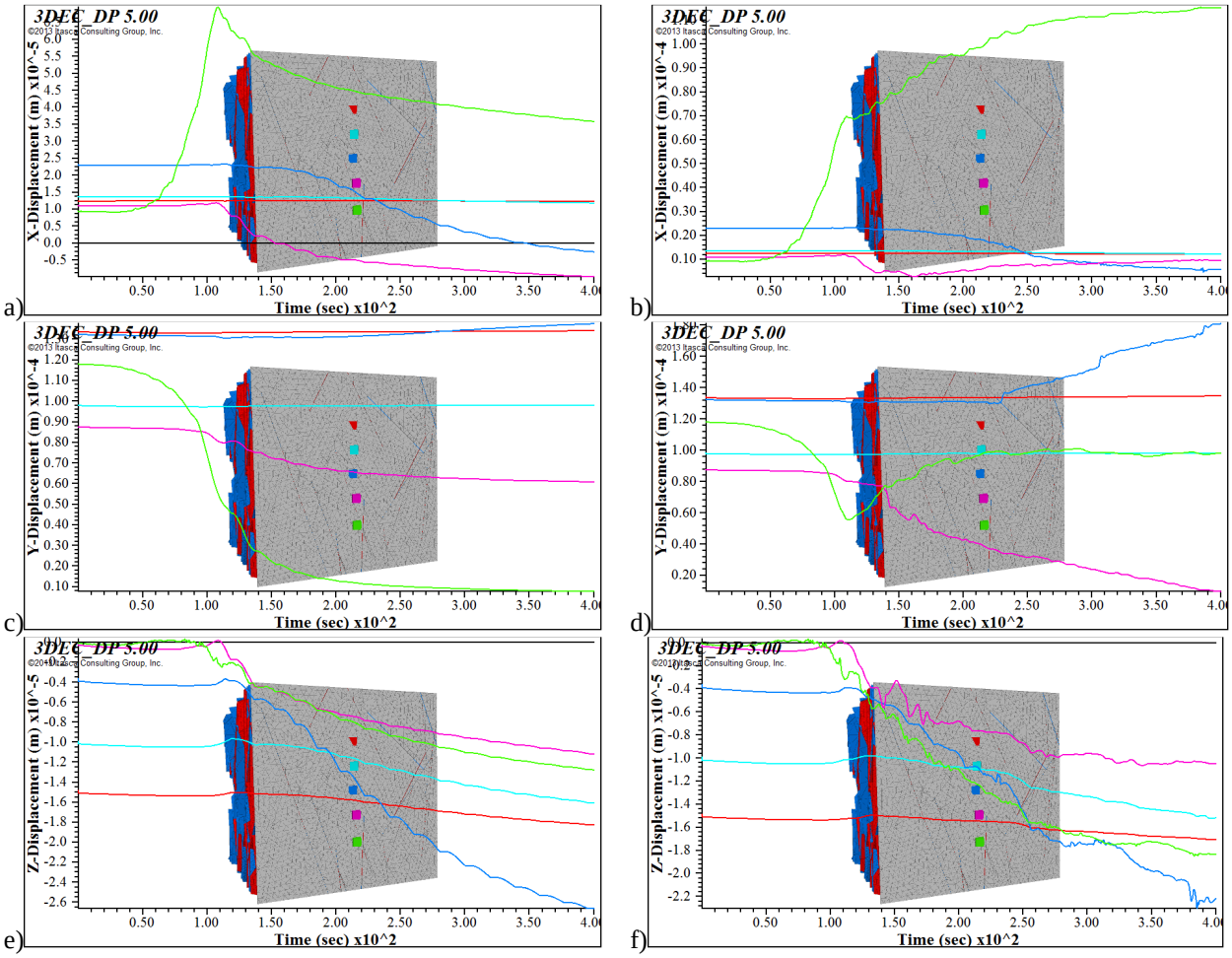

Figure 19 : Lower permeability case: a) X-displacement, c) Y-displacement, e) Z-displacement. Increased permeability case: b) X-displacement, d) Y-displacement, f) Z-displacement.

For the monitored points that are closer to the injection point (blue, fuchsia and green) there is almost in all cases a change on the curves at 110 sec that corresponds to the temporal point that the fluid meets the fault core, and that by the end of the calculations, no steady values have been reached. For all three directions, the magnitude of the displacements is very small because the fault core plane is aligned with the maximum principal stress direction and the vertical stress direction. No large displacements were expected and we can state that in most cases, the different patterns are attributed to the heterogeneous displacement induced by the fracture network. If the stress field is modified by adding shear components it is expected that the recorded displacements will be larger as the fault core will be triggered by the decrease of effective stress due to the fluid propagation.

It is therefore worth testing the resulting displacements in the case where the stress tensor is rotated according to the data from the Tournemire site. More specifically, the insitu pore pressure, the displacement boundary conditions and the aperture of the fault core remain the same but the stress tensor is rotated by 8 degrees resulting in the following:
$[\sigma_{xx}, \sigma_{yy}, \sigma_{zz}, \sigma_{xy}, \sigma_{xz}, \sigma_{yz}]$ = [-3.96MPa, -2.14MPa, -3.8MPa, 0.26MPa, 0, 0]. The resulting pore pressure distribution and failure indicators on the fault core joint are shown below.

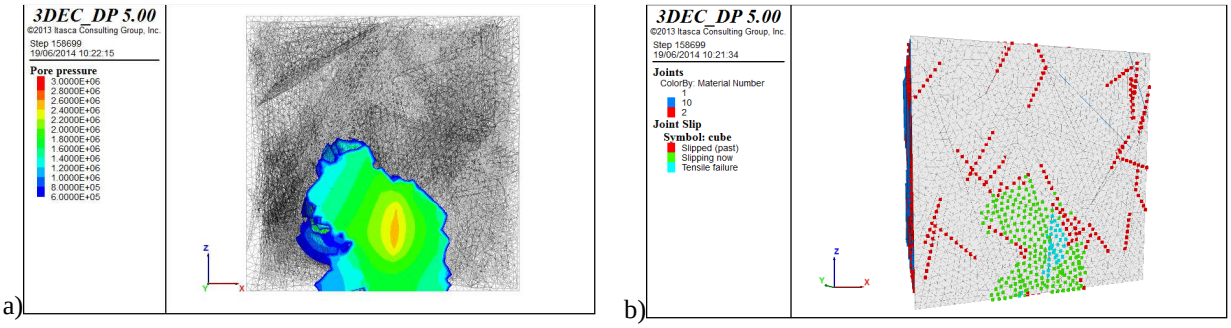

Figure 20 : Rotated stress tensor: a) Pore pressure distribution, b) failure indicators on the fault core joint

Concerning the pore pressure distribution there is no significant difference with the case of the more permeable fault core in terms of pore pressure magnitude at the different parts of the fault core joint. However it can be seen that a larger surface is now shown to be moving and more particularly to be slipping (green points) as a larger surface of the fault core joint seems to be affected by the injection due to the rotation of the stress tensor and the existence of a shear stress component acting on the plane of the fault core joint, even if it is very low (σ_{xy} = 0.26 MPa). The X-, Y- and Z-displacement magnitudes remain almost the same as the second case examined (increased fault core permeability). The recorded displacements are still very low even if the shear stress component has been introduced. It is therefore possible to conclude that the insitu stress conditions are of high importance and for the given maximum injection pore pressure (3 MPa) and insitu stress field and orientation of the fault core it is not possible for larger displacements to take place.

CONCLUSION

The hydromechanical modeling of fractured fault zones was attempted using the Discrete Element Method. For this purpose, the Tournemire site was considered and modeled by the 3DEC code. From the parametric study performed on a single fracture case, it was shown that the fracture aperture and the fluid bulk modulus are first order parameters and by changing their values there is a significant effect on the real time needed for the calculation and the stability of the system. The hydromechanical simulations for the Tournemire site showed that in the first case (low permeable fault core) the fluid propagates in the DFN and when the fault core is met at the intersections with fractures, there is an increase in pressure causing localized opening of the fractures. In the second case (increased fault core permeability), the fluid can propagate within the fault core resulting in a different pore pressure distribution and failure occurring at a larger part of the fault core. However the displacements along the fault core are very low, given the fault core orientation and the insitu stress field that does not allow large displacements to occur for a maximum pore pressure value of 3 MPa.

REFERENCES

Henry P., “Fluids and Faults: Relationship between fault permeability, stress and fluid pressure in clay rich formations”, Appendix 1, 31 pages, 2013

Itasca (2013) “ 3DEC Version 5.0, 3 Dimensional Distinct Element Code,” User’s Manual, Itasca Consulting Group Inc., Minneapolis, MN

Jing, L. (2003) “A review of techniques, advances and outstanding issues in numerical modeling for rock mechanics and rock engineering,” International Journal of Rock

Mechanics and Mining Sciences, Vol. 40, pp. 283-353Imposimato, S. & Nova, R. 1998. An investigation on the uniqueness of the incremental response of elastoplastic models for virgin sand. *Mechanics of Cohesive-Frictional Materials* 3: 65-87.

Matray, J. M., Savoye, S., & Cabrera, J. (2007). Desaturation and structure relationships around drifts excavated in the well-compacted Tournemire's argillite (Aveyron, France). Engineering Geology, 90(1), 1-16.

Rejeb, A., Tijani, M., 2003. Stress field in the Tournemire argillaceous. In situ measurements and interpretation. Rev. Fr. Géotech. 103, 75–84.

Rejeb, A., and J. Cabrera. "Time-dependent evolution of the excavation damaged zone in the argillaceous Tournemire site." GeoProc international conference on coupled T–H–M–C processes in geosystems. 2006

Rice, J.R., E.M. Dunham and H. Noda, Thermo- and hydro-mechanical processes along faults during rapid slip, Meso-Scale Shear Physics in Earthquake and Landslide Mechanics, eds. Y. Hatzor, J. Sulem and I. Vardoulakis, CRC Press, 2009

Numerical simulations of dense suspensions rheology using a DEM-Fluid coupled model

D.Marzougui, B.Chareyre
Laboratoire Sols, Solides, Structures, Grenoble, France
donia.marzougui@3sr-grenoble.fr, bruno.chareyre@3sr-grenoble.fr
and
J.Chauchat
Cemagref de Grenoble - Unité ETNA, Saint Martin d'Hères, France
julien.chauchat@grenoble-inp.fr

ABSTRACT

The understanding of dense suspensions rheology is of great practical interest for both industrial and geophysical applications and has led to a large amount of publications over the past decades. This problem is especially difficult as it is a two-phase media in which particle-particle interactions as well as fluid-particle interactions are significant. In this contribution, the plane shear flow of a dense fluid-grain mixture is studied using the DEM-PFV coupled model. We further improve the original model: including the deviatoric part of the stress tensor on the basis of the lubrication theory, and extending the solver to periodic boundary conditions. Simulations of a granular media saturated by an incompressible fluid and subjected to a plane shear at imposed vertical stress are presented. The shear stress is decomposed in different contributions which can be examined separately: contact forces, lubrication forces and drag forces associated to the poromechanical couplings.

INTRODUCTION

The rheology of grain-fluid mixtures is subject of practical interest for both industrial and geophysical applications. When the solid fraction of such mixture is high enough, *i.e.* in dense suspensions, the bulk behavior is affected by intricated phenomena combining the viscosity of the fluid phase as well as the interactions between the solid particles through solid contacts. Moreover, the contact interactions may be modified by the presence of the fluid, as described by lubrication theories. Additionally, in transient situations, poromechanical couplings may develop long range interactions by coupling the local rate of volume change to the pore

pressure field. Direct particle-scale modeling of this problem is a promising way to better evaluate the interactions between phases and to link the micro-scale properties and phenomena to the quantities measured for the bulk material, as it needs much less simplifications than former analytical developments (such as [Frankel et al. 1967, Brule et al. 1991, Ancey et al. 1999]). This modeling can be based on lubrication models [Rognon et al. 2011], or more elaborated methods to reflect the fluid viscosity through pair interactions between particles [Yeo et al. 2010]. This is advantageous as it does not need to actually solve Navier-Stokes (NS) equations in the fluid phase. The price to pay is that long range interactions due to poromechanical couplings are difficult to reflect. An alternative is to really solve NS in the fluid phase using a CFD solver, or to use a lattice-Boltzman model [Ladd et al. 2001]. It is to be noted that direct resolution of NS does not eliminate the need for a proper modeling of the lubrication forces, due to mesh size dependencies [Nguyen et al. 2002]. The main difficulty associated to this approach is the high computational cost, so that following large deformations of thousands of immersed particles in 3D remains a challenging task.
A new method to simulate fluid-particle interactions has been developed recently and may be of some help to tackle the computational challenge [Catalano et al. 2013]. In this method, the solid phase is modelized with the discrete element method (DEM), and the fluid flow is solved using a pore-scale finite volume method (PFV). The key aspects of this DEM-PFV coupling are recalled in the first part of this paper. It was implemented in the open source code Yade-DEM [Smilauer et al. 2010]. Extensions of this method in order to study dense suspensions are being undertaken by the first author. Namely, the original model lacks a coupling term to link the fluid forces to the deviatoric strain, as explained hereafter. We also generalized the boundary conditions in order to allow very large deformations of the suspension in simple shear. Typical results of the preliminary enhanced model are presented in the last part.

NUMERICAL MODEL

Original DEM-PFV Coupled Model

Our DEM approach defines the mechanical properties of the interaction between grains whose shape is assumed to be spherical. Following Newton's laws, the positions of particles are updated and calculated at each time-step of the DEM simulation. As introduced in [Catalano et al. 2011], the PFV formulation is based on a simplified discretisation of the pore space as a network of regular triangulation and its dual Voronoi graph (figure 1).

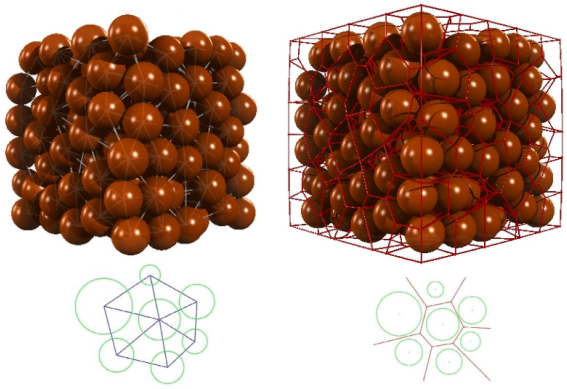

Figure 1: **Regular triangulation (left) and Voronoi graph (right).**

This network simplifies the formulation and resolution of the flow problem. The continuity equation is expressed for each pore, linking the rate of volume change of one tetrahedral element $\dot{V}_i^f$ to the fluxes q_{ij} through each facet. Each flux can be related to the pressure jump between to elements via a generalised Poiseuille's law, so that

$$\dot{V}_i^f = \sum_{j=j_1}^{j_4} q_{ij} = \sum_{j=j_1}^{j_4} K_{ij}(p_i - p_j) \tag{1}$$

couples the particles velocity to the fluid pressure field. The expression of conductivity K_{ij} has been validated recently by comparisons with glass beads experiments [Tong et al. 2012].
The total force exerted by the fluid on particle *k* can then be defined as [Chareyre et al. 2012]:

$$F^k = \int_{\partial\Gamma_k} p\, n\, ds + \int_{\partial\Gamma_k} \tau\, n\, ds \tag{2}$$

Lubrication forces

As classical poromechanics, the original DEM-PFV model takes into account the isotropic part of the stress and strain tensors (pressure and divergence of solid phase velocity) in the coupling (equation 1). The contribution of the fluid to the bulk shear stress is de facto neglected. It is worth noting that the shear part of the coupling is similarly lacking in discrete models inspired by the coupling equations of poromechanics, such as the continuum-discrete methods [Zeghal 2004, Zhao et al. 2013].
In order to deal with sheared suspensions, another viscous contribution has to be introduced for modeling the shear stress. Various ways may be used for this purpose such as viscous forces obtained in the framework of the lubrication theory. Lubrication effects are defined for all the elementary motions described in figure 2. Let's denote k and k' two particles in interaction of radius a_k and $a_{k'}$, linear velocities $\boldsymbol{v}_k$ and $\boldsymbol{v}_{k'}$ and angular velocities $\boldsymbol{\omega}_k$ and $\boldsymbol{\omega}_{k'}$, respectively. $a = (a_k + a_{k'})/2$ is their average radius and h *is* the inter-particle distance (surface to surface). The relative motions between the particles k and k' can be decomposed in four elementary motions corresponding to normal displacement (subscript n), shear displacement (s), rolling (r) and twisting (t). Lubrication forces and torques induced by these elementary motions are:

$$F_n^L = \frac{3}{2}\pi\eta\frac{a^2}{h}v_n \tag{3}$$

$$F_s^L = \frac{\pi\eta}{2}[-2a + (2a+h)\ln(\frac{2a+h}{h})]v_t \tag{4}$$

$$C_r^L = \pi\eta a^3(\frac{3}{2}\ln\frac{a}{h} + \frac{63}{500}\frac{h}{a}\ln\frac{a}{h})[(\omega_k - \omega_{k'})n] \tag{5}$$

$$C_t^L = \pi\eta a^2\frac{h}{a}\ln\frac{a}{h}[(\omega_k - \omega_{k'}).n]n \tag{6}$$

where $\mathbf{v}_n = ((\mathbf{v}_{k'} - \mathbf{v}_k)\cdot\mathbf{n})\mathbf{n}$ is the normal relative velocity, $\mathbf{v}_t = (a_k(\boldsymbol{\omega}_k - \boldsymbol{\omega}_n) + a_{k'}(\boldsymbol{\omega}_{k'} - \boldsymbol{\omega}_n))\times\mathbf{n}$ is an objective expression of the tangential relative velocity and $\boldsymbol{\omega}_n = (\boldsymbol{v}_{k'} - \boldsymbol{v}_k) \times \mathbf{n}/(a_k + a_{k'} + h)$ is the angular velocity of the local frame attached to the interacting pair. The normal and

shear forces, $\boldsymbol{F}_n$ and $\boldsymbol{F}_S$, are based on Frankel & Acrivos [Frankel et al. 1967, Brule et al. [1991] whereas C_r and C_t are based on Jeffrey & Onishi 1984. The reason of this choice will be discussed later. The total lubrication force $\boldsymbol{F}_k^L$ (resp. $\boldsymbol{F}_{k'}^L$) applied by particle k' on particle k (resp. by particle k on particle k') and the total torque $\boldsymbol{C}_k^L$ (resp. $\boldsymbol{C}_{k'}^L$) applied by particle k' on particle k (resp. by particle k on particle k') relative to the particle center read:

$$F_k^L = -F_{k'}^L = F_n + F_s \tag{7}$$

$$C_k^L = (a_k + \frac{h}{2}) F_s + C_r + C_t \tag{8}$$

$$C_{k'}^L = (a_{k'} + \frac{h}{2}) F_s - C_r - C_t \tag{9}$$

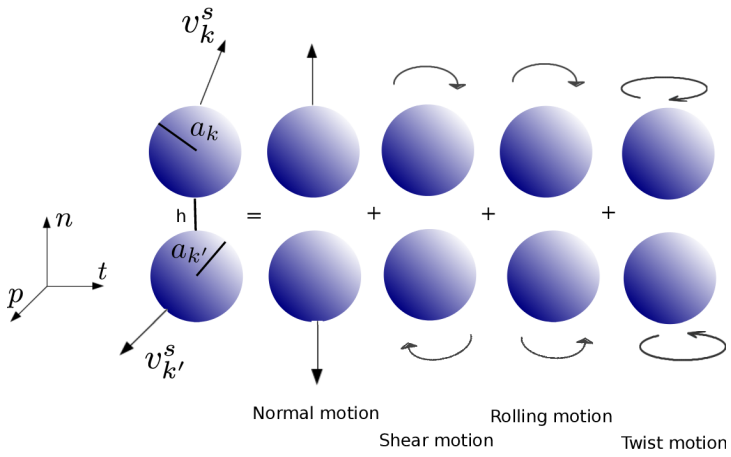

Figure 2: **Relative motion between particles [Marzougui et al. 2015].**

Figure 3 shows the comparaison of the FEM results performed on a simple configuration of identical spheres rotating at a given angular velocity, with that of equation 4 where F_S^L is determined alternatively using the expression from Jeffrey & Onishi ($F_s = \pi \eta a \ln \frac{a}{h}$) [8] and from Frankel & Acrivos 1967 (equation 4). Both expressions are asymptotically equivalent for $h \rightarrow 0$ but that of Frankel & Acrivos is in much better agreement with the FEM results for small h. The expression of Jeffrey & Onishi leads to negative torques for large h. This can alter the stability of the numerical scheme.

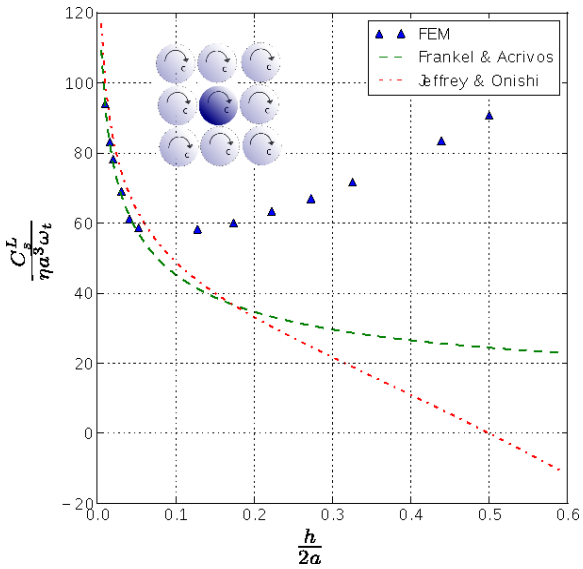

Figure 3: **Comparaison of viscous shear forces for the case of rotating sphere in a regular assembly of particles. h is the surface-to-surface distance and a is the particles radius [Marzougui et al. 2015].**

The normal interaction between two elastic-like particles in a viscous fluid is described by the Maxwell visco-elastic scheme (figure 4) which combines a spring of stiffness k in series with a pad of viscosity η. This combination between the lubrication and the elasticity is close to that adopted by Rognon [Rognon et al. 2011]. k_n is the contact stiffness and $v_n(h)$ is the instantaneous viscosity of the interaction as defined in eq. (3), such that $F_n^L = v_n(h)v_n$. The real velocity of approach between the two surfaces is $v_n - \dot{u}_n^e$, where $u_n^e = F_n^L / k_n$ is the elastic deformation. The evolution of the normal lubrication force obeys, then, the differential equation

$$\dot{F}_n^L = v_n(h)\left(v_n - \frac{F_n^L}{k_n}\right) \tag{10}$$

Eq. 10 is integrated over time-steps using the form

$$\dot{F}_n^L = k_n\left(v_n - \frac{F_n^L}{v_n(h)}\right) \tag{11}$$

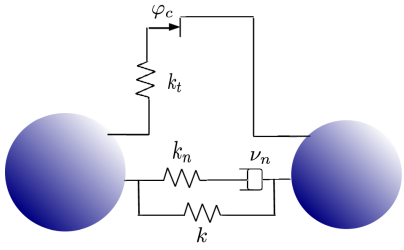

Figure 4: **Visco-elastic scheme of the interaction between two elastic-like particles [Marzougui et al. 2015].**

Periodic Boundary Conditions

As the system is considered infinite in the flow direction, some problems can arise from the boundary effects in the numerical simulation. In order to avoid such problems, periodic boundary conditions are implemented in the PFV model (figure 5) (the periodicity for the DEM part was developped independently). Denoting by $\mathbf{S} = [s_1,s_2,s_3]$ (figure 5) the period size in the three dimensions and by $\mathbf{i} \in \mathbb{N}^3$ is the distance between one point of coordinates $\mathbf{r}$ and its periodic image $\mathbf{r'} = \mathbf{r} + \mathbf{S} \cdot \mathbf{i}$ in an adjacent period, then the pore pressure is expressed as follow:

$$p' = p + \nabla p \,.S * i \qquad (12)$$

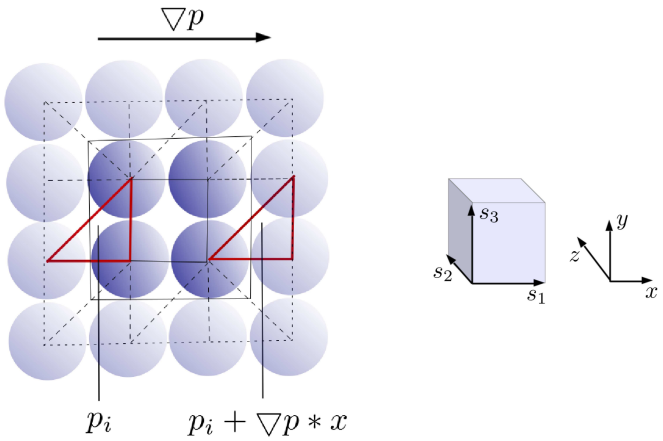

Figure 5: **(a): 2D periodic cell, (b): simulation period of size S = [s_1,s_2,s_3] in [x,y,z]**

NUMERICAL RESULTS

We generate an assembly of N=1000 frictional grains of average radius a = 0.025 ± 0.01 m, density ρ = 2500kg/m^3 and friction angle Φ = 30°. The assembly (Figure 6) is H = 18a high, L = 12a large and l = 12a wide. The granular material is first confined under a constant vertical stress T_y, then sheared without gravity, between two parallel walls distant from H and moving at a velocity ±V/2 = 0.75m/s respectively. In order to avoid slip zones near the plates, the first layer of spheres in contact with the plates is fixed to that ones by highly cohesive contacts. The boundary conditions for the top plate are the velocities $v_x = V/2$, $v_z = 0$, the total vertical stress T_y = 750 Pa and the fluid pressure p = 0. At the bottom plate, $v_x = -V/2$, $v_z = 0$ and the fluid velocity along the y axis $v_y^f = 0$. Periodic boundary conditions are applied along the horizontal axis for both the particles and the fluid. For the latest we impose a null pressure gradient at the macro-scale, i.e. $\nabla p_x = \nabla p_z = 0$.

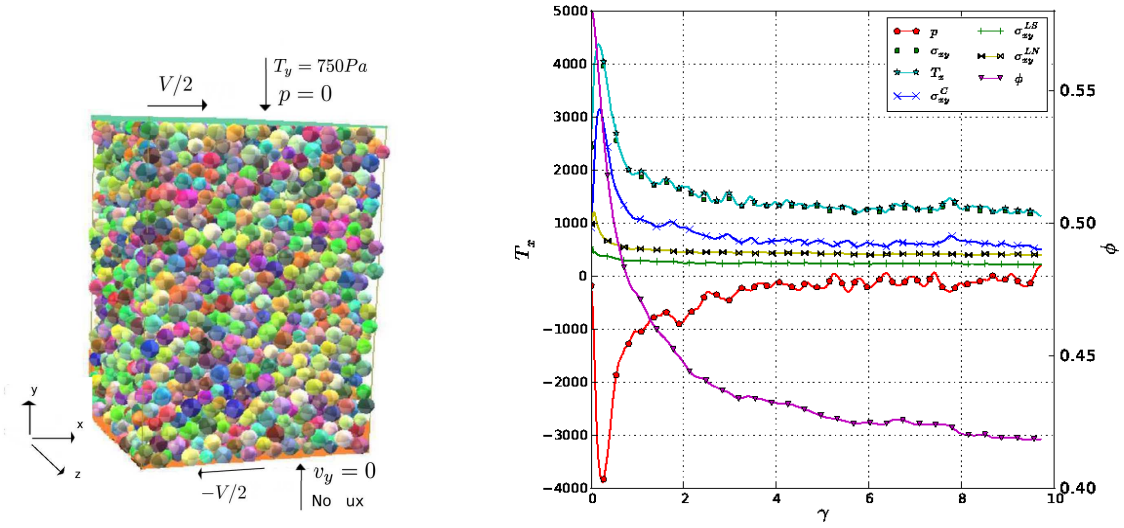

Figure 6: S**imulation cell (left). Evolution of the shear stress and the solid fraction as the deformation (right) [Marzougui et al. 2015].**

Simulations of such an assembly saturated of an incompressible fluid of viscosity η and submitted to a simple shear with shear rate $\dot{\gamma} = \frac{dV}{dH}$ at imposed vertical stress T_y are presented. The viscous stress is decomposed in different contributions which can be examined separately:

$$\sigma = \sigma^C + \sigma^L + p\,I + \sigma^I \tag{13}$$

$\sigma^C = \frac{1}{V}\sum F_{ij}^C \otimes l_{ij}$ is the contact stress applied on particles in contact where l_{ij} is the branch vector between particles *i* and *j*. $\sigma^L = \frac{1}{V}\sum F_{ij}^L \otimes l_{ij}$ is the lubrication stress [Ancey et al. 1999], which is the sum of the normal and shear components of the lubrication force. p is the pressure associated to the poromechanical coupling [Catalano et al. 2014]. $\sigma^I = \sum m_k v_k \otimes v_k$ reflect the inertial effects as defined in [Savage et al. 1981] where m_k and v_k are the mass and the velocity of particle k respectively. In figure 7, both $T_x = F_x / S$ (F_x is the force applied in the top plate and S is its area) and σ_{xy} are plotted and these two expressions compare consistently.

Figure 7 shows the different contributions of each force applied on the granular media for $I_v = 0.21$. The inertial stress σ_{xy}^I (not represented here) is negligible compared with the total stress ($\sigma_{xy}^I \ll 2.5\,T_x$). This indicates that the suspension is dominated by contacts and viscous interactions for the value of I_v investigated. The contact stress contributes to approximately half of the total stress. Contrary to what is sometimes postulated in the literature, our numerical results show that tangential lubrication forces ($\sigma_{xy}^{LS} \ll 20\,\%\,T_x$) are significant compared with the normal ones ($\sigma_{xy}^{LN} \ll 20\,\%\,T_x$).

The different contributions are investigated for different values of the viscous number I_v . I_v is a dimensionless form of the shear rate [Boyer et al. 2011], reflecting the magnitude of viscous effects, and is defined as:

$$I_v = \frac{\eta|\dot{\gamma}|}{T_y} \qquad (14)$$

The results obtained with only normal lubrication forces match qualitatively the empirical evolution of shear stress with I_v. However, the solid fraction obtained with this model is almost constant for $I_v \geq 0.02$, while the experiments suggest a monotonic decrease. The normal lubrication alone leads to a satisfactory stress ratio but overestimate the solid fraction. When the shear lubrication forces are included, the results get closer to the phenomenological laws $\mu(I_v)$ and $\phi(I_v)$. Consequently, the shear lubrication forces play a significant role to the dilatancy law, and they also contribute to the shear stress. The rolling torques, the twist torques and the poromechanical coupling have only marginal effects.

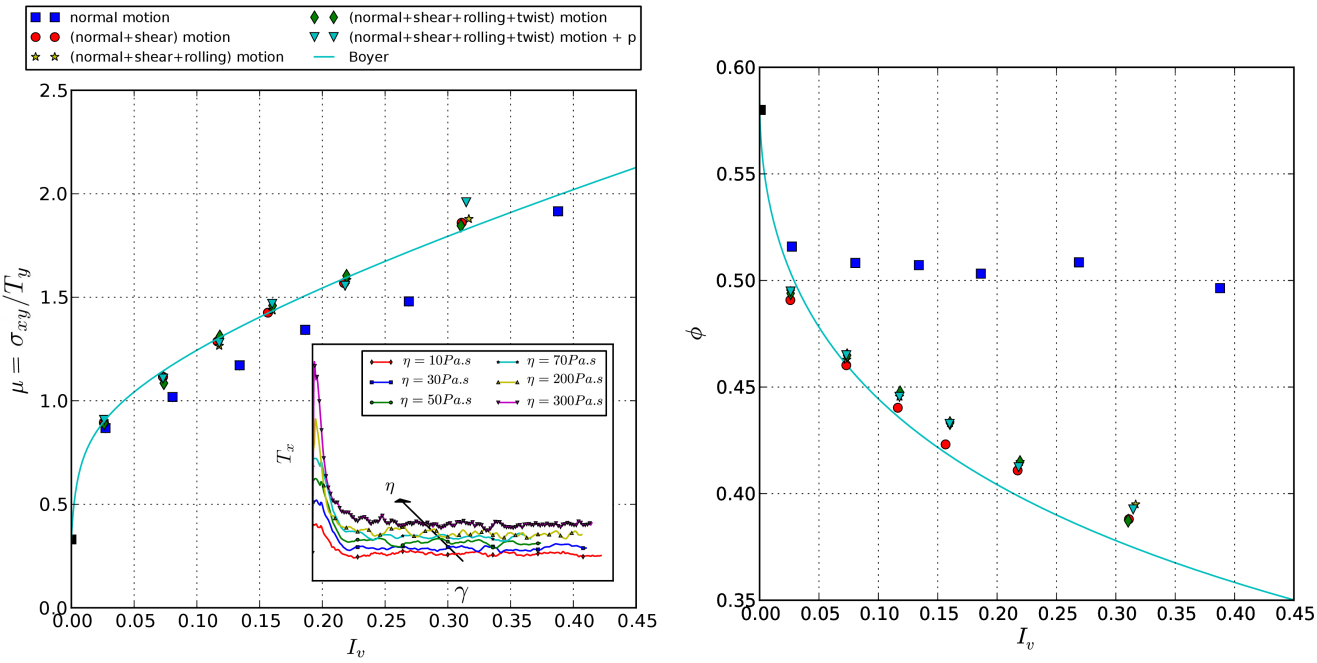

Figure 7: **Stress ratio μ (left) and the solid fraction φ (right) at steady state versus Iv . Each symbol represents a different combination of lubrication terms. The solid line is the phenomenological law of Boyer et al. 2011. Inset: the total shear stress for different values of fluid viscosity [Marzougui et al. 2015].**

CONCLUSION

In this contribution, we presented an original hydromechanical coupled model able to describe the behavior of dense granular materials subjected to a shear flow under constant pressure. The analysis of the various contributions to the bulk stress: contact forces, hydrodynamic forces and fluid pressure suggest that both the contact stress and the lubrication stress increase monotonically in the range of I_v investigated. The numerical model reproduces the behavior of dense suspensions described experimentally by the phenomenological laws from the experiments of Boyer et al [2] $\mu(I_v)$ and $\phi(I_v)$.

REFERENCES

Ancey, C., Coussot, P. and Evesque, P. (1978-present). A theoretical framework for granular suspensions in a steady simple shear flow. *Journal of Rheology* 43(6):1673–1699, 1999.

Boyer, F., Guazzelli, E. and Pouliquen, O. 2011. Unifying suspension and granular rheology. *Physical Review Letters*, 107(18):188301.

Catalano, E., Chareyre, B., Cortis, A., and Barthelemy, E. 2011. A Pore-Scale HydroMechanical Coupled Model For Geomaterials. In Onate, E. and Owen, D.R.J., editor, Particle-based methods II: Fundamentals and Applications, pages 798–809, 2011. *2nd International Conference on Particle-Based Methods - Fundamentals and Applications (Particles)*, Barcelona, Spain, oct 26-28.

Catalano, E., Chareyre, B. and Barthélémy, E. 2014. Pore- scale modeling of fluid-particles interaction and emerging poromechanical effects. *International Journal for Numerical and Analytical Methods in Geomechanics*, 38(1):51–71.

Chareyre, B., Cortis, A., Catalano, E. and Barthélémy, E. 2012 . Pore-scale modeling of viscous flow and induced forces in dense sphere packings. *Transport in Porous Media*, 92(2):473–493.

Frankel, N.A. and Acrivos, A. 1967. On the viscosity of a concentrated suspension of solid spheres. *Chemical Engineering Science*, 22(6):847–853.

Jeffrey, D.J. and Onishi, Y. 1984. Calculation of the resistance and mobility functions for two unequal rigid spheres in low-reynolds-number flow. *Journal of Fluid Mechanics*, 139:261–290.

Jeffrey, D.J. and Onishi, Y. 1984. The forces and couples acting on two nearly touching spheres in low-reynolds-number flow. *Zeitschrift fur angewandte Mathematik und Physik ZAMP*, 35(5):634–641.

Ladd, A.J.C. and Verberg, R. 2001. Lattice-boltzmann simulations of particle-fluid suspensions. *Journal of Statistical Physics*, 104(5-6):1191–1251.

Marzougui, D., Chareyre, B. and Chauchat, J., Microscopic origins of shear stress in dense fluid-grain mixtures, (to appear in) *Granular Matter*, (2015).

Nguyen, N-Q. and Ladd, A.J.C. 2002. Lubrication corrections for lattice-boltzmann simulations of particle suspensions. *Physical Review E*, 66(4):046708.

Rognon, P.G., Einav, I., Gay, C. 2011. Flowing resistance and dilatancy of dense suspensions: lubrication and repulsion. *Journal of Fluid Mechanics*, 689(1):75–96.

Savage, S.B. and Jeffrey, D.J. 1981. The stress tensor in a granular flow at high shear rates. *Journal of Fluid Mechanics*, 110:255–272.

Smilauer, V. and Chareyre, B. Yade Dem Formulation. In V. Smilauer, editor, *Yade Documentation*. The Yade Project, 1st edition, 2010. http://yade-dem.org/doc/.

Tong, A-T., Catalano, E., and Chareyre,B. 2012. Pore-Scale Flow Simulations: Model Predictions Compared with Experiments on Bi-Dispersed Granular Assemblies. *Oil & Gas Science and Technology-Revue d'IFP Energies Nouvelles*, 67(5):743–752.

Van den Brule, B. and Jongschaap, R.J.J. 1991. Modeling of concentrated suspensions. *Journal of statistical physics*, 62(5):1225–1237.

Yeo, K. and Maxey, M.R. 2010. Simulation of concentrated suspensions using the force-coupling method. *Journal of computational physics*, 229(6):2401–2421.

Zeghal, M. and El Shamy, U. 2004. A continuum-discrete hydromechanical analysis of granular deposit liquefaction. *International journal for numerical and analytical methods in geomechanics*, 28(14):1361–1383.

Zhao, J. and Shan T. 2013. Coupled CFD–DEM simulation of fluid–particle interaction in geomechanics. *Powder Technology*, 239(0):248 – 258.

Double scale validation of a micro mechanics-based model for Cemented Granular Materials

A. Tengattini[1,2], C.Viggiani[2] and I.Einav [1]

1: The University of Sydney

2: Laboratoire Sols, Solides, Structures, Grenoble, France

alessandro.tengattini@sydney.edu.au cino.viggiani@3sr-grenoble.fr
itai.einav@sydney.edu.au

ABSTRACT

A novel thermomechanically sound constitutive model for cemented granular materials has recently been proposed [1, 2]. This model is based on measurable and micro-mechanics based internal variables describing the evolution of the dominant inelastic processes. In this contribution the model capability to reproduce the material behaviour both in terms of stress-strain response and of localization patterns starting from a few physically meaningful parameters is briefly overviewed.

A key aspect of the proposed model is its capability to link the observed macroscopic behaviour to the statistically averaged evolution of the micro structure. Given the bottom-up hierarchy in the model development, it is crucial to assess the model's capability to also capture the micro-scale processes embedded at its base.

For this purpose we have used high resolution x-ray tomography to scan artificially cemented granular materials and developed an array of image processing tools to quantitatively asses the evolution of the micro-structure, which beside allowing the double scale validation of the model, grants also an unprecedented understanding of the inter-dependence of the micro-scale phenomena.

1 . INTRODUCTION

Cemented Granular Materials (CGMs) are a broad class of geomaterials in which densely packed particles are bridged by cement, which partially or completely fills the interstitial space [3, 4]. The shared micro structure of this materials causes analogous micro-mechanisms

to lead the macroscopic response: grain crushing, cement damage and fragment reorganisation [5, 6]. Most existing models for CGMs ([7, 8, 9, 10]) are phenomenological adaptations of classic elastoplasticity and have demonstrated their capability to fit the experimentally observed macroscopic behaviour. Nonetheless the absence of direct links with the micro-scale processes often causes a high number of parameters and of the lack of physical interpretation for some of them. The relatively recent technological advancements in microscopic imaging are giving access to an increasing amount of informations about the evolution of the micro-scale properties, with an ever-improving spatial resolution. Also the advancements in computational power and numerical modelling (e.g. DEM) are allowing to get further understanding of such processes. This unprecedented insight on the physics involved at different scales allows the construction of new theories, capable of extracting and describing the crucial phenomena. This allows both practical advancements in the prediction of the material behaviour and give direction to further pertinent studies.
The micro-mechanical bases of the proposed constitutive model are reviewed in §2, and its macroscopic performance validated in §3. The feasibility of the direct measurement of the proposed internal variables in 3D, in-situ, x-ray images is assessed in §4.

2. A CONSTITUTIVE MODEL FOR CEMENTED GRANULAR MATERIALS WITH MICRO-MECHANICS BASED INTERNAL VARIABLES

Electronic microscopy and acoustic emissions measurements [5, 6, 11] have long been used to explore the micro-mechanisms involved in the inelastic evolution of CGMs and have evidenced the heterogeneity-dominated behaviour of the material at the micro-scale. The description of the physics involved should therefore be handled through statistical analyses. As argumented in [12], in fact, an ideal model should connect the many stochastic processes occurring at the microscale to a deterministic assessment of the macro response of a statistically homogeneous continuum.
Particular attention has been given to the choice of internal variables which should ideally be identifiable, measurable and related to the dominant modes of irreversible rearrangements of the material microstructure. ``Internal variables inferred from phenomenological evidence and selected to fit a particular stress strain-curve may provide a result that pleases the eye but seldom contributes to the understanding of the processes represented by the fitted curve" [13].
In CGMs, three main inelastic micro-scale processes [5, 6] drive the macroscopic behaviour: grain crushing, cement damage and fragment reorganization. The description of grain crushing has previously been tackled in [14, 15], measuring the evolution of the grain size distribution. The scalar Variable breakage B, described in Fig 1a has therein been proposed and has shown to successfully correlate the evolving micro-structure to the macroscopic behaviour.

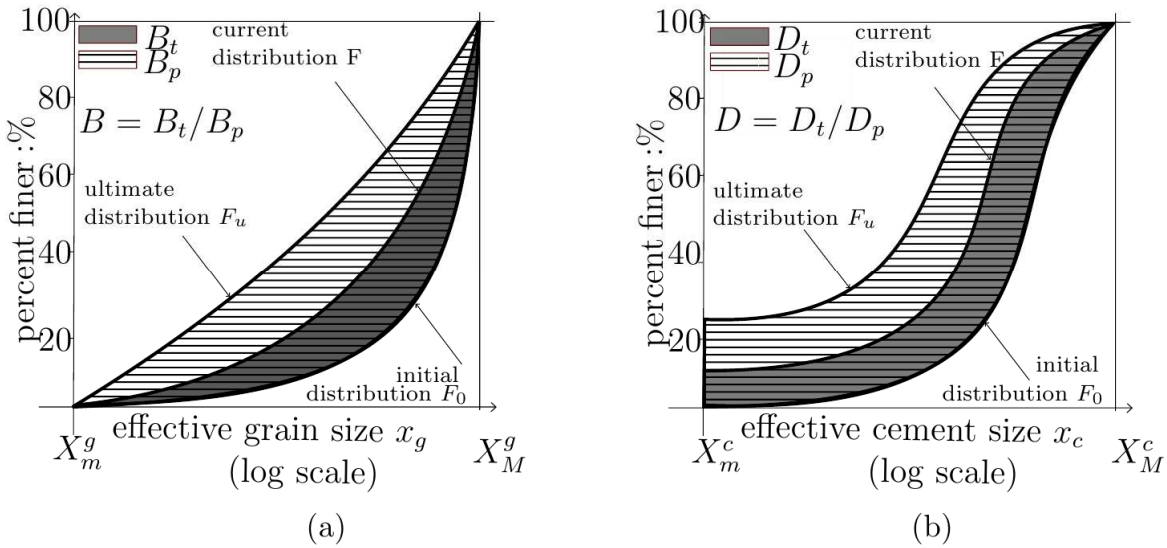

Figure 1. **Scalar internal variables: a) Breakage (B), [14], b) Damage (D) [1].**

The cement phase has an inherently different behaviour: it endows the system with tensile resistance, distributes the forces at the grain contacts, and enhances shear strength of the granular phase [16, 17, 18]. When damage occurs in the cement, its role in the system is strongly re-dimensioned [19, 20] and the mechanical contribution of its fragments to the force network is negligible to a first approximation. The proposed approach is therefore to describe damage through the evolution of the effectively working cement: when a cement bridge is partially cracked, we can in principle substitute it with another, with a smaller sectional area, but made of undamaged material with the same contribution to the system. It is then possible to define an effective cement size distribution and, analogously to the breakage (B) variable define damage as the area ratio in Fig.1b. The possibility to experimentally assess this variable directly is discussed in § 4.

The last inelastic microscopic process occurring, fragment reorganisation, can be effectively characterised by the plastic strain, which, describing the unrecoverable macroscopic strain, lends itself as an natural measure for this phenomenon.

2.1. THE MODEL AT A GLANCE

Beyond the possibility of having observable (at least in principle) descriptors of the micro-scale texture, the use of physically meaningful internal variables allows a rational connection between them, the evolution of the elastically stored energy and the energy dissipation. As shown in [14], in fact, it is possible to describe, through statistical homogenization over a Representative Elementary Volume (REV), the elastically stored energy in a granular material describing how the Helmholtz free energy is distributed according to the grain size. It is then possible to deduce the evolution of the elastically stored energy as grain crushing proceeds and to connect its loss to the increment of dissipation. Imposing the first two laws of thermodynamics, it is eventually possible to deduce the full constitutive model [1, 2].

3. MACROSCOPIC AND STRUCTURAL VALIDATION OF THE MODEL.

As detailed in [1, 2], the proposed model requires only 8 parameters and 3 geometrical indexes, each having a precise physical interpretation, to be compared with the 13 or more parameters of well-established models [9, 10]. An example of the capabilities of the model to reproduce the experimentally observed macroscopic response for Bentheim sandstone is reported in Fig 2. Implementing then the constitutive model within a finite element model with the very same set of mechanical parameters it is possible to reproduce the typical localization patterns experimentally observed in samples undergoing drained triaxial compression, as shown in Fig 3. An exhaustive description of the calibration process for the model parameters as well as the details of the finite element implementation and the localization analyses are reported in [2], but the aim of this contribution is to to explore the intriguing possibility to also verify the model predictions regarding the evolution of the micro-structure.

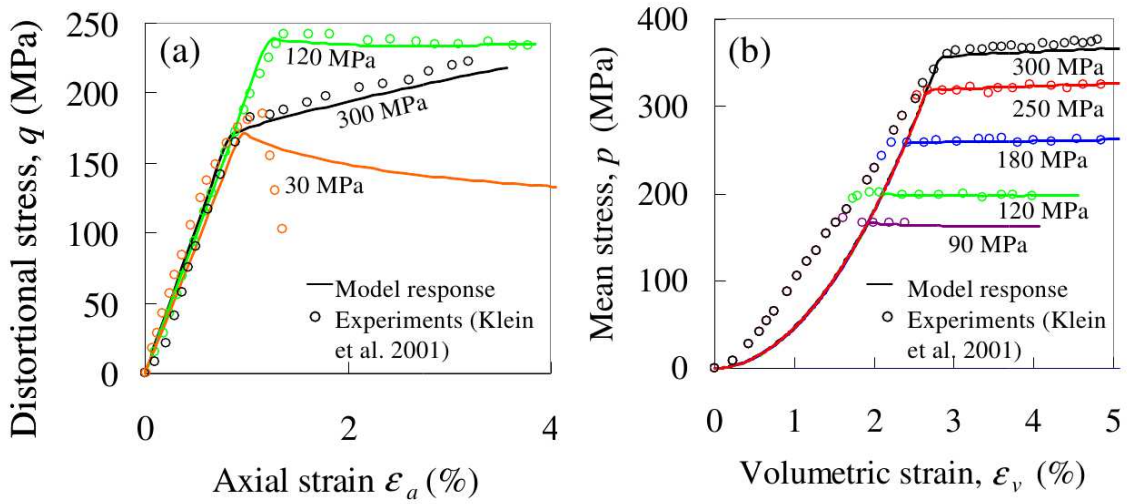

Figure 2. **Drained triaxial tests on Bentheim sandstone (Klein et al., 2001); experimental observation and model predictions.**

4 . MICROSCOPIC VALIDATION OF THE MODEL.

Recently, a number of experimental tools have been refined, allowing access to full-field measures of disparate mechanical informations at the micro (grain) scale in CGMs [6, 21].
A common element in the different technologies seems to be the trade off between the spatial resolution and the size of the considered specimen, that should be bigger than the Representative Elementary Volume to be interesting from a statistical viewpoint. The study of the acoustic emissions gives access to the distribution of the inelastic events of elastic energy release [22, 23], suggesting the fascinating possibility of measuring at least some of the energy dissipated in the system directly. Also, the use of ultrasonic tomography has lately shown its capability to get to full field measures of the elastic properties [24].

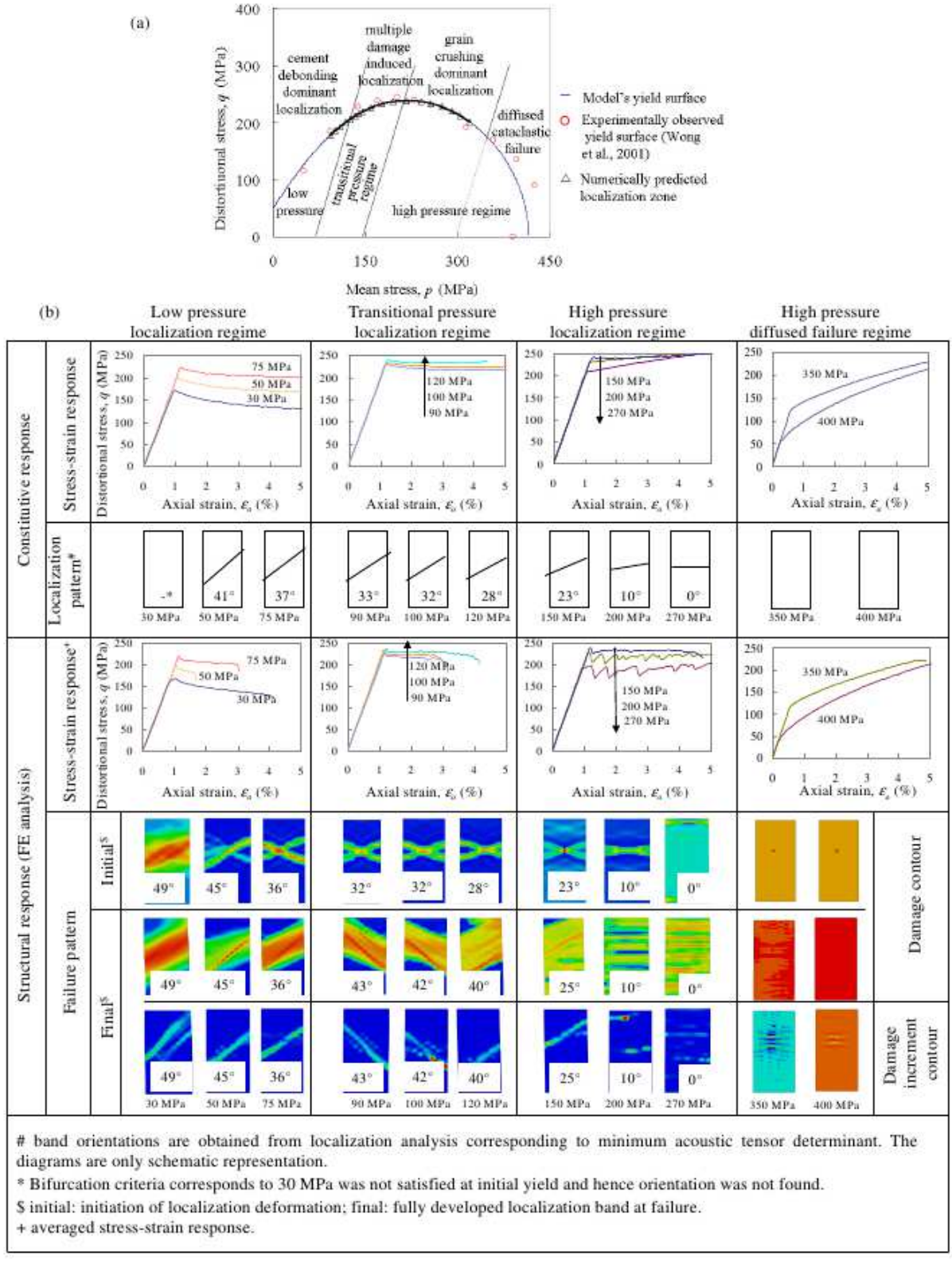

band orientations are obtained from localization analysis corresponding to minimum acoustic tensor determinant. The diagrams are only schematic representation.

* Bifurcation criteria corresponds to 30 MPa was not satisfied at initial yield and hence orientation was not found.

$ initial: initiation of localization deformation; final: fully developed localization band at failure.

\+ averaged stress-strain response.

Figure 3.**Failure modes of Bentheim sandstone: (a) yield envelope (the lines dividing zones are indicative only) (b) model responses under drained triaxial condition at different stress regimes.**

In this work we focus on high resolution x-ray Computed Tomography (CT), which has lately shown the potential of the reconstructed 3D map of absorption in the analysis grain scale processes. The three key phenomena occurring in CGM, grain crushing, cement damage and fragment rearrangement can easily be imaged with this technique, yet dedicated tools to quantitatively measure them need to be developed. In [25] and subsequent works a technique to follow the single grains throughout a test have been proposed, allowing an immediate measure of fragment rearrangement. Preliminary works exploring the in-situ 3D measure of the crushing-induced evolution of grain size distribution in granular materials have been proposed in [26, 27]. In this contribution we will explore the possibility to measure cement damage.

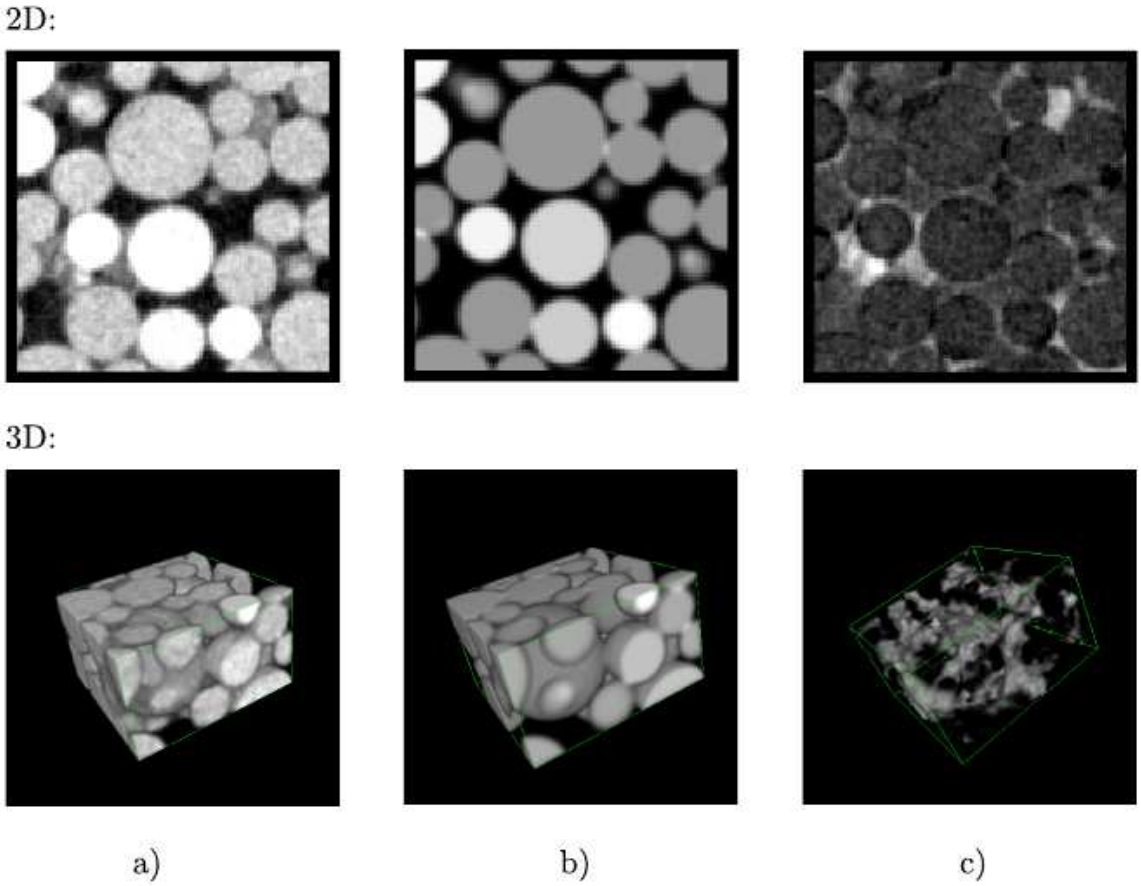

Figure 4. **Example of the application of the Kalisphera-based segmentation in 2D (top row) and 3D (bottom row): a) original image b) Kalisphera spheres obtained after the optimization of the radii of the spheres c) subtraction of the spheres from the original images.**

With the aim of isolating cement fragmentation, a model material has been designed to prevent other inelastic phenomena such as grain crushing. Also, since a simple geometry of the granular phase allows to take advantage of the grain topology for image post-processing, spheres have been selected. The material proposed is calcite-cemented glass ballottini, with a D50 of about 300μm. Two different phases of image processing aimed to measuring damage can broadly be identified: cement identification and damage measure.

The former is commonly known as segmentation and in the case of three phase materials is referred to as 'image trinarization'. Despite the large number of existing approaches developed, none of the methods proposed in literature has so far provided accurate, user-independent results. For this very reason a new tool, taking advantage of the spherical shape of the granular part has recently been proposed [28]. As sketched in Fig. 4, the idea of the method is to identify, through a template matching procedure, spheres in 3D images. It is at that point straightforward to remove the granular component from the images, obtaining an image containing only cement and voids. These remaining phases can be easily classified based on their grey value, adopting any of the existing histogram-based methods, which are straightforward reliable for two-phase materials.

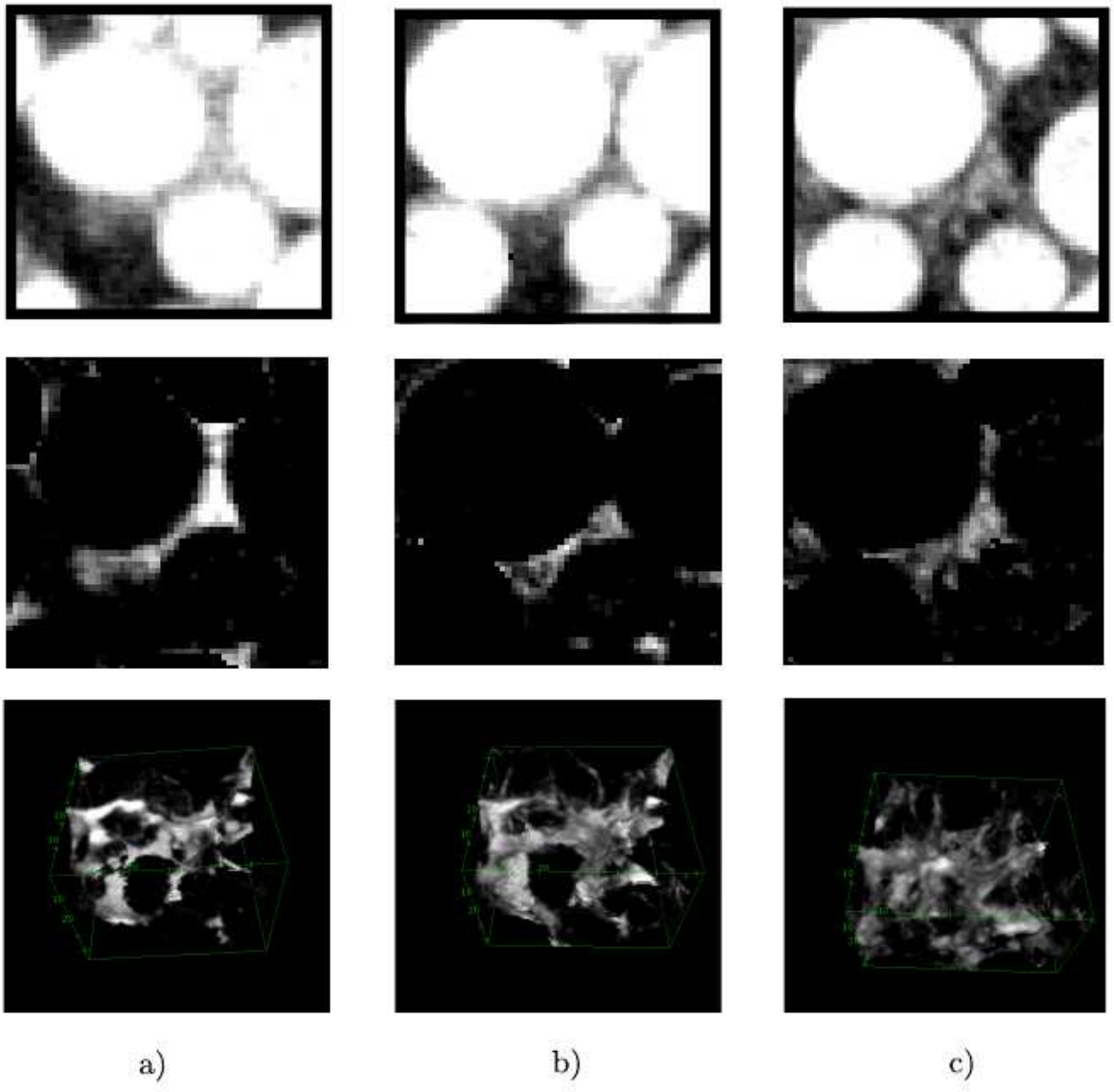

Figure 5. **Example of the evolution of damage in the sample at the initial (a) intermediate (b) and final stages of the test (c). In the top row is reported the original image. In the middle row the grains have been removed to isolate the cement. The bottom row reports the 3D rendering of the evolution of the cement**

With a clear distinction of the existing phases it is straightforward to follow the evolution of cement throughout the test, as shown for a single cement bridge in Fig. 5. Alternative

measures of damage can at this point be proposed, although it is already evident that the richness of information deriving from the possibility to correlate local damage and the single grain kinematics deriving from tools such as the ones presented in [25] is unprecedented. The choice of the optimal definition of damage, its comparison to the model's predictions as well as its relations to grain kinematic and macroscopic behaviour will be explored in forthcoming publications.

5. CONCLUSION

In the present paper the fundamental hypotheses of a novel micro-mechanics based constitutive model for Cemented Granular Materials are discussed and its micro-mechanics based internal variables described. Its capability to reproduce both the macroscopically observed mechanical response and the structural (specimen-scale) localization patterns is highlighted. The micro-mechanics based nature of the model calls though for a further level of validation, to assess its capability to predict the evolution of the grain-scale inelastic processes. To do so it is has been necessary to develop *ad-hoc* image processing tools to extract quantitative, statistically representative informations regarding the evolving processes (grain crushing, cement damage and fragment rearrangements). This contribution focuses on the experiments and post-processing tools required to measure the evolution of each cement bridge of a mechanically representative sample of calcite cemented glass ballottini. The possibility of measuring *in-situ* cement damage goes well beyond the model validation itself and opens unprecedented possibilities in the understanding of the inter-relations of the micro-scale inelastic phenomena occurring in cemented granular materials

ACKNOWLEDGEMENTS

Alessandro Tengattini wish to thank the University of Sydney International Scholarship scheme.

REFERENCES

[1] Alessandro Tengattini, Arghya Das, Giang D. Nguyen, Gioacchino Viggiani, Stephen A. Hall, Itai Einav, A thermomechanical constitutive model for cemented granular materials with quantifiable internal variables. Part I—Theory, Journal of the Mechanics and Physics of Solids, Volume 70, October 2014, Pages 281-296, ISSN 0022-5096,

[2] Arghya Das, Alessandro Tengattini, Giang D. Nguyen, Gioacchino Viggiani, Stephen A. Hall, Itai Einav, A thermomechanical constitutive model for cemented granular materials with quantifiable internal variables. Part II – Validation and localization analysis, Journal of the Mechanics and Physics of Solids, Volume 70, October 2014, Pages 382-405, ISSN 0022-5096

[3] Topin, V., Delenne, J.-Y., Radjai, F., Brendel, L. and Mabille, F. Strength and failure of cemented granular matter. Eur. Phys. J. (2007) E 23: 413-429.

[4] Delenne, J.-Y., Topin, V. and Radjai, F. Failure of cemented granular materials under simple compression: experiments and numerical simulations. Acta Mech. (2009) 205: 9-21

[5] Menendez, B., Zhu, W., and Wong, T. Micromechanics of brittle faulting and cataclastic flow in Berea sandstone. Journal of Structural Geology,(1996) 18: 1-16.

[6] Wong, T., and Baud, P. The brittle-ductile transition in porous rock: A review. Journal of Structural Geology. (2012) 44: 2-53

[7] Gens, A., Nova, R. (1993).Conceptual bases for a constitutive model for bonded soils and weak rocks. Proc. Geotechnical Engineering Hard Soils-Soft Rocks

[8] Lagioia, R., and Nova, R. An experimental and theoretical study of the behaviour of a calcarenite in triaxial compression. (1995) Geotecnique, 45(4): 633-648.

[9] Nova, R., Castellanza, R., and Tamagnini, C. A constitutive model for bonded geomaterials subject to mechanical and/or chemical degradation.(2003) Int. J. Numer Anal Met, 27(9): 705-732.

[10] Vatsala, A., Nova, R., and Murthy, S. Elastoplastic Model for Cemented Soils.(2001)J. Geotech. Geoenv. Eng. 127(8): 679-687.

[11] Zhang, J., Wong, T-F., Yanagidani,T. and Davis, D.M. Pressure-induced microcracking and grain crushing in Berea and Boise sandstones: acoustic emission and quantitative microscopy measurements (1990) Mech. of Mater. 9 1-15

[12] D. Krajcinovic. Damage Mechanics, Elsevier, (1996)

[13] D. Krajcinovic. Selection of damage parameter Art or science ? (1998) Mechanics of Materials 28: 165-179,

[14] Einav, I. Breakage mechanics-Part I: Theory. (2007)J. Mech. Phys. Solids.. 55(6):1274-1297.

[15] Einav, I. Breakage mechanics-Part II: Modelling granular materials. (2007) J. Mech. Phys. Solids.. 55(6): 1298-1320.

[16] M. R. Coop and J. H. Atkinson, The mechanics of cemented carbonate sands, (1993) Geotecnique 43,1: 53-67.

[17] D. Airey, Triaxial Testing of Naturally Cemented Carbonate Soil. (2006) J.Geot. Eng. 119,9 : 1379-1398.

[18] Zang, A., and Wong, T.F.. Elastic Stiffness and Stress Concentration Cemented Granular Material.(1995) Int. J. Rock Mech. Min Sci. and Geomech. Abstr., 32(6) 563-574.

[19] J. Huang and D. Airey, Properties of artificially cemented carbonate sand. (1998) J. Geot. Geoenv. Eng. 124,6 :492-499.

[20] S. Fernando, P. Pedro, and N. C. Consoli, Characterization of Cemented Sand in Triaxial Compression. (2001) J. Geot. Geoenv. Eng. 127,10 :857-868.

[21] Viggiani, G., Hall S. Full-field measurements in experimental geomechanics: historical perspective, current trends and recent results (2012) ALERT Doctoral School 2012: Advanced experimental techniques in geomechanics

[22] E.-M. Charalampidou, S. A. Hall S. Stanchits, H. Lewis and G. Viggiani, Characterization of shear and compaction bands in a porous sandstone deformed under triaxial compression. (2011) Tectonophysics 503: 8-17

[23] E. Townend, B.D. Thompson, P. M. Benson,P. Baud, and R. P. Young Imaging compaction band propagation in acoustic emission locations (2008) Geoph. res. Lett. 35

[24] S. A. Hall, E. Tudisco Full-field ultrasonic measurement (ultrasonic tomography) in experimental geomechanics. (2012) ALERT Doctoral School 2012: Advanced experimental techniques in geomechanics

[25] Ando, E., Hall, S.A., Viggiani, G., Desrues, J., Besuelle, P. Grain-scale experimental investigation of localised deformation in sand: a discrete particle tracking approach,(2011) Acta Geotech. 7-1: 1-13

[26] Tengattini, Alessandro, et al. "Double-Scale Assessment of Micro-mechanics Based Constitutive Models for Granular Materials Undergoing Mechanical Degradation."*Bifurcation and Degradation of Geomaterials in the New Millennium*. Springer International Publishing, 2015. 175-180.

[27] Gkiousas-Kapnisis, Marios, et al. "Development of image analysis tools to evaluate in-situ evolution of the grain size distribution in sand subjected to breakage." Bifurcation and Degradation of Geomaterials in the New Millennium. Springer International Publishing, 2015. 253-258

[28] Tengattini Alessandro, Andò, Edward: "Kalisphera: an analytical tool to reproduce the partial volume effect of spheres imaged in 3D" submitted

Part Four: Gravitational instability

DEM simulation of dry granular flow impacting a rigid wall

A. Albaba, S. Lambert & F. Nicot
Irstea de Grenoble - Unité ETNA, Saint Martin d'Hères, France
Adel.albaba@irstea.fr stephane.lambert@irstea.fr
francois.nicot@grenoble.cemagref.fr
and
B. Chareyre
Laboratoire Sols, Solides, Structures, Grenoble, France
bruno.chareyre@3sr-grenoble.fr

ABSTRACT

This study presents a model for simulating the impact behavior of dry granular flow against a rigid wall using Discrete Element Method (DEM). The simulations were carried out using poly-dispersed clumps consisting of two overlapping spherical particles accounting for the shape effects of gravel particles. The particles were flowing in an inclined flume where different inclination angles were tested and interaction forces with the wall were recorded. The model calibration was in particular based on particle shape and flow thickness measurements. Compared with the experimental results, the model showed good agreement regarding the peak impact force, the time of the peak force and the final (residual) force at the end of the tests.

INTRODUCTION

The rapid increase of urban activities in mountainous areas encouraged more attention to be given to the mitigation of threats caused by natural hazards such as rockfalls and debris flow. Due to their high flow velocity and impact forces, long runout distance and poor temporal predictability, granular flows have been classified as one of the most hazardous landslides (Jakob & Hungr 2005). However, their hazard can be mitigated by the use of protection structures similar in principle to rockfall barriers (Guasti et al. 2011). Such structures are either retaining walls (Kishi et al. 2000) or flexible structures made of nets (Nicot et al. 2001). The estimation of total impact force exerted by granular flows on such structures is an important factor in their design. Such a force generally varies with slope angle, thickness of the flowing material and velocity at the moment of the impact.
Numerical models of granular flows have been generally classified into continuum and discrete models. Continuum treatment has often been adopted where flows characteristics are

analyzed by the Eulerian forms of continuity and momentum equation (Azana et al. 1999). On the other hand, with the use of a Discrete Element Method (DEM), Silbert et al. (2001) carried out 2D and 3D simulations of mono-dispersed particles flowing in a steady-state condition where observations were taken regarding structure and rheology of the flow. Faug et al. (2009) proposed a hydrodynamic model based on depth-averaged momentum conservation which was used to predict DEM numerical results of a free-surface gravity-driven dense flow overflowing a wall. On the experimental side, a variety of experimental studies have been carried out ranging from studies on geological debris flows to well characterized laboratorial granular flows down an inclined plane (Azana et al. 1999). However, none of the experiments considered coarse-grained flow of angular particles which is the main case for actual dry granular flow.

The aim of this paper is to present a DEM-based model which is able to simulate the impact behavior of dry granular flow of angular particles against a rigid wall. First, we will describe the experimental data (Jiang & Towhata 2013) available for model calibration and validation. Next, we describe the model in terms of contact law, particles shape and flume characteristics. Afterwards, the model calibration and validation are presented with discussion of obtained results. Finally conclusions of the presented work are drawn.

EXPERIMENTAL DATA

Jiang & Towhata (2013) recently studied the impact behavior of dry granular flow against a rigid retaining wall using poly-dispersed mixture of limestone gravel. Particles were of a poly-dispersed gravel mixture ranging from 10 mm to 20 mm in diameter. The samples (which had specific weight of 13.5 kN/m^3) were prepared in a box with varying lengths (from 14 cm to 44 cm with a 5 cm step) and heights (from 5 cm to 20 cm with a 5 cm step) but with a 30 cm fixed width. The samples were released in a dam-break manner in which the gate was pulled instantaneously.

The flume was rectangular in cross section with 219 cm length, 30 cm width and 35 cm height. Different inclination angles α were tested ranging from 30˚ to 45˚. The friction angle of the flume base, flume sides and the rigid wall were 25˚, 15˚ and 21˚ respectively. At the end of the flume, a perpendicular rigid wall divided into six horizontal segments (marked from 1 to 6 starting from the bottom) was used. Interaction forces were recorded with each 5-cm in height segment of the wall.

Measurements of normal impact force vs. time were recorded along with observations of flow thickness and flow velocity at the time where the total normal force on the wall reaches its maximum. These experimental data were selected for our model calibration and validation. This is because it considers elongated coarse-grained flow of angular particles which is the main case for actual dry granular flow. In addition, the study provided detailed measurement of normal impact force for different heights (different segments of the rigid wall).Three different tests have been presented in the paper: Test L34-H15-$\alpha 45^o$, Test L44-H15-$\alpha 40^o$ and Test L44-H20-$\alpha 40^o$. For instance, Test L44-H15-$\alpha 40^o$ represents a sample having 44 cm in length, 15 cm in height and 40˚ inclination angle.

NUMERICAL MODEL

DEM has been used to carry out the simulation of the dry granular flow. Nowadays DEM is widely used for modeling granular media. It is particularly efficient for static and dynamic simulation of granular assemblies where medium can be described at a microscopic scale. The method is based on the molecular dynamics approach proposed by Cundall & Strack (1979).

Compared with Finite Element Method (FEM), DEM makes large displacements between elements easy to simulate. In addition, DEM surpasses FEM when dealing with discontinuous problems where FEM becomes computationally demanding. YADE software has been used as a modeling tool which is an extensible open-source framework for discrete numerical models, focused on Discrete Element Method (Šmilauer et al. 2010).

Contact law

A visco-elastic contact law with Mohr-coulomb failure criterion (Figure 1) has been adopted where normal and tangential contact forces F_n, F_t between particles were calculated as follows:

$$\vec{F_n} = (k_n u_n - \gamma \dot{u}_n)\vec{n} \tag{1}$$

$$\vec{F_t} = \begin{cases} \frac{k_t \vec{u_t}}{|k_t \vec{u_t}|} |\vec{F_n}| \tan\varphi & \text{if } |k_t \vec{u_t}| > |\vec{F_n}| \tan\varphi, \\ k_t \vec{u_t} & \text{otherwise} \end{cases} \tag{2}$$

where k_n and k_t are the normal and tangential stiffness parameters, u_n and u_t are the normal and shear displacements, $\tan\varphi$ is the friction coefficient and γ is the viscous damping coefficient. k_t was taken as (2/7) k_n as previously suggested by Silbert et al. (2001).

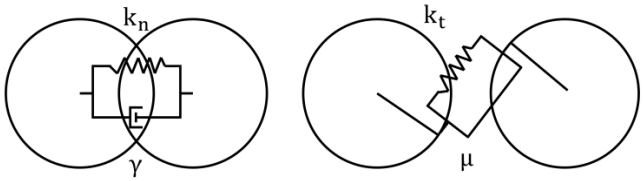

Figure 1. **Normal and tangential interaction forces of the contact**

Based on Schwager & Pöschel (2007), with the restitution coefficient (ε) being the ratio between velocities after and before the impact, $\varepsilon_{n,t}$ (normal and tangential) can be calculated as follows:

$$\beta_{n,t} = \frac{\gamma_{n,t}}{m} \tag{3}$$

$$\omega_{n,t} = \sqrt{\left(\frac{2k_{n,t}}{m_{eff}}\right)^2 - \beta^2} \tag{4}$$

$$\varepsilon_{n,t} = \frac{\dot{u}(t_c^0)}{\dot{u}(0)} = e^{-\beta\pi/\omega} \tag{5}$$

where $m_{eff} = (1/m_1 + 1/m_2)$, m_1 and m_2 are the masses of two interacting particles and $\dot{u}(t_c^0)$, $\dot{u}(0)$ are velocities after and before the collision respectively.

Contact law

Two shapes were compared: a simple spherical shape and a clump. The clump consists of two identical spheres (with a radius R) overlapping over a distance R thus having an aspect ratio of 3/2.

With the total weight of the sample being equal to the weight of a single D_{50}-sphere multiplied by the number of particles, the number of generated particles (num) was calculated as follows:

$$num = \left(\frac{V_t \gamma_t}{V_s \gamma_s}\right) \quad (6)$$

where V_t is the total volume of the sample, γ_t is the specific weight of the sample (13.5 kN/m^3), V_s is the volume of a single D_{50}-sphere and γ_s is the specific weight of gravel particles (taken as 26.5 kN/m^3 for the limestone gravel considered). Afterwards, each spherical particle was replaced with a clump consisting of two equal spheres. Radii of clumped-spheres were calculated so that the density and volume of the clump is equal to that of the particle which it replaces meaning that the overlapping volume is not counted twice.

MODEL CALIBRATION

The model calibration has been carried out considering the shape of the particles and the value of ε based on the flow thickness measurements. It is worth noting that, due to the absence of lubricated contact, the tangential viscous damping coefficient has been set to zero (i.e. ε_t = 1.0) as suggested by Ghaisas et al. (2004). Particle stiffness k_{par} = E D/2 where E is the Young's modulus (taken as 10^8 Pa) and D is the particle diameter. In order to ensure rigidity, the wall stiffness was taken ten times the stiffness of D_{50} particle. Friction angles of flume base, side walls and rigid wall were taken similar to values provided by the experimental data (Section 2). The model has been calibrated and validated for Test L34-H15-α45°, Test L44-H15-α40° and Test L44-H20-α40°. Results shown in the calibration section are for Test L44-H15-α40°.

Clumps vs. spherical particles

Two samples were tested: the first having spherical particles and the second having clumped ones. Clumps proved to be advantageous in lowering rotational energy (Figure 2a), adding interlocking effect between particles and improving shape representation of the angular gravel. Furthermore, the simulation is kept rather inexpensive (with the use of only two spheres for forming the clump).

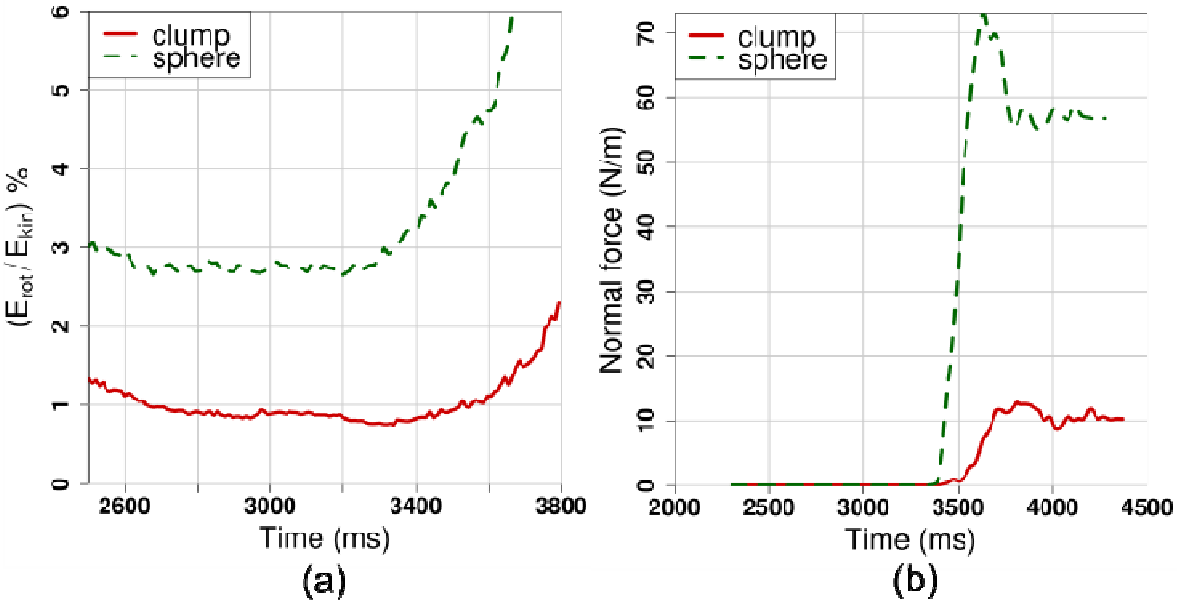

Figure 2. **Test L44-H15-α40°: (a) Ratio of rotational energy to total kinetic energy for clumps and spheres, (b) Normal force on part 6 of the wall**

Consequently, compared with the spherical particles, peak and residual values (Figure 2b) on the sixth segment of the wall for clumped particles are closer to the experimental (experimental values: $F_{peak} \approx 14$ N/m, $F_{res} \approx 10$ N/m). This might be due to the rolling resistance provided by the clump shape which prevents the particles from rolling over the dead zone deposit and accumulate behind part 6 of the wall. As a result, clumped particles are used for the rest of the tests as they proved superiority over spherical ones.

Flow thickness and velocity

The targeted part of the flow for calculating velocity and thickness were particles within a distance ranging from 40 to 50 cm away from the wall. However, since the flow has two regimes along the flow thickness-collisional and frictional-, cumulative frequency were drawn in which thickness and velocity values were taken at 90% of total frequency of particle center. A value of $D_{50}/2$ was added to 90% cumulative frequency of the flow thickness to account for the free surface of the flow.

Different values of restitution coefficient were tested and flow thickness values were observed for each corresponding restitution coefficient. It was found that $\varepsilon = 0.3$ is suitable for our flow based on flow thickness measurements resulting in a model value of 3.9 cm which well-correspond to the experimental value of 3.9 cm (Figure 3a).

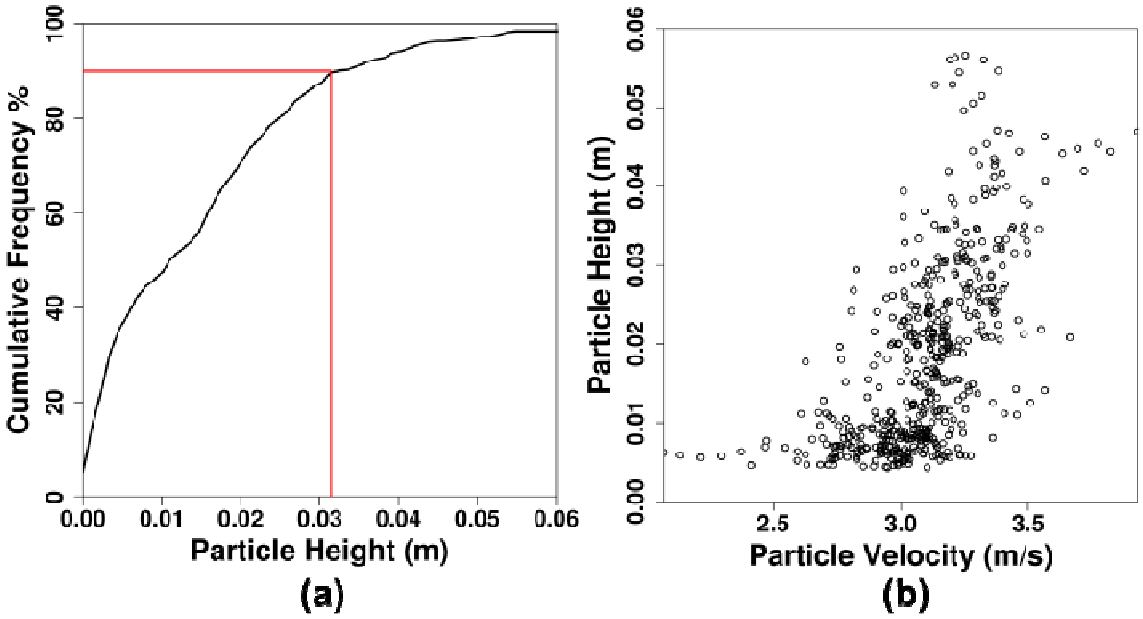

Figure 3. **Test L44-H15-α40°: (a) Cumulative frequency of gravity center of particles height, (b) Variation of particles velocity with heights**

However, velocity measurement of test L44-H15-α40° in the model (Figure 3b) taken at the considered flow thickness (at 90% for cumulative frequency) was found to be lower than experimental value (model: 3.33 m/s, exp: 4.13 m/s) which still needs further investigation. However, it is worth highlighting that measurements of velocity were taken only for the particles at the top surface of the flow.

MODEL VALIDATION

The rigid wall response against the granular flow impact has been investigated in details. Indeed, special attention has been given to the normal force applied on each part of the rigid wall where curves of normal impact force vs. time were analyzed. Due to the tendency of DEM results showing large fluctuation, a data treatment was needed. Data treatment was carried out using smooth spline method where a smooth curve is fitted to a set of noisy data using spline function. The advantages of using splines are their computationally speed and simplicity, as well as the clarity of controlling curvature directly (Chambers & Hastie 1992).

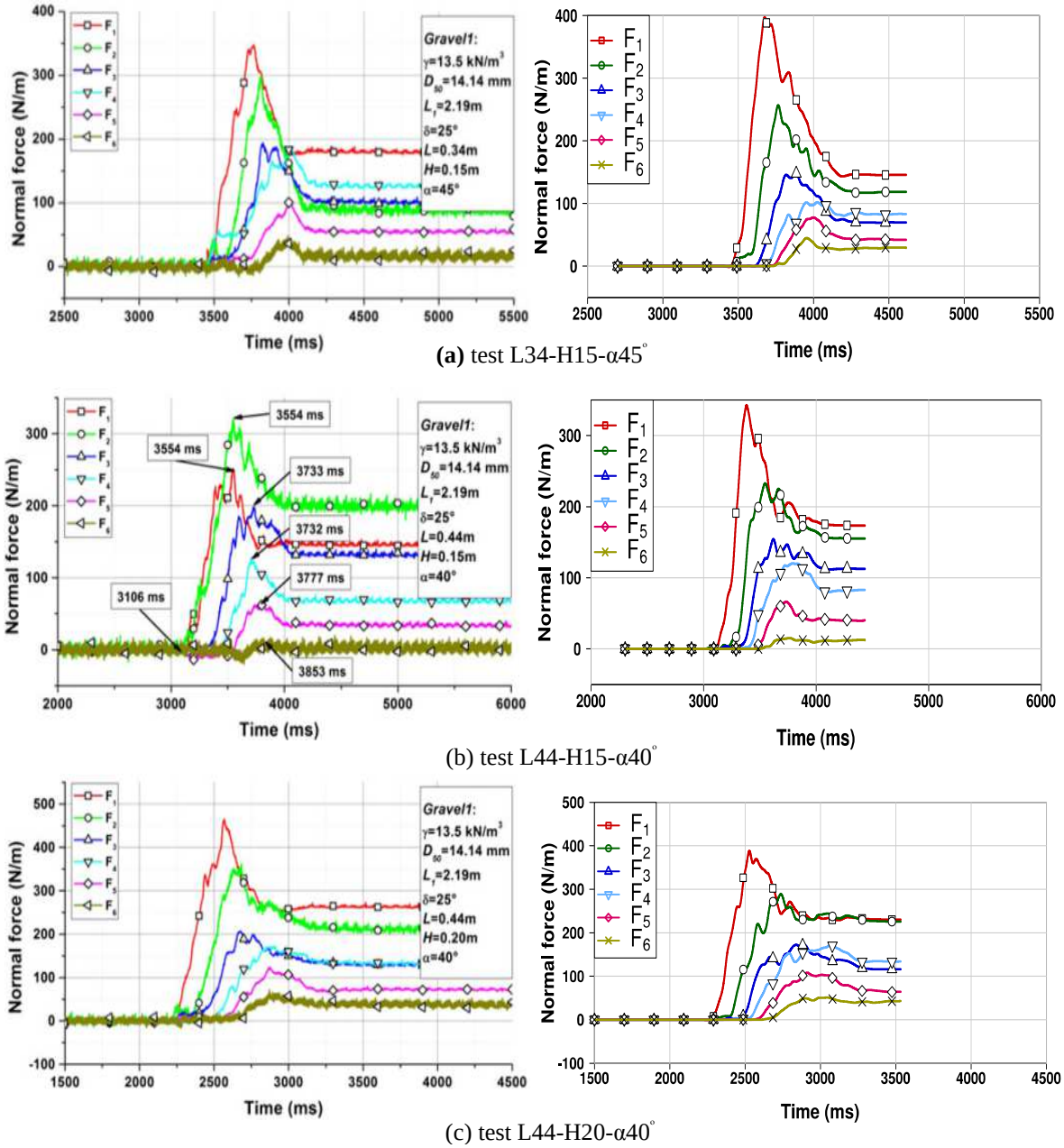

(a) test L34-H15-α45°

(b) test L44-H15-α40°

(c) test L44-H20-α40°

Figure 4. **Time history of normal force variation: model (right) and experiment (Jiang & Towhata 2013) (left)**

Test L34-H15-α45°

In this test (Figure 4a), for the first element of the wall (F_1), the peak force was found to be 396 N/per wall width which is fairly close to the experimental value (around 350 N/m). Moreover, the time of the peak force F_1 is relatively similar to the experiment with a value around 3676 ms but with a lower residual force in the model (145 N/m) compared with the experiment (175 N/m). Likewise, in contrast to F_1, the peak value of F_2 in the model (256 N/m) was lower than the experimental value (300 N/m). For F_3 and F_4, the model captured the

peak time of forces fairly well (being 3883 and 3994 ms for F_3 and F_4 respectively) but with a lower peak value. The peak force and timing of the peak on F_5 and F_6 were fairly captured by the model along with their residual force values.

Test L44-H15-α40˚

For this test, the peak impact force values were 341 and 232 N/m for F_1 and F_2 respectively (Figure 4b). Compared to the experiment, similar values were observed but with a reversed order ($F_2 > F_1$). Concerning the rest of the wall, the model managed to capture the peak forces of F_3, F_4, F_5 and F_6 (with a small exception for F_3) with values of 154, 120, 66 and 15 N/m respectively along with peak times 3619, 3808, 3733 and 3761 ms respectively. Residual forces on these parts were found to be 112, 82, 40 and 12 N/m respectively which are close to the experimental observations.

Test L44-H20-α40˚

With the use of higher volume of the sample, the trend of the impact force curves was better captured with the model along with the time lag between each force curve. For instance, F_1 peaks at 2523 ms with a value of 387 N/m (450 N/m in the experiment) which is followed by a peak of F_2 with 288 N/m (340 N/m in the experiment) at 2737 ms (Figure 4c). Residual forces of F_1 and F_2 were found to be similar to the experiment with values of 227 and 226 N/m respectively. Very good agreement has also been observed for F_3, F_4, F_5 and F_6 in terms of peak forces (172, 172, 108 and 51 N/m) the time of the peak (2864, 3070, 2912 and 3043 ms) and residual force values (116, 134, 65 and 43 N/m).

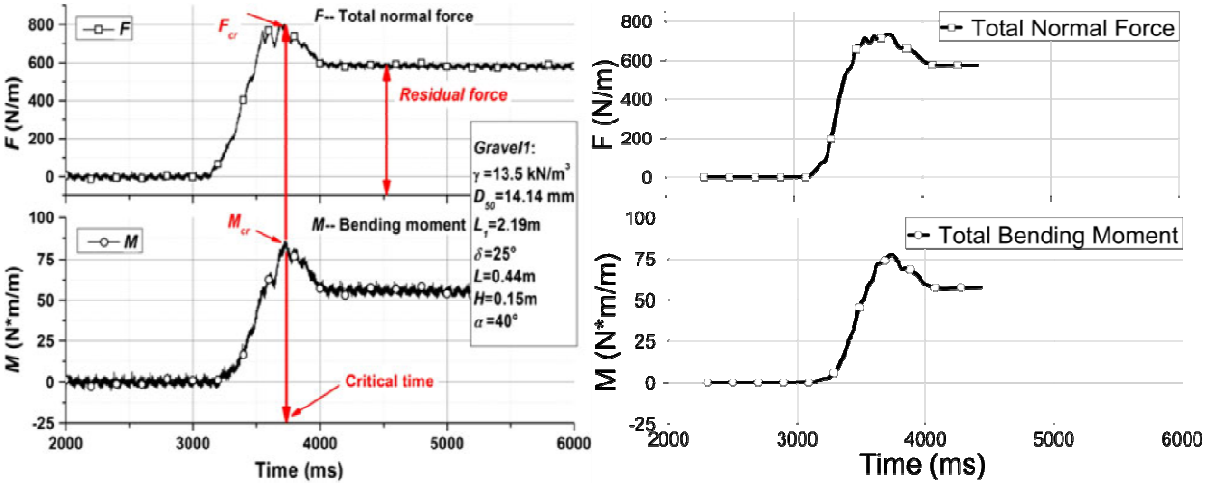

Figure 5. **Time history of total normal force and bending moment, test L44-H15-α40°: model (right) and experiment (Jiang & Towhata 2013) (left)**

Total normal force and bending moment

By considering the normal force on each part of the wall (F_i) and the distance between the centroid of the wall's parts and bottom of the retaining wall (h_i), the total normal force (F) and bending moment (M) can be calculated as follows:

$$F = \sum_{i=0}^{6} F_i \tag{3}$$

$$M = \sum_{i=0}^{6} F_i \, h_i \tag{4}$$

For the total normal force (Figure 5), the model fairly agrees with the experiment in terms of the peak force (735 N/m), peak time (3733 ms) and residual total force (576 N/m). The bending moment results (Figure 5) from the model also agrees with the experiment having a maximum bending moment of 80 N*m/m and peaking at the same time of the total force peak (3733 ms).

DISCUSSION

Comparing spherical to clumped particles, the use of clumps was preferred over spherical particles. The use of clumps led to controlling rotational velocity which was reduced by 70% leading to a better representation of the final deposition and force distribution closer to the experimental values.
In addition, by quantitative comparison with experimental results, good agreement has been observed in terms of the peak force on each part of the wall, the time of the peak and the residual force at the end of the test. Comparing impact forces, we have observed a non-linear distribution on different parts of the wall. In particular, the force at the toe of the wall is sometimes smaller than the one on the segment above. According to Jiang & Towhata (2013), this might be due to an arching effect forming an arch-like protective layer on segment 1 of the wall resulting in a non-linear distribution of forces with depth. Such a layer is also thought to affect the residual force values. For the model, to some extent, arching was observed to be present in the model, especially for residual forces of F1-F2 and F3-F4 which might be due to the force chain distributions and particles shape arrangement behind the wall. Force chains are strongly depending on the particles position and orientation with respect to the wall. The distribution of contact forces on the wall, and consequently the arching, is expected to be different from one test to another, even if conducted in the same initial conditions. It is thought that the forces measured on each segment of the wall are extremely variable. As a consequence, matching between numerical simulations and experiments should mainly concern the total force on the wall rather than on each segment. This variability should be investigated in future work, with investigations at the particle scale.

CONCLUSION

We have numerically studied the impact behavior of dry granular flow made of clumped particles (resembling gravel particles) against a segmented rigid wall. The numerical model has been calibrated considering the shape of the particle and the available experimental data of flow thickness. The model has been validated for impact force measurements against the wall. As a result, the model can be used to study impact against other types of structures (e.g. a flexible structure made of net element). Arching effect and forces variation (for the same test) on different parts of the wall depending on the initial arrangement at the beginning of the test are to be investigated.

ACKNOWLEDGEMENTS

The research leading to these results has received funding from the People Programme (Marie Curie Actions) of the European Union's Seventh Framework Programme FP7/2007-2013/ under REA grant agreement n° 289911.

REFERENCES

Azana, E., Chevor, F., Moucheront, P. 1999. Experimental study of collisional granular flows down an Inclined plane. *Journal of Fluid Mechanics*. 400, 199 – 227.

Chambers, J. M. Hastie, T. J. (1992): Statistical models in S, Wadsworth & Brooks/Cole, Pacific Grove, California, 1992.

Cundall, P.A., Strack, O.D.L. 1979. A discrete numerical model for granular assemblies. *Géotechnique*. 29(1), 47–65.

Faug. T., Beguin. R., Benoit C. 2009. Mean steady granular force on a wall over-flowed by free-surface gravity-driven dense flows. *Phys. Rev. E*, 80, 021305.

Ghaisas, N., Wassgren, C.R., Sadeghi, F. 2004. Cage Instabilities in cylindrical roller bearings. *Journal of Tribology*. 126(4): 681–689.

Guasti, G., Volkwein, A., Wendeler, C. 2011. Design of flexible debris flow barriers. In: Genevois, R.; Hamilton, D.L.; Prestininzi, A. (Eds) *5th International Conference on Debris-Flow Hazard. Mitigation, Mechanics, Prediction and Assessment. Padua, Italy, 14-17 June 2011*. 1093-1100.

Jakob, M., Hungr, O. 2005. Debris-flow hazards and related phenomena, Chichester: Springer.

Jiang, Y., Towhata, I. 2013. Experimental study of dry granular flow and Impact behavior against a rigid retaining wall. *Rock Mechanics and Rock Engineering* 46(4): 713-729.

Kishi, N., Ikeda, K., Konno, H., Kawase, R. 2000. Prototype Impact test on rockfall retaining walls and Its numerical simulation. *Proceedings of Structures under Shock and Impact IV, Cambridge, England*. 351-360.

Nicot, F., Cambou, B., Mazzoleni, G. 2001. Design of rockfall restraining nets from a discrete element modeling. *Rock Mech Rock Eng*, 34(2): 99–118.

Schwager, T., Pöschel, T. 2007. Coefficient of restitution and linear–dashpot model re-visited. *Granular Matter*. 9(6): 465–469.

Silbert, L. E., Erta¸s, D., Grest, G. S., Halsey, T. C., Levine, D., and Plimpton, S. 2001. Granular flow down an Inclined plane: Bagnold scaling and rheology. *Phys. Rev. E*, 64, 051302.

Šmilauer, V., Catalano, E., Chareyre, B., Dorofeenko, S., Duriez, J., Gladky, A., Kozicki, J., Modenese, C., Scholtès, L., Sibille, L., Stránský, J., Thoeni, K. 2010. Yade documentation (V. Šmilauer, Ed.), the Yade project, 1st Ed., 2010. Http://yade-dem.org/doc/.

Experimental and numerical approaches of geosynthetic reinforcements overlying voids

A. Huckert
Egis Géotechnique, Grenoble, France
audrey.huckert@egis.fr
and
P. Villard
Laboratoire Sols, Solides, Structures, Grenoble, France
pascal.villard@3sr-grenoble.fr
and
L. Briançon
Cnam, Paris, France
laurent.briancon@cnam.fr

ABSTRACT

The design of geosynthetic-reinforced embankments over sinkholes remains problematic due to the complexity of interaction mechanisms involved. To complement current knowledge, full-scale experiments were carried out. Measurements are then used to validate a discrete numerical model, which enables to get further information about the load transfer mechanisms within the soil material and about the vertical load acting on the geosynthetic sheet sited over the void. Both experimental and numerical results are then combined to propose an optimization of the current analytical design methods for the case of non-cohesive granular embankment.

INTRODUCTION

The construction of new transportation lines more and more occurs in area where the ground has rather low or heterogeneous mechanical characteristics. In the case of a karstic area or former mining exploitation, this can even lead to the formation of sinkholes. Hence in such areas, constructions and embankments need some surface reinforcement.
Geosynthetic-reinforced embankments provide an economic, environmental and easy-to-use method that is more and more used. The designing of such structures remains problematic due to complex mechanisms combining arching, membrane effect and load transfers within the reinforced embankment overlying a void.

First French research works on this subject began with the R.A.F.A.E.L project (Railway and Highway Embankments Reinforcement against sinkholes, Gourc et al. 1999) which lead to a widely used analytical design method (Blivet et al. 2001) later complemented (Villard et al. 2002, Briançon and Villard 2006, Villard and Briançon 2008). Nevertheless, several physical phenomena remain not well understood, such as the volume of the collapsed zone over the void, the expansion mechanism within the granular material, the intensity and shape of the load distribution on the geosynthetic sheet and its mechanical behavior in anchorage areas. Other aspects such as the use of non-linear reinforcements or embankments made of treated granular materials also lead to questions.
In order to improve current knowledge, experimental and numerical studies (Huckert 2014) were lead as part of the French FUI (Inter-Ministry Fund) research project GeoInov, supported by the competitiveness poles Techtera (Technical Textiles Rhône Alpes) and Fibres as part of the 10th call for project of the DGCIS (Direction Générale de la Compétitivité, de l'Industrie et des Services). This work was presented in 2014 at the 23rd European Young Geotechnical Engineers Conference in Barcelone by Audrey Huckert who has received the prize of the best paper and presentation (Huckert et al. 2014).

FULL-SCALE EXPERIMENTATION

Experimentation principle

The full-scale experiments consist in simulating the progressive formation of a circular void of rising diameter under a geosynthetic-reinforced embankment. A specially designed device combining a trapdoor, clay pebbles and concentric inflated tubes is thus buried under the reinforcement (Fig. 1). The platform is then completed, and a geosynthetic-reinforced embankment is built on the surface.

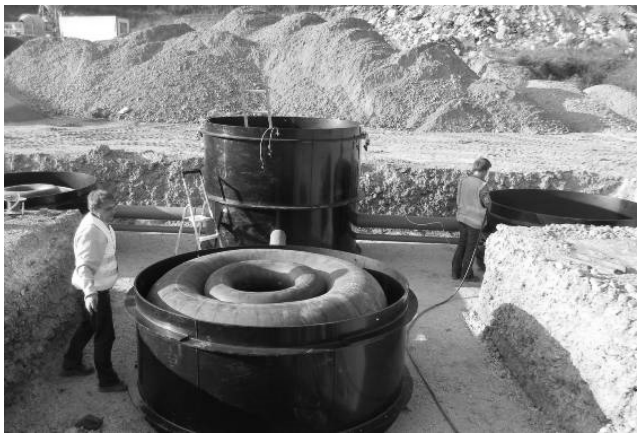

Figure 1. **Installation of the experimental device for the progressive opening of a circular sinkhole under the geosynthetic-reinforced embankment**

The opening of the trapdoor and the progressive deflating of the tubes enables three stages of opening of the sinkhole: 0.75 m, 1.25 m and 2.2 m diameters, this latest 2.2 m diameter being the only one that remains fully controlled.
After the opening of the void, the whole section is left waiting for 20 days to enable the stabilization of load transfer mechanisms within the reinforced structure. Traffic tests and

overloading are then realized thanks to a shovel going back and forth 10 times, resulting in a 1t overload over the center of the sinkhole, or using the shovel's bucket to apply a vertical punctual 4t overload over the void's center.

Description of the experimental sections

Two experimental sections are here described using either a 1 m thick granular, non-cohesive embankment (section GR1) made of 20/40 mm clean rounded gravel, or a 0.35 m thick 2 % lime-treated 0/40 mm granular layer (section ST1). Both sections are reinforced with similar geosynthetics, which are specifically designed to obtain significant values of strains and displacements.
All experimental materials were carefully characterized (Tab. 1). Shear tests using a 0.3 x 0.3 m box were carried out to characterize soils by using the NF P94-071 (1994), and tensile tests were performed to characterize the geosynthetic by using the NF EN ISO 10319 (2008).

Table 1. **Description of experimental sections**

Section	Embankment			Geosynthetic		
	γ (kN/m^3)	C (kPa)	φ_{sol} (°)	Type	$J_{\varepsilon=3\%}$ (kN/m)	$\delta_{emb/gsy}$ (°)
GR1	15.5	0	36	GSY_1	2988	23
ST1	18.0	40	33	GSY_1	2988	32

INSTRUMENTATION AND AIM OF THE MEASUREMENTS

A specific instrumentation is installed to answer the aim of the experimentation. The cinematic of the reinforced structure is observed thanks to a topographic campaign, and a Ground Penetrating Radar analysis (GPR) associated with metallic reflectors within the embankment.
The deflection of the geosynthetic reinforcement is monitored using either the GPR analysis, or a laser sensor device located inside de cavity. The reinforcement's strains are measured with optical Fibre Bragg gratings.
Last, load transfers towards the edges of the sinkhole are measured using earth pressure cells. For all measurement systems used, the precision obtained depends on both the system itself, and on the site conditions with rather large granular particles.

MAIN RESULTS FOR THE 20/40 MM GRANULAR EMBANKMENT

During the opening of the cavity, the surface deflection at the top of the embankment progressively increases as well as the geosynthetic deflection. Once the diameter of the sinkhole reaches 2.2 m, the topographic and GPR analysis show a surface deflection of 0.14 m for a geosynthetic deflection of 0.23 m (Fig. 2).
Besides, this analysis underlines the fact that the granular material in movements is restrained to a cylinder above the sinkhole. Hence assuming a parabolic shape of both surface and geosynthetic deflections, a mean expansion factor of 1.04 can be determined.

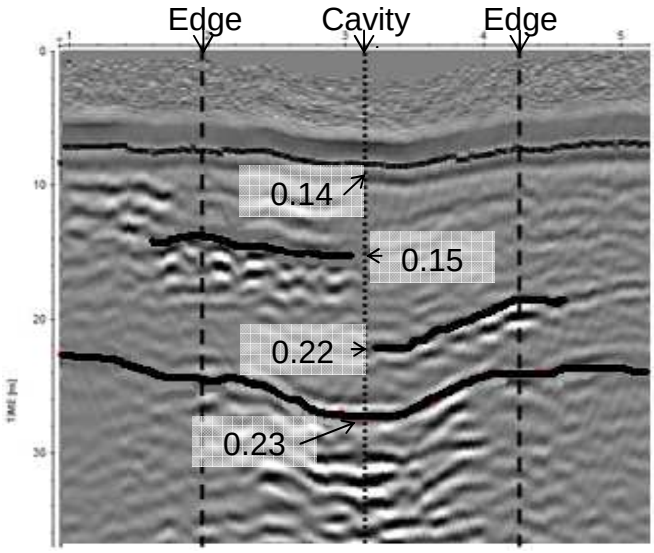

Figure 2. **Topographic and GPR analysis on section GR1**

MAIN RESULTS FOR THE TREATED SOIL LAYER

For the cohesive treated soil layer, no significant displacement is observed during the opening of the sinkhole. Hence the treated soil layers lies over the void as a flexion plate.
A load test consisting in applying a vertical punctual force above the center of the cavity then results in a brutal collapse of a treated soil block on the geosynthetic as soon as the overload reaches 1.7 t (Fig. 3). This block remains in one piece and has an approximate truncated conical shape.

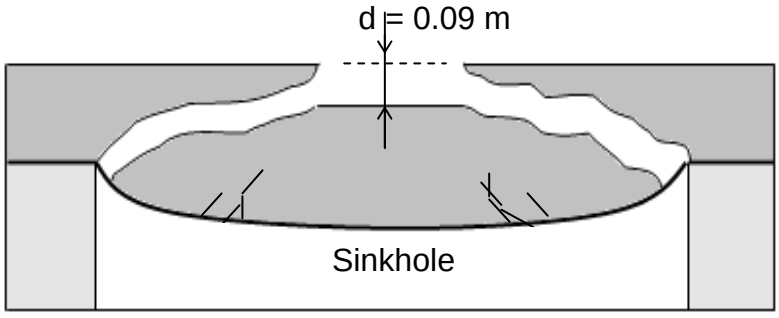

Figure 3. **Failure mechanism after 1.7t overload on section ST1**

The geosynthetic deflection is rather flat, and does not have such a high value (around 9 cm) as in the case of the 20/40 mm granular embankment. This suggests that the shape of the load distribution on the geosynthetic reinforcement differs from one case to another.

DISCRETE NUMERICAL SIMULATIONS

The numerical study is lead using a coupling between finite elements representing the continuous geosynthetic sheet, and discrete elements simulating the granular embankment (Villard et al. 2009).

DESCRIPTION OF THE NUMERICAL MODEL

The granular embankment is simulated by 15000 clusters (aggregates of two spherical discrete elements) interacting through contact points. These particles are generated by using a Radius Expansion Friction Decrease method (Salot et al. 2009), hence enabling a precise control of their mechanical properties. The values of the contact parameters between the numerical particles are deduced from the experimental material properties by the way of a numerical triaxial test process. This kind of modeling hence enables to take into account the interaction between aggregates, including rotations, load transfers, soil expansion or large displacements.
The elements used to describe the geosynthetic reinforcement are 3200 triangular shaped, thin, three nodes finite elements. This allows describing the unidimensional or two-dimensional structure of the reinforcement. Besides, the interface with granular particles is described thanks to specific contact laws, including normal and tangential stiffness and the soil/geosynthetic friction angle.

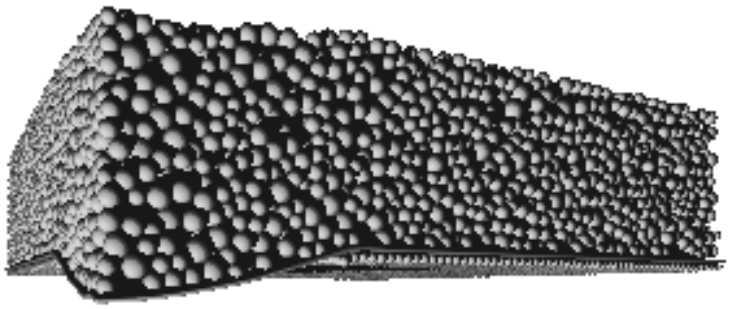

Figure 4. **Numerical model**

Last, spherical discrete elements, sited under the geosynthetic sheet, enable to define the lower boundary conditions and the progressive opening of the sinkhole. This process can either be used to represent the progressive opening of the experimental sinkhole or to simulate the vertical displacement of a circular trapdoor.
Before any other considerations, the relevance of the numerical model is tested by using experimental data such as the surface and geosynthetic displacements. Then numerical simulations are used to get information that could not be experimentally measured, such as the mean load on the geosynthetic over the sinkhole or the load distribution on the geosynthetic.

As an example, one interest of the numerical model is to show that the load distribution on the geosynthetic, for non-cohesive materiel, differs greatly following the procedure used to open the sinkhole (Fig. 5). Hence for a trapdoor, with a rather brutal opening of the sinkhole to an immediate large diameter, load transfers towards the edges of the sinkhole are rather high while the geosynthetic at the center of the sinkhole is relatively unloaded. In this case, the inverted triangular shape of the load distribution on the geosynthetic sheet is explained by the abrupt opening of the void. In case the sinkhole is opened with a rising diameter, the progressive opening of the sinkhole disturbs load transfers towards the evolving edge of the sinkhole, which results in a load distribution rather uniform on the geosynthetic overlying the final void (Fig. 5).

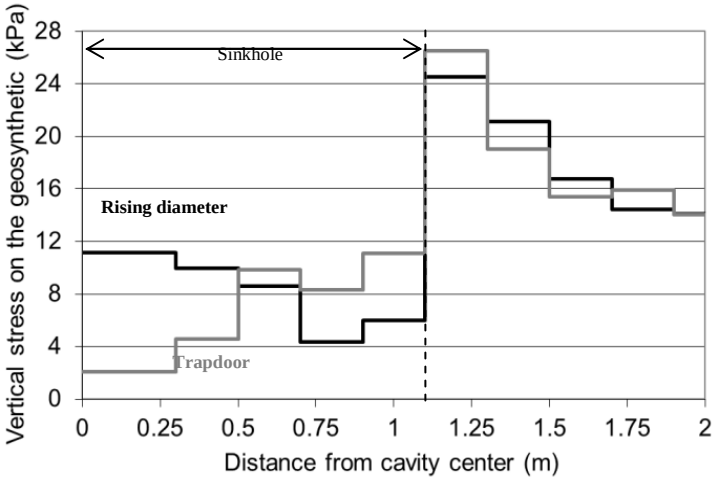

Figure 5. **Load distribution on the geosynthetic over a sinkhole obtained using a trapdoor, or with a progressive rising diameter**

Another numerical result is the computation of the mean vertical stress applied on the geosynthetic overlying the circular sinkhole. During the opening of the cavity, the mean vertical stress acting on the geosynthetic sheet over the cavity is computed. For the case of a non-cohesive material, this result is then compared to existing analytical methods computing load transfers over sinkholes (Fig. 6): Handy (1985), Marston and Anderson (1913), Terzaghi (1943), Vardoulakis et al. (1981). As a result, load transfers developed by using the numerical simulation are best fitted by Vardoulakis et al. method (1981) with the hypothesis of Roscoe.

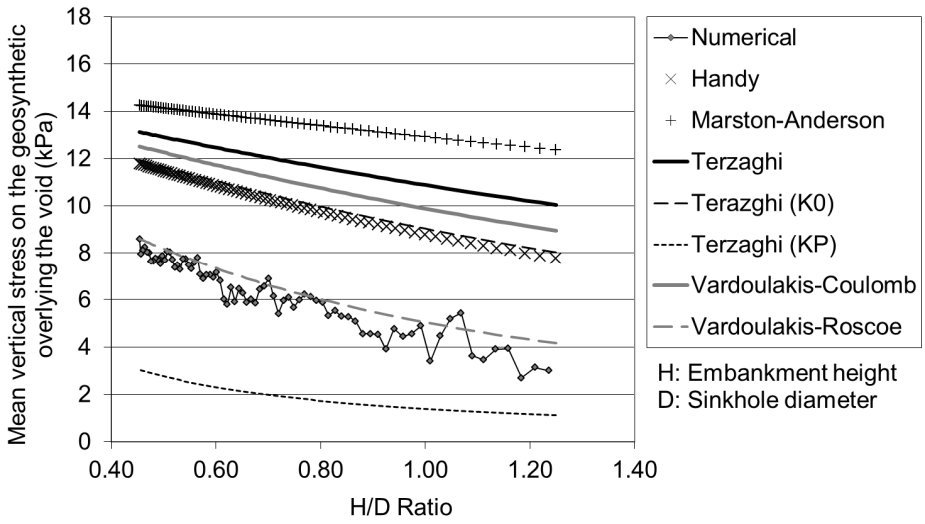

Figure 6. **Mean vertical stress on the geosynthetic over the void**

APPLICATION TO THE DESIGN OF GEOSYNTHETIC REINFORCEMENTS OVER SINKHOLES

Non-cohesive granular embankment

Numerical and experimental results are then used to improve the most recent analytical design model (Villard and Briançon 2008), which has the advantage to consider the frictional behavior of the geosynthetic in its anchorage area.

Following the numerical results, new equations are proposed to integrate an inverted triangular load distribution shape on the geosynthetic over a sinkhole of diameter L (Fig. 7). For the case of a uniform load distribution, the mean vertical stress q_0 is determined using Vardoulakis et al. (1981).

The maximal vertical stress Q on the geosynthetic above the void (inverted triangular load distributions) is then computed using the same total load above the cavity than the uniform case, and considering the three dimensional shape of the load distribution. Once the load equation defined for the new case is implemented in the analytical method. Table 2 gives an overview of the main dimensioning equations. In these relations, T_H is the value of the horizontal component of the tensile force in the geosynthetic at the vicinity of the edges of the cavity. This value is computed (Villard and Briançon 2008) by taking into account the behavior of the geosynthetic fabric sited over the cavity as well as the stretching and the friction of the geosynthetic in the anchorage areas sited at both sides of the cavity.

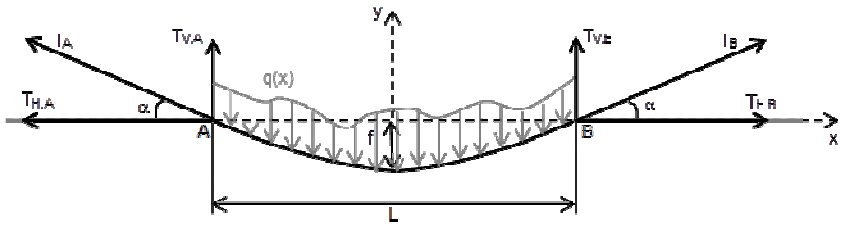

Figure 7. **Mechanical behavior of a geosynthetic reinforcement within a non-cohesive embankment**

Table 2. **Main equations describing the membrane behavior of the geosynthetic reinforcement for a non-cohesive embankment**

Uniform load distribution	Inverted triangular load distribution
Load distribution $q(x) = q_0$	Load distribution $q(x) = \frac{2Q}{L} x$
Geosynthetic deflection $z(x) = \frac{q_0.L}{2.T_H}\left(\frac{x^2}{L} - \frac{L}{4}\right)$	Geosynthetic deflection $z(x) = \frac{Q}{3.L.T_H}\left(x^3 - \frac{L^3}{8}\right)$
Geosynthetic tensile force $T(x) = \frac{q_0 L}{2\beta}\sqrt{1+\left[\frac{2x\beta}{L}\right]^2}$ with: $\beta = \frac{q_0 L}{2T_H}$	Geosynthetic tensile force $T(x) = \frac{QL}{4\beta}\sqrt{1+\left[\frac{4\beta.x^2}{L^2}\right]^2}$ with: $\beta = \frac{QL}{4T_H}$

This analytical proposition is then confronted to the results of the numerical study (Fig. 8). For the case of a 0.75 m diameter sinkhole (H/D = 1.33), which corresponds to a height of embankment greater than the diameter of the cavity and to a brutal initiation of the sinkhole, the inverted triangular distribution seems more adapted to reproduce the numerical results. When the diameter of the sinkhole increases, load transfer mechanisms are disturbed, hence modifying the shape of the load distribution on the geosynthetic. Indeed, for a 2.2 m diameter sinkhole (H/D = 0.45), the analytical approach fitting well the numerical results is based on a uniform load distribution.

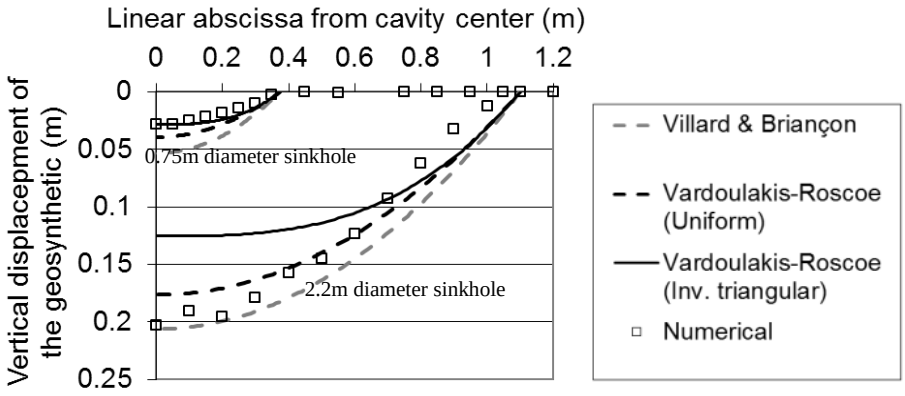

Figure 8. **Confrontation between numerical results and analytical propositions**

CONCLUSION

Full-scale experimentations reproduced the progressive opening of sinkholes under a geosynthetic-reinforced non-cohesive embankment or a treated soil layer, and confirmed the role of these reinforcements above cavities. While the whole instrumentation provided a consequent and original data base, both topographic and GPR analysis specified the geometry of the collapsed soil. Experimental measures then validate a numerical model based on a coupling between finite elements for the geosynthetic, and discrete elements for the embankment material. This model provides information such as the shape of the load distribution or the mean total load on the geosynthetic overlying the sinkhole.
Both experimental and numerical results are then combined to optimize an analytical design method for the case of non-cohesive embankments. An alternative analytical load distribution is suggested and compared to numerical data. As a result, the shape of the load distribution depends on the process of the opening of the void and its brutal or progressive formation.

ACKNOWLEDGEMENTS

The authors would like to thank the competitiveness poles Techtera and Fibres, as well as researchers Fayçal Rejiba and Albane Saintenoy (Paris 6 and 11 University), the society Carrey TP, Grenoble IUT1, and the society Texinov.

REFERENCES

Blivet, J.C., Khay, M., Gourc, J.P. & Giraud H. 2001. Design considerations of geosynthetic for reinforced embankments subjected to localized subsidence. Proc. of the geosynthetics'2001 conference, February 12-14, Portland, Oregon, USA, 741-754.

Briançon, L. & Villard P. 2006. Dimensionnement des renforcements géosynthétiques de plateformes sur cavités. Revue Française de Géotechnique, n°117, 4° trimestre 2006, 51-62.

Gourc, J.P., Villard, P., Giraud, H., Blivet, J.C., Khay, M., Imbert, B., Morbois, A. & Delmas, P. 1999. Sinkholes beneath a reinforced earthfill – A large scale motorway and railway experiment. Proc. Of Geosynthetics'99, Boston, Massachusetts, USA, 28-30 April 1999, 2: 833-846.

Handy, R.L. 1985. The arch in arching, Journal of Geotechnical Engineering, ASCE, 111 (50), 302-318.

Huckert, A. 2014. Approches numérique et expérimentale du dimensionnement de renforcements géosynthétiques sur cavités et inclusions rigides, Thèse de doctorat-Université de Grenoble, 223p.

Huckert, A., Villard, P. & Briançon, L. 2014. Experimental and numerical approaches of the design of geosynthetic reinforcements overlying voids. 23rd European Young Geotechnical Engineers Conference, EYGEC, Barcelone, Espagne, 2-5 Sept 2014, 133-136.

Marston, A. & Anderson, A.O. 1913. The theory of load on pipe ditches and tests of cement and clay drain tile and sewer pipes, Iowa Engineering Experiment Station Armes, Bull. 31.

Salot, C., Gotteland, Ph. & Villard, P. 2009. Influence of relative density on granular materials behavior: DEM simulations of triaxial tests. Granular Matter, Vol. 11, N° 4, pp. 221-236.

Terzaghi, K. 1943. Theoritical Soil Mechanics, John Wiley & Sons, NY.

Vardoulakis, I., Graf, B. & Gudehus, G. 1981. Trapdoor problem with dry sand: a statical approach based upon model test kinematics. International Journal for Numerical and Analytical Methods in GeomechanicsI, 5: 57-78.

Villard, P., Gourc, J.P. & Blivet, J.C. 2002. Prévention des risques d'effondrement de surface lies à la presence de cavités souterraines: une solution de renforcement par géosynthétique des remblais routiers et ferroviaires. Revue Française de géotechnique, 99:23-34.

Villard, P. & Briançon, L. 2008. Design of geosynthetic reinforcements of platforms subjected to localized sinkholes. Canadian Geotechnical Journal, vol. 45, 2: 196-209.

Villard, P., Chevalier, B., Le Hello, B. & Combe, G. 2009. Coupling between finite and discrete element methods for the modeling of earth structures reinforced by geosynthetic. Computers and Geotechnics, doi:10.1016/j.compgeo.2008.11.005.

Discrete element modeling of a rockfall in the south of the “Massif Central”, France

S. Cuervo, D. Daudon, V. Richefeu, P. Villard
Laboratoire Sols, Solides, Structures, Grenoble, France
stiven.cuervo@3sr-grenoble.fr
dominique.daudon@3sr-grenoble.fr
vincent.richefeu@3sr-grenoble.fr
pascal.villard@3sr-grenoble.fr
and
P. Plotto
IMSRN, Montbonnot, France
pierre.plotto@imsrn.com

ABSTRACT

This work aims to model the mechanical behaviour of a natural rockfall of approximately 1000 m^3 using the discrete element method (DEM). The cliff geometry, fracture network, deposit geometry and slope topography, resulted from field measurements. The numerical model used for this study accounts for the energy dissipated by collisions and friction/abutment in the bulk of the rock mass as well as at the rock-slope interface. The contact parameters needed for the numerical simulation are issued from the literature. A sensitivity study was performed in order to analyze the role played by the contact parameters, the blocks shape and the slope geometry (roughness) in some important indicators (mass distance propagation, energy dissipation and rockfall deposit geometry). From the results obtained, it appears that the numerical model is able to provide, only from basic inputs collected in-situ, a valuable description of natural rockfall propagation and stop. Assessment of different physical quantities such as energy dissipation modes (by collisions or friction/abutment), allowed us to also improve the understanding of rockfall events.

INTRODUCTION

Gravitational movements are considered as the most frequent and unforeseen natural hazards in hilly regions. The complexity of the involved mechanisms has motivated the development

of a number of numerical models depending on the kind of natural hazard phenomena and the materials concerned. Some models only consider individual rock particles. The “lumped mass methods” are based on the kinematics of a single point that describes the rock motion by ignoring its shape and rotation (Bourrier et al. 2009, Dorren 2003). For important or very important volumes, models have been developed on the basis of shallow fluid flows (Pirulli and Mangeney 2007). For intermediate volumes and uneven topographies, the discrete element approach seems to be promising (Cundall & Strack 1979). Applied to rockfalls, this method considers the rock mass as a group of solids in interaction.
The numerical DEM model used in this study was validated with laboratory tests performed in the framework of the European project MASSA (Medium and Small Size rockfall hazard Assessment) (Banton et al. 2009, Mollon et al. 2012, Richefeu et al. 2012). The contact law proposed is defined by four parameters and takes into consideration the energy dissipated by collisions and friction/abutment between rock blocks and with the soil (Richefeu et al. 2012). In order to test the applicability of the model to real scale events, a natural rockfall that happened for real has been simulated and compared with in-situ measurements. Contact parameters were taken from the literature as a first guess and then adapted in order to target the right propagation distances of the front (runout) and of the mass center. The objective was to analyze the relative importance of contact parameters and to identify the most adapted ones to give a valid account of the rockfall motion. Finally, energy dissipation modes were also analyzed to better capture the phenomena underlying the rockfall propagation.

ROCKFALL EVENT

The rockfall event took place in 2007 close to the city of Millau in the south of the Central Mountains in France. Around 1000 m^3 of limestone benches approximately one meter thick released by sliding on the quasi vertical cliff without toppling and spread on a natural soil sloped of 30.5° stopping finally into a nearly horizontal surface. As a preventative measure, highways and most of the buildings situated in the rockfall area had to be closed. Figure 1 shows the geometry and dimensions of the terrain, the dropped mass, and the blocks.

The main deposit is about 50 m long and 40 m width throughout the tipped up mountainside. Popped blocks stopped close to the buildings (at a distance higher than 70 m from the cliff toe).

About 30 blocks ranging from 10 m^3 and 36 m^3 were identified inside the main deposit and spotted using a GPS tool. They actually represent 85% of total mass volume and reflect somehow the rockfall deposit boundary. Approximately ten rock blocks have very important volumes (between 33 m^3 and 36 m^3) and very similar sizes (6 m length, 3.5 m weight and thickness ranging between 1 and 1.5 m according to the initial cliff fracture networks (Fig. 1b and Fig.1c).

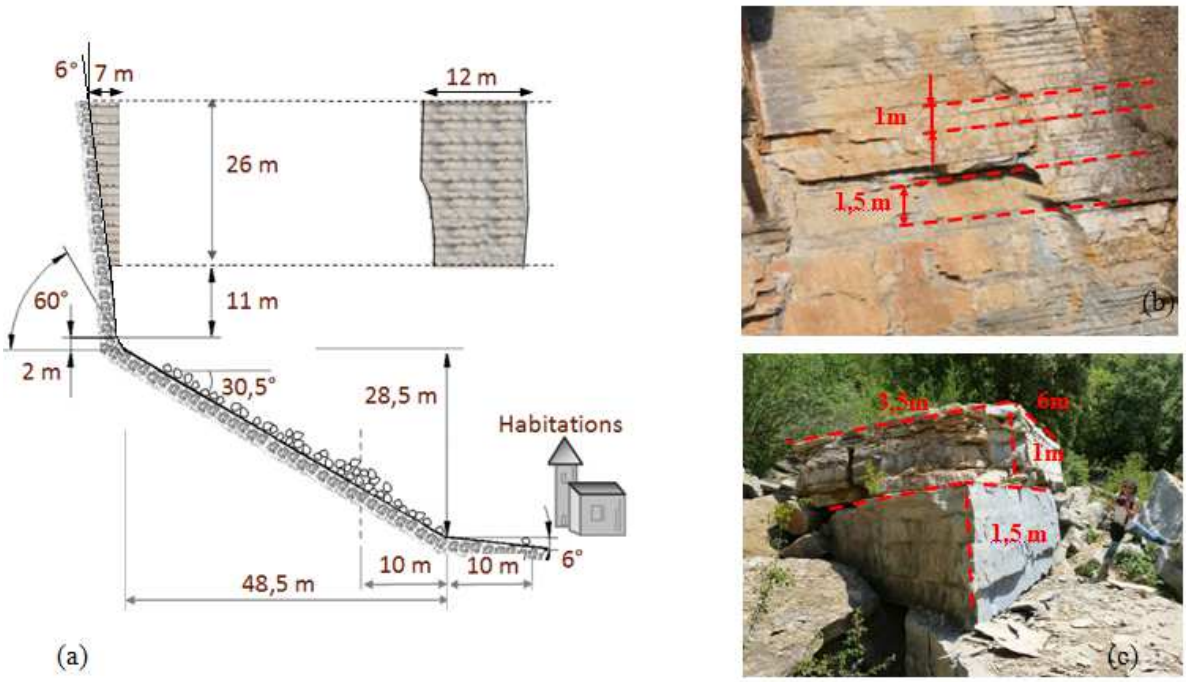

Figure 1. **(a) Slope geometry (b) Cliff fracture network & (c) blocks geometry**

NUMERICAL MODEL

We used the discrete element method that allows for simulating the dynamic motion of a group of rigid bodies. The realistic shape (when compared to spheres) of the rock blocks are sphero-polyhedra and the contact/collision laws take into account elastic contact stiffnesses and different energy dissipation mechanisms through four parameters (Richefeu et al. 2012) defined as follows:

- The coefficient of normal energy restitution (e_n^2).
- The tangential dissipation coefficient (μ) that accounts for both resistive friction and buttress forces taking place in case of important interpenetrations between rocks and soft substrate.
- The normal and tangential contact stiffnesses (k_n and k_t respectively).

Simplified but realistic initial mass geometry was considered. This unstable mass was cut up by horizontal and vertical plans according to the fracture network identified on the cliff as well as the block sizes observed in the deposit (Fig. 1). A total of 122 rock blocks were created.

Cohesion within the fracture network was not modeled, this means that their fracture energy is negligible compared with the energy developed after first impact of the mass as a result of a free fall motion (from high). This free fall and the interactions of the blocks between themselves and with the natural ground were merely simulated by initially setting the mass in an unstable state.

Contact law parameters were initially guess from orders of magnitude generally recognized in the literature and then slightly adapted as a result of a sensitivity analysis showing the best adequacy between measured and numerical runout and mass center distance of propagation.

RESULTS AND ANALYSIS

The results of the sensitivity analysis are reported in Figure 2. The error functions are length differences between simulations and field measurements. The white zone in Figure 2 defines the best restitution coefficients for the reproducibility of both mass-center distance and deposit length. A comparative scheme of real and simulated deposits, obtained by using the best set of parameters leading to errors below 5%, is presented in Figure 3. The obtained quantitative characteristics are summarized in Table 1 showing the good concordance between all the characteristics of the numerical and real block mass deposits. Most of the numerical blocks (96%) were stopped inside the same envelope as the real event. The 4% remaining blocks represents mainly big blocks that were actually observed in the falling neighborhood. Besides, other subtle behaviors were also retrieved in the numerical deposit such as a high density of blocks concentrated at the base of the slope and noticeable positions of some blocks (spotted in red in Figure 3).

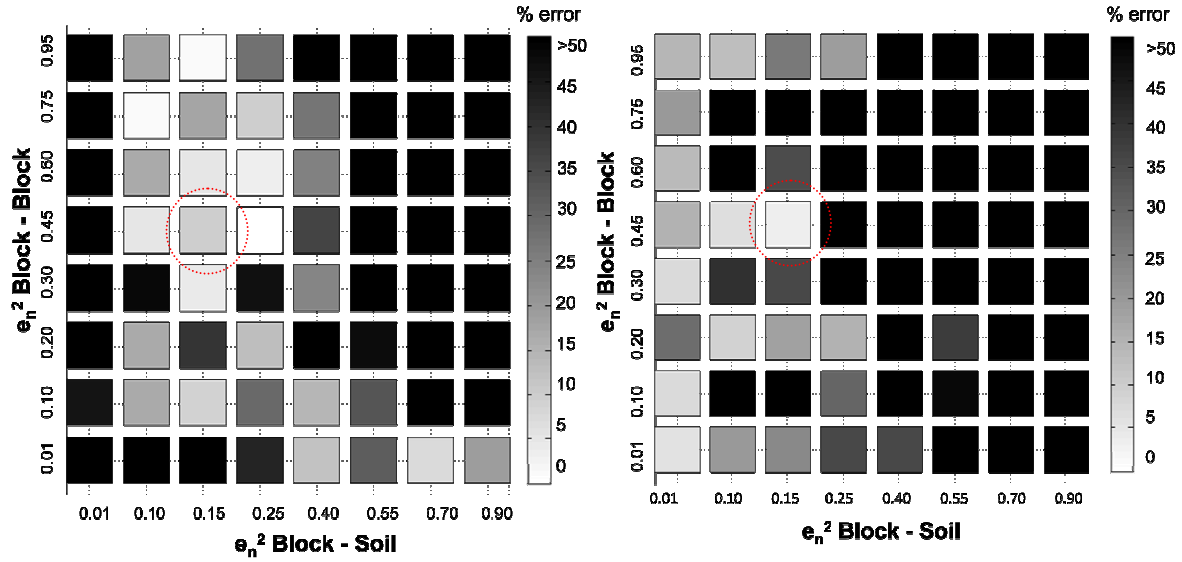

Figure 2. **Example of sensitivity analysis of the normal restitution coefficients showing the likelihood of the simulated rockfalls in terms of mass-center distance (left) and deposit length (right)**

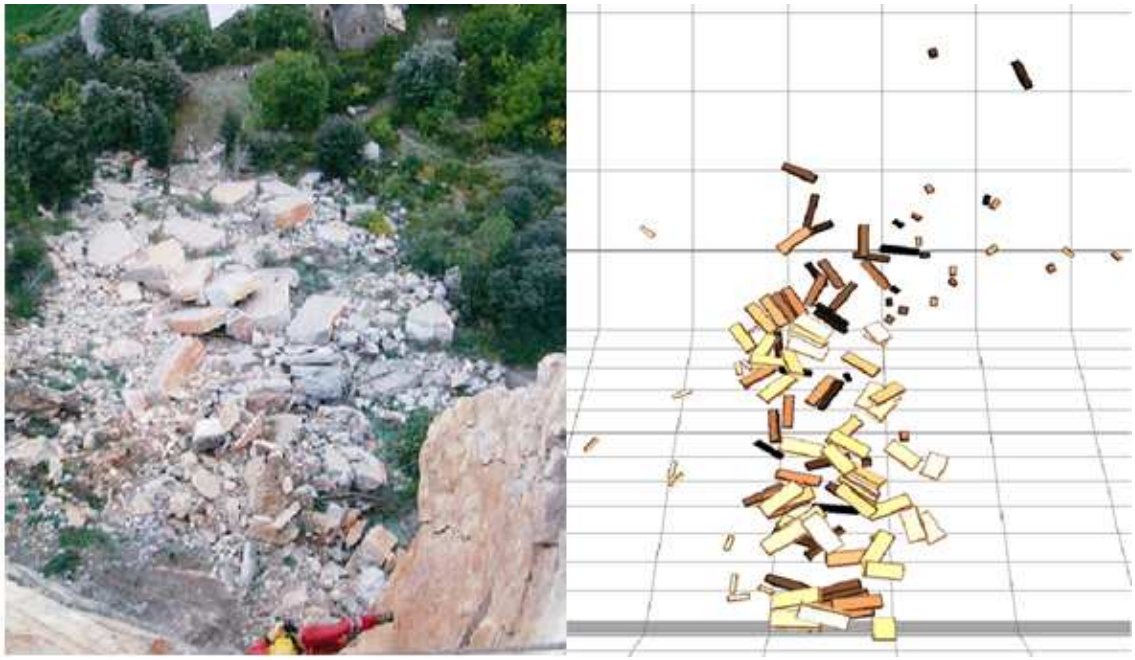

Figure 3. **Natural (left) and numerical (right) deposit**

Table 1. **A comparison of some quantitative characteristics between the real and the numerical deposit**

	IN-SITU	DEM
Deposit width (m)	40	43.2
Deposit length (m)	66	68.5
Runout distance (m)	67	70
Deposit thickness (m)	3	3,8
Fahrböschung propagation angle (°)	45,5	47

Energy dissipations by friction and impact within the granular mass and between blocks and ground (hardly measurable in-situ) are also followed among the mass motion. Figure 4 shows the location of the energy dissipated according to their mode. We can easily distinguish two different regions: (1) the first impact zone where at least 41% of total energy is dissipated, mostly by block interactions (36% by friction and 34% by collisions) and (2) propagation zone along the slope where energy is mainly dissipated by friction between blocks (25%) or between blocks and the slope (55%). Interestingly, for the geometry tested, the total energy dissipated at first impact appears to be always the same (about 41%) and thus not related to the contact parameters.

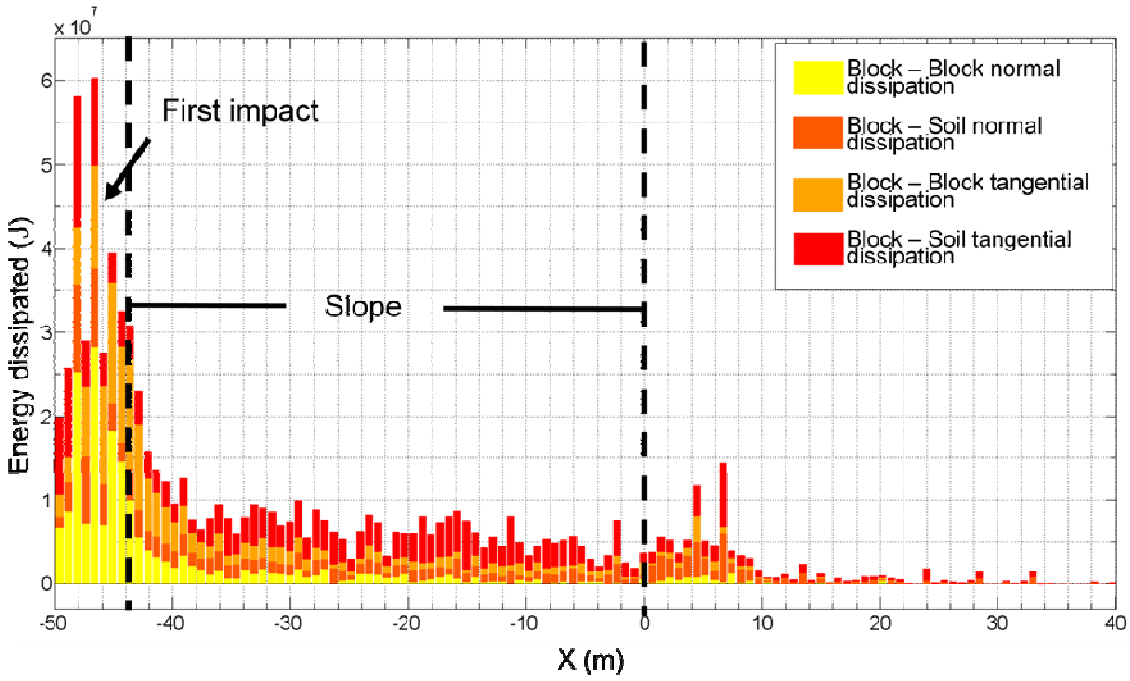

Figure 4. **Energy dissipated along the propagation axis X**

CONCLUSION

A natural rockfall event of about 1000 m^3 was simulated using a discrete element model that integrates the energy dissipation within the granular mass and between blocks and ground. At first, contact law parameters were derived from a literature review and slightly adapted using a sensitivity analysis. The particle shapes complied with real blocks geometries. The comparison between the numerical and real deposit geometries showed that the numerical model is able to restore satisfactorily the mechanical behavior of this type of rockfalls by using adequate contact law parameters and realistic particle shapes. Not only the runout distance, but also more sophisticated features such as the shape of the deposit and block arrangements (either stacked or dispersed) were well reproduced by simulation.

The analyze of the dissipative modes showed that, for the geometry tested, the energy dissipated at the first impact is about 41% of the total energy whatever the contact parameters. At the first impact the energy is dissipated mostly in-between the blocks (agains about 30% at the base of the impacting mass) while along the slope the energy is mainly dissipated by friction within the granular mass or between blocks and the slope (about 80% of the total energy dissipated in this area).

The relevance of the numeral model, demonstrated in this particular case, needs however to be confirmed by simulating other natural events that involve more sophisticated topography and complex geometry of the blocks.

REFERENCES

Banton, J., Villard, P., Jongmans, D., & Scavia, C. 2009. Two-dimensional discrete element models of debris avalanches: parameterisation and the reproducibility of experimental results. *Journal of Geophysical Research*, *114*.

Bourrier, F., Dorren, L., Nicot, F., Berger, F., & Darve, F. 2009. Toward objective rockfall trajectory simulation using a stochastic impact model. *Geomorphology*, *110*(3-4), 68–79. doi:10.1016/j.geomorph.2009.03.017.

Cundall, P. ., & Strack, O. D. 1979. A Discrete Numerical-Model for Granular Assemblies. *Geotechnique*, *29 (1)*, 47–65.

Dorren, L. K. A. 2003. A review of rockfall mechanics and modelling approaches. *Progress in Physical Geography*, *27*(1), 69–87. doi:10.1191/0309133303pp359ra.

Mollon, G., Richefeu, V., Villard, P., & Daudon, D. 2012. Numerical simulation of rock avalanches: Influence of a local dissipative contact model on the collective behavior of granular flows. *Journal of Geophysical Research*, *117*(F2), F02036. doi:10.1029/2011JF002202.

Pirulli, M., & Mangeney, a. 2007. Results of Back-Analysis of the Propagation of Rock Avalanches as a Function of the Assumed Rheology. *Rock Mechanics and Rock Engineering*, *41*(1), 59–84. doi:10.1007/s00603-007-0143-x.

Richefeu, V., Mollon, G., Daudon, D., & Villard, P. 2012. Dissipative contacts and realistic block shapes for modeling rock avalanches. *Engineering Geologyeology*, *149-150*, 78–92.

The use of photogrammetry and 3D Discrete Element Models to better assess Rock Slope Stability

V. Bonilla-Sierra[1,2] **& F.V. Donzé**[1]
[1]*Univ. Grenoble Alpes / CNRS, UMR 5521 3SR, 38000 Grenoble, France*
[2]*IMSRN, Parc Pré Millet – 680 Rue Aristide Bergès, 38330 Montbonnot, France*
viviana.bonillasierra@3sr-grenoble.fr
frederic.donze@3sr-grenoble.fr

L. Scholtès
Université de Lorraine / CNRS / CREGU, UMR 7359 GeoRessources, BP 40, 54501 Vandœuvre-lès-Nancy, France
luc.scholtes@univ-lorraine.fr

M. K. Elmouttie
CSIRO Energy Flagship, PO Box 883, Pullenvale, QLD 4069, Australia
Marc.Elmouttie@csiro.au

ABSTRACT

Structural and mechanical analyses of rock masses are main elements for rock slope stability assessment. The complementary use of structural analyses and discontinum numerical modelling provides a methodology that can be applied to analyse three-dimensional (3D) jointed rock masses. Fracture persistence is generally assumed and can lead to inaccurate modelling and misleading conclusions. To overcome this limitation, a recently developed numerical model based on the coupling of Discrete Fracture Network with Discrete Element Method (DFN-DEM), which describes both yielding along pre-existing discontinuities and fracturing of the intact rock matrix is used here, in combination with photogrammetric techniques to assess the stability of potentially unstable rock slopes.

INTRODUCTION

Failure process can reach high levels of complexity in jointed rock masses because they combine the mechanical properties of the rock matrix, the geometry and properties of the structural defects and the progressive failure of the rock matrix in the presence of non-persistent discontinuities.

The geometry and structural properties of the rock slope can be estimated when outcrops are available. Terrestrial photogrammetric techniques provide sufficiently precise data to construct realistic digitalized and georeferenced slope surfaces (Poropat, 2006; Sturzenegger *et al.*, 2011). From the structural analysis of the digitalized surface, a DFN can be setup from the detection and mapping of discontinuities. The digitalized surface and its associated DFN can thus be imported into numerical software packages to setup the rock mass mechanical model (Firpo *et al.*, 2011; Sturzenegger & Stead, 2012).
One key requirement for the successful integration of the geological model within the mechanical model is for field data to be sufficiently accurate and well pre-processed for importation. In this study, Sirovision software (Sirovision, 2010) was chosen to map rock slope surfaces and structures from stereo photographs, motivated by the fact that the digitalized surfaces resulting from the numerical treatment can be conveniently imported into a mechanical model which explicitly considers these features. With regard to its DFN-DEM modelling capabilities, YADE Open DEM software, was selected here to simulate the mechanical response of the rock mass (Scholtès *et al.*, 2011; Scholtès & Donzé, 2012; Harthong *et al.*, 2012).

DATA ACQUISITION

Generating and georeferencing 3D surfaces

Digital outcrop model creation and 3D mapping were done using Sirovision, a software package created specifically for geological and geotechnical mapping. This software uses overlapping stereo pairs of digital photographs and survey information to create 3D digital models that are scaled and oriented within a specified coordinate system (Gates & Haneberg, 2012). The software consists of two components: one for 3D model creation and one for rock mass discontinuity mapping, visualization, and analysis (Haneberg, 2008).
The equipment used in the present study consists in a camera Canon EOS 5D Mark II with 21.1 megapixel resolution and a lens of 135mm. Two photographs of the same slope and from two different positions were taken at a distance close to 1,500 m. The depth accuracy of the rock slope depends on a correct ratio baseline between camera positions and the distance to the face, typically ranging from 1:10 to 1:6. Regarding the accuracy of the method, given the equipment used here, the range measurement set at 1,500 m and using a baseline of 1/7, the theoretical resolution, *i.e.* ground pixel size, of the 3D images is equal to 50 mm. The planimetric accuracy is 25 mm (considered as ½ of the ground pixel size (Birch, 2006)), and the corresponding depth accuracy is equal to 100 mm. Note that the final model accuracy is more controlled by the accuracy of the georeferencing procedure than by the photogrammetric precision.
Additionally, a laser range finder (±1-m error) was used to obtain the horizontal distance from the camera, height, azimuth and inclination of three control points selected on the rock surface. A GPS device (1-m precision) was used to acquire the position of each camera station, and then treated to georeference the resulting 3D image.

Identification of sets of discontinuities and their orientations

Structural features of the slope are extracted from the 3D digital image using the Sirovision geotechnical analysis software (Sirovision, 2010). The planes for processing the discontinuity orientation characterization are manually detected on the 3D surface, and described as coloured discs (Figure 2, left).

INTEGRATION OF THE MECHANICAL MODEL BASED ON A DFN-DEM FORMULATION

Geometrical configuration

The 3D digitalized and meshed surface is processed by a mesh-processing software to define the studied rock mass as a closed volume (Figure 1).

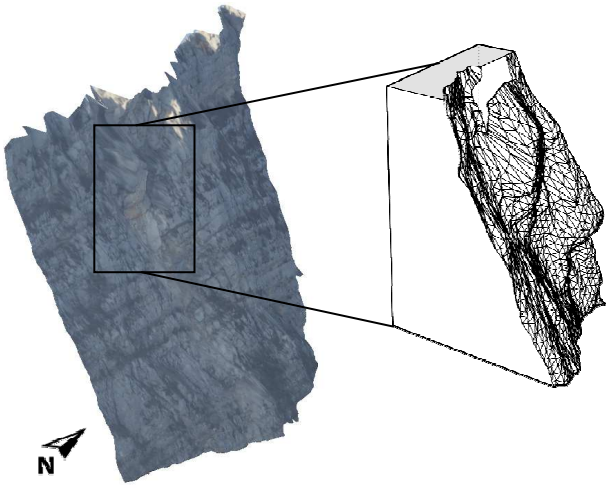

Figure 1. **The meshed closed volume (right) extracted from the 3D model of the slope (left)**

The discontinuities are then modelled as planar circular surfaces whose sizes and orientations were selected according to the structural analysis (Figure 2, right). The planar assumption is commonly used in rock engineering (Zhang & Einstein, 2000) and has the advantage of greatly simplifying the modelling and the numerical analyses.

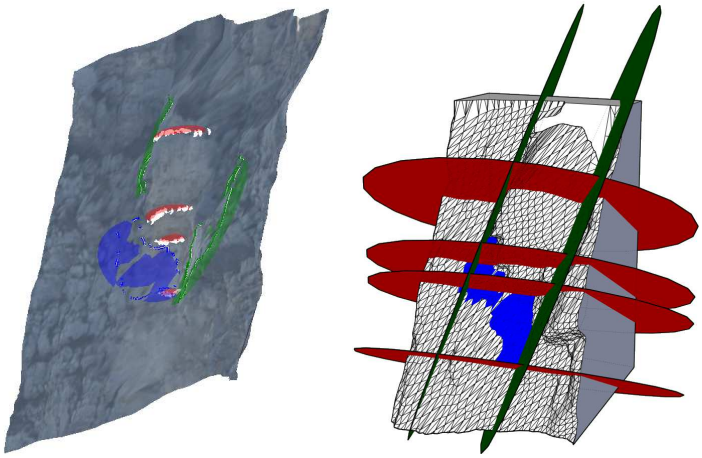

Figure 2. **On the left, the discontinuities involved in the studied rock block and identified from the structural analysis. On the right, the associated discrete fracture model which has been used for the mechanical simulations**

Mechanical configuration

The presence of potential rock bridges on the back face of the hanging block plays a major role in the rock mass stability. That is the reason YADE Open DEM package (Kozicki &

Donzé, 2008, 2009; Šmilauer *et al.*, 2010) is chosen to simulate the likely progressive failure of the rock bridge. Like in classical particle models, the intact rock is represented by an assembly of discrete elements (DE) glued together by cohesive bonds that can break either by tension or shear failure to simulate the progressive development of fracturing induced by an external loading. The bond behaviour is defined according to a cohesive frictional contact law that needs to be preliminarily calibrated to simulate the desired material behaviour (Scholtès & Donzé, 2013).

Discontinuities are represented in the DFN-DEM model with a specific contact formulation that can be related to the work done by Cundall and co-authors for the development of the Synthetic Rock Mass (Cundall *et al.*, 2008; Mas-Ivars *et al.*, 2011). The DFN previously generated (Figure 2, right) is thus imported into the closed volume, filled up with DE, for the identification phase. The presence of the potential rock bridge is reproduced by keeping an intact zone within the model, just behind the hanging block. The interacting pairs of DE separated by a discontinuity plane are then identified.

The micromechanical properties of the rock mass and the interactions making up the discontinuities are calibrated here based on the properties obtained from laboratory tests performed on Urgonian limestone joints by Frayssines and Hantz (2009).

The model is then submitted to gravity loading in order to mimic the in-situ stress field. Once the model is stabilized under gravity, discontinuities properties are assigned to their in-situ values. The influence of the DFN geometry and of the discontinuity properties can thus be explored since they represent an issue of critical importance in the stability assessment.

STRENGTH REDUCTION METHOD FOR ASSESSING ROCK SLOPE STABILITY

In presence of rock bridges, the rock mass can eventually remain stable after the stress initialization. In this case, a tensile and shear strength (TSSR) reduction method is used in order to promote failure. This TSSR method, operated through the progressive and simultaneous decrease in the local inter-particle bond tensile and shear strengths, induces a progressive decrease in the macroscopic tensile and compressive strength of the rock mass. The strength reduction (SR) induced at the macro-scale is appreciatively proportional to the one assigned at the local scale through the SR factor which is equal to the ratio between the initial strength and the updated assigned strength (Bonilla-Sierra *et al.*, 2015).

Applying the tensile and shear strength reduction method

To progressively reduce the strength of the rock matrix, the bond tensile and shear strengths are iteratively multiplied by a SR factor equal to 0.75. Each time this strength reduction is performed, the system is allowed to return to equilibrium before a new strength reduction is applied. Ultimately, failure occurs when the rock mass is overcome by the gravity loading. Following this iterative process, bonds break, leading the system or at least part of it, to an unstable regime, *i.e.* independent groups of particles move apart due to gravity. A possible way to follow the evolution of system weakening is to follow the increasing amount of broken bonds, also called micro-cracks, as the strength reduction is performed (Figure 3). In this case, as the strength is reduced to 0.24 times its initial value, the amount of micro-cracks notably increases.

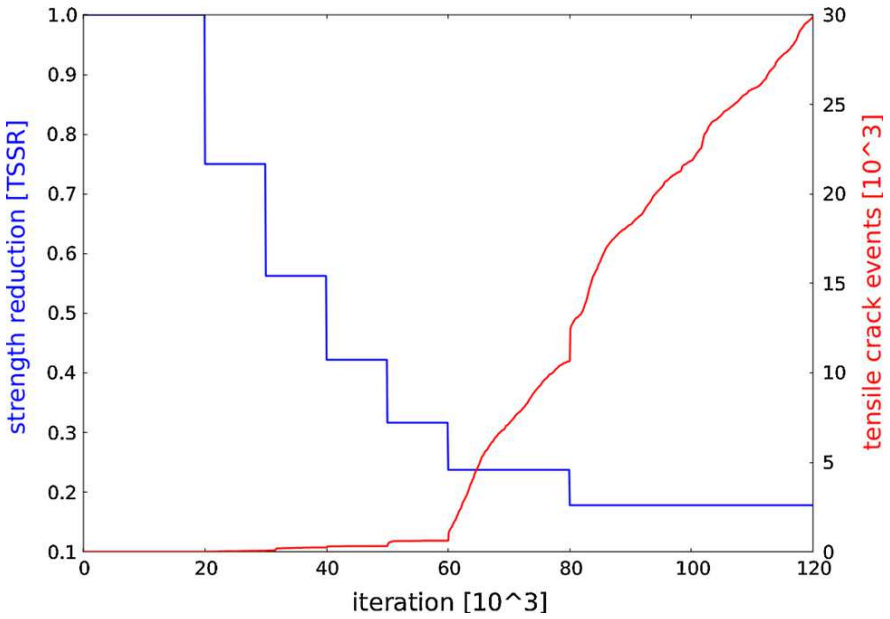

Figure 3. **Decrease in the strength as a function of the simulation time (blue curve) and the corresponding cumulative amount of micro-cracks (red curve)**

In Figure 4, the spatial distribution of micro-cracks is plotted at several times of the simulation to follow the progressive failure of the rock bridge behind the rock block.

Figure 4. **Vertical cut of the model. The set of discrete elements is in yellow. In grey, the discrete fractures and in red the cracks are represented. The upper left figure is plotted after 60,000 iterations, the upper right after 70,000 iterations, the lower left, after 80,000 iterations and the lower right after 120,000 iterations**

In consequence of this progressive failure mechanism, the sub-block located below the upper first bedding plane is first separated from the face and slides. Then, the sub-block located above separates from the rock mass and collapses in a combination of toppling and sliding. Figure 5 illustrates the velocity field as failure progresses until the entire block falls.

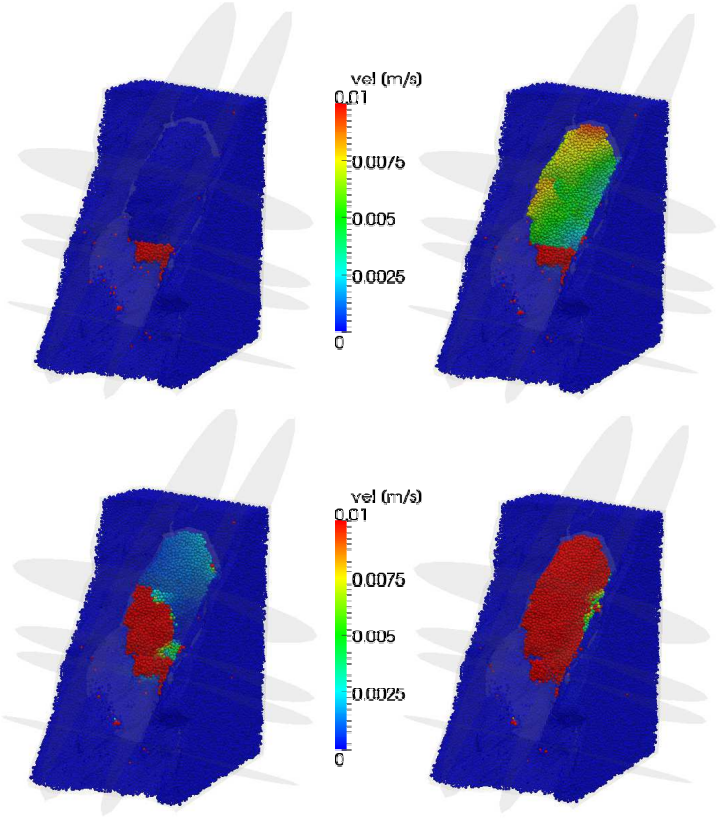

Figure 5. **3D view of the velocity field. The upper left figure is plotted after 60,000 iterations, the upper right after 70,000 iterations, the lower left, after 80,000 iterations and the lower right after 120,000 iterations.**

CONCLUSION

The Sirovision photogrammetry system was used to map the discontinuities and slope 3D geometry for a rockfall hazard. These data was processed to construct the structural model of a rock slope which was then used as input in a mechanical model to carry out a stability analysis. DFN-DEM formulation was chosen for modelling since it can explicitly take into account the sets of discontinuities generated by Sirovision and for its ability to reproduce progressive failure mechanism. Therefore, a modelling strategy must be established in order to identify the key features which control the stability of a fractured rock slope.
A Factor-of-Safety (FoS) can potentially be established applying the TSSR method. However, the meaning of the defined FoS needs to be considered with caution as its value depends on many assumptions, such as fracture mechanical and geometrical properties, rock bridge size and initial strength of the intact rock matrix.

ACKNOWLEDGMENTS

This work has been partly supported by the IMSRN company through a CIFRE grant N°2012/0710, the Research network "Vulnerability of structures undergoing a natural or technological hazard" (Grenoble, France) and the Sirovision project (CSIRO, QCAT, Pullenvale, Australia).

REFERENCES

Birch J (2006) Using 3DM analyst mine mapping suite for rock face characterisation, in ARMA 2006. In: Tonon F, Kottenstett (eds), Proceedings, laser and photogrammetric methods for rock face characterisation workshop, Golden

Bonilla-Sierra, V., Scholtès, L., Donzé, F.V. & Elmouttie, M. 2015. Rock slope stability analysis using photogrammetric data and DFN-DEM modelling. *Acta Geotechnica*, doi: 10.1007/s11440-015-0374-z

Cundall, P.A., Pierce, M.E. & Mas Ivars, D. Quantifying the Size Effect of Rock Mass Strength. 2008. *SHIRMS 2008 Proceedings, 1st Southern Hemisphere International Rock Mechanics Symposium, Perth, Western Australia, September 2008, Y. Potvin et al., Eds. Nedlands, Western Australia: Australian Centre for Geomechanics*, 2:3-15.

Frayssines, M. & Hantz, D. 2009. Modeling and back analyzing failures in steep limestone slopes. *International Journal of Rock Mechanics and Mining Sciences*, 46:1115-1123.

Firpo, G., Salvini, R., Francioni, M. & Ranjith, P.G. 2011. Use of Digital Terrestrial Photogrammetry in rocky slope stability analysis by Distinct Elements Numerical Methods. *International Journal of Rock Mechanics and Mining Sciences*, 48(7):1045-1054.

Gates, W.C.B. & Haneberg, W.C. 2012. Comparison of Standard Structural Mapping Results to 3-D Photogrammetric Model Results: Boundary Transformer Banks Rockfall Mitigation Project, Metaline Falls, Washington, in *Proceedings American Rock mechanics Association, 46th US Rock Mechanics / Geomechanics Symposium held in Chicago, IL, USA*, 24-27 June.

Haneberg, W.C. 2008. Using close range terrestrial digital photogrammetry for 3-D rock slope modeling and discontinuity mapping in the United States. *Bulletin of Engineering Geology and the Enviroment*. 67:457-469.

Harthong, B., Scholtès, L. & Donzé, F.V. 2012. Strength characterization of rock masses, using a coupled DEM-DFN model, *Geophysical Journal International*, doi: 10.1111/j.1365-246X.2012.05642.x.

Kozicki, J. & Donzé, F.V. 2008. A new open-source software developed for numerical simulations using discrete modeling methods, *Comp. Meth. In Appl. Mech. And Eng*. 197:4429-4443.

Kozicki, J. & Donzé F.V. 2009. YADE-OPEN DEM: an open--source software using a discrete element method to simulate granular material, *Engineering Computations*, 26(7):786-805.

Mas Ivars, D., Pierce, M.E., Darcel, C., Reyes-Montes, J., Po-tyondy, D.O., Young, R.P & Cundall P.A. 2011. The syn-thetic rock mass approach for jointed rock mass modelling. *International Journal of Rock Mechanics and Mining Sciences*, 48(2): 219–244.

Poropat, G.V. 2006. Remote 3D Mapping of Rock Mass Structure. Laser and Photogrammetric Methods for Rock Face Characterization. *American Rock Mechanics Association. Golden, Colorado*, June 17-18.

Scholtès, L., Donzé, F.V. & Khanal, M. 2011. Scale effects on strength of geomaterials, case study: coal, *Journal of the Mechanics and Physics of Solids*, 59(5):1131-1146.

Scholtès, L. & Donzé, F.V. 2012. Modelling progressive failure in fractured rock masses using a 3D discrete element method, *International Journal of Rock Mechanics and Mining Sciences*, 52:18-30.

Scholtès, L. & Donzé, F.V. 2013. DEM model for soft and hard rocks: role of grain interlocking on strength, *J. Mech. Phys. Solids*, 61:352-369.

Sirovision. 2010. Commonwealth Scientific and Industrial Research Organisation CSIRO, Sirovision 3D Imaging Mapping System Manual Version 4.1.

Šmilauer, V., Catalano, E., Chareyre, B., Dorofenko, S., Duriez, J., Gladky, A., Kozicki, J., Modenese, C., Scholtès, L., Sibille, L., Stránsky, J. & Thoeni, K. 2010. *Yade Reference Documentation. In: Smilauer, V. (Ed.), Yade Documentation, 474 1st Edition. The Yade Project*, http://yade-dem.org/doc/.

Sturzenegger, M., Stead, D. & Elmo, D. 2011. Terrestrial re-mote sensing-based estimation of mean trace length, trace intensity and block size/shape, *Engineering Geology*, 119:96-11.

Sturzenegger, M & Stead, D. 2012. The Palliser rockslide, Canadian Rocky Mountains: characterization and modeling of a stepped failure surface, *Geomorphology*, 138:145-161.

Zhang, L. & Einstein, H.H. 2000. Estimating the intensity of rock discontinuities, *International Journal of Rock Mechanics and Mining Sciences* 37:819-837.

Influence of the morphology of slope and blocks on the energy dissipations in a rock avalanche

S. Cuervo, G. Mollon, D. Daudon, P. Villard & V. Richefeu
Laboratoire Sols, Solides, Structures, Grenoble, France
Stiven.Cuervo@3sr-grenoble.fr

ABSTRACT

A discrete element model was used to determine the influence of block shape and surface topography on energy dissipative modes occurring during rockfalls or avalanches. By using realistic shapes of particles and a specific contact law able to represent the main dissipation phenomena at the contact-rebound point, we analyze the contribution of tangential and collisional effects within the granular material or at the base of the flow. It was shown that the particle shape and the slope geometry have a major influence on the energy dissipative modes and need to be accounted for in numerical models.

Adapted from: 10.1016/j.crme.2014.11.003

INTRODUCTION

Rock avalanches are among the most frequent and unpredictable natural events that need to be taken into account to define the risks in the mountainous infrastructures. The complexity of the interacting mechanisms involved during the flow has a great influence on the morphology of the deposit and on the propagation distance of a rock mass. The nature of the flow patterns and the mode of interaction between blocks strongly depend on the shape, size and number of blocks as well as the geometry of the surface topography. The influence of these parameters on the kinematics of the flow and on the amounts of energy dissipated at the base and within the moving granular mass is one of the key points that must be raised in order to predict satisfactorily the propagation and deposition areas of the granular mass.

Usually, the trajectory of individual block and the position of the stop zone are approximated using softwares based on mass-point mechanics for which the energy dissipation at each contact depends on damping and frictional coefficients (Habib, 1976; Descoeudres, 1997; Evans & Hungr, 1993). Small avalanches may be studied with a probabilistic approach of the precedent trajectory methods (Dorren et al., 2006; Bourrier et al., 2009), but energy dissipation is modeled through restitution coefficients, defined in normal or/and tangential directions, which may be expressed either with velocity ratios or kinetic energy ratios (Wu, 1985; Descoeudres, 1997; Okura et al., 2000; Bozzolo & Pamini, 1986; Azzoni & De Freitas, 1995; Chau et al., 1999). Some authors have shown that the kinetic of the impact depends strongly on the substrate nature related to soft or hard contacts (Fornaro et al., 1990; Giani et

al, 2004; Habib, 1976; Evans & Hungr, 1993), on the shape of the blocks and on the impact angle (Wu, 1985; Chau et al., 1999; Heidenreich, 2004; Wu et al., 2003). So, different values and definitions of the restitution coefficient are proposed in the literature, leading in some cases (transformation of rotational energy into translation energy for example) to unphysical values greater than the unity limit (Ferrari et al., 2013).The Discrete Elements Modeling (DEM) seems to be relevant in modeling medium and small volumes of rock avalanches (Campbell et al., 1995; Calvetti et al., 2000; Cleary & Prakash, 2004; Staron, 2008; Valentino et al., 2008; Taboada & Estrada, 2009; Banton et al., 2009). The contact law between particles becomes a factor of importance and the classical elastic laws with friction are used (Chang & Taboada, 2009; Cundall & Strack, 1979; Valentino et al., 2008). Some dissipation parameters may be added as in Walton laws (Walton & Braun, 1986; Favier et al., 2009). The particles shape may be taken into account by using polygons (Cundall & Strack, 1979), spheres, clumps of spheres, ellipsoids, spheropolyedrons (Alonso-Marroquin, 2008).
The model proposed here is able to take account of realistic block shapes (Richefeu et al., 2012) and is based on the definition of specific interaction laws which makes physical parameters easily assessable by means of simple laboratory experiment of block launch retro-analysis (Mollon et al., 2012). Each block is modeled by a spheropolyedron, which is the shape resulting from the sweeping of a sphere onto the surface of a polyhedron (Van Den Bergen, 2003)allowing to obtain realistic shapes, to optimize the contact detection algorithm and to minimize the time calculation. The contact model, described in the following section, is tested and validated with laboratory experiments performed at EPFL (Manzella & Labiouse, 2009), which consist in the release of an assembly of small bricks on a bi-plane. Then, the model is used to highlight the energy dissipation mechanisms occurring along the slope, the undulation of the slope, and the effect of the slope transition between the two planes.

CONTACT LAW AND CALIBRATION OF PARAMETERS

The contact model that we used to simulate the dissipative mechanisms occurring during an impact between two solids is deliberately minimalist and defined by four parameters that can be easily identified by laboratory tests (e_n^2, μ, k_n and k_t)The parameter e_n^2 reflects the amount of energy restored in the direction perpendicular to the contact plane at each cycle of loading/unloading of the contact. This coefficient integrates a very complex set of mechanisms (damage, plastification, elastic wave, heat generation, etc.) not exactly included in the chosen behavior law. It allows in a comprehensive manner, to access to the amount of energy dissipated during impact.
The parameter μ introduces the energy dissipation in the tangential direction to the contact plane : dynamic friction coefficient between two rigid bodies and for a contact between a boulder and loose soil this coefficient incorporates in addition to frictional forces, abutment force and shear strength of the soil of the impacted area. However, it behaves exactly like a classical coulomb friction coefficient.
The parameters k_n and k_s are respectively associated to the stiffness of the contact in the normal and tangential directions.
During contact between two particles, the normal and tangential forces of interaction $F_n(t)$ and $F_t(t)$ are calculated incrementally at each time step δt based on the normal interpenetration h_n between particles and on their normal and tangential velocities ($\dot{h}_n$ and $\dot{h}_t$); Equations 1 and 2. Note that the tangential force is formally written as in two-dimensional case for a sake of simplicity.

$$\begin{aligned} F_n(t+\delta t) &= F_n(t) + k_n \dot{h}_n \delta t \quad \text{if } \dot{h}_n \geq 0 \\ F_n(t+\delta t) &= e_n^2 k_n h_n \quad \text{otherwise} \end{aligned} \tag{1}$$

$$F_t(t+dt) = \min\left[F_t(t) + k_t \dot{h}_t dt; mF_n(t)\right] \tag{2}$$

To carry out the modeling of the experiments performed at EPFL (Manzella & Labiouse, 2009), we have implemented a specific procedure, currently operational in laboratory, to identify the numerical contact parameters. This procedure consists in analyzing the fall and rebound of a single particle on a horizontal plane identical as those of EPFL experiments, using a device consisting of two synchronized high-speed cameras shooting at 1000 fps (Fig 1).Several rebounds allows optimizing the values of the numerical parameters by using an error function that characterizes the difference between the actual trajectory of the particle, before and after rebound, and the one restored by the numerical model.

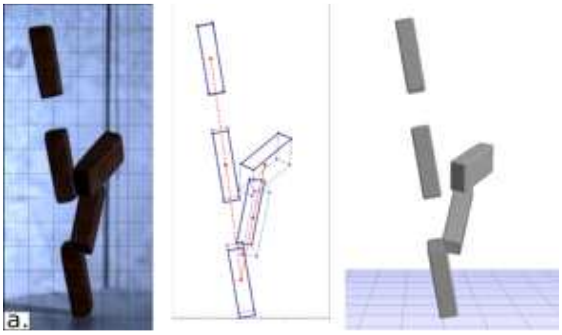

Figure 1. **parameters identification procedure**: (a) Camera 1, identification of the trajectory, numerical simulation;

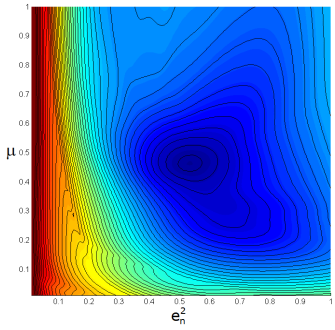

Figure 2. **Isovalue curves of the error function** associated to the parameters e_n^2 and μ (brick/support interaction).

The optimization procedure consists in varying the four numerical parameters and in calculating, an error function based on the comparison between the actual trajectories of particles and those returned by the numerical model. Figure 2 presents the isovalue curves of the error function associated to the parameters e_n^2 and μ, which are the most influent parameters to restore the trajectory after impact (Richefeu et al., 2012). The values obtained for the brick/support or brick/brick interactions are given Table 1.

Table 1. Optimal parameters obtained by minimizing the error function.

	e_n^2	μ	k_n (N/m)	k_t/k_n
Brick/support	0.53	0.46	10^5	0.42
Brick/brick	0.13	0.86	10^5	0.27

VALIDATION OF THE NUMERICAL MODEL

After calibration of the contact parameters, the robustness of the numerical model was validated by comparison with small-size laboratory experiments implementing an assembly of small bricks (size of 31 mm × 15 mm × 8 mm) propagating along an inclined slope and then stopping on a horizontal plane (Fig. 3). The advantage of such simulations is to test the predictive ability of the numerical model to predict the collective flow of a granular mass,

based on contact parameters obtained by studying the bounce of a single particle. This makes it possible to understand, by calculating variables which are difficult to measure, what are the key parameters influencing the kinematics of the flow and the final position of the granular depositAs the influence of the particle shape and of the topography geometry on the modes of energy dissipation (at the base or within the flow, by shocks or friction) is of importance.
The experiment used for the validation of the numerical model consists in the release and the flow on an inclined plane of 6300 small bricks randomly poured in a starting box (size of $0.2\ \text{m} \times 0.4\ \text{m} \times 0.6\ \text{m}$) is descried in Figure 3. Material needed to determine the contact parameters were obtained obtained through a collaboration established as part of the European projet Alcotra MASSA. The experimental characteristics of the deposit zone (*i.e.*, dimensions, position, shape) are measured by optical technique (Manzella & Labiouse, 2009). Specific algorithms have been developed to define the geometry of the deposit and some characteristics of the kinematics of the flow (average speed and front velocity of the flow).

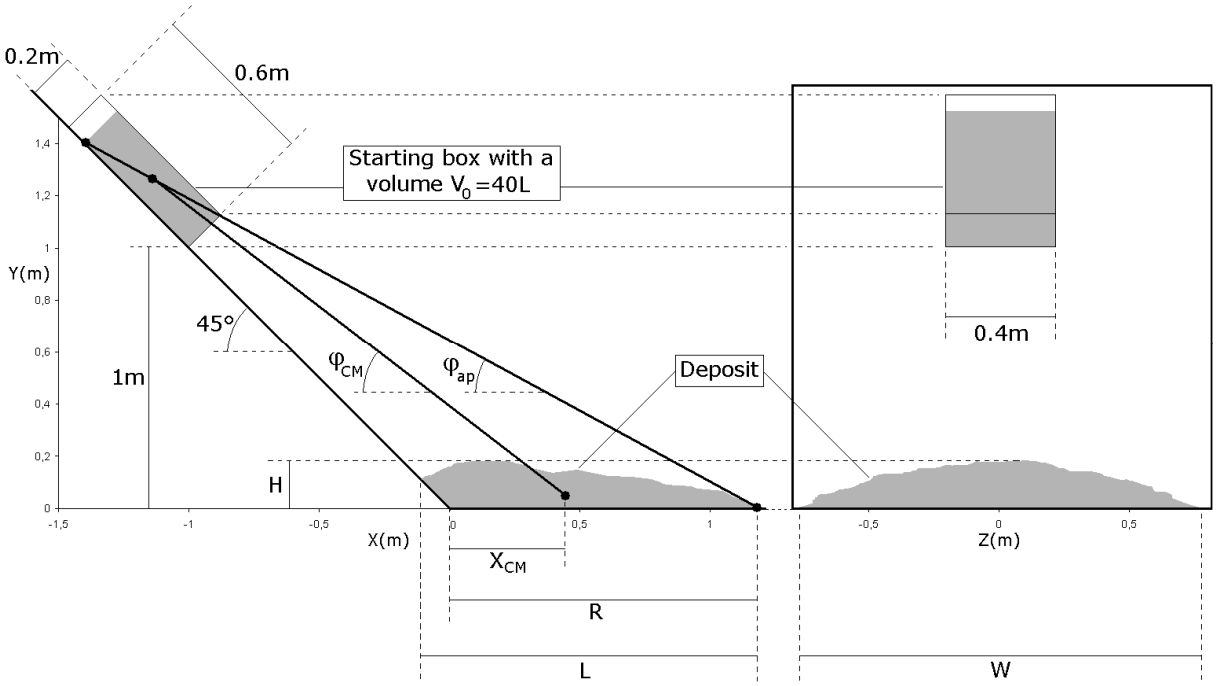

Figure 3. experimental device and description of the geometric parameters.

The comparisons between the physical experiments and the numerical model, presented in Table 2, are based on the characteristics of the granular deposit (size, position of the centre of gravity) and on typical quantities of the rockfalls framework (Fahrböschung angle φ_{app} and travel angle φ_{CM}), and the comparison between the numerical and experimental deposit shapes is satisfactory, in terms of horizontal dimensions and little a less in terms of height. the travel angle φ_{CM} related to the center of mass and Fahrböschung angle φ_{app} related to the extreme points of the granular deposit are very accurately reproduced Differences between the height of the granular deposit are attributed to the difficulty to measure experimentally and to define numerically the shape deposit and may be considered with caution

Table 2. Geometric characteristics of the position and shape deposit with errors relative to the experimental values.

	H (m)	L (m)	W (m)	R (m)	φ_{CM} (°)	φ_{app} (°)	X_{CM} (m)
Experimental	0.075	0.093	1.400	0.840	40.0	32.0	0.370
Numerical	0.120	0.882	1.383	0.824	40.1	32.2	0.332

Relative error (%)	+60.00	-5.16	-1.21	-1.90	+0.25	+0.62	-10.27

The comparison between experiment and modeling on a collective release of particles shows, that due to multiple interactions between particles within the flow, it is possible to approach very satisfactorily the main features of the deposit. Imperfections in brick shape or uncertainties on the contact parameters have consequently little influence on the collective behavior of the granular mass but may not be accurate for the trajectory of an individual block. The energy dissipation mechanisms have been properly modeled for collective behavior. A sensitivity study of the contact parameters on the energy dissipation mechanisms are studied by the identification of the contact force work and the deduction the amount of energy dissipated at each time step through (Mollon et al., 2012)

INFLUENCE OF MORPHOLOGICAL PARAMETERS

The focus is on how the avalanche is affected by (*i*) the aspect ratio of the block shape, (*ii*) the presence of block-sized undulations onto the slope, and (*iii*) a less steep transition in the slope gradient at the device toe. These three changes concern only geometric features, and the mechanical parameters are deliberately kept the same; . We will use as a reference the simulation of brick release previously validated, and compare it with other simulations for which only one geometric parameter (block shape, slope undulation or transition curvature) is modified at a time (Fig. 4).

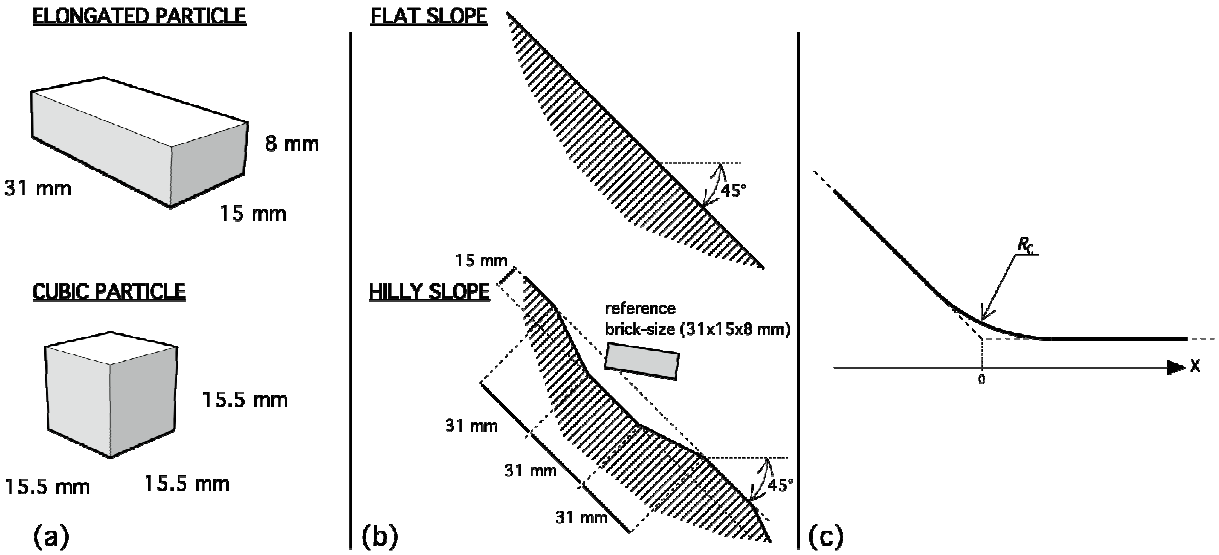

Figure 4. Geometric features (a) shapes aspect ratio, (b) slope undulations, (c) rounding of the slope transition.

ASPECT RATIO OF THE BLOCKS AND BUMPY TERRAIN

The role of the aspect ratio of the blocks is regarded by comparing the reference release of elongated bricks (aspect ratio of about 2) with the release of cubes of the same volume Figure 4a. Three zones of spreading are considered: zone 2, surrounding the change in gradient, separates the slope (zone 1) from the stop area (zone 3). Four modes of dissipation (work of contact forces by unit horizontal

length along the propagation direction) are distinguished: collisions with the support W_n^{BS}, in-between the particles W_n^{BB}, friction with the support W_t^{BS}, and friction within the mass W_t^{BB}. a noticeable difference with cubes is noticed on the final position of the blocks (deposit and isolated particles) and on the dissipative energy modes: Whatever the zone, most of the energy was dissipated within the bulk for the cubes, while most of the energy was dissipated by friction for the bricks. the cubeflow is disturbed by the collisional movement of particles, while the bricks have a greater tendency to slip, which promotes the dissipation by friction both in the mass and at the base of the flow. The greater rolling ability of cubes induces a slight increase in the number of collisions in transision zone (2) that limites the reduction of the energy dissipated by friction at the base of the transition zone.

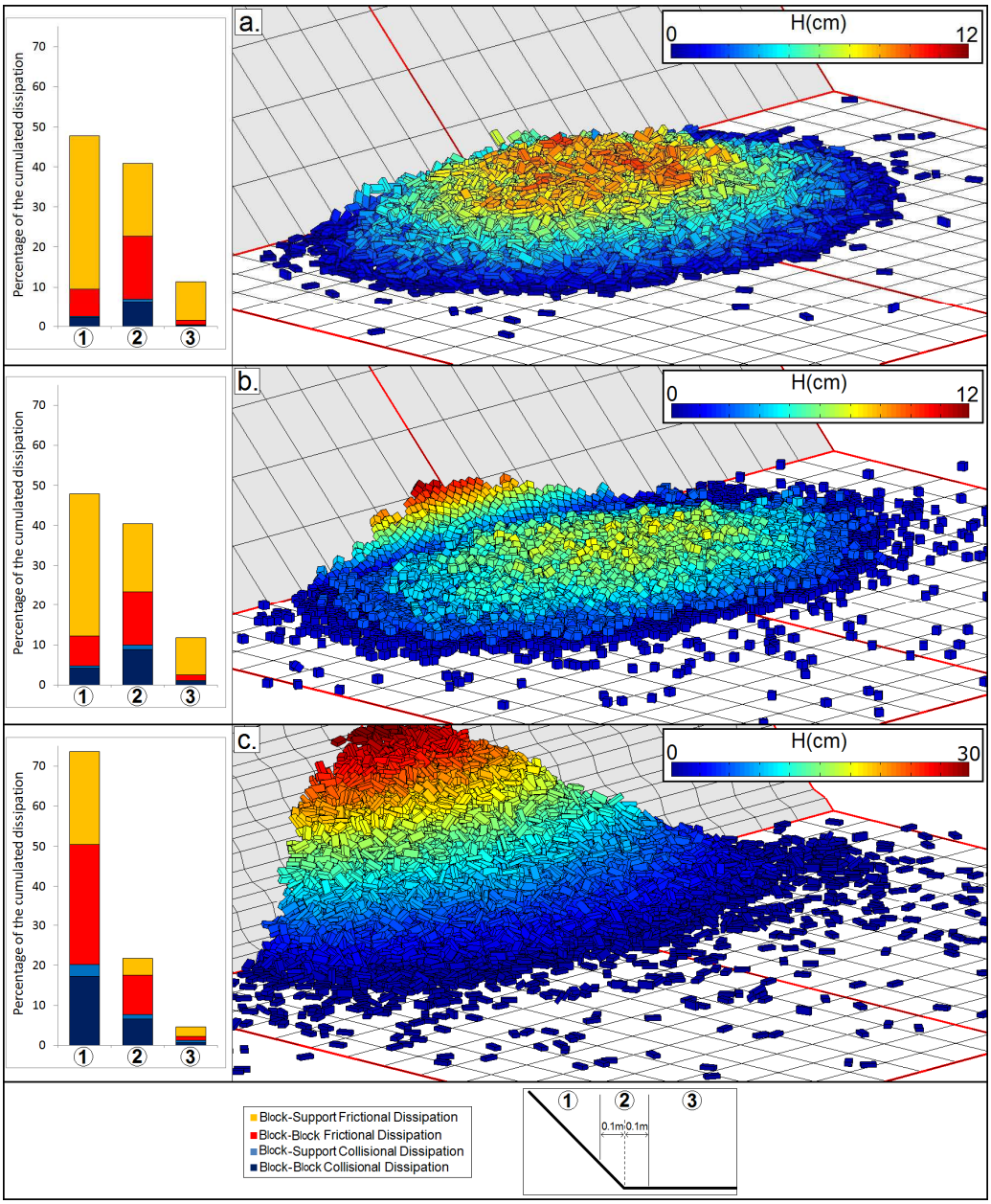

Figure 5. (left) **Energy dissipation type cumulated in slope, transition and stop area** and (right) **screenshot of the deposit** for (a) the reference simulation with bricks on flat slope, (b) cubes on flat slope and (c) bricks on hilly slope. The particle colored by altitudes.

However, the total amount of energy dissipated in each zone seems not be significantly affected by the aspect ratio of the blocks used . The collisional dissipated energy during the rolling of cubes on the stop zone is higher than the frictional dissipated one during the sliding of the bricks on the same zone due to the chozen values of e_n^2 and μ, and explain the longer runout distance for the reference release with bricks.
For the chosen contact parameters, and despite an equal amount of energy dissipated in each zone, both deposits have significant differences (table 3). A cubic shape leads to a smaller deposit length and runout distance, and a larger deposit width despite, a larger spreading of the isolated particles. The manner the energy is dissipated, by friction or by collisions, has strong consequences on the efficiency of the mass stop. The scattering of the isolated cubes is also a consequence to the greater rolling ability of cubes compared to bricks.

Table 3. Main characteristics of the deposits for releases of bricks and cubes on flat slope, and bricks on hilly slope.

	R (m)	L (m)	W (m)	φ_{CM} (°)	φ_{app} (°)
Bricks on flat slope	0.84	0.91	1.37	31.5	40.1
Cubes on flat slope	0.76	0.84	1.40	32.3	40.2
Bricks on hilly slope	0.48	0.81	1.48	36.0	45.5

The block-sized ripples play a crucial role on the propagation slope (Fig. 5a and 5c). In particular the runout distance is clearly shorter due to more dissipated energy in the bumpy slope (Table 3). The energy loss is incremented in the slope by an increase of collisions and friction between the blocks, due to undulations disturbance, and allows higher relative velocities between the blocks, both in tangential and normal contact directions (Fig 6). The particle friction is more potent in the flowing mass, particularly in the zone 1 (Fig 5c).
Since nearly 75% of the energy has been lost before the transition zone, the dissipation is lower in this zone and it is mainly the interparticle friction that has been reduced that makes the transition smoother. The runout distance is smaller with a bumpy slope, but the isolated blocks go further. Considering that a single free block in a real rockfall can cause considerable damage it is of importance.

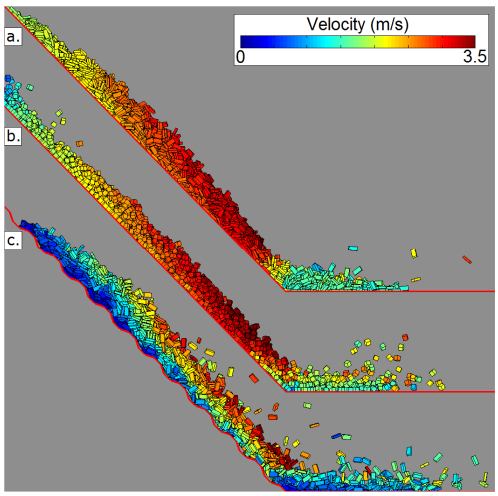

Figure 6. Lateral view of the particle velocities soon after the mass crossed the transition for the reference simulation (a), cubes on flat slope (b) and bricks on hilly slope (c).

SMOOTHNESS OF A TRANSITION

The role of the regularity of the gradient in the transition is regarded by varying the radius R_C of an added curvature tangent to both slopes (Fig 4c). The amounts of energy dissipated are computed as the work W by unit of length of the normal or tangential forces – subscripted by n or t respectively, with the support or in-between the particles – superscripted by BS or BB respectively. The total energy lost by collisions (W_n^{BS} and W_n^{BB}, Fig 7a and 7c) clearly vanishes in the transition zone as the radius increases, as it makes the transition smoother. For regular slopes and smooth transitional zones, the potential energy was dissipated only by friction at the base of the granular flow, considering frictional parameter greater between blocks than the one between slope and blocks.

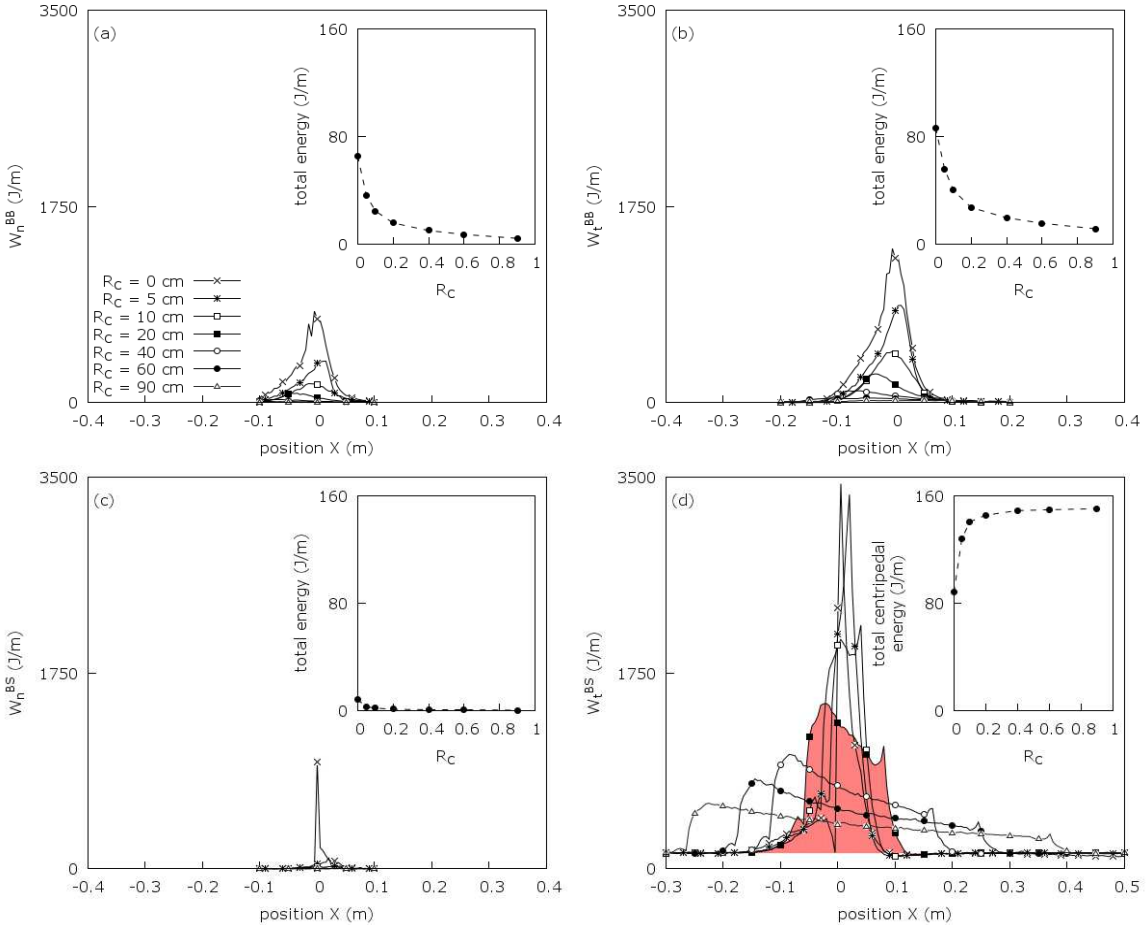

Figure 7. **Dissipated energy around the transition for the tested radii of curvature R_C.** (a) brick-brick collisions, (b) brick-brick friction, (c) brick-support collisions, (d) brick-support friction. Insets plots (a) to (c) : energy cumulated on the entire test as a function of the radius R_C. Inset plot (d) : excessive basal frictional energy, caused by the centripetal acceleration.

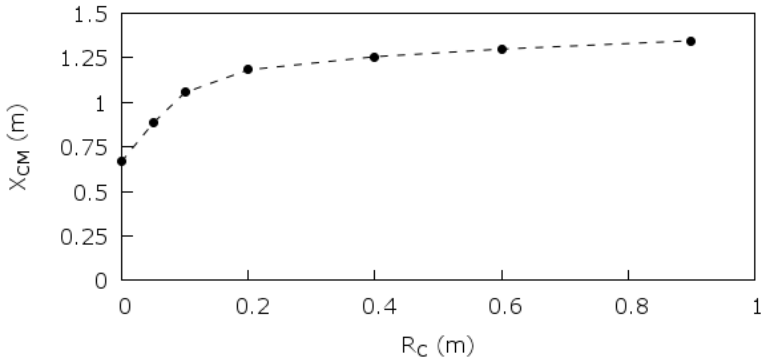

Figure 8. Position X_{CM} of the deposit mass-center (relative to the position of the slope transition) as a function of the curvature radius R_C.

The total loss of energy dissipation by block-block friction (W_t^{BB}, Fig. 7b) declines when R_C is increased.The peak of energy of dissipation by friction at the base (Fig. 7d) declines but is activated for a longer time. Moreover, the basal frictional energy loss does not vanish apart from the transition zone where the density of work W_t^{BS} stabilizes at nearly 120 J/m. Considering constant level of frictional dissipation along the slope, the excess in dissipation is attributed to the centripetal acceleration amplifying the force normal to the curvature surface, and thus magnifying the friction force threshold. Surprisingly, the total amount of energy due to the centripetal acceleration and dissipated by friction of particles on the support, (inset of Fig. 7d), first begins to increase with R_C and saturates from $R_C = 0.2$ m to a value of the density of work W_t^{BS} at nearly 120 J/m. The initial increase might be explained by a larger flat surface where the particles acquire a better opportunity to slip as R_C increases. The saturation of dissipated energy to a constant value, less obvious to understand, can be explained : the curved surface scales with R_C multiplied by the slope angle α, while the gain in the friction force threshold scales with μR_C. The friction of a particle sliding from the beginning to the end of the curvature dissipates thus an energy that scales with $\mu\alpha$, without dependence on R_C (see Fig. 8 showing the increase of the propagation length of the mass center X_{CM}). The stabilization is reach from $R_C \approx 0.2$ m corresponding to the situation where the particles have the possibility to remain in sliding contact with the entire curvature.

CONCLUSIONS

The influence of the geometrical parameters affecting dissipated energy in collisional and frictional modes within a granular flow has been studied by using the discrete element method. The relevance of the numerical model was proven by comparisons with small scale laboratory experiments. A particular attention was paid for taking account of realistic shapes of blocks and to well reproduce the dissipative mechanisms acting within the granular mass or at the base of the flow. The contact parameters were obtained by back analysis of a set of launch of single particles and the numerical model was successfully validated by laboratory experiments involving an assembly of small bricks flowing down to an inclined plane. Then, the numerical model was used to investigate the influence of geometrical parameters on the dissipative modes involved during the flow.
Main conclusions are :
-aspect ratio of the particles does not affect so much the runout and the position of the deposit.

-particle shape strongly changes energy dissipated way : cubes, more likely to roll than to slip, promote collisional dissipative mechanisms, as bricks allow more friction dissipation.
-dispersion of cubes is more spreading due to their rolling ability.
-bumpy terrain strongly disturbed the particle flow due to increased friction and number of collisions within the flow. The runout of the deposit was smaller than with a flat slope.
-bumpy terrain affects the flow regime, generating a strong vertical velocity gradient.
-number and distance of ejected particles (pertinent for the zoning process of rockfall hazard) are also increased.
-regular transition zone mostly dissipate the energy by basal friction.
-the transition zone is subject to an increase in friction forces at the base of the flow due to the centripetal acceleration.
-the energy dissipation saturate after a critical value of to the slope radius transition: the granular flow is strongly disturbed (collisions and rotation of particles) only for small values. The amount of the dissipated energy by collisions and friction within the granular flow increases with the bending radius leading to a decrease of the runout distance.

The geometric parameters have a great influence on the kinematics of the flow and on the dissipative energy modes (by friction or collisions) and the results obtained in the present study are highly dependent on the values of the contact parameters chosen. Nevertheless, the energy dissipation modes are correctly depicted. The derivation of fluid-like models, well used in the engineering of rock (Hungr, 1995; Voellmy, 1955; Mangeney-Castelnau et al., 2003; Pirulli & Mangeney, 2008 may be improved by the results in their behavior law.

REFERENCES

Alonso-Marroquin, F. 2008. Spheropolygons: A new method to simulate conservative and dissipative interactions between 2D complex-shaped rigid bodies. *Europhysics Letters*. 83.

Azzoni, A., De Freitas, M. 1995. Experimentally gained parameters, decisive for rockfall analysis. *Rock Mechanics and Rock Engineering*. 28: 111-124.

Banton, J., Villard, P., Jongmans, D., Scavia, C. 2009. Two-dimensional discrete element models of debris avalanches: parameterization and the reproducibility of experimental results. *Journal of Geophysical Research*. 114: F04013.

Bourrier, F., Dorren, L.K.A., Nicot, F., Berger, F., Darve, F. 2009. Towards objective rockfall trajectory simulation using a stochastic impact model. *Geomorphology*. 110: 68-79.

Bozzolo R., Pamini R. 1986. Simulation of rock falls down a valley side. *Acta Mechanica*. 63: 1-4.

Calvetti, F., Crosta, G.B., Tatarella, M. 2000. Numerical simulation of dry granular flows: From the reproduction of small-scale experiments to the prediction of rock avalanches. *Rivista Italiana di Geotecnica*. 2: 1-38.

Campbell, C., Cleary, P., Hopkins, M. 1995. Large-scale landslide simulations of global deformation, velocities and basal friction. *Journal of Geophysical Research, Solid Earth*. 100: 8267-8283.

Chang, K. J., Taboada, A. 1999. Discrete element simulation of the Jiufengershan rock-and-soil avalanche triggered by the 1999 Chi-Chi earthquake, Taiwan. *Journal of Geophysical Research*. 114: F03003.

Chau, K., Wong, R., Liu, J., Wu, J., Lee, C. 1999. Shape effects on the coefficient of restitution during rockfall impacts. *Proc. of the 9th International Congress on Rock Mechanics: International Society for Rock Mechanics* (ISRM). 541-544.

Cleary, P.W., Prakash, M. 2004. Discrete-element modeling and smoothed particle hydrodynamics: potential in the environmental sciences. *Philosophical Transactions of the Royal Society A: Mathematical, Physical and Engineering Sciences*. 362: 2003-2030.

Cundall, P.A., Strack, O.D.L. 1979. A Discrete Numerical-Model for Granular Assemblies. *Geotechnique*. 29: 47-65.

Descoeudres, F. 1997. Aspects géomécaniques des instabilités de falaises rocheuses et des chutes de blocs. *Publications de la Société Suisse de Mécanique des Sols et des Roches* 135, Montreux, 7 nov 1997.

Dorren, L.K.A., Berger, F., Putters, U.S. 2006. Real size experiments and 3D simulation of rockfall on forested and non-forested slopes. *Natural Hazards and Earth System Sciences*. 6: 145-153.

Evans, S., Hungr, O. 1993. The assessment of rockfall hazard at the base of talus slopes. *Canadian Geotechnical Journal.* 30: 620-636.

Favier, L., Daudon, D., Donze, F.V., Mazars, J. 2009. Predicting the drag coefficient of a granular flow using the discrete element method. *Journal of Statistical Mechanics: Theory and Experiment*.

Ferrari, F., Giani, G.P., Apuani, T. 2013. Why can rockfall normal restitution coefficient be higher than one ? *Rend.Online Soc. Geol. It.* 24: 122-124.

Fornaro, M., Peila, D., Nebbia, M. 1990. Block falls on rock slopes: application of a numerical simulation program to some real cases. *Proceedings of the 6th International Congress IAEG*. 2173-2180.

Giani, G., Giacomini, A., Migliazza, M., Segalini, A. 2004. Experimental and theoretical studies to improve rock fall analysis and protection work design. *Rock Mechanics and Rock Engineering*. 37: 369-389.

Habib, P. 1976. Note sur le rebondissement des blocs rocheux. *Proceedings Meeting on Rockfall Dynamics and Protective Works Effectiveness*. 123-125.

Heidenreich, B. 2004. Small and half-scale experimental studies of rockfall impacts on sandy slopes, *Ph.D. Thesis*, EPFL, Lausanne.

Hungr, O. 1995. A Model for the Runout Analysis of Rapid Flow Slides, Debris Flows, and Avalanches. Can. Geotech. J.. 32: 610-623.

Mangeney-Castelnau, A., Vilotte, J. P., Bristeau, M.O., Perthame, B., Bouchut, F., Simeoni, C., Yerneni, S. 2003. Numerical modeling of avalanches based on Saint Venant equations using a kinetic scheme. *Journal of Geophysical Research.* 108: 2527.

Manzella, I., Labiouse, V. 2009. Flow experiments with gravel and blocks at small scale to investigate parameters and mechanisms involved in rock avalanches. *Engineering Geology*, 109: 146-158.

Mollon, G., Richefeu, V., Villard, P., Daudon, D. 2012. Numerical simulation of rock avalanches: influence of local dissipative contact model on the collective behavior of granular flows. *Journal of Geophysical Research*. 117: F02036.

Okura, Y., Kitahara, H., Sammori, T. 2000. Fluidization in dry landslides. *Engineering Geology*. 56: 347-360.

Pirulli, M., Mangeney, A. 2008. Results of back-analysis of the propagation of rock avalanches as a function of the assumed rheology. *Rock Mech. Rock Eng.*. 41: 59-84.

Richefeu, V., Mollon, G., Daudon, D., Villard, P. 2012. Dissipative contacts and realistic block shapes for modelling rock avalanches. *Engineering Geology*. 149-150: 78-92.

Staron, L. 2008. Mobility of long-runout rock flows: a discrete numerical investigation, *Geophys. J. Int.*. 172: 455-463.

Taboada, A., Estrada, N. 2009. Rock-and-soil avalanches: theory and simulation. *Journal of Geophysical Research*. 114: F03004.

Valentino, R., Barla, G., Montrasio, L. 2008. Experimental analysis and micromechanical modelling of dry granular flow and impacts in laboratory flume tests. *Rock Mech. Rock Eng.* 41:153-177.

Van Den Bergen, G. 2004. Collision Detection in Interactive 3D Environments (The Morgan Kaufmann Series in Interactive 3D Technology). Morgan Kaufmann publishers.

Voellmy, A. 1955. Über die Zerstorungskraft von Lawinen. *Schweizerische Bauzeitung*. 73: 212-285.

Walton, O.R., Braun, R.L. 1986. Viscosity, granular temperature, and stress calculations for shearing assemblies of inelastic, frictional disks. *Journal of Rheology*. 30: 949-980.

Wu, C., Thornton, C., Li, L. 2003. Coefficients of restitution for elastoplastic oblique impacts. *Advanced Powder Technology*. 14: 937-960 .

Wu, S. 1985. Rockfall evaluation by computer simulation. *Transportation Research Record*. 1031:1-5.

Material Point Method to model gravity hazards

F. Gracia[1,2], P. Villard[1] & V. Richefeu[1]
[1]*Laboratoire Sols, Solides, Structures, Grenoble, France*
[2] *IMSRN, Montbonnot F-38330, France*
fabio.gracia@3sr-grenoble.fr, pascal.villard@3sr-grenoble.fr
vincent.richefeu@3sr-grenoble.fr

ABSTRACT

In the following study, the development of a code in C++ has been made using the Material Point Method (MPM). The MPM is generalized using a variational form and a Petrov-Galerkin discretization scheme. It is an alternative to methods such as the Discrete Element Method. It allows the modeling of continuum media undergoing large deformations. It is therefore a suitable approach to landslides, as well as providing rather low calculation times. In this study, detailed steps of how the MPM works are presented, as well as some enhancements done to the code using previous improvements related to the DEM. Some tests were performed in order to show how the model behaves in different situations. Validation of one of the tests is done. Finally, some of the perspectives are provided, showing that there is scope for improvement.

INTRODUCTION

The prediction of the geotechnical behavior of structures constitutes a major field in geotechnics. The Finite Element Method (FEM) is one of the most popular methods used to model different types of geotechnical problems. Its current stage of development permits the geotechnical field model geotechnical structures with enough reliability to be used as a numerical tool. One of its advantages, as other continuous methods, is its small computational cost when compared with other methods. Nevertheless, it has shown some complications when large deformation takes place. Given the fact that the background grid used to make calculations deforms with as the body deforms, periodical remeshing is necessary to avoid mesh entanglement. This method is thus not appropriate when dealing with bodies undergoing large deformations.
Another method currently used in the field of geotechnics is the Discrete Element Method (DEM). This method is able to model the granular scale physics of bodies. Particles are not linked to a mesh, therefore avoiding complications presented by the FEM when handling

large deformations. However, this method is computationally very costly even though computational techniques such as parallel processing, among others, are currently being used. This limits for instance the number of particles, which in the case of large scale gravitational phenomena is not appropriate.
Continuous models are widely used in the engineering field due to their “ease-of-use” and small computational times. Hence, a continuous and meshfree, or at least partially free, approach is required. The Material Point Method (MPM) (Sulsky et al., 1994), a Particle-in-Cell (PIC) numerical technique, has been largely used in the field of fluid mechanics. It is able to model history dependent materials such as highly distorted fluids. This method interpolates information between a background grid (Eulerian) and material points (Lagrangian) that store information. In this case, the mesh is not linked to the points during the simulation. Instead, the grid nodes stay in the same initial position, and are used only to make the required calculations, since the material points carry the information. Given the fact that the material points follow a Lagrangian state, it is possible to represent large deformations such as that achieved during avalanches.

THE MATERIAL POINT METHOD

The material point method is a numerical method for the solution of problems in continuum mechanics, in which large deformations can be accomplished.
This method solves the variational form of the conservation of momentum by discretizing the continuum into material points. Since the mass remains unchanged during the computation, the conservation of mass is also satisfied. A background grid is then used to project the information carried by the material points and solve the equations of motion. The solutions found in the mesh are used to update the information contained in the material points. This interpolation/extrapolation between the mesh and the material points is done using shape functions.

Background Grid

In the FEM, body fixed meshes have accuracy problems when undergoing large deformations due to mesh distortion, which in the end require remeshing. In the MPM a discretization in points takes place, thus avoiding a body fixed mesh. This makes it suitable to approach landslide problems, which is our main aim.

This method provides interpolation between the grid and the Lagrangian points by means of shape functions. The grid properties are then reset at the end of each step, thus keeping the updated solutions in the material points. During the interpolation between material points and grid total mass and momentum are conserved. The grid is thus a temporary place where calculations are done, with the main purpose of helping the material points make the necessary calculations to achieve the solution (Bardenhagen & Kober, 2004). As said before interpolation and extrapolation between the grid and the material points are made by means of shape functions. The type of shape functions used so far has been four node quadrangular elements.

A structured grid was used because of its great ease to locate the material points. In the MPM, the material points (so called particles in the following) are supposed to contribute to the four nodes surrounding it, in the 2D case. In this case, by using the actual position of the material point and by the use of equation (1), it is possible to locate a reference node to which the four

corresponding nodes are linked. This prevents us from looping over the nodes that are not related to the current position of the material point (Buzzi et al., 2008).

$$n_p^* = trunc\left(\frac{x_p - x_{min}}{\Delta x}\right) + trunc\left(\frac{y_p - y_{min}}{\Delta y}\right) N_x \quad (1)$$

Here, x_{min} and y_{min} refer to the minimum grid nodes coordinates, x_p and y_p are the position coordinates of the material point, N_x is the number of nodes in the x direction, and Δx and Δy are the regular spacing of nodes in the x and y direction respectively. Once located, corresponding shape functions related to the current material point are calculated, to then carry out the extrapolation.

Computing strain by means of velocity

Once the interpolation of mass and momentum from material points to the grid nodes has been done, or in other terms, the grid has been initialized, we proceed with the calculation of the strain in the material points using the velocities in the nodes by means of a volume weighted average over each particle. In equation form it reads:

$$\Delta\varepsilon_p = \Delta t \sum_n \frac{1}{2}\left(v_n \otimes G_{np} + G_{np} \otimes v_n\right) \quad where\ G_{np}\ is\ {}^{dN_n}/_{dp} \quad (2)$$

The corresponding stresses are computed according to an appropriate constitutive relation.

Constitutive Equation

In order to represent the mechanical behavior of the continuum, plane strain and plane stress elasticity were used as means of representing the initial (elastic) behavior of the continuum. After imposing an appropriate yield criterion, the model was able to reproduce the expected plastic behavior.

In the code, Von Mises criterion was used in order to make a first approach to plastic behavior. A Mohr-Coulomb criterion was then used to model in a more reasonable way the plastic behavior of geomaterials such as rocks and soils. In order to make plasticity computations, we need to take into account the following fundamental concepts: yield criterion, the flow rule describing the relationship between stresses and strains once the material has gone plastic, and the consistency condition which prevents stresses from exceeding the yield limit (Krabbenhøft, 2002).

In computational plasticity, the procedure undertaken consists in applying small load increments (in order to approach in a very cautious manner to the yield surface) and therefore obtaining respective strain increments. At some point during the load increment, the stress state will be outside of the yield surface. As it was mentioned before, this region is inadmissible and thus we need to find out solutions to make it return to the surface. Various ways exist to deal with this type of problem. One of the most common, the return algorithm, was used in the model to make the correction.

The Von Mises Criterion is one of the criteria used so far in the code in order to predict plastic behavior. It uses the return algorithm explained above to ensure stresses are always inside the yield surface. This criterion assumes that yield occurs once the second invariant of the deviatoric stress J_2 reaches a critical value (Jaeger et al., 2009). This yield surface doesn't vary along the principal stress space diagonal. This is a valid assumption for metals, but in the case of geomaterials, where the yield stress increases with increasing normal stress, is not valid.

The Mohr-Coulomb criterion was therefore chosen as a suitable criterion to model in a more realistic way the behavior of rocks since it takes into account that the yield stress increases when the normal stress is increased. In our case, this criterion is an appropriate first approach to model the mechanical behavior of landslides. It must be noted that the return algorithm explained above is also used to fulfill the yield condition, and in this case since the Mohr-Coulomb criterion is linear, only one step is necessary to return if the plastic potential is also linear. Given the fact that the Mohr-Coulomb criterion has certain regions such as intersections between planes which create lines or even points, care was taken in order to return to the appropriate region on the yield surface following the method proposed by Clausen et al. (2007).
Linear yield criteria in principal stresses are visualized as planes in principal stress state. These planes intersect in lines and point, thus giving three possible types of stress return:

- Return to a yield plane.
- Return to a line when two yield planes intersect.
- Return to a point when three or more yield planes intersect.

Forces

Three types of forces are computed in the algorithm. First, we calculate the internal forces, which are obtained from the stresses using the following equation:

$$\Delta f_n^i = \sum_p V_p \sigma_p \cdot G_{pn} \tag{3}$$

Where V_p refers to the volume discretized in each material point.
Then we proceed to calculate the external forces, or body forces, as follows:

$$\Delta f_n^e = \sum_p m_p b_p S_{pn} \tag{4}$$

And finally, we proceed to compute the forces related to the boundary conditions in both the normal and tangential direction.
In the case of the boundary conditions, various solutions can be found in the literature. At first, the algorithm would manage the boundary conditions by initially setting to zero the values of momentum once the grid point belonging to the boundary was reached. That is, as soon as it was part of the grid points that were used in the interpolation. The same procedure of zeroing was used for the rate of momentum. Since the material point uses the four grid points around it to complete its necessary calculations, some problems regarding contact arose. The grid point would not allow the material point to go any further and thus, it would model the contact before it actually happened.

A second procedure borrowed from the discrete element method (DEM) (Banton et al., 2009) was used. In this procedure the boundary is modeled as a reacting normal force following an elastic law. It has two different stiffness values depending on whether the material point contact is loading or unloading (Figure 1). The value of the normal force will also depend on how much overlap is achieved. This is clearly related to the time step value. The two equations modeling the boundary (Richefeu et al. , 2012) are:

$$\Delta f_n = \begin{cases} k_n^+ \Delta h_n \cdot n & if\ \dot{h}_n > 0 \\ k_n^- \Delta h_n \cdot n & otherwise \end{cases} \tag{5}$$

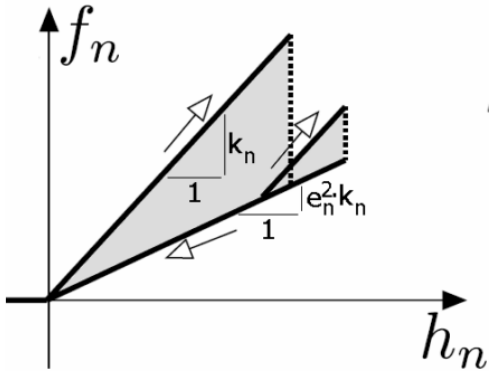

Figure 1: Normal force-displacement relation (Mollon et al., 2011)

Where k_n^+, k_n^- and h_n are the loading stiffness coefficient, the unloading stiffness coefficient and the overlap respectively.

Given the fact that two different stiffness coefficients are taken into account, a minimalistic dissipation method is easily introduced by reducing the value of k_n^-. In that case, it's possible to find the dissipation rate in the normal direction as:

$$e_n^2 = \frac{k_n^-}{k_n^+} \tag{6}$$

In the case of tangential direction an incremental law was also applied. Borrowing the friction law (Richefeu et al., 2012), where a force f_t is applied in the tangent direction opposite to the sliding direction, the friction force is incrementally updated by use of the relative tangential displacement Δh_t in the sliding direction. A maximum value for the tangential force is set by using the coefficient of friction and the normal force (Figure 2). The equations governing friction are:

$$f_t = min\left\{ \sum_{t_0}^{t} k_t \Delta h_t \, ; \, \mu f_n \right\} \tag{7}$$

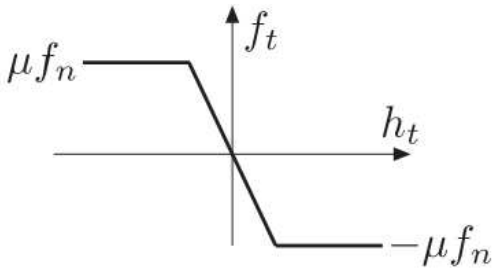

Figure 2: Tangential force-displacement relation (Richefeu et al., 2012)

Momentum

Once all the forces affecting the system have been calculated, taking into account that the forces related to the boundary condition belong to the external forces, we proceed to find the rate of momentum in each node as:

$$\dot{\boldsymbol{q}}_n = \boldsymbol{f}_n^e - \boldsymbol{f}_n^i \tag{8}$$

Once it has been found, it is possible to integrate it and thus find the respective increment of momentum as follows:

$$\Delta \boldsymbol{q}_n = \dot{\boldsymbol{q}}_n \Delta \boldsymbol{t} \tag{9}$$

Position and Velocity Update

After having done all the previous steps, and having found the momentum in the nodes for the current step, it is possible to finally update the positions and velocities of the material points. In order to achieve that, we must extrapolate back the solution of momentum and rate of momentum back to the material points. We use the weighted approach using shape functions as explained earlier:

$$\Delta \boldsymbol{x}_p = \Delta \boldsymbol{t} \sum_n \frac{\boldsymbol{S}_{np} \boldsymbol{q}_n}{\boldsymbol{m}_n} \tag{10}$$

$$\Delta \boldsymbol{v}_p = \Delta \boldsymbol{t} \sum_n \frac{\boldsymbol{S}_{np} \dot{\boldsymbol{q}}_n}{\boldsymbol{m}_n} \tag{11}$$

Visualization

Since we discretize the continuum into material points, which in the end is what carries the position and velocity among other relevant information, it is then appropriate to represent each one of these points as the volume it discretized. By doing this, it is possible to see the continuum rather than points interacting with each other.

In order to achieve this, we make use of the deformation gradient tensor, related to each particle, on each one of the corners of the discretized volume. This deformation gradient tensor is easily found since velocities are computed at each step. The procedure is explained in Andersen & Andersen (2012). An extra element added in order to improve visualization is called splitting. This technique refers to splitting the elements belonging to a particular material point into two, once any value of its deformation gradient tensor achieves a large value. With the use of this technique, resolution of the continuum is improved, also avoiding badly deformed (needle-shaped) elements.

RESULTS

Collapsing Soil Column

The first set of results was obtained once the model was able to make plastic computations using the Mohr-Coulomb criterion. It was then possible to make a first validation by comparing our results with those obtained by Andersen & Andersen (2009). Our simulation is shown on the left, while Andersen's is on the right.

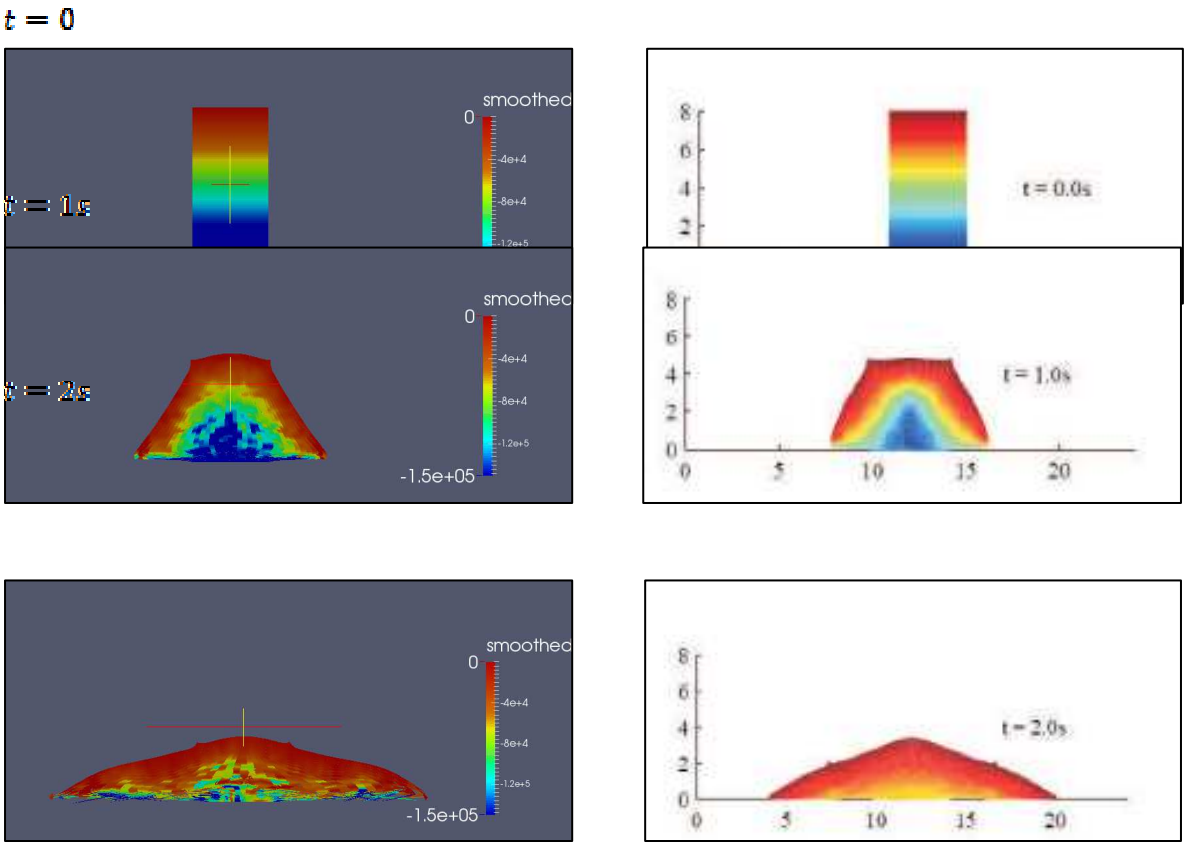

Block of soil with elastic wall

The second test performed by the code was a block of soil simulating a very instable mass, next to a very rigid wall in this case being the boundary condition. An elastic block recreating in a very simple manner a retaining wall has been put in order to see the way it affects the flowing mass. The magnitude of the velocity vector is shown in the simulation in m/s.

$t = 0.0$

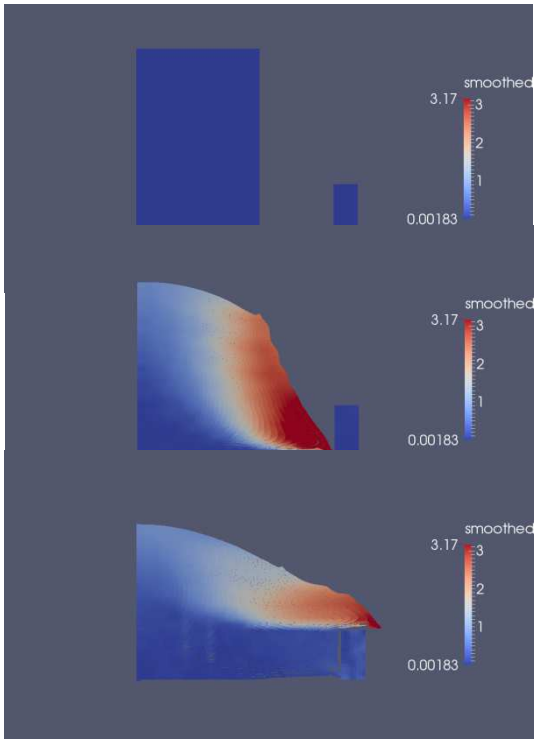

$t = 0.5$

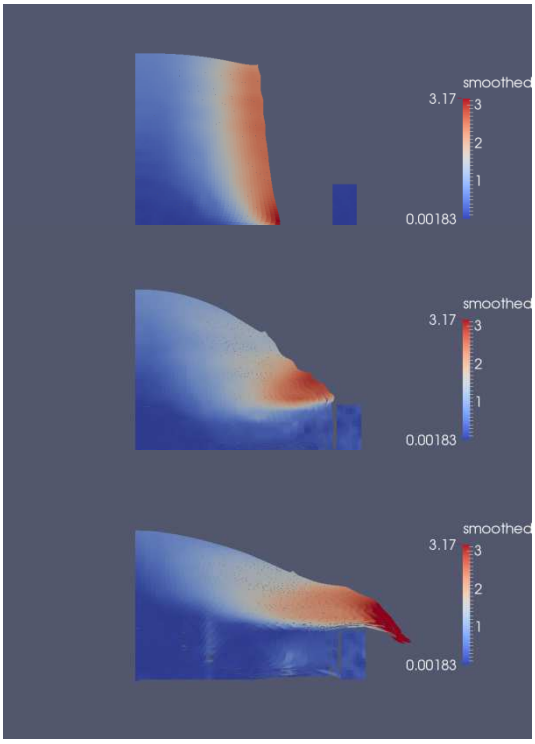

Block of soil on slope

In this last test performed, a block of soil following the Mohr-Coulomb criterion is put in a slope in order to make our first approach to a landslide modeling. In this case, is must be noted that an irregular grid is used in order to model the slope. It must also be taken into account that a second grid was included in this case, showing that the possibilities are endless in terms of mesh shape.

This first approach to landslides on slopes has not been validated yet, but shows very promising results, since the results show an expected behavior of the mass.

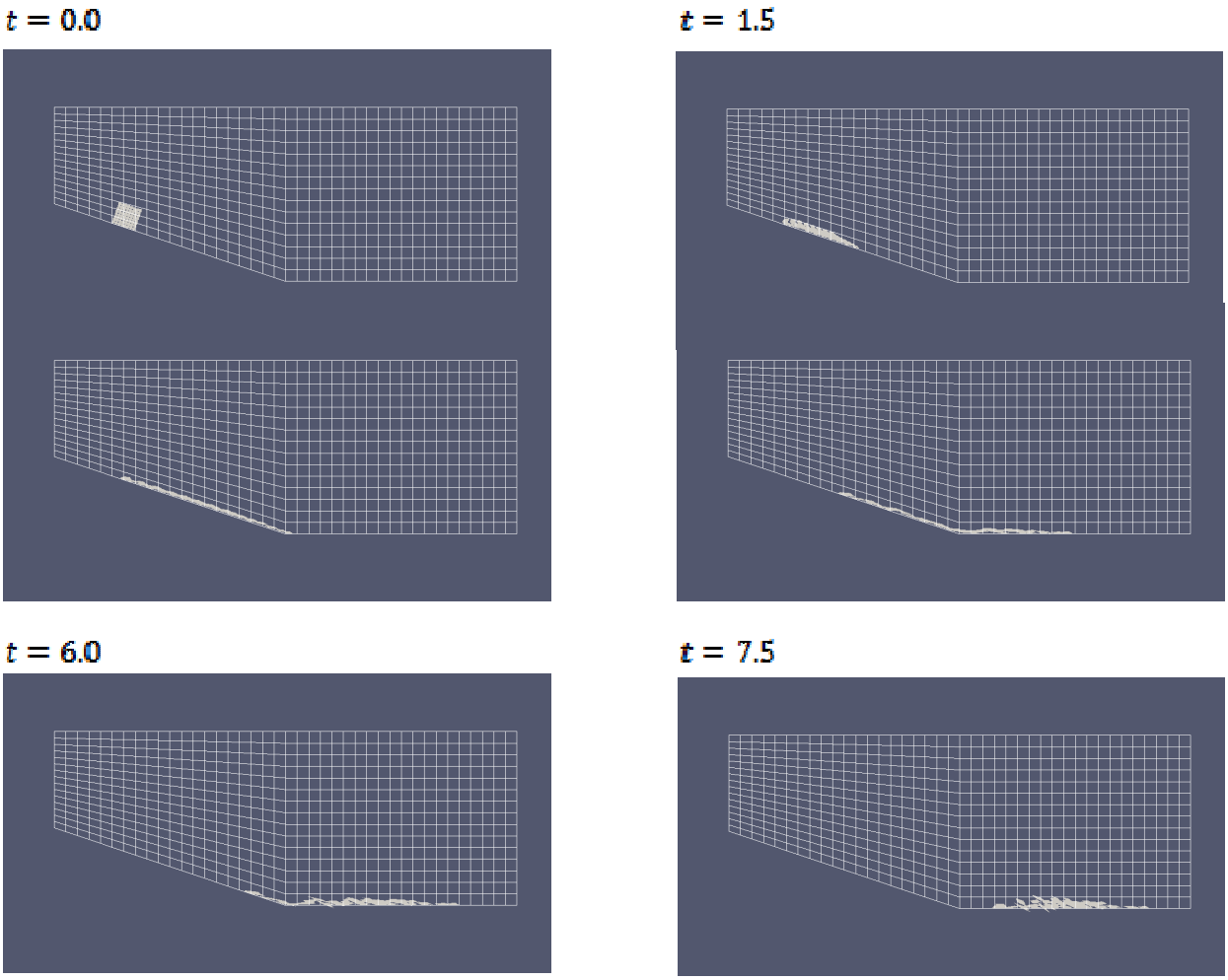

PERSPECTIVES

Since the code is still being developed, there is room for improvement. Improvements to be developed include constitutive laws for dynamic flow of geomaterials. It is a major improvement since the current constitutive law being used for geomaterials is Mohr-Coulomb. It is able to model quasi-static flows, but it is definitely not the best approach for dynamic flow. Another major improvement currently under development is the introduction of 3D. With the introduction of 3D models, it will be possible to make much more appropriate simulations, as well as to compare with current DEM models. This will allow us to validate our code as well as to see how big the influence of the parameters is in order to have similar types of simulations.

One important objective is the possibility to calculate slope stability slopes reinforced with piles. Currently the interaction between piles and moving soil is not very well known, leading to overdimensioning in some cases. The determination of stress solicitations acting on piles will allow a better dimensioning of piles, which is currently done empirically in most cases.

As for some other improvements, different types of contact laws shall be introduced. Current developments in discrete models will be used to justify those that will be used in our continuous model. Also, different types of constitutive relations such as viscoelasticity and

viscoplasticity, among others, will be introduced, giving us the possibility to model new behaviors.

CONCLUSIONS

The Material Point Method has proved useful in order to model continuum media subjected to large deformations. It reduces drastically the calculation time when compared with the Discrete Element Method. Some of the results obtained were validated using results presented by other authors. Stresses and positions were very similar which gives us some confidence about the model. Other results are presented, showing a behavior that is to be expected in the modeling of landslides. Within the model it must be noted that different types of dissipation methods exist such as friction with the surface, normal force exerted by the boundary, and plasticity. The fact that the friction between blocks is controlled by a constant parameter in DEM, and not by a yield surface as is the case in MPM, can surely yield different types of dissipation in both methods. This is something to look into once comparisons between MPM and DEM simulations take place.

REFERENCES

Andersen, S., & Andersen, L. (2009). Analysis of Stress Updates in the Material-point Method. *The Nordic Seminar on Computational Mechanics*, (11), 129–134.

Andersen, S., & Andersen, L. (2012). Post-Processing in the Material-Point Method.

Banton, J., Villard, P., Jongmans, D., & Scavia, C. (2009). Two-dimensional discrete element models of debris avalanches: Parameterization and the reproducibility of experimental results. *Journal of Geophysical Research*, *114*(F4), F04013. doi:10.1029/2008JF001161

Bardenhagen, S., & Kober, E. (2004). The generalized interpolation material point method. *CMES- Computer Modeling in Engineering & Sciences*, *5*(6), 477–495.

Buzzi, O., Pedroso, D. M., & Giacomini, A. (2008). Caveats on the Implementation of the Generalized Material Point Method, *1*(1), 1–21.

Clausen, J., Damkilde, L., & Andersen, L. (2007). An efficient return algorithm for non-associated plasticity with linear yield criteria in principal stress space. *Computers & Structures*, *85*(23-24), 1795–1807. doi:10.1016/j.compstruc.2007.04.002

Jaeger, J., Cook, N., & Zimmerman, R. (2009). *Fundamentals of rock mechanics*. *Vasa*.

Krabbenhøft, K. (2002). Basic Computational Plasticity. *Lecture Notes*, (June).

Richefeu, V., Mollon, G., Daudon, D., & Villard, P. (2012). Dissipative contacts and realistic block shapes for modeling rock avalanches. *Engineering Geology*, *149-150*(2012), 78–92. doi:10.1016/j.enggeo.2012.07.021

Sulsky, D., Chen, Z., & Schreyer, H. (1994). A particle method for history-dependent materials. *Computer Methods in Applied Mechanics and Engineering*, (June 1993). Retrieved from http://www.sciencedirect.com/science/article/pii/0045782594901120

Part Five: YADE special

Yade-DEM: (not so) recent advances and steps toward multiphase couplings

B. Chareyre
Univ. Grenoble Alpes, 3SR, F-38000Grenoble, France
CNRS, 3SR, F-38000Grenoble, France
bruno.chareyre[A]3sr-grenoble.fr

ABSTRACT

The paper offers a partial overview of what happened to the Yade-DEM code since the last reports of the "Discrete Element group" of Grenoble (2008). The project has matured considerably. It is now truly international. It has a stable codebase and a large community of users. It provides a rich toolbox for discrete element modeling, applied by researchers in different fields of science. The code has proved to be a robust and flexible foundation for developing innovative numerical methods. It is being extended continuously, in various ways and by different research groups. Some recent developments done at 3SR lab. are outlined, especially those in relation with micro-scale simulations of multiphase problems.

1. INTRODUCTION

Prof. Frédéric Victor Donzé was organizing annual reports of the "Discrete Element Group for Hazard Mitigation" from 2004 to 2008[9]. These reports were good places to discuss not only results obtained with the discrete element method (DEM) but also progresses of the open-source code Yade (dedicated to DEM, and initiated under the supervision F. Donzé). The present annual report is in a sense a descendant of those annual reports, now reflecting the activities of a larger group – for good. It is an ideal opportunity for another progress report regarding Yade. It will partly and quickly fill gaps between 2008 and now (section 2). Some features and perspectives of Yade in the present state will be discussed (section 3). The last part is more focused on the research of the author, it provides a synthetic view of the solid-fluid coupling models developed in the last years (section 4).

2. SHORT HISTORY

The project of an open-source code for DEM has been initiated by F.V. Donzé for two main reasons:

[9] http://people.3sr-grenoble.fr/users/fdonze/Discrete_Element_Group_FVD.html

- an increasing demand for developing (that is, not only “using”) new DEM models, but
- a very limited support locally for developing and maintaining computer codes.

Hence, the idea of stopping Donze's in-house code “SDEC” and to start a more ambitious project which could gather more manpower from different research institutions. Surely, one has to be as optimistic as Frédéric to believe that such an idea has more than a 1% chance of success. Retrospectively, it sounds like a message in a thrown away bottle. Even worst, the actual message in the bottle was “look, my project is ambitious but there is no manpower. Come join us, there is a lot of work and no immediate results expected”. After all, 98% of the open-source projects are dead after one year on Github[10] (not counting those projects which never even reach any public repository). It was very likely to fail. Apparently it did not. There may be rational factors to explain that. Namely, “Open-source projects flourish when developers are also users of the software“[11], yet a good part of luck is not to be excluded.

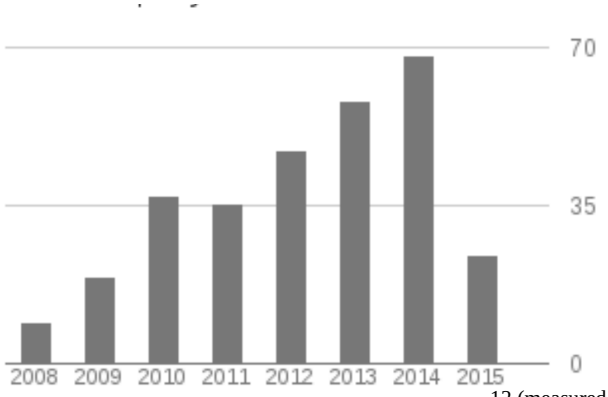

Figure 1. Citations per year in scientific papers[12] (measured 02/2015) .

Lines of code	74,384
Languages	C++ 62%, Python 34%, other 4%
License	GPL-2.0
Commits	4752
Contributors	42
Cost estimate (basic COCOMO Model[13])	18 person-years, $1,006,365

Table 1. Facts and figures (January 2015)

Olivier Galizzi and Janek Koziciki started the project from scratch in 2004. Galizzi commited the first versioned code in january 2005[14] and left the project (and his PhD work) one year

[10] http://redmonk.com/dberkholz/2014/05/02/github-language-trends-and-the-fragmenting-landscape/#ixzz30wEgsUif
[11] http://www.pbs.org/idealab/2013/08/6-things-to-know-about-successful-open-source-software
[12] http://scholar.google.fr/citations?user=hZB8GGcAAAAJ&hl=en
[13] http://en.wikipedia.org/wiki/COCOMO

later. In 2006 some key ideas of the design were already firmly established (as found in Kozicki and Donzé 2009), but Yade was still far from a ready-to-use software. The main deficiencies were reported by Smilauer (2006). Smilauer's paper was in fact announcing the main steps that were effectively taken in the next four years, mainly by Smilauer himself or under his expert guidance (two of them appear in section 3). This evolution came through an almost complete refactoring of the code, which was already quite large and growing at that time. Conducting the infrastructural changes without breaking the superstructure (i.e. mechanical models) needed considerable time and efforts. It did not happen without significant removal (or *cleaning*) of less used or unmaintained parts of the program, occasionally triggering hot debates between the developers. Two years after this big plan had been set up, the deep changes were only starting to reach that part of the iceberg visible to ordinary humans, as suggested by the title of the real last paper about Yade from the Discrete Element Group (Duriez 2008).

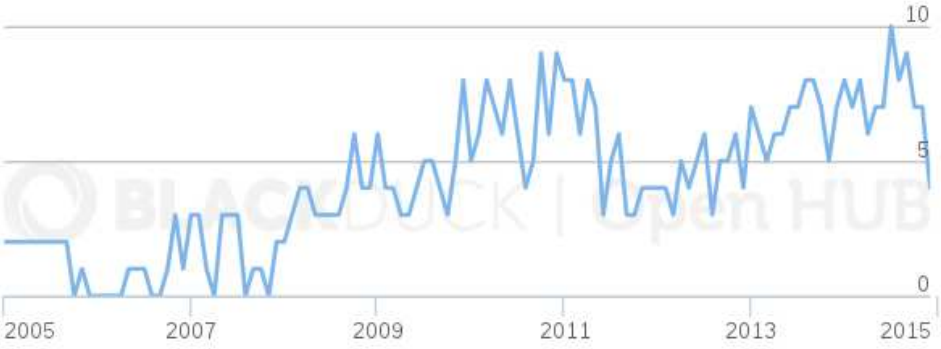

Figure 2. Number of contributors to the source code per month (after BlackDuck OpenHUB[15])

It needed another two years - or almost - to consolidate them and to make them really useful for the average user. In the meantime, another major step had been prepared by Anton Gladky (TU Freiberg): packaging. In other words: integrating the code in standard linux distributions in the form of binary libraries. It enabled running DEM simulations without the need to compile the code. Yade thus became one of those softwares that one finds on the shelf after installing a linux system. It made using Yade even easier, and it helped to keep compatibility with ever-changing operating systems (keeping compatibility is still a serious amount of work, tackled efficiently by Gladky until now).
While all this was happening, researchers[16] where still working on physics models and post-processing methods, enabling progressively the simulation of a large variety of situations. The advances on both sides led a growing audience to adopt Yade for DEM simulations in research. This is assessed by the increasing number of citations per year (fig. 1, mainly cited by papers reporting works done with Yade). The number of developers has been also growing steadily (fig. 2).
In late 2011, Šmilauer started the project Woo-DEM (initially a fork of Yade-DEM) in relation with consulting activities in DEM[17]. The author has been coordinating the Yade project since then.

[14] http://bazaar.launchpad.net/~yade-pkg/yade/git-trunk/files/1
[15] https://www.openhub.net/p/yade
[16] Including the author and students he was supervizing
[17] http://woodem.eu/

3. SOME CHANGES BETWEEN 2009 AND 2015

In this part some important changes since 2009 are commented. More details can be found in the PhD thesis of Šmilauer (2010) or in Yade's documentation (Šmilauer et al. 2010, based on the PhD thesis for a large part).

3.1. BYE BYE I/O FILES, HELLO INTERACTIVE PROGRAMMING

Many computer codes for numerical simulation in physics are based on input data files, first read by a pre-processor or directly by a solver running the mathematical steps. In turns, the solver will write the results in output files (long lists of numbers, typically). Eventually, a post-processor would be used to convert the output files to graphical representations. Yade pre-2010 was not an exception to this good old “I/O files” paradigm (Duriez 2008). The average user had to code a simulation scenario in a C++ class (inheriting form the generic *PreProcessor* class), recompile the code, then run simulations with this pre-processor. It was possible to change some input parameters of the simulation without recompiling (through input files or graphical interfaces), but every pre-processor would run the same scenario forever. A graphical user interface (GUI) was giving the feeling of interactivity, but practically it was only providing to the user the option of time-stepping forward or not (fig. 3). A consequence of this workflow was that one had to be able to write some C++ code and compile it before performing any DEM simulation. This is way above the standard requirements for doing a PhD in physics and mechanics. Moreover - as for every software rooted in the I/O files approach - defining complex situations with different loading steps and conditional transitions between them was tedious if not impossible.

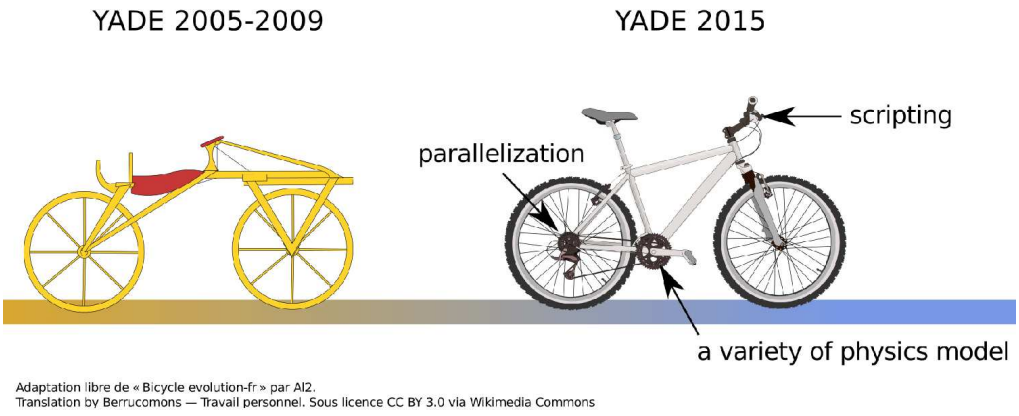

Figure 3. A simplified view of the evolution of Yade over the years.

Integrating the Python language in Yade for commanding and scripting (de facto turning Yade into a Python module) changed this picture completely. It was maybe the most brilliant step taken by Šmilauer. Nowadays, Python is to Yade what Matlab™ is to Comsol Multiphysics™: a powerful programming language with a large set of mathematical and graphical libraries, commanding a more specialized solver interactively. A user can play with particles, add/delete

them, change the velocity of an object or a boundary condition, and get an immediate feedback. Graphical representations of the results through dynamic graphs, 3D views or color maps can be generated on the fly. It thus enables true *numerical experiments*, an invaluable method for prototyping numerical models and, simply, for understanding complex mechanical systems. The users need only a basic knowledge in Python programming, which is much less demanding than C++ and does not require compilation[18]. Looking backward gives the feeling that the old PreProcessor class[19] was implying the same level of awkwardness than recompiling Comsol Mutliphysics for solving a different boundary value problem with FEM.

3.2. COUPLING CODES

Interactive programming is not the sole advantage of the Python interface. Another one is that it enables the efficient resolution of coupled problems using partitioned schemes, by combining specialized solvers. Using state-of-the-art solvers developed independently is indeed becoming a method choice in computer simulations. It does not require one to re-implement everything in a single all-singing-all-dancing code (which would result, typically, in sub-optimal versions of every part and unmaintainable framework in the long run with limited manpower). In this context a communication between the codes is required., but the naive approach of communicating through data files is to be avoided. It would be an efficient performance killer (as well as a hard-drive killer). With a higher level command language such as Python, data exchanges can go through live memory easily. Exchanges are even avoided sometimes, when the same memory can be shared by multiple codes. This method can combine programs written in different languages without problems, Fortran, C and C++ typically.Practical examples of code couplings using Yade (fig. 4) include multi-domain and multi-scale DEM-FEM couplings (Stránský and Jirásek 2012, Guo and Zhao 2014), DEM-CFD coupling based on Open Foam (Chen et al. 2011) or in-house fluid model (Maurin et al. 2013), DEM-DNS coupling (Yade-Yales2[20], currently implemented by Deepak Kunhappan[21]). A general coupling framework has been proposed by Jan Stránský (Stránský 2014).

[18]Python scripts are actually compiled, but it is hidden away from the user.
[19]The PreProcessor class is in fact still present in the code and ready to be used, but nobody used it in the recent years.
[20]http://www.coria-cfd.fr/index.php/YALES2
[21]PhD of Univ. Grenoble Alpes, "Numerical modelling of the mechanical behaviour of cellulose fibers in a fluid flow" , work in progress.

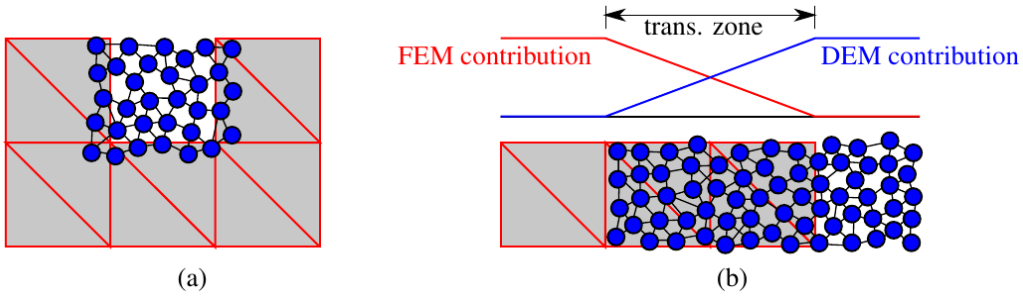

(a) (b)

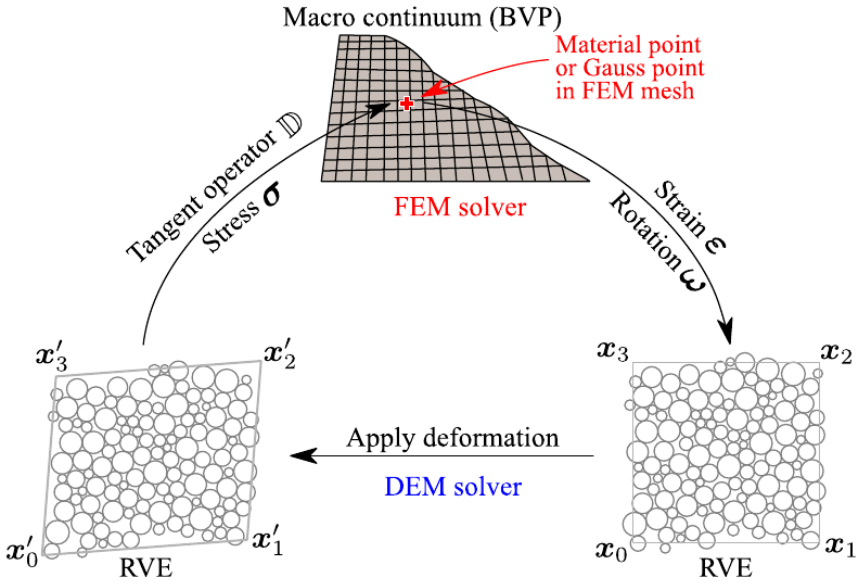

(c)

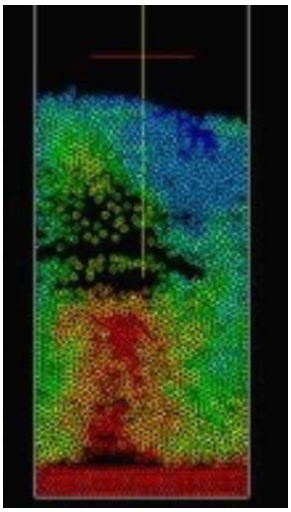

(d)

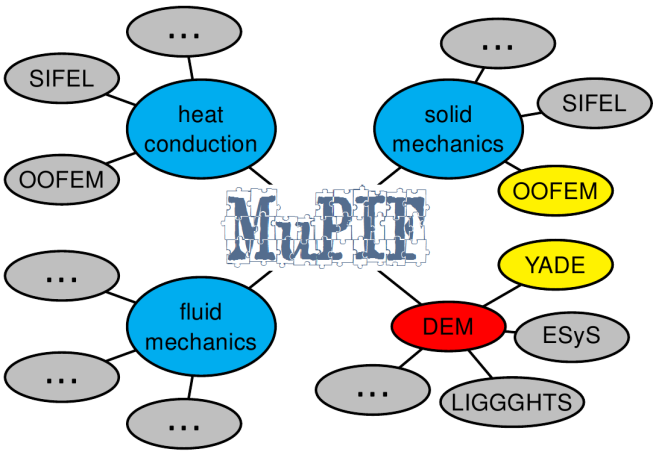

(e)

Figure 4. Examples of code couplings. (a) and (b) multidomain FEM-DEM (Stransky 2012), (c) multiscale FEM-DEM (Guo 2014), (d) DEM-CFD (Chen 2011, fluidized bed), (e) a general framework (Stransky 2014).

3.3. PARALLELIZATION

Parallelization and performance have been subjects of continuous brainstorming over the years (Šmilauer 2007, Jakob 2012, Thoeni 2013, Eulitz 2014, Chareyre 2014, Smilauer 2014) even though flexibility has been the primary objective of the design. Šmilauer accomplished the shared memory parallelization of important loops (mainly contacts update and newton integration) using OpenMP. After parallelization of the last non-parallel section (collision detection[22]) by the author, the code was fully OpenMP parallelized. The shared memory approach was, of all possible strategies, the easiest to implement. It can improve the performances by factors up to 7 or 8 for typical large problems on multicore systems (Eulitz 2014). It does not benefit further from large clusters though. This is probably where Yade under-performs some of the other DEM codes[23]. One cure is known: domain decomposition for taking advantage of distributed memory systems (MPI), possibly nesting OpenMP parallelism. Clearly, the lack of manpower is the reason why it did not happen yet. Besides, experiments on many-core computers are still to be performed (Intel's Xeon-Phi co-processors) ; again the man-hours involved in the compilation and the tuning/benchmarking steps is the limiting factor.

4. MULTIPHASE PROBLEMS AT THE MICROSCALE

Numerical models of multiphase granular materials can be obtained by coupling a DEM code with other codes dedicated to fluid dynamics (see section 3.2). This is of course only possible when coupling relatively conventional methods, for which computer codes are available (mainly FEM, CFD, SPH, LBM). When developping less conventional methods and/or couplings, one has – of course – to implement it. The development framework of Yade-DEM has prooved to be an efficient basis for such task. Of course, it provides a ready-to-use DEM library, but it also favors efficient programming through python binding (with a support framework including a set of C++ macro for binding), and inline documentation. Among others, the author pushed developments of this kind, and they are now available as part of Yade.

4.1. ONE PHASE FLOW AT THE PORE SCALE (DEM-PFV)

The pore-scale approach of fluid flow in porous media (the so-called *pore-network* modeling) has been applied to sphere packings and extended to deformable media (Chareyre et al. 2012, Catalano et al. 2014). The numerical scheme – called DEM-PFV – is formaly a special case of ALE methods, where the mesh of the fluid problem follows the movements of the solid particles. Mathematicaly, the problem to be solved is a discrete analog of the coupled equations of poromechanics. Initially written for strictly incompressible fluids, it has been later extended to compressible flow for applications to seabed sediments (Scholtès et al. 2015). A rheological property of saturated materials which does not result simply from the equations of poromechanics is the bulk viscosity. Donia Marzougui showed that this property can be recovered by complementing the poromechanical coupling with short range lubrication forces (Marzougui et al. 2015a/2015b). These developements are done in cooperation with the MEIGE group at lab. LEGI. They are fully integrated in Yade-DEM thus providing a unique

[22] https://yade-dem.org/wiki/Colliders_performace

[23] such as Esys (https://launchpad.net/esys-particle), though no direct benchmarks comparing the two codes are available – unfortunately

tool for applications to various coupled processes (see also Papachristos et al. 2015, and in this volume Toraldo et al. 2015, Tejada et al. 2015, Albaba et al. 2015, Aboul Hosn et al. 2015).

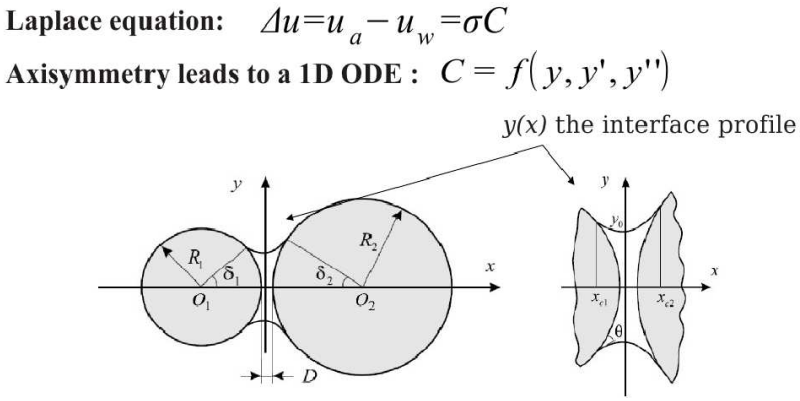

Figure 6. The pendular bridge between two spherical particles.

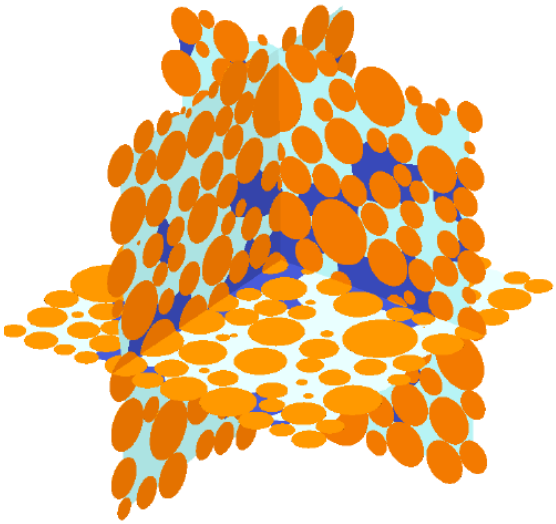

Figure 7. Trapped wetting phase at the end of a simulated drainage (Yuan et al. 2014).

4.2. TWO PHASE PROBLEMS

There has been a number of applications of the DEM to unsaturated materials in the pendular regime in recent years, following Jiang et al. 2004 (2D) and Richefeu et al. 2006 (3D) (see a comparison of various models in Gladkyy and Rüdiger (2014)). The first implementation in Yade is due to Luc Scholtès (Scholtès et al. 2009). An enriched version of this model is being implemented by Caroline Chalak for an accurate determination of interfacial areas (Chalak et al. 2014, Chalak et al. 2015 – in this volume).

The pendular regime is the only case in in which a semi-analytical treatment of Young-Laplace equation is tracktable (fig. 6). In order to approach the full range of saturation, including dynamic regimes in two phase flow, recent developments aims at generalizing the DEM-PFV method for two phases (Yuan et al. 2014, Sweijen et al. 2014, see fig. 7), with

local jump conditions between phases during drainage/imbibition events. This a challenging problem, and there is still quite a lot of brainstorming ahead of us. Fortunately, we can count on close cooperations with acknowledged experts at Univ. of Utrecht (Majid S. Hassanizadeh and Ehsan Nikooee / Hydrology Group), advanced experimental techniques there and locally at 3SR (Kaddhour et al. 2013), and through Yade the perfect numerical platform for implementation and dissemination. No excuse to not progress.

ACKNOWLEDGEMENTS

The author wants to thank past and present developers of Yade-DEM for their invaluable contributions, enthusiasm, and professional commitment to provide an efficient tool for DEMing in research and industry, and the Yade community as a whole for feedback, questions, and discussions on the mailing lists yade-users@lists.launchpad.net and yade-dev@lists.launchpad.net. Project hosting by Launchpad and GitHub is greatly appreciated, as well as technical support by Rémi Cailletaud (3SR, Grenoble). Let us not forget the developers of the many third-party libraries used by Yade.
The author wants to acknowledge the support of Grenoble INP for starting the research on hydromechanical coupling (BQR 2008 – PhD of E. Catalano), of the ministry of Ecology Sustainable Development and Energy through project “Hydrofond” (C2D2 program / RGCU), and of the ITN Mumolade (EC FP7).

REFERENCES

Aboul Hosn, R. Sibille, L. Chareyre, B. Benhamed N. (2015), Description of the mechanical degradation of soils subjected to an internal erosion process by suffusion, Geomechanics group annual report.

Albaba, A. Lambert, S. Nicot, F. Chareyre, B. (2015), DEM simulation of dry granular flow impacting a rigid wall, Geomechanics group annual report.

Catalano, E., Chareyre, B., Barthélémy, E. (2014), Pore-scale modeling of fluid-particles interaction and emerging poromechanical effects. International Journal for Numerical and Analytical Methods in Geomechanics (38), pages 51–71.

Chalak, C., Chareyre, B., Nikooee, E., Hassanizadeh, M., & Darve, F. (2014) DEM Simulations of Unsaturated Soils Interpreted in Thermodynamic Framework. In *ALERT Geomaterials Workshop*, p.11.

Chalak, C., Chareyre, B., Darve, F. (2015), DEM simulations of unsaturated soils interpreted in a thermodynamic framework., Geomechanics group annual report.

Chareyre, B. (2014). What happened to the insertion sort collider? *in Booklet of the 1st YADE Workshop*, Grenoble, 2014.

Chareyre, B., Cortis, A., Catalano, E., Barthélemy, E. (2012), Pore-scale modeling of viscous flow and induced forces in dense sphere packings. Transport in Porous Media (92), pages 473-493.

Chen, F., Drumm, E., Guiochon G. (2011), Coupled discrete element and finite volume solution of two classical soil mechanics problems. Computers and Geotechnics. DOI 10.1016/j.compgeo.2011.03.009

Duriez, J. (2008), Yade for the non-geeks, in Annual Report of Discrete Element Group for Hazard Mitigation.

Eulitz, A. (2014). Performance benchmarking in Yade. *in Booklet of the 1st YADE Workshop*, Grenoble, 2014.

Gladkyy, A., Schwarze, R. (2014), Comparison of different capillary bridge models for application in the discrete element method. Granular Matter, 16(6), 911-920.

Guo, N., & Zhao, J. (2014). A coupled FEM/DEM approach for hierarchical multiscale modelling of granular media. *International Journal for Numerical Methods in Engineering*, *99*(11), 789-818.

Jakob, C. (2012). *Comparison with PFC3D*, online content on the Yade-DEM website. https://yade-dem.org/wiki/Comparisons_with_PFC3D

Jiang, M. J., Leroueil, S., & Konrad, J. M. (2004). Insight into shear strength functions of unsaturated granulates by DEM analyses. Computers and Geotechnics, 31(6), 473-489.

Kaddhour, G., Andò, E., Salager, S., Bésuelle, P., Viggiani, C., Hall, S., & Desrues, J. (2013). Application of X-ray Tomography to the Characterisation of Grain-Scale Mechanisms in Sand. In Multiphysical Testing of Soils and Shales (pp. 195-200). Springer Berlin Heidelberg.

Kozicki, J., Donzé, F.V. (2009), Yade-open dem: an open-source software using a discrete element method to simulate granular material. Engineering Computations (26), pages 786–805.

Marzougui, D., Chareyre, B., Chauchat, J. (2015b), Numerical simulations of dense suspensions rheology using a DEM-Fluid coupled model, Geomechanics group annual report.

Marzougui, D., Chareyre, B., Chauchat, J. (2015a), Microscopic origin of shear stress in dense fluid-grain mixtures, Granular Matter (to appear).

Maurin, R., Chareyre, B., Chauchat, J., & Frey, P. (2013). Discrete element modelling of bedload transport. In *Two-pHase modElling for Sediment dynamIcs in Geophysical Flows* (pp. 6-p).

Papachristos, E., Scholtès, L., Donzé, F.-V., Chareyre, B. Pourpak, H. Hydraulic fracturation simulated by a 3D coupled HM-DEM model. (2015 - to appear) in *13th International ISRM Congress 2015*, 10 pages.

Richefeu, V., El Youssoufi, M. S., & Radjai, F. (2006). Shear strength properties of wet granular materials. *Physical Review E*, *73*(5), 051304.

Scholtès, L., Chareyre, B., Michallet, H., Catalano, E., Marzougui, D. (2015), Modeling wave-induced pore pressure and effective stress in a granular seabed. Continuum Mechanics and Thermodynamics (27), pages 305–323.

Scholtès, L., Chareyre, B., Nicot, F., Darve, F. (2009), Micromechanics of granular materials with capillary effects. International Journal of Engineering Science (47), pages 64–75.

Stránský, J. (2014). OPEN SOURCE DEM-FEM COUPLING. *in Booklet of the 1st YADE Workshop*, Grenoble, 2014.

Stránský, J., Jirásek, M. (2012). OPEN SOURCE FEM-DEM COUPLING. in Proc. 18th Int. Conf. Engineering Mechanics, Pragues, 2012, pp. 1237-1251.

Šmilauer, V. (2007), The splendors and miseries of yade design. in Annual Report of Discrete Element Group for Hazard Mitigation.

Šmilauer, V. (2014). DEM on GPU. *in Booklet of the 1st YADE Workshop*, Grenoble, 2014.

Šmilauer, V. (2010), Cohesive particle model using the discrete element method on the yade platform. PhD thesis at Czech Technical University in Prague, Faculty of Civil Engineering & Université Grenoble I – Joseph Fourier, École doctorale I-MEP2.

Šmilauer, V. Catalano, E. Chareyre, B. Dorofeenko, S. Duriez, J. Gladky, A. Kozicki, J. Modenese, C. Scholtès, L. Sibille, L. Stránský, J. Thoeni K. (2010), Yade Documentation. The Yade Project. (http://yade-dem.org/doc/)

Sweijen, T., Hassanizadeh, M., and Chareyre B. (2014), Pore-scale modeling of swelling porous media; application to superabsorbent polymers. In XX. International Conference on Computational Methods in Water Resources, Stuttgart, page 227.

Tejada, I.G., Sibille, L., Chareyre, B. (2015), Micromechanical modeling of internal erosion by suffusion in soils, Geomechanics group annual report.

Thoeni, K. (2013). *Performance test*, online content on the Yade-DEM website. https://yade-dem.org/wiki/Performance_Test

Toraldo, M., Chareyre, B., Sibille, L. (2015), Numerical modelling of the localized fluidization in a saturated granular medium using the coupled method DEM-PFV, Geomechanics group annual report.

Yuan C., Chareyre, B., Darve, F. (2015), Pore-scale simulations of two-phase flow in granular materials, Geomechanics group annual report .

Yuan, C., Chareyre, B., and Darve F. (2014), Pore-scale simulations of drainage for two-phase flow in dense sphere packings. *In XX. International Conference on Computational Methods in Water Resources*, Stuttgart, page 232.

Part Six: Earth construction

Adobe construction modeling by discrete element method: first methodological steps

Dominique Daudon[a24], Yannick Sieffert[a], Osvaldo Albarracín[b], Lucas Garino Libardi[c], Gustavo Navarta[c],

[a] *Univ. Grenoble Alpes, 3SR, F-38000Grenoble, France, firstname.name@3sr-grenoble.fr*

[b]*IRPHa, Univ. San Juan- I. de la Roza y Meglioli. C.P. 5400. San Juan, Argentina. osvaldo_albarracin@yahoo.com.ar.;* [c]*IDIA, Univ. San Juan, Av. Gral. San Martín 1290 (O) - CP 5400 - San Juan – Argentina. lgarino@unsj.edu.ar, gnavarta@unsj.edu.ar.*

ABSTRACT

Adobe constructions are used worldwide but especially in regions where transportation of constructing manufactured materials or wood are costly like in Andean or oriental Himalayan mountains. These regions are often very seismic and this type of housing is very vulnerable. However, vernacular architecture may be the way to more sustainability, as thermal, acoustical property, and environmental impact reveals his qualities. But it suffers of less mechanical resistance especially to earthquake and do not have any codification of building rules in the majority of the countries. In order to fill this gap, numerical modeling is necessary. A few studies are made with the discrete elements method. The paper presents experimental and DEM studies at a real scale and at a small scale in order to valid the ability of DEM for modeling adobe housing.

First published in 4th International Conference on Building Resilience & 3rd Annual ANDROID Disaster Resilience Network -Procedia Economics and Finance, Volume 18, Pages 1-976 (2014),(ISSN: 2212-5671).http://dx.doi.org/10.1016/S2212-5671(14)00937-X

INTRODUCTION

Adobe constructions

The adobe bricks have been used for about eleven millennia. Adobe bricks are a sun-dried earth bricks, and are one of the most used vernacular earth construction process such as rammed earth, and quincha-baharaque walls. In Europe, the onset of adobe architecture in the

24

* Dominique Daudon. Tel.: +33-4-7682-7044; fax: +33-4-7682-7043.*E-mail address:* Dominique.daudon@3sr-grenoble.fr.

western basin Mediterranean has revealed the complexity of the origins that can be attributed to a "phenomenon" that develops at the beginning of the Iron Age (Chazelles 1995). It is the testimony of the architecture of many centuries.

In European countries also, some vernacular architecture are using earth construction and the south of France near Toulouse is one of the French region who still have some old farm in adobe or mixt adobe cooked earth brick (fig 1).

In some South America's cities , there are churches of the 17eme in Adobe still in run but the premises where relieved in 900 BC (Zegarra 2000). In these countries, the adobe constructions are an old construction process (Cirvini 2011) devoted now to quite poorest places as types of construction are often linked, such as South America and Himalaya, with difficulties to build in some part of the world: in high mountain and less forested parts, highest seismicity zones and generally arid regions.

As it is not cooked and stabilized the adobe bricks are fragile and also susceptible to be largely damaged by climatic events. To prevent degradation they need to be highly maintained and generally covered by earth, cement, and painted.

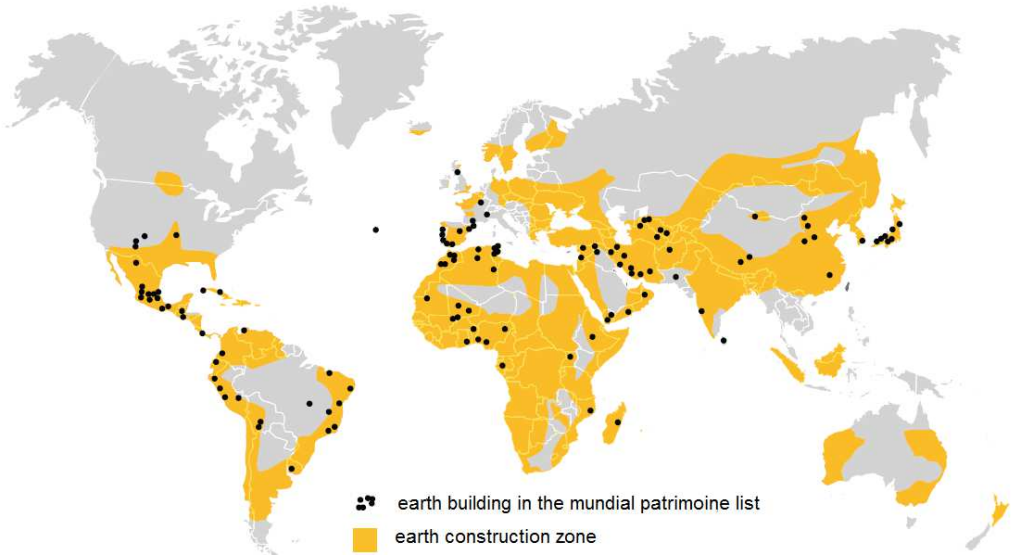

Fig. 1: **earth construction in the world with patrimonies UNESCO (**adapted from Gandreau & al 2010)

Characterization studies

Nowadays, the use of adobe is declining because of the abundance of manufactured building material (Parra-Saldivar, Batty, 2006). Some recommendation guides for adobe construction exists see Morales et al. (1993), Minke (2001), HIAEE (2004) et ASTM (2010) and in Peru a building code is used (Waffer 2010) because this material and auto-building technic are really common and escape to the actual marketing and building lobbies. In 2010, ASTM provides the first recommendations guide that may be offers more legal future to adobe constructions. In some country such as Argentina, this type of construction is prohibited due to the seismic vulnerability. Two major earthquakes suck this country in 1861 in Mendoza and in 1945 in San Juan's. Nevertheless adobe constructions still remain largely used by the rural populations for tradition and/or financial reasons, and lot of vestiges exists in the Cuyo region (Cirvini 2011).

Seismic behavior of adobe masonry

As said before, the regions where adobes are the most dwelling coincide with high seismic regions. Large earth cities have been destroyed in the past and in the recent time: Bam's

citadel in southeastern Iran was the largest adobe city built before his destruction by a seismic event in 2003. The fortified town on the Silk Road was built in the first century BC. Listed as UNESCO heritage; it was always inhabited until the 2003 earthquake which devastated the city. The mud brick adobes therefore appear to be an efficient material that can withstand for centuries except in case of an earthquake. This weakness is due to the fact that the constructions are not reinforced. Earth constructions; at the level of material, have low strengtheners resistance, even compacted, except if cement or fiber (generally vegetal) is added in the paste (Alvarez-Ramirez 2012). In the Himalayan range, in order to increase the seismic behavior people insert wood in constructions, creating some isolators and separating between wall panels which leads to limited the total deformation of panels.

In South America, the seismic resistance of adobe constructions have been studied largely in Colombia, Chili, Argentina, but overall in Peru by pioneer M. Blondet's research team. For example, the last earthquake of 2010 in Chile has destroyed more than 140000 houses with a majority constructed in adobe without anti-seismic reinforcement. (Fundación Terram, 2010). The problems of adobe constructions are caused mainly by the weight of the structure, the low resistance and its behavior breaking (Blondet, 2003). The contemporain studies were essentially focused on construction amelioration designs in avoiding currents construction errors: height of the house, too large panels without chain, room disposition, house position in the relief and also good fabrication of the adobe himself with right proportion of each component (Minke 1993, Jimenez 2007, Morales 1993, et cetera. Large studies have been done by the university catolica pontifica de Peru for years in order to understand the seismic behavior and structural approaches to strengthen : wall's corners with plastic network, metallic on, adding cane bars near the top to circle, and to repair the dwelling after the event when possible(Cristafulli 2008). In fact, all countries would tend to replace the dried brick by the cooked one, more rigid, and more reliable if correctly used, and the most new constructions when financially is met is to build housing and building in "mamposteria encadenada" that is to say, to constructs reinforce concrete column and beams around mamposterias panels)

Resilience and sustainability of adobe constructions

With sustainability approaches and re-using development in Civil engineering (Sieffert 2014), adobe construction is a way to rediscover. A lot of recent books and articles on this subject are actually easily to find (Schroder 2010, Morton 2010 Seth 2012, Sanchez 2008) Note that the pioneer work is the architect Minke (2000, 2001, 2006) who also have travelled in Himalayan and Andean countries in order to increase and promote the local construction technic to resist to seism event.

Almost all land mineral clay could be used in constructions (Houben, 2006). At all stages of its use, it requires very little gray energy. Available locally, the land requires no transportation, no processing or expensive cooking energy. Maintenance and repairs are easy. End of life, the frame is destroyed and the earth can be re-used or returned to the soil. Its ecological footprint close to zero represent a huge advantage over the warmer climate and the need to reduce energy consumption, as demonstrated by Shukla (2009) in the study of a new construction in India.

Waffer 2010 demonstrated in his studies that adobe has significant advantages over materials industrial. It has the ability to regulate the air humidity, the stored heat, save energy consumption, produce virtually no pollution, to be 100% reusable, and preserve the wood and other materials while absorbing organic pollutants in the indoor air of homes.

In a scenario where natural resources are limited, the adobe constructions could be a very interesting material, not only in developing countries but also in countries Cold America and Europe (Chel and Tiwari, 2009). Indeed, earth is cheap, environmentally sustainable and especially abundant (Binici et al., 2005). The issue for the future is then to try to study this type of material and building in the modern context, and needs of security, aesthetic, and take experience of the previous constructions cultures. For example, thermal properties are quite good as for a density of 1600 kg/m3 (2500 kg/m3 for reinforced concrete), it gives a thermal conductivity of 0.81 ((W/m.K)) better than concrete (1.81 (W/m.K)) and a specific warm de 650 (J/Kg.K) in comparison with 850 (J/Kg.K) for concrete.

Numerical modelling of masonry structure is well done in finite elements, using some homogenization technic as MEF with largely numbers of interface elements are generally a challenge in geometry description, parameters evaluation and in time calculation (Illampas 2011). In fact, the numerical method to use depends on the aims of the calculation, and homogenization techniques are needed in the FEM when a global behavior is required for the study, especially in the elastic domain (Colas 2009). But when some more local process is or when it is not possible to study globally like in arches architecture, or in some antic architecture like column, the FEM method may be not pertinent. Cundall (1971) proposes a discrete element methods code for some study of geotechnical material (rock slopes with joints). As fractured rock massif modelling is not so far from masonry modelling, pioneers applications are devotes to Lourenco (1996) and Lemos (1997) as the method could describe the behavior of every collection of solids interacting together. A lot of different vernacular and more contemporizing construction have been studied by this way, for example the Pont du Gard (Chetouane 2004, Kiyono 2006), behavior of classical masonry in cooked earth brick (Bui 2012) and stone masonry (Mohebkhah 2012). When done after a disaster, and aiming to re-analysis the FEM calculation of the behavior of a structure consisted in general in first static loading and naturel vibration mode calculation (ref Peruvian church), in order to understand the collapse scheme. Some experimental studies are also modelled in order to get the parameter needed in the code, and proceed then to various exploratory studies. The common are the simple compression, shear and tension of the jointed structure and of a brick itself. Then more complex tests are modelled as cyclic ones and real seismic one on vibrating table in real or reduced scales.

In fact both numerical method finite element and discrete element fail in the representation of the real structures behaviors as parameters properties and overall its variability may need a specific approach that may be sometime rapid (Daudon 2012), but with strong hypothesis on the variability of the parameters (Baroth 2012).

As a resume, the capacity of the vernacular adobe construction to be one of the sustainable materials of the future is not to demonstrate more. Facing disaster situation, it is generally a fragile material as special care as not be done in many points: material, but also anarchic disposition. In fact disaster situation is the key possibility of reconstructing with the attention needed to pursuit the vernacular architecture that is generally in the zone and better it in order to gain is sustainability, reliability and increase resilience. As only few building codification and resistance verification exist in the world for this construction, the way to design this type of auto construction is always open. In order to explore the possibility, the authors have performed reduced scale, and real scale tests aimed to characterize mechanicals parameters for furthers exploratory studies over the seismic loading of Caceute (Argentine 1977) of a real tested structure.

NUMERICAL MODELING WITH 3DEC DEM

Discrete elements modeling rose in the 1970 with first application to soil and rock materials. This type of calculation codes consider the structure or matter as a collection of particles in interaction one from each other over the 2nd principle of dynamical equations. It was first developed in 2 dimension with circular particle due to contact properties to manage. Large amount of different particles codes exist now in 3D accepting various shapes of particles and various problems.

In the case of masonry structures, this type of code is well adapted as the bricks are considered as a particle, and the joint may be assumed by the contact behavior laws chosen. The contact law is the key parameter when the particles are considered as rigid solid.

The law may be very simple as elastic one for example, needing only 2 parameters assumed to be the rigidity in normal contact and in tangential contact. More complex one's may integrate some contact laws cut in shear or tension, with or without frictions, as plastic ones with the needed parameters to fulfill.

In the case of adobe structures modeling, the particle may be rigid and the damage will concentrate only on the joints or elastic-plastic in order to consider the possible damage of the brick itself.

The chosen code to verify the DEM ability to model such construction is Itasca's one 3DEC (Itasca 2011). In the context of future professional work and teaching modelling, the code gives the tutorial support needed and allows a lot of other possibility such as thermal behavior, rebar's inclusion, and seismic calculation. Lot of literature exist on the discrete element method (Cundall 1971, Donze 2009)

Ability of the DEM code to reproduce the behavior

In the discrete element model of a adobe or brick construction some mechanical parameters are needed. The brick one's are: density, rigidity normal and tangential, and if needed by the behavior choice: elastic brick or rigid one young and Poisson modulus. The numerical values of the parameters may be defined according to experiments and literature if not know (table 1)

And the joint may be as for the bricks, rigidity normal and tangential, and if needed by the behavior choice: elastic brick or rigid one young and Poisson modulus, and friction coefficient.

A simple shear test of an earth joint between two commercial adobe bricks of dimension 24cm*12.5cm*7.5cm was modelled in order to reproduce the experimental shear resistance obtained of 172 daN that is approximately 0.57 MPa, in current range values for this type of material (de Almeida 2012, Mile 1980).

Fig 2: a) experimental vertical stress/strain curve b) Shear test by 45° compression of the adobe assembly . c) End of the test

The load displacement curve is represented in figure 2a, that lead to a wall shear strength value of approximately 0.9 MPa, not too far from the single brick one. The shear test was reproduced using the parameters in the table 1

The figure 3 presents both the experimental and the numerical wall. It shows that the displacement are in the same range even if not exactly same due to choice of the numerical collapse time. Moreover, the numerical vertical loading curve gives a similar value of the collapse vertical force that has been applied to the wall sample (7.8kN for the experimental one and 8kN for the numerical one.

Table 1: Mechanical parameter of the simulation

Mechanical properties	range
Density of Adobe	1800 kg/m3
Bulk modulus	64 MPa
Shear Modulus	48 MPa5
Joint Normal Rigidity	220 GigaN
Joint Tangential Rigidity	32 GigaN
Joint Shear Rupture	5.6 MPa
Joint Tension Rupture	0.49 MPa
Joint Dilation Angle	0
Joint Friction angle	25°

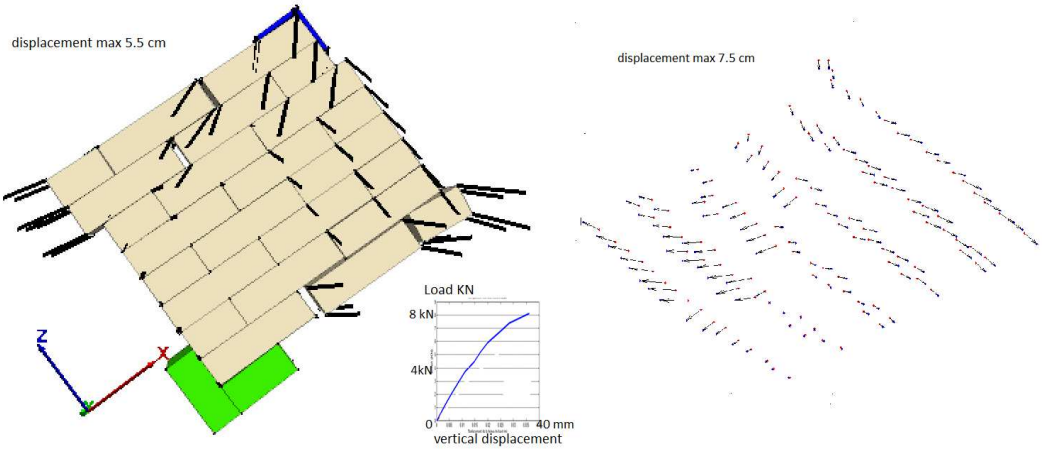

Fig.3: numerical wall displacements by 3DEC with measured one afterimage analysis by TRACER (Combe & Richefeu 2013) and force/displacement numerical curve at the collapse.

Vibrating table test modeling

Dynamic tests of a 1:2 scale model built with adobes were made(Fig 4a). For this test the shaking table of Earthquake Research Institute of the National University of San Juan, Argentina, was used.This table is essentially a metal platform of 2.90m by 2.10m of side, connected to the foundation by two vertical planes bi-articulated .The capacity table is 10t and can reach for this mass an horizontal acceleration of 0.50 g . The horizontal acceleration is achieved by a double acting hydraulic actuator that includes a system of closed loop control .The model has a height of 1.45m by 2.00m of side, and has two side openings. The dynamic test is divided into two stages. First, the period of vibration of the structure is located. Then, for this period, dynamic tests were performed using sine waves with gradual increases acceleration.

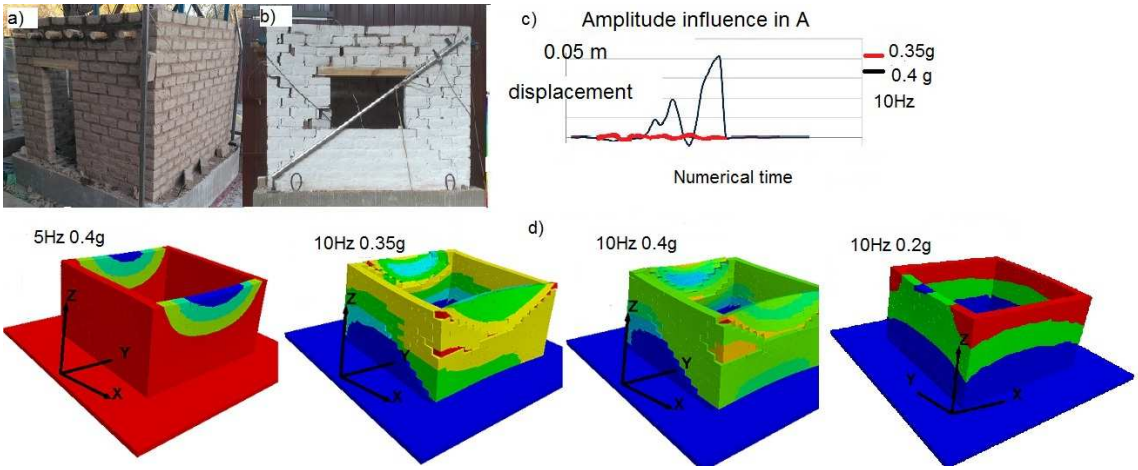

Fig.4 : a) the Adobe House, b) final state of a the end of the 3 serial tests c) Amplitude influence on joints displacements from the numerical simulation d) Displacement scheme at the same step, for the numerical simulation tests. from left to right the maximum amplitude of displacement of the brick is 7.6 cm(5Hz-0.4g) ;11,3 cm(10Hz-0.35g) ; 15cm(10Hz-0.4g) 6cm (10hz-0.2g);

Figure 4b shows the final state of the model after the application of a dynamic movement with a horizontal acceleration of 0.40g and a frequency of 5Hz. The entire experimental tests were tried in the numerical model but without the opening windows and doors in a first intention (fig 4d). The influence of the frequency is well demonstrated by the comparison of the 2 first left schemes. The amplitude influence is easy to see on the 2 right ones. The down curves show influences of amplitude acceleration for (frequency 10Hz) on the top point of the out of plane wall (Fig 4c).

Other numerical simulations of small scale experimental tests (not presented here) where done in order to validate the ability of reproducing natural frequency of the construction in the aim of proposing a calibration methodology of the numerical parameters. In fact, some nondestructive characterization technique of building health are using a natural frequency characterization by ambient noise and the challenge of characterizing the mechanical characteristic of some modeling parameters may be done by this way in elastic behavior (Montella 2013, Miggliaccio 2013).

Rather few results are presented here, and it has to be completed and exploited with more rigorous developments in order to compare with measurements of the preliminary numerical tests, but the possibilities are interesting in order to do large influence parameters campaigns in the future, when complete calibrations of the numerical parameters is done.

CONCLUSION

The aim of this paper is to present some modeling that may be used in the future for earth construction modeling. As this vernacular type of construction largely used from centuries, may be one of the future, regarding to the great advantage it presents in the sustainability way of re-using, law impact Carbone, and raw materials avoiding such as large amount of sand as in the concrete construction. In fact, as the building codes for adobe construction exist only in few countries, it may be a challenge to enlarge that those code to European country in order to define new design construction codes that would allow this type of sustainable constructions. In the case of the present study, other simulations have been done but not presented as the

characterization of the existing construction may be done by natural frequency measuring. In fact, the development for the future is in term of mechanical parameters characterization by numerical optimization on the discrete element simulations. Moreover, it will be possible to have adequate procedure in order to describe a building code as it exist for concrete structure and enchained masonry ones.

ACKNOWLEDGEMENTS

The author would like to acknowledges : all the students of Licence 3 MMK, Master 1 GCI, Master 2 SIM, and the two Italians Erasmus students of San Frederico (Napoli) that have participated, for there help and enthusiasm in developing the numerical tools; The VOR federation for supporting financially the Erasmus students, and the new collaboration with IDIA San Juan university Argentina, and the Rhone Alpes region for providing the founding for the 3DEC version in innovative teaching at the Grenoble University.

This paper from 3SR laboratory is part of the Labex Tech21.

REFERENCES

Alavéz-Ramírez, R., Montes-García, P., Martínez-Reyes, J., Altamirano-Juárez, D. C., & Gochi-Ponce, Y. (2012). The use of sugarcane bagasse ash and lime to improve the durability and mechanical properties of compacted soil blocks. Construction and Building Materials, 34, 296-305.

Mohebkhah A.. Tasnimi A (2012) Distinct Element Modeling of Openings Masonry-Infilled Steel Frames The Open Construction and Building Technology Journal, 2012, 6, (Suppl 1-M2) 42-49

ASTM (2010). Standard Guide for Design of Earthen Wall Building Systems. WestConshohocken, ASTM International. (Standard E2392, 2010).

Baroth J., Schoefs F., Breysse D. (coord), Construction reliability, ISTE Ltd - Wiley, 368 p., 2011.

Binici, H., Aksogan, O. and Shah T. (2005). Investigation of fibre reinforced mud brick as a building material. Construction and Building Materials, n°19, p.313-318.

Blondet, M., Villa García G., Loaiza¿ C. (2003)Viviendas Sismoresistantes De Tierra ?: Una Vision A Futuro. Capítulo de Ingeniería Civil del Consejo Departamental de Loreto del Colegio de Ingenieros del Perú XIV Congreso Nacionale De Ingeniera Civil - Iquitos 2003

Bui T.T., Limam A., (2012)"Masonry Walls under Membrane or Bending Loading Cases: Experiments and Discrete Element Analysis", in B.H.V. Topping, (Editor), "Proceedings of the Eleventh International Conference on Computational Structures Technology", Civil-Comp Press, Stirlingshire, UK, Paper 119, 2012. doi:10.4203/ccp.99.119

Chazelles C.A.(1995) Les origines de la construction en adobe en Extrê1lle-Occident Sur les pas des Grecs en Occident Collection Etudes Massalièles, 4 (1995), pp. 49-58

Chel, A. and Tiwari G.N., (2009). Thermal performance and embodied energy analysis of a passive house - Case study of vault roof mud-house in India. Applied Energ., 86: 1956-1969.

Chetouane B., (2004) Approche combinée éléments finis-éléments discrets pour la modélisation des structures maçonnées, PhD thesis, Université de Montpellier 2, 2004.

Cirvini S.A. (2011) Vernacular Architecture in the Cuyo Region (Argentina) ACE: Architecture, City and Environment = Arquitectura, Ciudad y Entorno [en línea]. 2011, Año VI, núm. 17 Octubre. P. 15-36

Colas A.S., Morel J.C. and Garnier D.(2009) 2D modelling of a dry joint masonry wall retaining a pulverulent Int. J. Numer. Anal. Meth. Geomech. 2009; pp:1–13

Combe G., Richefeu V. (2013). TRACKER : A particle image tracking (PIT) technique dedicated to nonsmooth motions involved in granular packings. In AIP Conference Proceedings, vol. 1542, p. 461.

Crisafulli FJ.(2008) Rehabilitacion sismica de una bodega de adobe 20eme Jornadas Argentinas de Ingeniería Estructural 15-17 octobre 2008 – Buenos aires

Cundall P. A (1971)., "A computer model for simulating progressive large scale movements in blocky rock systems", Proceedings Symposium Int. Soc. Rock Mech., Nancy Metz, vol. 1, p. Paper II–8, 1971

Daudon,D. Baroth J, Ma Y, Perrotin P, Mommessin M (2013)Sensitivity of a reinforced concrete protective gallery under a snow avalanche load Structural Safety 41, 47-56 2013

Donzé FV, Richefeu V, Magnier SA (2009) Advances in discrete element method applied to soil, rock and concrete mechanics Electron J Geotech Eng 8,

Fundación Terram (2010). Sismo deja desastre ecológico en Chile. In Fundación Terram,[www.terram.cl, on 26 juin 2014].

Gandreau D., Delboy L.(2010), sous la direction de Joffroy T., CRAterre-ENSAG, 2010. Patrimoine mondial, Inventaire et situation des biens construits en terre, UNESCO/CH/CPM, Paris //

HEIAA (2010) Centro de Investigación Hábitat y Energía Instituto de Arte Americano n°4 Construcción con tierra ISSN 1669-8932 -

Houben, H Guillaud, H.,., CRAterre, (2006). Traité de construction en terre, éditions Parenthèses, Marseille. /

Islam, M.S. and Watanabe, H. (2004). FEM simulation of seismic behaviour of adobe structures. 13th World Conference on Earthquake Engineering.

ITASCA (2011) – 3DEC reference guide

Jimenez D., C. and Canas G., I. (2007). The selection of soils for unstabilised earthbuilding: A normative review. Construction and Building Materials, n°21, p.237-251

Kiyono, J. ,Robin J.S. Spence and Tadayoshi Nakashimac (2006) Dynamic behavior of masonry structures under pyroclastic flows Journal of Natural Disaster Science, Volume 28, Number 2, 2006, pp73-83

Lemos, L.V. (1997) "Discrete element modeling of the seismic behavior of stone masonry arches", Computer Methods in Structural Masonry-4, In Pande, Middleton and Kralj Eds., E and FN Spon: London,1997, pp. 220-227.

Lourenco,P.B. 1996"Computational strategies for masonry structures",Ph. D. Thesis, Delft University of Technology, Delft, The Nether-lands, 1996

Montella V. (2013) Master 2 erasmus student report University Joseph Fourier, available at author's mail direction

Migliaccio M. (2013) Master 2 erasmus student report University Joseph Fourier, available at author's mail direction4

Minke, G. (2000) Earth Construction Handbook: The Building Material Earth in Modern Architecture

Minke, G. (2001). Manual de construcción para viviendas antisísmicas de tierra.Forschungslabor für Experimentelles Bauen , Universidad de Kassel, Alemania. 51 p.

Minke, G. (2006). Building with Earth Design and Technology of a Sustainable Architecture. Birkhäuser - Publishers for Architecture, Berlin. 198 p.

Morales, R., Yamashiro, R., Sánchez, A., Torres, R., Irala, C., Morales, O. y Rengifo, L.(1993). Diseno sismico de construcciones de adobe. In Biblioteca Virtual En Salud yDesastres, [En ligne].http://desastres.usac.edu.gt/documentos/pdf/spa/doc12964/doc12964-contenido.pdf

Morton,T. (2010) Earth Masonry: Design and Construction Guidelines

Parra-Saldivar, L. and Batty W. (2006). Thermal behaviour of adobe constructions . Building and Environment, n°41, p.1892-1904

Illampas R., Charmpis D.C., and Ioannou I Dynamic finite element analysis of the eath masonry structures on experimental materials datas Y COMPDYN 2011 III g M. Papadrakakis, M. Fragiadakis, V. Plevris (eds.)Corfu, Greece, 26–28 May 2011

Sanchez L., Sanchez A.,(2008) Adobe Houses for Today: Flexible Plans for Your Adobe Home

Schroder L, Ogletree, V. (2010) Adobe Homes for All Climates Simple, Affordable, and Earthquake-Resistant Natural Building Techniques by Kindle Edition

Seth S. and Seth L. (2012) Adobe Homes and Interiors of Taos, Santa Fe, and the Southwest

Sieffert, Y. Huygen J.M., Daudon D. (2014) Sustainable construction with repurposed materials in the context of a civil engineering–architecture collaboration Journal of Cleaner Production, Available online 16 December 2013,

Shukla, A., Tiwari, G.N. and Sodha, M.S. (2009). Embodied energy analysis of adobe house. Renewable Energy. n°34, p.755-761.

Wafer RF (2010) L'adobe, une solution durable pour la construction d'habitation écologique en zone à forte activité sismique comme le chili Mémoire de Master Centre universitaire de formation en environnement Sherbrooke, Québec, Canada, Octobre 2010

Zegarra, Ls S., Bartolomé, A, Quiun, D and Villa Garcia G. (2000)Reinforcement of existing adobe houses-Arid Lands Newsletter May 2000, Issue No. 47ISSN: 1092-5481

Special thanks to our sponsors and partners